Towards Identification of Rotordynamic Properties for Seals in Multiphase Flow Using Active Magnetic Bearings. Design and Commissioning of a Novel Test Facility.

Voigt, Andreas Jauernik

Publication date:
2016

Document Version
Publisher's PDF, also known as Version of record

Towards Identification of Rotordynamic Properties for Seals in Multiphase Flow Using Active Magnetic Bearings

Design and Commissioning of a Novel Test Facility

PhD Thesis

$$(EIv'')'' = q - \rho A \ddot{v}$$

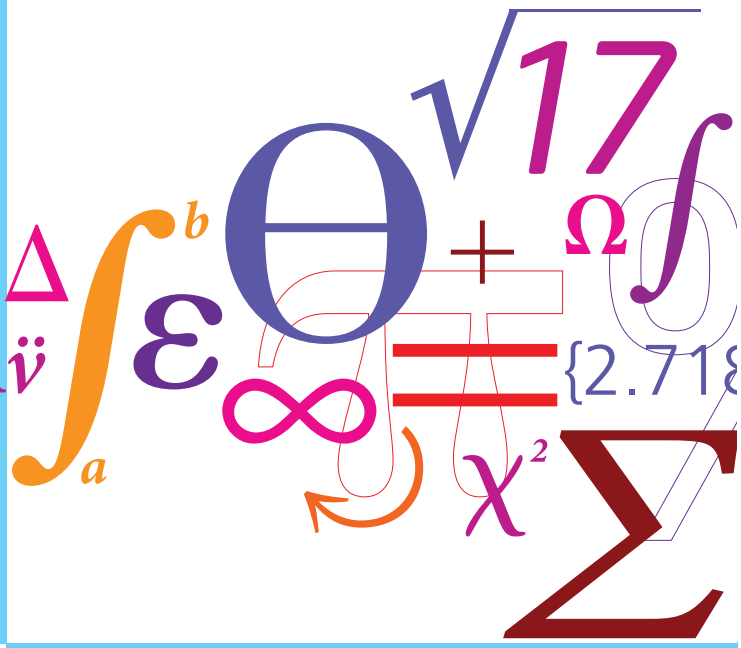

Andreas Jauernik Voigt
DCAMM Special Report No. S212
June 2016

DTU Mechanical Engineering
Department of Mechanical Engineering

Towards Identification of Rotordynamic Properties for Seals in Multiphase Flow Using Active Magnetic Bearings

Design and Commissioning of a Novel Test Facility

Andreas Jauernik Voigt

Technical University of Denmark
Kgs. Lyngby, Denmark, 2016

Title of the thesis
Towards Identification of Rotordynamic Properties for Seals in Multiphase Flow Using Active Magnetic Bearings – Design and Commissioning of a Novel Test Facility

PhD student
Andreas Jauernik Voigt
ajavo@mek.dtu.dk

Principal supervisor
Ilmar Ferreira Santos
ifs@mek.dtu.dk

Industrial supervisor
Kenny Krogh Nielsen
kenny.krogh-nielsen@lr.org

Third party supervisor
Harald Underbakke
hun@statoil.com

Technical University of Denmark
Department of Mechanical Engineering
Section of Solid Mechanics
Nils Koppels Allé, Building 404
DK-2800 Kgs. Lyngby
Denmark
Phone: (+45) 45 25 25 25
Email: info@mek.dtu.dk
www.mek.dtu.dk

DCAMM Special Report no.: S212
ISBN: 978-87-7475-464-0

Summary (English)

The energy sector's recent drive towards subsea oil and gas production brings about a requirement to locate process equipment in deep-water installations for which performing liquid and gas separation on the well stream is limited. Consequently, the subsea installed pumps and compressors are now required to handle multiphase fluids. The difference between fundamental properties of single phase and multiphase flows entails that multiphase flow impact on the rotordynamics of rotating machines requires special treatment. Furthermore, turbomachinery seals are pivotal for the performance of pumps and compressors for which reason the ability to predict the complex interaction between fluid dynamics and rotordynamics within these seals is a key aspect in the design of rotating equipment. Numerical tools offering predictive capabilities for seals subjected to multiphase flow conditions are currently being developed and refined, however a pronounced lack of experimental data renders benchmarking and validation impossible.

This thesis focusses on documenting the design and commissioning of a test facility enabling the much needed experimental identification of rotordynamic properties for turbomachinery seals in both single phase and multiphase flow. The commissioning phase of the test facility solely employs single phase air flow for performance assessment of the test facility and no experimental multiphase results are included in the thesis. The test facility consists of four modules of which an industrial scale rotordynamic test bench consisting of two radial active magnetic bearings with an embedded Hall sensor system, a rigid rotor, and a drive unit acts as the hub. In addition, the test facility includes a module facilitating calibration of the state of the art system of Hall sensors which provides important contact free force measurement capabilities. The third module houses the smooth annular test seals and the fourth module adds a single phase air flow supply to the test facility infrastructure. For experimental identification purposes the ability to acquire precise information of the forces exerted onto the rotor by the seal flow is of paramount importance. Consequently, this subject receives substantial attention throughout the thesis with a strong focus on the calibration necessary for the Hall sensor system to be of any practical use. The presented calibration results and subsequent performance validation campaign documents that the test facility is capable of quantifying forces with high precision. With the addition of rotor displacement measurements the rotordynamic properties of the test seals can be determined. This is demonstrated for a limited range of seal flow perturbation frequencies using a time domain identification scheme. Additionally, the use of commercial computational fluid dynamics software for estimating rotordynamic properties of seals in a range of multiphase flow conditions is exemplified in the thesis. The thesis documents a first step towards establishing validated numerical models for multiphase seal analysis and forms a fundamental basis for future studies within the research field.

Resumé (Dansk)

Energisektoren bevæger sig i stigende grad imod undersøisk olie- og gasproduktion, hvilket medfører placering af procesudstyr i anlæg under havets overflade. Muligheden for separation af væske- og gas-fraktionerne i brønd-flowet er under disse forhold stærkt begrænset og forbundet med store økonomiske omkostninger. Dette medfører et ønske om, at undersøisk installerede pumper og kompressorer nu skal kunne håndtere flerfase strømninger. De grundlæggende egenskaber for enfasede og flerfasede strømninger er signifikant forskellige, hvilket medfører, at flerfase strømningernes indflydelse på rotordynamikken af roterende maskiner kræver særbehandling. Ydermere er turbomaskineritætninger afgørende for funktionaliteten af pumper og kompressorer, hvorfor evnen til at forudsige den komplekse interaktion mellem fluid- og rotordynamik i disse tætninger er et centralt aspekt ved design af roterende udstyr. Numeriske værktøjer, der kan forudsige rotordynamiske egenskaber for tætninger udsat for flerfase flow, er under udvikling, men den udtalte mangel på eksperimentelle data umuliggør benchmarking og validering af disse værktøjer.

Denne afhandling dokumenterer designet og indkøringen af en testmaskine, som faciliterer eksperimentel identifikation af turbomaskineritætningers rotordynamiske egenskaber i både enkeltfase og flerfase flow. Indkøringen af testmaskinen er udført udelukkende ved brug af enkeltfase luftflow med det formål at vurdere test maskinens funktionalitet og der præsenteres ingen eksperimentelle multifase resultater i afhandlingen. Testmaskinen består af fire moduler, hvoraf en rotordynamisk testbænk baseret på aktive magnetiske lejer med et state of the art Hall-sensor system udgør kernen. Desuden inkluderer testmaskinen et kalibreringsmodul til kalibrering af Hall sensor systemet. Det tredje modul huser testtætningerne og det fjerde modul tilføjer en enkeltfase luftforsyning til testmaskinens infrastruktur. Evnen til at kunne identificere de rotordynamiske egenskaber af testtætningerne er stærkt afhængig af en præcis kvantificering af de kræfter, der udøves på rotoren af strømninger i tætningerne. Derfor er der igennem afhandlingen fokus på den nødvendige kalibrering af Hall sensor systemet, hvilket tilvejebringer kraftmålingsfunktionaliteten af testmaskinen. De i afhandlingen præsenterede kalibrerings- og validerings-resultater dokumenterer, at Hall sensor systemet gør testmaskinen i stand til at kvantificere kræfter med høj præcision. Med tilføjelsen af rotor positionsmålinger kan de rotordynamiske egenskaber af testtætningerne bestemmes ved brug af en tidsdomæne identifikationsmetodologi. Dette er i afhandlingen dokumenteret for et afgrænset udvalg af operationsbetingelser. Ydermere dokumenterer afhandlingen anvendelse af et kommercielt tilgængeligt computational fluid dynamics software til numerisk at estimere rotordynamiske egenskaber for tætninger i multifase strømninger. Afhandlingen dokumenterer et første skridt imod validering af numeriske modeller for flerfase tætningsanalyser og lægger fundamentet

for fremtidige undersøgelser inden for forskningsfeltet.

Preface

This thesis is submitted as partial fulfilment of the requirements for obtaining the Danish PhD degree. The work has been carried out from January 2012 to June 2016 at the Section of Solid Mechanics (FAM), Department of Mechanical Engineering (MEK), Technical University of Denmark (DTU) and at Lloyd's Register Consulting (LRC). The work was funded by LRC and the Innovation Fund Denmark under the Industrial PhD programme. Financial support for the test facility was provided by DTU, LRC, TOTAL and OneSubsea. The project was supervised by university supervisor Professor, Dr.-Ing., Dr.techn. Ilmar Ferreira Santos (DTU), industry supervisor Dr. Kenny Krogh Nielsen (LRC) and third-party supervisor Harald Underbakke (STATOIL), to whom I wish to express my sincere gratitude.

I am truly indebted to professor Ilmar Ferreira Santos for his motivation, guidance and support in both professional and personal matters throughout my Bachelor, Master, and PhD studies. Ilmar's dedication to his work is inspiring and his emphatic and welcoming nature is pivotal for making the mechatronics research group at DTU a great joy to work in. Dr. Kenny Krogh Nielsen has provided me with a unique opportunity by employing me to do this PhD for which I am grateful. I owe Kenny a special thank you for his trust and support throughout the project. Kenny's positive outlook, vast technical expertise and emphatic disposition makes him a great team leader and a joy to work with.

Thanks to my closest colleagues at DTU, Alejandro V. Cerda, Jon S. Larsen, Said Lahriri, Bo B. Nielsen, Nikolaj A. Dagnæs-Hansen, Jonas S. Lauridsen, Emil Bureau, Søren Enemark, Jorge A. G. Salazar, Cesar A. L. L. da Fonseca, Geraldo F. de S. Rebouças, Fabián G.P. Vásquez, Lukas R. S. Theisen, Martin Sander Nielsen and Sebastian von Osmanski for the countless hours shared at the office exchanging ideas and knowledge. I also thank my closest colleagues at LRC, Eythor Sigurdsson, Morten R. Bøgild, Piero Iudiciani, Robert Stronach, Stefan L. Glimberg, Max La Cour Christensen, Morten Theill Jensen, Henning Hartmann, Anna Geske Dylander and Helle Hansen for their support (moral and otherwise) throughout the project.

I owe thanks to the workshop staff at DTU MEK and especially: Torben B. Christensen, Jan Frank Pedersen, Casper Beyer Larsen, Per Bo Nielsen, Allan Rohlin Martensen, Karsten Dahl, Jan Horne Hansen, Morten Berger Jørgensen, Poul-Erik Hyldbo, Claus Grølsted, Benny Edelsten, and Jan Thomas Justesen for their support in what turned

out to be an odyssey into mechatronic design and manufacturing processes.

I wish to thank the Bachelor and Master students whom I have co-supervised during my PhD studies: Mie La Cour Christensen, Leon Nagel, Mikkel Grauballe, Reza Ansari Shirvan, and last but not least Christian Mandrup-Poulsen. I would also like to thank Professor Jens Honore Walther for the collaboration on Mie's and Reza's projects.

I thank my family and friends for their patience and support. I owe a special thank you to my mother Ilona for putting up with the seemingly endless absence and for lending an ear for me to vent my frustrations. Without her unconditional support, especially in the very personally challenging times in the first part of this project, I would not have managed to see it through. Most of all I would like to thank my ever-understanding girlfriend Gry for her selfless and constant support. Her strength and ability to persevere in the face of adversity is something to aspire to.

For my father

Appended publications

[P1] A. J. Voigt, P. Iudiciani, K. K. Nielsen, and I. F. Santos, "CFD Applied for the Identification of Stiffness and Damping Properties for Smooth Annular Turbomachinery Seals in Multiphase Flow," *Proceedings of the ASME Turbo Expo 2016*, 2016.

[P2] A. J. Voigt, C. Mandrup-Poulsen, K. K. Nielsen, and I. F. Santos, "Design and Calibration of a Full Scale Active Magnetic Bearing Based Testing Facility for Investigating Rotordynamic Properties of Turbomachinery Seals in Multiphase Flow," *Proceedings of the ASME Turbo Expo 2016 and accepted for publication in the ASME Journal of Engineering for Gas Turbines and Power*, Seoul, South Korea, 2016.

[P3] A. J. Voigt, J. Lauridsen, C. Mandrup-Poulsen, K. K. Nielsen, and I. F. Santos, "Identification of Parameters in Active Magnetic Bearing Systems," *Accepted for publication in the proceedings of ISMB15*, 2016.

[P4] A. J. Voigt and I. F. Santos, "Theoretical and Experimental Investigation of Force Estimation Errors Using Active Magnetic Bearings With Embedded Hall," *Proceedings of ASME Turbo Expo 2012*, Copenhagen, 2012, pp. 1–15.

Table of Contents

Abbreviations and nomenclature

This nomenclature covers the thesis. The nomenclatures of the appended publications may differ.

Abbreviations

ACT	Actuator
A/D	Analogue to Digital
AMB	Active Magnetic Bearing
ADC	Analog to Digital Converter
BC	Boundary Conditions
CAD	Computer Aided Design
CFD	Computational Fluid Dynamics
CNC	Computer Numeric Control
D/A	Digital to Analogue
DOF	Degree of Freedom
DNS	Direct Numerical Simulation
DSM	Design Structure Matrix
DSP	Digital Signal Processing
DTU	The Technical University of Denmark
EM	Electromagnet
FBD	Free Body Diagram
FE	Finite Element
FEA	Finite Element Analysis
FEM	Finite Element Method
FOSG	Fiber Optic Strain Gauge
FRF	Frequency Response Function
GVF	Gas Volume Fraction
InAs	Indium Arsenide
I/O	Input/Output
IPM	Instationary Perturbation Method
LES	Large Eddy Simulations
LRC	Lloyd's Register Consulting

LVF	Liquid Volume Fraction
MAE	Mean Absolute Error
MBE	Magnetic Bearing Exciter
NDA	Non-Disclosure Agreement
OEM	Original Equipment Manufacturer
PC	Personal Computer
PCB	Printable Circuit Board
PID	Proportional Integral Derivative
PLC	Programmable Logic Controller
PMB	Passive Magnetic Bearing
RANS	Reynolds Averaged Navier-Stokes (equiations)
RMS	Root Mean Square
RSS	Root-Sum-Squared
SDOF	Single Degree of Freedom
SISO	Single Input, Single Output
SHA	Seal Housing Assembly
SST	Shear Stress Transport
VSD	Variable Speed Drive

Latin symbols

$\mathbf{A}$	Vector Potential	[Wb/m]
$\mathbf{B}$	Magnetic flux density vector	[T]
$\mathbf{B}_{sat}$	Saturation flux density vector	[T]
$\mathbf{F}_m$	Lorentz force vector	[N]
$\mathbf{F}_{body}$	Body force	[N]
$\mathbf{F}_{surface}$	Surface force	[N]
$\mathbf{F}_{Hall}$	Force measured by Hall sensors	[N]
$\mathbf{F}_{ext}$	Externally applied force	[N]
$\mathbf{F}_C$	Coupling force	[N]
$\mathbf{F}_I$	Inertia force	[N]
$\mathbf{F}_S$	Seal force	[N]
$\mathbf{I}_H$	Hall sensor control current vector	[A]
$\mathbf{H}$	Magnetic field intensity tensor	[A/m]
$\mathbf{J}$	Current density vector	[C/(m^{2}s)]
$\mathbf{J}_H$	Hall sensor current density vector	[C/(m^{2}s)]
$\mathbf{e}_x$	Unit vector	[—]
$\mathbf{g}$	Gravitational acceleration vector	[—]
$\mathbf{n}$	Surface normal	[-]
$\mathbf{v}_e$	Velocity vector for charge carrier	[m/s]
$\mathbf{v}$	Velocity vector	[m/s]
A	Hall sensor cross sectional area	[m^2]
A_a	Air gap cross section area	[m^2]
A_j	Amplitude	[-]

A_z	2D vector potential	[Wb/m]
B	Scalar magnetic flux density	[T]
C	Damping coefficient	[N$cdot$m/s]
E_t	Total energy	[J]
F	Force	[N]
$F_{A,x}$	AMB A force	[N]
$F_{A,y}$	AMB A force	[N]
$F_{B,x}$	AMB B force	[N]
$F_{B,y}$	AMB B force	[N]
$F_{c,x}$	Coupling force	[N]
$F_{c,y}$	Coupling force	[N]
F	Force	[N]
$F_{app,x}$	Applied force	[N]
$F_{app,y}$	Applied force	[N]
F_{AMB}	AMB force	[N]
$F_{e,x}$	Counter acting Lorentz force	[N]
$F_{m,x}$	Lorentz force	[N]
F_g	Gravitational force	[N]
$F_{num.,AMB}$	Numerical estimation of AMB force	[N]
F_x	x-directional force	[N]
F_y	y-directional force	[N]
Geo	Geometric scaling factor	[−]
H	Magnetic field intensity	[T]
I	Current	[A]
I_H	Scalar Hall sensor control current	[A]
J_z	Current density in z-direction	[C/(m^{2}s)]
K_2	Hall sensor two sensitivity factor	[N/V^2]
K_4	Hall sensor four sensitivity factor	[N/V^2]
K_i	Force equation coefficients	[N/A]
K_x	Force equation coefficients	[N/m]
K	Stiffness coefficient	[N/m]
L	Inductance	[H]
L_{app}	Length parameter	[m]
L_A	Length parameter	[m]
L_B	Length parameter	[m]
M	Inertia coefficient	[kg]
$M_{c,x}$	Coupling moment	[Nm]
$M_{c,y}$	Coupling moment	[Nm]
N	Number of coil turns	[-]
P	Pressure	[Pa]
P_e	Electrical power	[W]
P_m	Mechanical power	[W]
Q	Thermal energy	[J]

R	Electrical resistance	[ohm]
T	Temperature	[°C]
V_H	Hall voltage	[V]
W	Work done	[J]
W_m	Stored energy (potential)	[N·m]
a	Stator pole surface diameter	[m]
b	Stator inner diameter	[m]
c	Stator outer diameter	[m]
d	Height of Hall element	[m]
dv	Differential segment of air volume	[m^3]
e	Charge	[-]
e_i	Internal energy	[J]
f	Force	[N]
f_x	x-directional force	[N]
f_y	y-directional force	[N]
g	Internal stator rounding radius	[m]
h	Enthalpy	[J]
i	Current	[A]
i_0	Bias current	[A]
i_x	Control current	[A]
i_y	Control current	[A]
k	Force coefficient	$[Nm^2/A^2]$
k_i	Force/current factor	[N/A]
k_x	Force/displacement factor	[N/m]
k_u	Voltage/velocity factor	[V·s/m]
l	Length of triangular element side	[m]
$m_{equiv.}$	Mass properties of equivalent SDOF system	[kg]
n	Arbitrary discreet counter	[-]
p	Pole width	[m]
q_e	Charge carrier	[C]
r	Radius of arc	[m]
s	Air gap variable	[m]
s_0	Nominal air gap	[m]
u_i	Error	[-]
w	Width of Hall element	[m]
x	Position variable	[m]
$\dot{x}$	Velocity variable	[m/s]
$\ddot{x}$	Acceleration variable	[m/s^2]
x_i	True value	[-]
$x_{measured,i}$	Measured value	[-]
y	Position variable	[m]
$\dot{y}$	Velocity	[m/s]
$\ddot{y}$	Acceleration	[m/s^2]

z	Position variable	[m]

Greek symbols

α	Angle	[rad]
ω	Perturbation frequency	[Hz]
Ω	Rotational velocity	[Hz]
δ	Nominal seal clearance	[mm]
δ_{ij}	Kronecker delta function	[-]
ϵ	Nominal seal eccentricity	[mm]
η	Angle	[rad]
Φ	Flux	$[\mathrm{T{\cdot}m^2}]$
μ_0	Permeability of vacuum	$\left[\mathrm{N/A^2}\right]$
μ	Permeability	$\left[\mathrm{N/A^2}\right]$
μ_v	Viscosity	[cP]
μ_t	Eddy viscosity	[cP]
μ_r	Relative permeability	[—]
λ	Flux linkage	[Weber-turns]
ρ	Density	$\left[\mathrm{m^{-3}}\right]$
σ_i	Standard deviation	[-]
θ	Angle	[rad]
τ_{ij}	Stress tensor	$[\mathrm{N/m^2}]$

Subscripts

xx	Direct terms	[-]
yy	Direct terms	[-]
xy	Cross-coupling terms	[-]
yx	Cross-coupling terms	[-]

Chapter 1

Introduction

This chapter constitutes the introduction to the research project. The background and the motivation for undertaking the project is presented followed by sections outlining the state of the art for the different main aspects dealt with within the project. Firstly the state of the art for turbomachinery seals in both single phase and multiphase flow is elucidated followed by a section dealing with the state of the art for identification of seal properties. A significant part of the PhD project deals with measuring forces using Active Magnetic Bearings (AMBs) why the different methodologies employed in the literature are reviewed here. Finally the state of the art for applying AMBs in rotordynamic testing is presented.

1.1 Background

The continuously increasing demand for higher productivity and reliability in the energy sector motivates a drive towards designing more efficient rotating machines. In turn, the drive for higher efficiency fuels technology development and research within scientific fields interfacing with the energy sector. The field of rotordynamic research is one of these.

Today industrial rotating machinery employed in the oil and gas industry, such as centrifugal pumps and compressors, are complex and technologically advanced machines consisting of a multitude of component groups. From a rotordynamic viewpoint key components are:

- Rotor transferring energy from a drive unit to an impeller.
- Impellers transferring energy from the rotor to the process fluid.
- Bearings employed to support the rotating rotor.
- Turbomachinery seals employed to mitigate internal pressure leakage by separating regions of high and low pressure while allowing the rotor to rotate freely.

Fig. 1.1 shows a conceptual sketch of a smooth annular seal. For illustrative purposes it is assumed that $P_1 > P_2$ in Fig. 1.1, thus entailing a pressure driven leakage flow

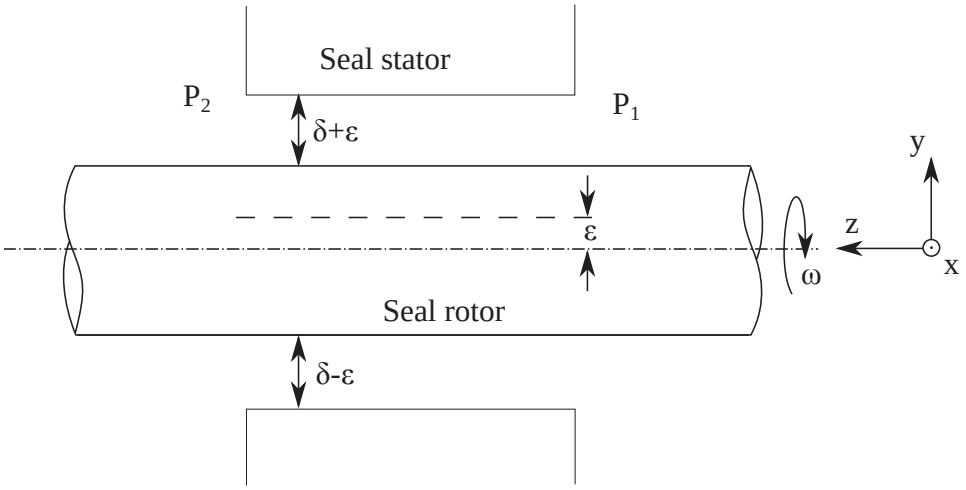

Figure 1.1: Conceptual sketch of an annular seal.

component in the positive z-direction, from the domain with pressure P_1 towards the domain with P_2. The nominal radial seal clearance is defined by δ, and should be kept as small as possible to minimise leakage. Assuming a completely concentric rotor and stator ($\epsilon = 0$), as well as a completely uniform and homogeneous flow field upstream to the seal, the radial seal forces cancel out. However, as the rotating rotor moves within the seal clearance δ, e.g. induced by a mass unbalance or process loads, resulting forces acting on the rotor are generated.

High pressures, small seal clearances and high rotational velocities in compressors and pumps ensure high productivity. However, the rotational velocities are limited by the stability margins of the rotating machinery, specifying the operational range of these [1, 2]. It is well known that the rotordynamic forces generated by the interaction of process fluid, seal rotor and seals stator are of primary importance for the rotordynamic stability and thereby operability and life span of rotating machinery [3, 4]. This renders seal dynamics, the overlying topic of this thesis, a very important subject of study.

A fundamental aspect in the design of efficient and reliable rotating machinery is the ability to accurately predict the rotordynamic behaviour of the machine under operation. Generally mathematical models, based on the laws of physics, provide the necessary predictive capabilities. For rotordynamic modelling purposes high fidelity numerical models of the rotor, generally based on finite element models, commonly act as the backbone for a mathematical model of the rotating machine. Bearing, impeller and seal components are modelled individually and added to the rotor model to form a global rotordynamic model. For the global model to be capable of representing the behaviour of the rotordynamic system, it is of paramount importance that the individual components are modelled with high accuracy. This calls for component level investigations aimed at assessing the precision with which the dynamic behaviour of the individual components can be predicted. To assess the applicability of the component level models it is common practice to validate these models by comparing theoretical results with experimental results, rendering component level experimental testing of e.g. seals strictly necessary.

Generally pumps are employed to transport liquids while compressors are used to transport gases, and the seals featured in these, respectively, are designed and optimised for that particular type of fluid. A completely liquid or gaseous fluid is in general referred to as a single phase fluid, and extensive research has been done over the last 40 years to identify the rotordynamic properties of seals subjected to single phase flows, both theoretically and experimentally.

However, as oil and gas reserves presently in production are depleting, the global oil and gas industry continues to move towards production from fields at greater sea depth and in the Arctic regions. The production from many of these fields requires compression and pumping to take place on the sea floor where the possibility of performing liquid and gas separation on the well stream is very limited and costly. Consequently, the subsea installed pumps and compressors have to cope with streams that can not be considered single phase. Multiphase fluid mixtures will have significantly different fundamental properties as compared to single phase fluids, and therefore the modelling of the multiphase seal flow impact on rotordynamics requires special treatment.

The interplay between fluid dynamics and rotordynamics renders the treatment of seals difficult and adding multiphase flow characteristics further increases the complexity of the engineering problem. The theoretical treatment of seals in multiphase flow is limited in the literature, but even more pronounced is the lack of experimental data to support and validate the numerical models developed and refined in recent years.

1.2 State of the Art

The work documented in this thesis encompasses aspects of multiple scientific fields. The following sections will provide literature reviews for the most relevant of these.

1.2.1 Turbomachinery Seals in Single Phase and Multiphase Flow

Forces generated by turbomachinery seals will significantly influence the stiffness and damping properties, and thereby the stability of the rotating machine under operation [3, 4]. Most predominant is the influence of the relatively long balance piston and division wall seals over which the pressure differentials are large entailing larger forces compared to impeller eye and inter stage seals. Many different types of seals exist such as annular smooth seals, labyrinth seals, honeycomb seals, hole-pattern seals, brush seals and pocket damper seals which are all designed to mitigate leakage of a specific fluid type, while keeping unwanted impact on rotordynamic stability to a minimum [5]. The extensive amount of research performed on seals reflects how vital they are for the rotordynamic performance. The body of both experimental and theoretical work is further enlarged by the vast number of different seal design and fluid types investigated, hence an exhaustive review of the literature is considered out of the scope of this thesis. Below an outline of the research field is given.

Generally two globally applied approaches for mathematically modelling single phase seal dynamics can be traced out. The first is the classical approach of building seal bulk flow models, which originated in the 1980s and continues to be applied [3, 6–10].

Bulk flow models are characterised by being relatively simple and computationally inexpensive, but they require empirical corrections in order to represent experimental results in a satisfactory manner [9, 11–16] thus lacking generality.

As an alternative to bulk flow seal codes, the use of Computational Fluid Dynamics (CFD) for seal modelling has advanced in recent years, as the available computational power has increased [11, 12]. CFD-based commercial tools are now an integral part of the toolbox available for Original Equipment Manufacturers (OEMs) design engineers and consultants dealing with the complex rotor-fluid interaction in seals.

In contrast to bulk flow seal codes a CFD-based mathematical model does not heavily rely on empirical corrections [17] in order to represent experimental results in a satisfactory manner and can handle complex geometries out of reach for bulk flow codes. Additionally, CFD can be used to investigate flow details such as local volume fractions, separation regions, and local flow distributions which is especially advantageous for studying multiphase seal flows [18]. CFD is however computational expensive and not likely to replace bulk flow codes but rather supplement these. CFD models have been implemented with success by multiple authors through discretisation of the (simplified) Navier-Stokes equations [11, 12, 17, 19–28].

Predictive bulk flow or CFD-based models for single phase seals are relatively mature as indicated above, yet the need for a continued effort was emphasised in the 2007 study presented by Kocur et al. [29]. Kocur, et al. found very large variations in rotordynamic coefficients for gas labyrinth seals predicted by survey participant from both academia and the industry.

The subject of expanding these models to include multiphase flow conditions is largely untouched in comparison, however, some work has been done. In the late 1980's and early 1990's models to predict liquid-vapour leakage flow in smooth annular seals were presented [30, 31], however these did not treat multiphase flow impact on rotordynamic seal coefficients directly. Arauz and San Andrés presented a bulk flow model for a cryogenic damper seal subjected to a liquid-vapour multiphase flow [32, 33]. This work presented theoretical prediction of rotordynamic seal coefficients. Recently, Arghir et al. published an analysis of textured annular seals subjected to multiphase (bubbly) flow [34]. In this work a bulk flow code was used to determine rotordynamic seal coefficients, and found these to be dependent on the excitation frequency. Similar findings were reported by San Andrés [35], in a study where a bulk flow code was applied to investigate a smooth annular seal, in this case for varying Liquid Volume Fractions (LVFs) between 0% and 100%. In a very recent paper by Vannini et al. [18] a CFD based study was conducted to investigate the impact of both a tooth on stator labyrinth and a pocket damper balance piston seal design on the overall rotordynamic performance of a centrifugal compressor subjected to wet gas conditions (0% to 3% LVF). The paper offered a physical explanation of the sub-synchronous vibrations found in a previously conducted experimental test campaign [36]. However, rotordynamic seal coefficients were not presented in the paper.

A major constraint on the development of valid predictive models that are able to precisely evaluate multiphase flow impact on rotordynamic seal coefficients, is the

scarcity of experimental data. Iwatsubo and Nishino [37] were the first to publish a data set for seals in multiphase flow albeit this was practically unusable for validation purposes, since crucial details were omitted. San Andrés et al. recently published experimental data for a short length smooth annular seal subjected to wet gas conditions (0% to 4% LVF) with a stationary journal [38]. The paper reports an increase in the direct damping coefficients with increasing LVF, but no clear tendencies are evident in the stiffness data.

1.2.2 Identification of Rotordynamic Seal Properties

Due to the inherent similarities between journal bearings and turbomachinery seals, the procedures developed for experimentally identifying rotordynamic properties for journal bearings are directly applicable to seals. A good overview of these identification techniques is presented in [39, 40].

For general rotordynamic modelling purposes it is conventional to cast the seal model in one of the following forms [3]

$$-\begin{Bmatrix} F_x \\ F_y \end{Bmatrix} = \begin{bmatrix} K_{xx} & -K_{xy} \\ K_{yx} & K_{yy} \end{bmatrix} \begin{Bmatrix} x \\ y \end{Bmatrix} + \begin{bmatrix} C_{xx} & -C_{xy} \\ C_{yx} & C_{yy} \end{bmatrix} \begin{Bmatrix} \dot{x} \\ \dot{y} \end{Bmatrix} \tag{1.1}$$

$$-\begin{Bmatrix} F_x \\ F_y \end{Bmatrix} = \begin{bmatrix} K_{xx} & -K_{xy} \\ K_{yx} & K_{yy} \end{bmatrix} \begin{Bmatrix} x \\ y \end{Bmatrix} + \begin{bmatrix} C_{xx} & -C_{xy} \\ C_{yx} & C_{yy} \end{bmatrix} \begin{Bmatrix} \dot{x} \\ \dot{y} \end{Bmatrix} + \begin{bmatrix} M_{xx} & -M_{xy} \\ M_{yx} & M_{yy} \end{bmatrix} \begin{Bmatrix} \ddot{x} \\ \ddot{y} \end{Bmatrix} \tag{1.2}$$

in which x and y describes the lateral motion of the seal rotor relative to the seal stator. Conventionally the seal stator is stationary entailing that the coordinates x and y describes the seal rotor displacement, specifically. F_x and F_y are the resulting seal reaction forces, K_{xx} and K_{yy} are the direct stiffness coefficients and K_{xy} and K_{yx} denotes the cross-coupling stiffness coefficients. C_{xx} and C_{yy} denote the direct damping coefficients while C_{xy} and C_{yx} denote the cross-coupling damping coefficients. The direct inertia coefficients are denoted M_{xx} and M_{yy} and the cross-coupling inertia coefficients are denoted by M_{xy} and M_{yx}. The cross-coupling inertia coefficients in Eq. (1.2) are often omitted [3, 16]. The above mentioned coefficients are conventionally referred to as the equivalent linear dynamic coefficients of seals, and the models shown in Eq. (1.1) and (1.2) are generally valid for small perturbations of the seal rotor position around a centred position [3]. A note on notation: It is common to assume that $K_{xx} = K_{yy} = K$, $K_{xy} = K_{yx} = K$, $C_{xx} = C_{yy} = C$, $C_{xy} = C_{yx} = C$, $M_{xx} = M_{yy} = M$ and $M_{xy} = M_{yx} = m$, however throughout this thesis the notation used in Eq. (1.1) and (1.2) is retained to preserve generality. It should be noted that the effects of potential angular misalignment are not considered here.

Eq. (1.1) is commonly applied for modelling seals in single phase gaseous flows for which the inertia terms included in the liquid seal model are negligible [3]. For modelling seals in liquid processing applications, seal dynamics can be represented using Eq. (1.2), [3, 41, 42]. What distinguishes the liquid seal model, Eq. (1.2), from the gas seal model of Eq. (1.1) is the addition of inertia terms, allowing the liquid seal model

to represent second order behaviour of the rotordynamic forces. The coefficients M_{xx} and M_{yy} are often referred to as added mass coefficients, as they can be considered to represent fluid mass added to the rotor. A similar model, referred to as the KCM model, have been applied to model Tilting Pad Journal Bearings (TPJB) in the past [43, 44], even though some disagreement exists as to the physical interpretation and validity of this model under certain flow conditions [45, 46]. If the KCM model is used as a basis for identifying rotordynamic coefficients, it is not uncommon to experimentally identify added mass terms that are unphysically large, or even negative under certain conditions [43, 45, 46]. However, there are fundamental differences between seals and journal bearings to be considered. Firstly, seals have a pressure driven axial flow component not present in conventional bearings entailing pronounced convective effects. Secondly, seals often have significantly larger radial clearances compared to bearings, entailing high axial and rotational Reynolds numbers commonly resulting in fully turbulent flows. Additionally, frequency dependence of the seal coefficients is reported in the literature for purely gaseous seal flows in conjunction with some seal geometries, e.g. honeycomb seals [17, 47, 48].

Seal models, irrespective of the fluid type, can be enabled to capture potential frequency dependence of the rotordynamic coefficients, albeit this is predominantly seen for gas seals. Frequency dependence can be modelled by letting the seal coefficients be an explicit function of the perturbation frequency as shown for the liquid seal model below

$$-\begin{Bmatrix} F_x \\ F_y \end{Bmatrix} = \begin{bmatrix} K_{xx}(\omega) & -K_{xy}(\omega) \\ K_{yx}(\omega) & K_{yy}(\omega) \end{bmatrix} \begin{Bmatrix} x \\ y \end{Bmatrix} + \begin{bmatrix} C_{xx}(\omega) & -C_{xy}(\omega) \\ C_{yx}(\omega) & C_{yy}(\omega) \end{bmatrix} \begin{Bmatrix} \dot{x} \\ \dot{y} \end{Bmatrix} + \begin{bmatrix} M_{xx}(\omega) \\ M_{yy}(\omega) \end{bmatrix} \begin{Bmatrix} \ddot{x} \\ \ddot{y} \end{Bmatrix} \tag{1.3}$$

Here Eq. (1.3) includes frequency dependence of the direct inertia terms for completeness, albeit this has little physical justification. The generality of Eq. (1.3) makes it a well suited candidate for modelling seals subjected to multiphase flow as no implicit assumptions are made regarding fluid type. It should be noted that in its most general representation the coefficients of Eq. (1.3) is a function of both the rotor rotational frequency Ω as well as the perturbation frequency ω, as displayed below

$$-\begin{Bmatrix} F_x \\ F_y \end{Bmatrix} = \begin{bmatrix} K_{xx}(\Omega,\omega) & -K_{xy}(\Omega,\omega) \\ K_{yx}(\Omega,\omega) & K_{yy}(\Omega,\omega) \end{bmatrix} \begin{Bmatrix} x \\ y \end{Bmatrix} + \begin{bmatrix} C_{xx}(\Omega,\omega) & -C_{xy}(\Omega,\omega) \\ C_{yx}(\Omega,\omega) & C_{yy}(\Omega,\omega) \end{bmatrix} \begin{Bmatrix} \dot{x} \\ \dot{y} \end{Bmatrix} + \begin{bmatrix} M_{xx}(\Omega,\omega) \\ M_{yy}(\Omega,\omega) \end{bmatrix} \begin{Bmatrix} \ddot{x} \\ \ddot{y} \end{Bmatrix} \tag{1.4}$$

Eq. (1.4) enables including variations in the coefficients for subsynchronous and supersynchronous perturbations of the seal flows.

The overall goal of experimental rotordynamic identification schemes for seals is to facilitate extraction of the stiffness, damping, and if relevant, inertia properties. All dynamic methods are based on the same fundamental principle; perturb the fluid flow between seal stator and rotor and quantify the resulting reaction forces while logging the displacement of the seal rotor within the stator. Generally two perturbation methodologies exist

- **Synchronous perturbation** in which the perturbation is of the same frequency as the rotational frequency of the spinning rotor, i.e. $\Omega = \omega$.

- **Non-synchronous perturbation** in which the perturbation frequency is independent of the rotational frequency of the spinning rotor, i.e. $\Omega \neq \omega$.

Synchronous perturbation is in practise relatively simple to realise by introducing a mass unbalance in the rotor [40, 49–52], however potential non-synchronous frequency behaviour of the seal parameters will not be captured using this method. Non-synchronous perturbation of the seal flow presents a more general approach and allows for identification of potential frequency dependent seal coefficients independently of the rotational frequency of the seal rotor [40]. This feature is of high importance for industrial applications where rotating machinery are exposed to non-synchronous excitations.

In practise dynamical non-synchronous perturbation of the seal flow can be achieved through two approaches

- Exciting the seal stator about a rotating seal rotor.

- Exciting the rotating seal rotor while keeping the seal stator stationary.

Previous authors, see e.g. [16, 42, 50, 53–56], have adopted the technique of exciting the seal stator around a rotating rotor due to the apparent simplicity of this method. This approach allows using conventional bearings, such as ball bearings or roller bearings, for supporting a rigid or flexible rotating rotor. However, the seal stator needs to be flexibly mounted around the rotor to allow transverse motion to be induced by shakers [16] in order to perturb the seal flow. This requires a seal stator suspension system that, if not carefully implemented, can potentially influence the quality of the experimental data negatively [16]. For high density seal flows another unwanted effect can be introduced: If the seal geometry is such that it is possible to trap fluid in e.g. stator holes or pockets, the acceleration of the fluid mass during excitation of the stator will generate reaction forces which will negatively influence the precision of the estimated seal coefficients. The method of exciting the rotor offers some advantages over the previously introduced method

- Exciting the rotor closely simulates real life operating conditions for a rotordynamic system, where the seal flow is perturbed by rotor movement.

- Mass loading problems introduced by fluid trapped in the stator is avoided.

- The seal stator can be mounted rigidly avoiding potential problems of test result contamination from a flexible stator suspension system.

However, it should be mentioned that these advantages comes at the cost of a more complex test facility e.g. through the introduction of Magnetic Bearing Exciters (MBEs) or AMBs. AMBs are very well suited for providing the necessary rotor perturbation functionality and their high level of controllability enable sophisticated perturbation patterns and thereby identification techniques. Utilising the perturbation functionality of AMBs the coefficients of Eq. (1.3) or (1.4) can be determined using both time and frequency domain techniques. A review of these are presented in [39].

1.2.3 Force Measurements with Active Magnetic Bearings

The hub component in the test facility designed and commissioned during this PhD project is the set of two radial AMBs. If accurate information about the magnetic forces generated by the AMBs are obtained, the AMBs can be used to perform dynamic testing in rotating machines [57]. With measurement of coil currents and rotor position [57, 58], structural pole leg deformation via fibre optic strain gauges [59–61], or the magnetic flux density in the air gap between AMB stator and rotor using Hall sensors [62–66], the AMB can function as a multidirectional load cell for quantification of radial AMB forces. With the further extension of rotor position measurements, the AMB constitutes a powerful all-in-one tool for parameter identification and diagnosis purposes [57, 63–66], based on e.g. Frequency Response Functions (FRFs). The need for high precision force measurements is pronounced, as force estimation errors will lead to disproportionally large errors in the FRFs of the rotor-AMB system, upon which many conventional parameter identification schemes are based.

High precision quantification of AMB forces is still an active research topic. The research may be sub-grouped into three main areas:

- Quantification of electromagnetic forces by measuring rotor to stator air gap and coil currents ($i-s$).
- Quantification of electromagnetic forces by measuring the magnetic flux density using Hall effect sensors.
- Quantification of electromagnetic forces by measuring pole structural deformation via conventional or fiber optic strain gauge techniques.

Though modern $i-s$ based techniques such as using reluctance network models [66] and the Multi-Point method [67] show promising results, the precision of the flux measurement method is still superior in terms of minimising force estimation errors [64, 68]. The main advantage of using the $i-s$ is the inherently low hardware complexity, due to the fact that information about coil currents (i) and rotor to stator air gap (s) is readily available from the AMB control system. Very low force estimation errors have been reported using fiber optic strain gauges [59–61], giving merit to a continued research effort. However, the relatively low level of experience with this method reported in the literature, and the fact that it is susceptible to calibration drift [59], makes it less proven than the two previously outlined force estimation approaches.

Conventionally, quantifying AMB forces using Hall sensors require an enlargement of the air gap between the rotor and AMB poles to accommodate the Hall sensors. Enlargement of the air gap leads to a loss in applicable electromagnetic force and reveals the fragile Hall sensors to potential impact from the rotor at large vibrational amplitudes, or during assembly of the rotor-bearing system. These difficulties can be overcome by mounting the Hall sensors in slots manufactured in the AMB pole surfaces as described in [66], at the cost of a slightly decreased ($< 2\%$, [66]) load capability. The main drawback from mounting the Hall sensors in slots is that the slot itself disturbs the path of the flux which is to be measured [63, 66, 69]. However, calibrating the Hall sensor system by conventional means can account for at least some of the additional discrepancies arising from embedding the Hall sensors [66]. Furthermore, it should

be noted that a precise quantification of the force estimation errors is key to gain the necessary precision for any force measuring methodology applied in rotordynamic testing.

1.2.4 Applying Active Magnetic Bearings for Rotordynamic Testing

This section provides an overview of the most project relevant literature regarding test facilities that utilises AMBs for rotordynamic testing of auxiliary machine components such as seals. The present section is included here as the development of AMBs represents a key activity during the underlying work of this thesis. Numerous researchers have utilised single stand-alone Magnetic Bearing Exciters (MBEs) for identification of rotordynamic properties of systems, where the support of the rotor is achieved by conventional means such as roller bearings or ball bearings. See e.g. [62, 66, 70–72]. However, to limit the scope of the review presented here, only literature regarding test facilities in which principal rotor support is performed by AMBs is included. In the following the term "rigid rotor" specifies that the first free-free natural frequency, corresponding to the first bending mode of the rotor, is sufficiently above the operating frequencies of the rotordynamic system.

As early as 1989 Wagner and Pietruszka [73] presented a test facility for rotordynamic seal testing. It features two radial AMBs supporting a relatively short hollow symmetric rotor enclosed in a bundle for testing different seal designs subjected to high pressure single phase gaseous flow [74, 75]. Axial support of the rotor is enabled through an elastic bar coupling. The test facility was revamped in 2005/2006 [28] and recently used by Wagner et al. in 2009 to produce data for validating CFD models of impeller-eye seals. This test facility utilises the $i-s$ methodology for quantifying rotordynamic seal forces. Neither the force estimation precision nor details on the maximum AMB force capability were explicitly stated in any of the related publications. Additionally, the rotor mass, amongst others, was not disclosed which is most likely due to Non-Disclosure Agreements (NDAs) between the authors and their employer. In 1994 Knopf and Nordmann presented a modular AMB based test rig for identification and fault diagnosis purposes within turbomachinery [64, 65]. The test rig, in the most recent iteration, features two radial and an axial AMB for complete magnetic suspension of the rotor. Different force measurement methodologies were tested including utilising pole surface mounted Hall sensors on all north poles of the AMB stators. The authors used a single stage centrifugal pump as the test subject in later studies [76]. The radial AMBs have a nominal radial air gap between AMB rotor and stator of 0.4 mm and a static load capacity of 750 N per AMB axis for supporting a rigid hollow rotor with an unspecified mass. Force estimation precision was estimated to approximately 1% of the maximum static bearing load [65].

Zutavern and Childs introduced a rotordynamic test bench based on a set of radial AMBs in 2008 [61]. The test bench is designed in a modular fashion and includes a flexible coupling for axial support. The test facility was used for quantifying rotordynamic properties of a smooth annular seal setup. Radial AMB forces were quantified using a Fiber Optic Strain Gauge (FOSG) based system introduced in 2004 [59], with uncertainties on the estimation results reported to 0.2% of the maximum nominal AMB load. The calibration of the FOSG was performed using the rotor inertial forces [61].

The aim of the study was to validate the use of FOSGs for determining forces from AMBs in rotordynamic testing applications. The AMBs each have 16 poles and a static load capacity of 3560 N supporting a solid rotor of approximately 217 kg [61].

Recently Vannini et al. presented details on a full industrial scale high pressure seal test vehicle [77]. This test facility is to a large extent conceptually similar to the one introduced by Wagner and Pietruszka [73]. The test rig features two radial AMBs supporting a hollow rigid rotor enclosed in a high pressure bundle. The test facility is designed to experimentally identify rotordynamic parameters of different seal designs subjected to single phase gaseous flow of up to 350 bar. AMB forces are measured via the $i-s$ methodology. The AMBs features 12 poles with an air gap of 1 mm between AMB rotor and stator. Information of the force estimation precision is not stated explicitly in the references.

1.3 About this Research Project

To accommodate the lack of experimental data for validating numerical models of seals subjected to multiphase flow conditions Lloyd's Register Consulting (LRC) and the Technical University of Denmark (DTU) engaged in a research collaboration 2011. The ongoing research collaboration primarily aims at establishing a state of the art test facility for multiphase seal testing purposes, and secondly driving the research on mathematical multiphase seal models forward. The vast majority of the available time resources have been allocated to establish the *industrial scale* test facility necessary for conducting the proposed research activities. The underlying work of this thesis is highly multi-disciplinary in nature, and involves aspects of diverse topics including electromagnetics, rotordynamics, fluid dynamics, solid mechanics, analogue and digital signal processing, and applied control theory.

This thesis contains a description of the efforts related to establishing a first iteration of the multiphase seal test facility, additionally including preliminary numerical and experimental results obtained during the PhD project. The aim of the underlying work have been to design and build the test facility and to conduct a commissioning process, where the performance of the facility is sought to be validated through different experimental efforts including identification of single phase seal rotordynamic properties for a subset of operational conditions. The main original contributions are listed below.

1.3.1 Original Contribution

- Design and commissioning of the first rotordynamic industrial scale test bench in which the rotor is fully radially supported by AMBs with an embedded Hall sensor system for force quantification.

- Design and commissioning of a novel calibration facility allowing fully automatised calibration of the Hall sensor system.

- Design of a novel seal housing assembly optimised for multiphase seal testing.

- First publication of the employment of CFD tools to specifically quantify the stiffness and damping properties of seals subjected to multiphase flow.

1.3.2 Thesis Outline

The PhD thesis is structured as an amalgamation of a monograph and a paper-based thesis. This entails that its foundation is based on the research papers written during the project period but additionally includes descriptive chapters documenting both theoretical and experimental efforts not published previously. Four papers, appended to the thesis document, were produced during the project. The description of tasks related to: Mathematical modelling of the dynamics of flexible and rigid rotors, experimental rotor model validation, modal reduction, AMB controller theory and synthesis, simulation of global system response, experimental tuning of controllers, implementation of run-out compensation schemes, and a multitude of secondary theoretical, practical, and experimental work performed during the commissioning phase have been omitted from the documentation to keep the manuscript relatively compact. The following outlines the structure of the thesis.

Chapter 2 presents the test facility designed and commissioned during the PhD project. The test facility is divided into four modules treated separately.

Chapter 3 deals with the CFD based modelling applied in the design of the test facility and in the seal analysis. The chapter includes selected CFD results relating to the design of the test facility and expands on the theoretical background for the simulation results presented in [P1].

Chapter 4 conveys preliminary experimental results obtained in the commissioning phase of the test facility. The chapter expands on the methodology and results included in [P2, P3].

Chapter 5 highlights the conclusions and presents subjects for future efforts.

Chapter 2

Design of the Multiphase Seal Test Facility

This chapter contains a description of the test facility designed and commissioned during the PhD project. Firstly the general functionality considerations and requirements will be outlined and discussed and subsequently the different modules of the test facility will presented along with key aspects of the design process.

2.1 Functionality Considerations and Requirements

The multiphase seal test facility is designed to enable component level experimental identification of rotordynamic properties of turbomachinery seals. The test results obtained through application of the test facility are to be used for benchmarking and performance evaluation of CFD based numerical tools as well as bulk flow models used for theoretical prediction of rotordynamic seal properties. The fundamental functionality of the test facility should enable conventional experimental parameter identification schemes applied for rotordynamic testing, which are based on non-synchronous frequency dependent perturbation of the seal flow. To achieve this goal the design of the test facility is subjected to the following basic requirements:

- Ensure baseline functionality that enables radial perturbation of the fluid between seal rotor and stator.
- Facilitate rotation of the rotor during fluid perturbation. The nominal design rotational velocity is chosen to be 10.000 rpm.
- The design should accommodate precision force measurement capabilities to quantify seal reaction forces.
- Precision position measurement capabilities are needed to quantify rotor movement.

Additionally the test facility should:

- Include a controllable fluid supply for the test seals.
- Be industrially relevant to the energy sector. This entails that the test facility should be comparable in scale to industrial rotordynamic systems which will avoid potential errors induced through scaling the results. In effect this means that the diameter of the seal rotor is chosen to 110 mm.
- Seek to minimise contamination of test results through design.

The test facility is designed to be able to mirror the Instationary Perturbation Method (IPM) applied for numerical estimation of seal properties using CFD as a minimal requirement. This method is described in detail in [17, P1, 78–80], and relies on non-synchronously perturbing the seal flow by moving the rotor in a prescribed sinusoidal pattern for multiple frequencies. Acquiring information on the reaction forces exerted on the seal rotor allows the coefficients of Eq. 1.3 to be determined by applying simple time domain identification techniques e.g. as described in [P1]. As indicated in the introduction AMBs are very well suited to provide the necessary perturbation functionality, and it should be mentioned that AMBs generally allow for much more sophisticated perturbation patterns and thereby identification techniques, than the baseline functionality referred to above. In addition to providing the perturbation functionality the AMBs can be used as the principal bearing element for supporting the rotating rotor. As discussed in the introduction AMBs can facilitate high precision force estimation by introducing Hall sensors to measure the magnetic flux density in the air gap between the AMB poles and the AMB rotor. Furthermore, the position of the rotor is readily available from the control system as AMBs require position feedback to operate.

2.2 General Layout of the Test Facility

The purpose of this section is to give the reader an overview of the test facility in its final form. The final design of the test facility is a result of an iterative process, in which numerous concepts have been crafted, evaluated and refined. The iterative nature of the design process is rooted in the fact that the design of individual test facility elements influences the design requirements for other elements. The decisions made in the design process are coloured by time constraints, financial constraints and practical constraints, which are all a natural part of any project. Consequently the final design does not necessarily represent the optimal technical solutions for a given test facility element, but is commonly a compromise between attaining the needed functionality and complying with the imposed constraints. A schematic overview of the test facility layout is presented in Fig. 2.1. The test facility is comprised of four modules

- **Module I** is an AMB based rotordynamic test bench.
- **Module II** is a calibration facility for the Hall sensor system.
- **Module III** is a seal housing assembly containing the test seals.
- **Module IIII** is the flow loop responsible for supplying flow to the test seals.

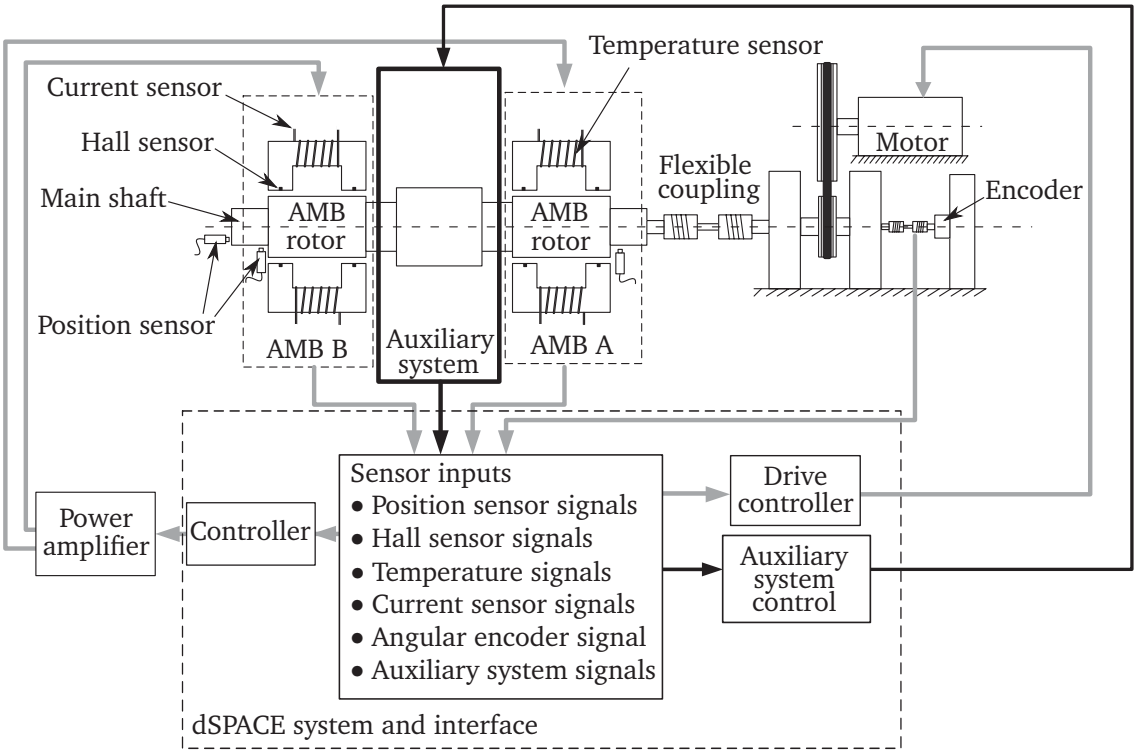

Figure 2.1: Schematic view of the test facility layout. Module II replaces the generic box called "Auxiliary system" in calibration mode. In seal test mode Module II is replaced by Module III.

The test facility can be operated in two modes: Calibration mode and test mode. In Calibration mode Module II is placed between the two AMBs thus replacing the generic box titled Auxiliary system in Fig. 2.1. In seal testing mode Module III replaces the box titled Auxiliary system in Fig. 2.1. Module I constitutes the hub module of the test facility, and its main components are conceptually shown in Fig. 2.1. Module I consists of a rigid solid rotor suspended in two radial AMBs. The AMBs feature a system of embedded Hall sensors which provides the required force measurement capabilities necessary for quantifying seal forces. A choice was made not to include an axial AMB in the design of the test facility, partly due to an expectation of no significant axial loads from the symmetric test seal configuration, and partly to limit the complexity of the test facility. This means that primary axial support of the rotor is supplied by the flexible coupling connected to an intermediate shaft. The coupling allows for radial movement of the rotor. The intermediate shaft and thereby the main rotor is driven by an electric motor trough a timing belt. The test facility is controlled using a dSPACE I/O system interfacing with a PC. In the following sections the design and functionality of all modules is described in detail.

2.3 Module I - Rotordynamic Test Bench

Module I is a rotordynamic test bench which acts as the hub for the test facility and the fundamental functionality of this is largely achieved through Module I's capabilities. Consequently, the majority of the test facility requirements stated in Section 2.1 are directly related to the design of Module I, and therefore it demands significant attention.

In the subsequent sections, the individual components of Module I are described.

2.3.1 Design of the Radial Active Magnetic Bearings

Module I is based on a set of radial AMBs that, in addition to supporting the rotor, also provides the rotor perturbation capabilities and features the embedded Hall sensor system used for contact free force estimation during testing. In the following sections the fundamental aspects of AMB design and the AMBs designed for the test facility will be presented.

2.3.1.1 Functional Principle of Active Electromagnetic Suspension

The main focus of this section is oriented at active electromagnetic suspension, the functional principle behind AMBs. However, AMBs passive counterpart, the Passive Magnetic Bearing (PMB), will be shortly introduced below. Magnetic suspension of a subset of the Degrees of Freedom (DOFs) for a body in space is possible using permanent magnets [81]. PMBs do not require any control action to operate, and the working principle is commonly based upon the repelling force generated between two magnetic poles with identical polarity. PMBs have been successfully applied for supporting rotors (see e.g. [82]), however stiffness and especially damping properties of these bearings are often insufficient for industrial application [69]. For a detailed review of magnetic suspension state of the art see e.g. [69]

Active electromagnetic suspension is the most common variant of magnetic suspension employed in the industry. The functional principle of AMBs adheres to this technology and is conceptually visualised in Fig. 2.2 showing the components required to enable active magnetic suspension of a so-called flotor. The controlled electromagnetic force exerted by the electromagnet works to counteract the gravitational force on the flotor the following way: A sensor measures the position of the flotor, which is used by the controller to determine an appropriate control signal for a power amplifier supplying current to the coil of the electromagnet. As a consequence of the flowing current, the electromagnet generates a force. Any change in the position of the flotor, as a result of the exerted force, is then again sent to the controller that adjusts the amplifier control signal accordingly. This process repeats until interrupted, and nicely and simplistically outlines the concept of closed loop or feedback-control. Another fundamental concept for AMB systems can be introduced using the simple example above, namely the concept of open loop instability. If for example the distance between the electromagnet and the flotor $S_0 = 1\text{mm}$ is defined as an equilibrium point for the flotor, maintained through the feedback control scheme introduced above, then that equilibrium point is said to be open loop unstable. This means that if the loop is opened e.g. by disconnecting the position sensor, it is not possible for the system to maintain the equilibrium. In effect, the flotor would fall down or latch to the electromagnet. This phenomenon is key to why an AMB is considered to be a significantly more complex bearing element than conventional types; active control is vital to its operation.

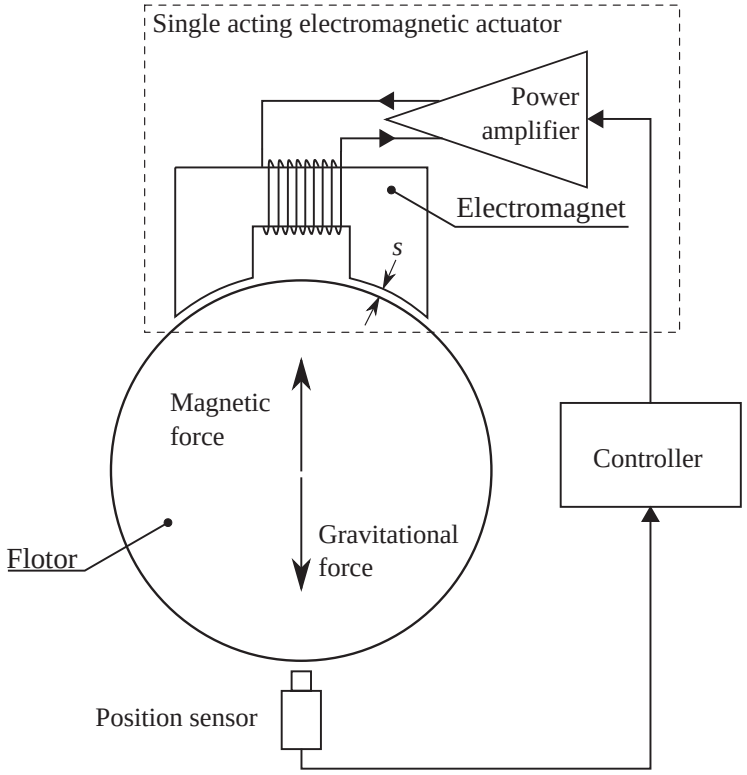

Figure 2.2: Functional principle of active magnetic suspension.

AMBs have advantages and drawbacks compared to conventional rotor bearing elements. These are shortly addressed below along-side fundamental aspects of AMB technology and operation.

- The absence of bearing friction losses in AMB based systems entail that high rotational speeds can be achieved and regular maintenance kept to a minimum, which provides cost saving incentives for operators.
- The rotational velocity of a rotor supported by AMBs is only limited by the strength of the rotor material and the bandwidth of the control system and AMB power supplies.
- AMBs do not require a lubrication system to operate making them ideal for clean tech applications where contamination of process fluid must be avoided.
- Omitting the lubrication system for machines based on AMBs generally reduces overall system complexity and consequently both design and operation costs.
- The high level of controllability allows AMB characteristics to be changed during operation and facilitates active control of rotor position and vibration. These aspects enable operators to cross critical speeds and adapt the performance of the machine to changing operating conditions.
- An AMB is inherently a mechatronic machine element that, in addition to performing the primary task of supporting a rotor, offers the possibility to perform in situ system monitoring and system identification.

- One major limitation for employing AMBs in some applications is the relatively low load carrying capacity [83]. The load carrying capacity obtained from the magnetic forces in AMBs do not match those generated in the fluid film of conventional journal bearings for similar rotor diameters.

- An additional drawback in the application of AMBs is the inherent complexity of the machine element. Designing and operating AMBs requires knowledge within a variety of technical disciplines such as power electronics, electromagnetics, rotordynamics, solid mechanics, digital control theory and digital signal processing.

2.3.1.2 Electromagnetism and Actuator Force Model

In electromagnets a magnetic field is generated by moving charges comprising a current flow. The flowing current in a straight wire generates a magnetic field tangential to the closed magnetic field lines that form around the wire as visualised in Fig. 2.3(a). Wrapping the wire into the shape of a solenoid around a solid core produces field lines that can be conceptually visualised as the single flux path shown in Fig. 2.4.

The magnetic field **H** is conventionally referred to as the magnetic field intensity, which serves to quantify the magnetic field only as a function of the externally applied driver, here current, and is independent of the medium in which the magnetic field is generated. For a thorough introduction to electromagnetism see e.g. [84]. As will be discussed later, the magnetic flux density **B** has an important role in the quantification of the force exerted by an electromagnetic actuator. The magnetic field intensity and magnetic flux density are linked through the following constitutive equation presented here on scalar form

$$B = \mu_0 \mu_r H \tag{2.1}$$

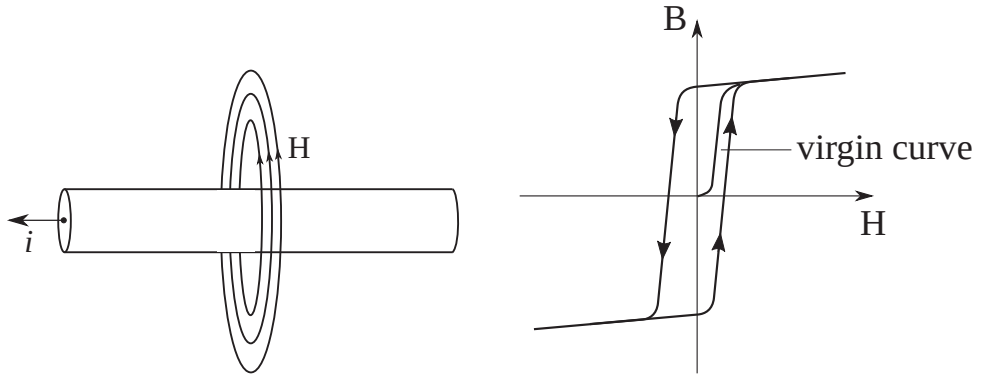

(a) Generation of magnetic field intensity. Figure depicts flowing current i, magnetic field intensity **H** and magnetic field lines.

(b) Generic **B**−**H** diagram for a soft ferromagnetic material.

Figure 2.3: Generation of magnetic fields.

in which μ_0 is the magnetic permeability of vacuum, and μ_r is the relative permeability of the magnetised material. In general Eq. (2.1) is non-linear and for soft ferromagnetic materials conventionally used in AMB stators the relative permeability can be high. Fig. 2.3(b) presents a visualisation of a $\mathbf{B}-\mathbf{H}$ diagram for a generic soft ferromagnetic material, and displays two important features for magnetic field generation, here simplistically exemplified using the electromagnet actuator system presented in Fig. 2.2. As the current in the coil is increased the magnetic field intensity **H** increases along with the magnetic flux density **B** following the upwards path sketched in Fig. 2.3(b). At a point along the upwards path, increasing the current in the coil and thereby the **H** field does not yield a significantly higher flux density. The material is said to be in saturation and the corresponding flux density is referred to as the saturation flux $\mathbf{B}_{sat}$. For a detailed description of magnetic saturation phenomenon see e.g. [85, 86]. Now, if the current in the coil and thereby the magnetic flux intensity is reduced the magnetic flux density will decrease following the downwards path sketched in Fig. 2.3(b), thus creating a hysteresis loop. Fig. 2.3(b) includes a visualisation of a virgin curve for a generic ferromagnetic material. The virgin curve describes the relationship between **B** and **H** when the material is subjected to a magnetic field for the first time. In practical AMB applications hysteresis phenomena entail that even if the current flow to the electromagnet is terminated, a residual magnetic flux density, and consequently also a residual force, will remain. Details on magnetic hysteresis phenomenon can be found in e.g. [86, 87].

In the process of designing an AMB, it is worthwhile to consider how electromagnetic forces are generated, which motivates the following. Fig. 2.4 presents a conceptual sketch of an electromagnet consisting of a C-core with N coil turns in which the current i is flowing. The variable s denotes the air gap between the electromagnet and the bar shaped magnetization target. The electromagnet and the bar shaped magnetization target constitute a magnetic circuit in which the flux Φ is present whenever a current i is flowing in the coil. For simplicity only one flux loop is visualised, but in reality a multitude of these will be present. The direction of the flux loops is dictated by the right hand rule [84], and the density of these is denoted **B** and referred to as the magnetic flux density. In the following it is assumed that the flux Φ is homogeneous and completely contained in the magnetic circuit with constant cross section in both iron and air gap parts $A_{fe} = A_a$, in which A_{fe} is the cross section area of the iron core. Consequently, flux fringing and flux leakage effects are neglected. In this case a scalar representation of the flux can be defined as $\Phi = B_{fe}A_{fe} = B_aA_a$, in which B_{fe} and B_{fe} are the identical flux densities in the iron core and the air gap, respectively. The derivation presented subsequently is based on the principle of virtual work founded in energy conservation considerations, and utilises the fact that an electromagnet can be viewed as a mechanism ultimately translating electrical energy into mechanical energy.

To obtain an expression for the attractive force generated by the electromagnet, the total energy stored in the air gap volume is quantified as [84]

$$W_m = \frac{1}{2}\int \mathbf{B}\cdot\mathbf{H}dv \tag{2.2}$$

in which dv represents a differential segment of the air volume between the pole face and rotor spanned by the pole surface A_a and the magnitude of s, see Fig. 2.4.

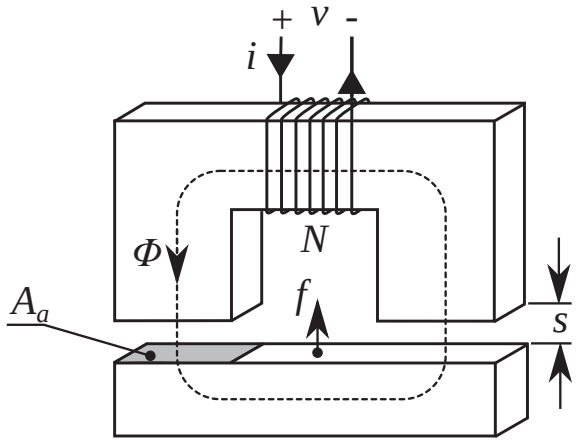

Figure 2.4: Generic representation of single electromagnet showing relevant definitions. i denotes the current flowing in the coil with N turns, s denotes the air gap between pole surface and magnetisation target upon which the force f is exerted. A_a is the surface area of the pole and Φ represents the flux.

Evaluating the integral in Eq. (2.2) and recognising that the air gap volume can be expressed as $2A_a s$, the energy stored in the air gap can be expressed as

$$W_m = \frac{1}{2} BH(A_a 2s) = BHA_a s \tag{2.3}$$

Since there is no initial magnetic polarisation of the air in the air gap, and as a consequence of the fact that the relative permeability of air is $\mu_{r,air}/\mu_0 = 1$ the field intensity H in the air gap is given by [84]

$$H = B/\mu_0$$

in which the permeability of air is assumed equal to μ_0. By substituting the above stated correspondence between field intensity and flux density into Eq. (2.3) the following is obtained

$$W_m = \frac{A_a}{\mu_0} B^2 s \tag{2.4}$$

Assuming that the system presented in Fig. 2.4 can be considered conservative and consequently loss free, it is possible to quantify the electrical power flowing into the system and the mechanical power output as [88]

$$P_e = vi = i\frac{\mathrm{d}\lambda}{\mathrm{d}t}, \qquad P_m = f\frac{\mathrm{d}s}{\mathrm{d}t} \tag{2.5}$$

in which P_e is the electrical power determined, in this case, by the product of the current in the coil i and the voltage v driving it. The voltage v can be defined as $v = \frac{d\lambda}{dt}$ where λ is referred to as the flux linkage. The expression for mechanical power P_m in Eq. (2.5) is given as the product of the exerted force f and the time rate of change of the air gap coordinate s. The time rate of change of the energy stored in the system can

be expressed as the difference between the imposed electrical power and the resulting mechanical power utilising the quantities defined in Eq. (2.5)

$$\begin{aligned} \frac{\mathrm{d}W_m}{\mathrm{d}t} &= P_e - P_m = i\frac{\mathrm{d}\lambda}{\mathrm{d}t} - f\frac{\mathrm{d}s}{\mathrm{d}t} \quad \rightarrow \\ \mathrm{d}W_m &= i\mathrm{d}\lambda - f\,\mathrm{d}s \end{aligned} \tag{2.6}$$

Furthermore, if the two variable λ and s are considered to completely describe the time rate of change of the stored energy then the chain rule can be applied to obtain the following

$$\begin{aligned} \frac{\mathrm{d}W_m}{\mathrm{d}t} &= \frac{\partial W_m}{\partial \lambda}\frac{\mathrm{d}\lambda}{\mathrm{d}t} - \frac{\partial W_m}{\partial s}\frac{\mathrm{d}s}{\mathrm{d}t} \quad \rightarrow \\ \mathrm{d}W_m &= \frac{\partial W_m}{\partial \lambda}\mathrm{d}\lambda - \frac{\partial W_m}{\partial s}\mathrm{d}s \end{aligned} \tag{2.7}$$

Equating Eq. (2.6) and Eq. (2.7) it becomes apparent that the force acting on the magnetization target can be determined using

$$f = \frac{\partial W_m}{\partial s} \tag{2.8}$$

under the assumption of constant coil current [69]. Inserting Eq. (2.3) into Eq. (2.8) and differentiating yields

$$f = \frac{A_a}{\mu_0}B^2 \tag{2.9}$$

Eq. (2.9) states the force exerted by a geometrically simple electromagnet on an equally simple magnetisation target as a function of the magnetic flux density. Additionally, Eq. (2.9) shows the quadratic dependence of electromagnetic force on the magnetic flux density magnitude B. The form of the force equation presented in Eq. (2.9) is important for the Hall sensor force estimation system as further discussed in Section 2.3.1.8. However, for control purposes the force model needs to be formulated as a function of a controllable quantity, in this case the coil current i. Neglecting the magnetisation of the iron in the C-core, it can be shown that the flux density in the air gap can be expressed as [69]

$$B = \mu_0\frac{NI}{2s} \tag{2.10}$$

The product NI of the number of coil turns N and the current in the turns I is referred to as the Magnetomotive Force (MMF) which drives the flux through the magnetic loop. Inserting Eq. (2.10) into Eq. (2.9), expanding and gathering coefficients yields

$$f = k\frac{i^2}{s^2} \tag{2.11}$$

in which $k \equiv \frac{1}{4}\mu_0 A_a N^2$. Eq. (2.11) shows the characteristic quadratic behaviour of the force as a function of the current, as well as the inversely quadratic dependence on the air gap.

A very important quantity for the overall dynamical performance of AMBs can be defined using the definition of flux linkage λ. Under the assumption of an electrically and magnetically linear system the flux linkage can be expressed as follows [69, 88]

$$\lambda = N\Phi = Li \tag{2.12}$$

in which Φ is the total flux induced by current in the coils, L is the inductance of the magnetic circuit visualised in Fig. 2.4 and i is the coil current. From Eq. (2.12) the inductance can be defined as

$$L = \frac{N\Phi}{i}$$

Furthermore, utilising the definition of flux previously introduced $\Phi = B_a A_a$ and the flux density defined in Eq. (2.10) together with Eq. (2.12) the inductance can be defined as

$$L = \frac{\mu_0 N^2 A_a}{2s} \tag{2.13}$$

The expression for the inductance presented in Eq. (2.13) provides a rough estimate of the inductance as it neglects flux leakage, reluctance in the C-core iron and the specific geometry of the magnetic circuit including the coil [69], however it is useful for design purposes as will be discussed later. A more general version of the magnetic circuit inductance can be introduced as

$$L = N\frac{\mathrm{d}\Phi}{\mathrm{d}i} \tag{2.14}$$

which expresses the inductance as a function of the rate of change of the flux with respect to the coil current. This formulation imposes no assumption regarding where on the $B-H$ diagram of Fig. 2.3(b) the electromagnet is operating, or on the geometric layout of the magnetic circuit. Nor is a constant core permeability assumed.

2.3.1.3 Differential Driving

A significant limitation of the electromagnetic actuator shown in Fig. 2.4 is that it can only exert a unidirectional force. Pairing two actuators, yielding the dual acting electromagnetic actuator shown in Fig. 2.5, alleviates this limitation. Additionally, the non-linear force current relationship of Eq. (2.11) is commonly unwanted for control purposes, as it prohibits using linear control schemes conventionally applied for AMB control. However, the dual acting actuator renders differential driving possible, which effectively linearises the force current relationship around an operating point defined by a nominal position x_0 and a bias current i_0. As visualised in Fig. 2.5 one of the opposing actuators is supplied with the sum of the bias current i_0 and the control current i_x, determined by the feedback controller, and the other with the difference. Commonly the nominal position x_0 corresponds to a centred rotor resulting in the air gap between rotor and stator s_0 being theoretically identical for both actuators. The force Eq. (2.11) is restated here with an amendment adjusting the angle of attack α to accommodate the curvature of the pole surface seen in Fig. 2.5

$$f = k\frac{i^2}{s^2}\cos\alpha \tag{2.15}$$

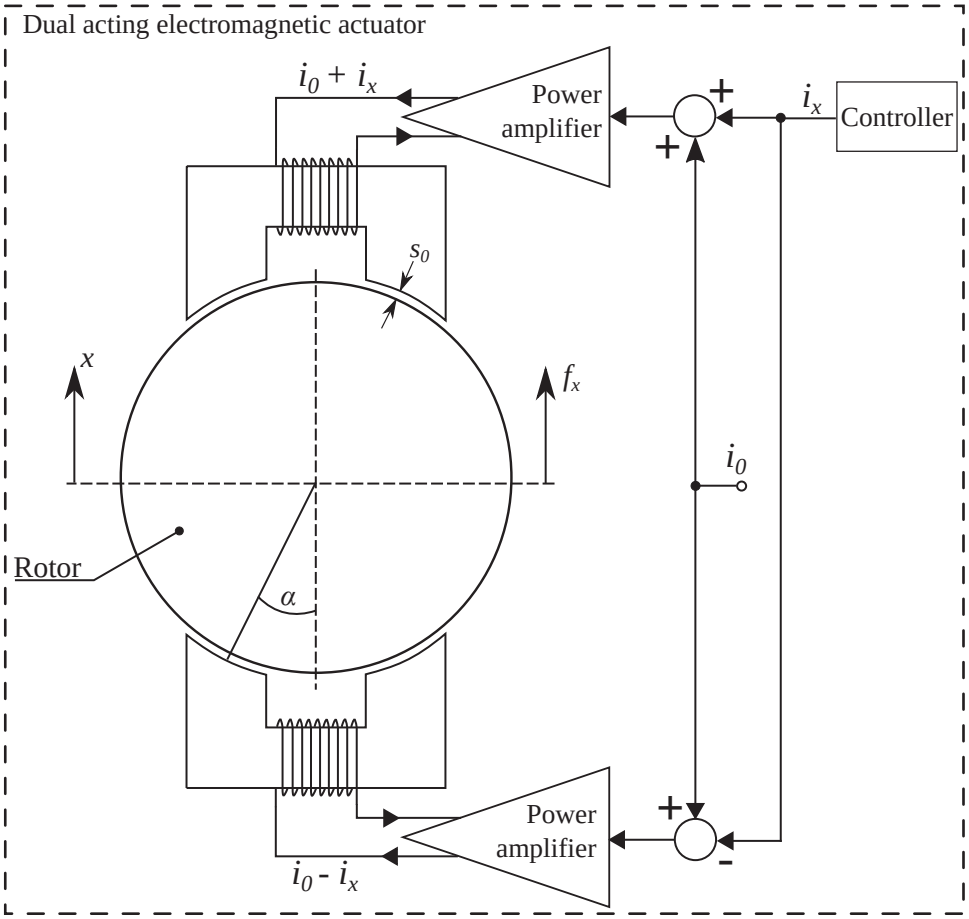

Figure 2.5: Generic representation of a dual acting actuator showing the definitions of differential driving, bias current i_0 and control current i_x.

However, since α can be considered a design specific constant, assuming small transversal displacement of the rotor, the coefficient $\cos\alpha$ can simply be included in the constant k as $k \equiv \frac{1}{4}\mu_0 A_a n^2 \cos\alpha$, thus retaining the form of Eq. (2.11). The resulting force f in Fig. 2.5 is the difference between the attractive forces exerted by the two opposing electromagnets which can be denoted f_+ and f_-, respectively. Utilising the concept of differential driving visualised in Fig. 2.5 while realising that the actuator specific air gap s in Eq. (2.15) can be defined as $s = s_0 - x$ and $s = s_0 + x$ for the two electromagnets, respectively, yields the following force equation

$$f_x \quad = \quad f_+ - f_- = k\left(\frac{(i_0+i_x)^2}{(s_0-x)^2} - \frac{(i_0-i_x)^2}{(s_0+x)^2}\right) \tag{2.16}$$

Linearising Eq. (2.16) with respect to $x \ll s_0$ gives [69]

$$f_x \quad = \frac{4ki_0}{s_0^2} i_x + \frac{4ki_0^2}{s_0^3} x = k_i i_x - k_s x \tag{2.17}$$

in which

$$k_i \equiv \frac{4ki_0}{s_0^2}, \qquad k_s \equiv \frac{4ki_0^2}{s_0^3} \tag{2.18}$$

An important feature of Eq. (2.17) is the negative sign of the force/displacement factor k_s entailing that if the rotor is displaced from its equilibrium towards an actuator a force will be generated in the same direction as the displacement. This is referred to as the negative stiffness properties of AMBs, and is in opposition to a conventional mechanical positive stiffness that would generate a restoring force as a function of the displacement. The negative stiffness property of AMBs adds to the definition of open loop instability introduced in Section 2.3.1.1, since if the feedback loop is broken the AMB will pull the rotor out of its inherently unstable equilibrium. The force/current factor k_i can also be regarded as a stiffness coefficient that produces a force when the coil control current i_x is varied. The magnitude of k_i is directly proportional to the bias current imposed on the dual acting actuator and decreases quadratically with the size of the air gap. The negative stiffness k_s increases quadratically with the bias current and decreases in a cubic fashion as a function of the size of the air gap.

The actuator model presented in Eq. (2.17) is fundamental for controller development. Additionally, it can be used in the design phase of an AMB to determine static load capabilities, and through the definition of k also geometrical aspects of the AMB design. However, the impact of the limiting assumptions made during the derivations is significant and the results will only suffice as an indicator of the capabilities of the final AMB design. More precise modelling of the AMB can be achieved through the application of magnetostatic Finite Element Analysis (FEA), which is the subject of Section 2.3.1.5.

2.3.1.4 Geometrical Layout and Magnetic Configuration of the Radial AMBs

The basic geometrical layout of the radial AMBs designed for the test facility can be seen in Fig. 2.6(a) along with fundamental geometry definitions. In Fig. 2.6(a) a denotes the pole radius of the stator, b is the inner radius of the stator, c is the outer radius of the stator, p denotes the pole leg width, d is the shaft radius, e denotes the AMB rotor outer radius. The air gap s_0 is defined as the difference between a and e. The parameter g denotes the pole leg rounding radius. The AMB design adopts the conventional eight pole stator design, widely applied in the industry. This layout provides a simple basis for controller design, due to the fact that it is based on two dual acting actuators, similar to that which was presented in Fig. 2.5, and consequently enables electromagnetic forces to be exerted in both directions of a Cartesian reference frame. Many different AMB stator layouts can be found in the literature and describing these is considered out of the scope of this thesis. However, it should be noted that two fundamental magnetic layouts for AMB stators exists, namely the heteropolar and homopolar layout. The homopolar layout generates reduced eddy current losses in a spinning rotor, compared to the heteropolar layout, but is more difficult to manufacture. The magnetic layout used in the designed AMBs follows a heteropolar layout, where the polarity of the stator poles shifts between north and south poles in the prescribed pattern illustrated in Fig. 2.6(b). The resulting sequence NS-SN-NS-SN in the rotational plane entails that the stray magnetic field between the electromagnets are kept to a minimum and that the flux follows the path Φ illustrated for $EM2$ in Fig. 2.6(b). The polarity pattern is determined by the coil current direction, and consequently care must be taken when winding the coils. The individual electromagnets are paired together to create two independent dual acting electromagnet actuators. With reference to Fig. 2.6(b) $EM1$

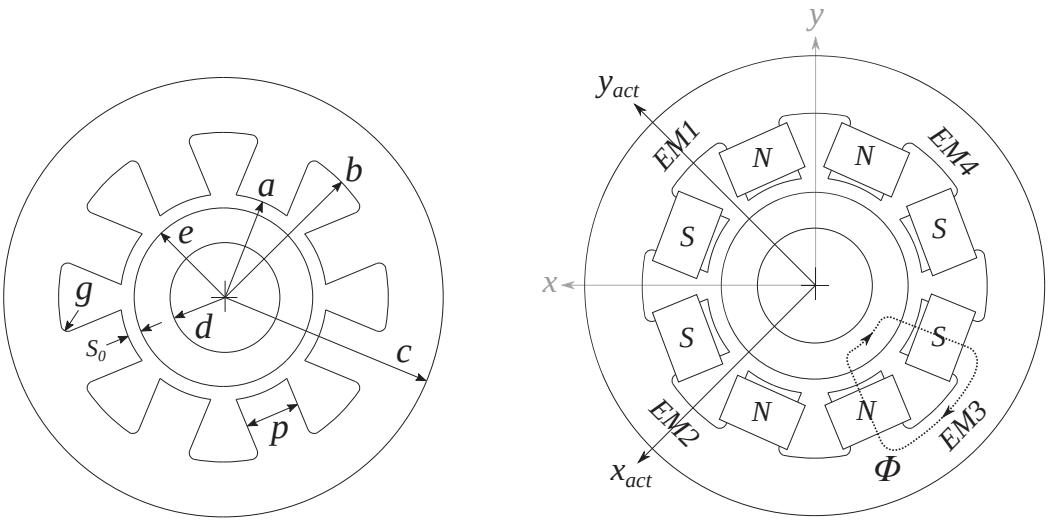

(a) Geometrical definitions for AMB stator and rotor.

(b) Definition of electromagnetic configuration and actuator reference frame.

Figure 2.6: Geometrical definitions and actuator configuration.

and $EM3$ are paired into actuator 1 ($ACT1$) and $EM2$ and $EM4$ are paired to yield actuator 2 ($ACT2$). In order to distribute the gravitational load of the rotor between the two dual acting actuators, the actuator reference frame, denoted $\{x_{act}, y_{act}\}$, is shifted 45° from the global reference frame $\{x_{glob}, y_{glob}\}$ as indicated in Fig. 2.6(b). Simple transformation matrices can be employed to navigate between the reference frames.

The electromagnetic force exerted by an AMB can be represented by evoking Eq. (2.17) for the two actuators $ACT1$ and $ACT2$ in the actuator reference frame as follows

$$\begin{aligned} f_x &= k_i i_x - k_s x \\ f_y &= k_i i_y - k_s y \end{aligned}$$

in which i_x and i_y are the control currents for each actuator. Here it is implicitly assumed that the AMB is completely geometrically as well as electrically symmetric in both actuator directions, such that the coefficients k_i are k_s are identical for the two actuators. In reality this is difficult to realise, and individual adjustments of the coefficients are often necessary.

2.3.1.5 Finite Element Modelling of AMBs

The first principle models of AMB actuators presented in the preceding sections provide a good basis for initial dimensioning of AMBs. However, the relatively complex geometry of AMBs motivates the use of Finite Element Methods (FEM) for detailed design and analysis. Throughout the design phase FEM has been used extensively for magneto-static modelling of the test facility AMBs which motivates including the following section. The FEM analysis documented here is based on the open-source FEM software FEMM developed by D. Meeker [89]. Aspects of the following sections are adapted from [90].

Governing Equations

A magneto-static problem is defined as a magnetic problem where the magnetic field intensity **H** and the magnetic flux density **B** are both time-invariant [91]. A magneto-static problem must obey [91]

$$\nabla \times \mathbf{H} = \mathbf{J} \tag{2.19}$$

$$\nabla \cdot \mathbf{B} = 0 \tag{2.20}$$

where **J** denotes a current density source. Eq. (2.19) is known as Ampère's circuital law or the fourth Maxwell's equations and states that the curl of the magnetic field intensity is equal to the imposed current density source. Eq. (2.20) is Maxwell's second equation also known as Gauss's law for magnetism. It states that the flux must form closed lines, which is equivalent to imposing that no magnetic monopoles can exist [92] and consequently that the divergence of the magnetic flux density is required to be zero. It is convenient to introduce the vector potential **A** as

$$\mathbf{B} \equiv \nabla \times \mathbf{A} \tag{2.21}$$

which implicitly requires that

$$\nabla \cdot \mathbf{A} = 0 \tag{2.22}$$

in order to fulfil

$$\nabla \cdot (\nabla \times \mathbf{A}) = 0 \tag{2.23}$$

The relationship between **H** and **B** is here given by

$$\mathbf{B} = \mu \mathbf{H} \tag{2.24}$$

in which μ denotes the permeability of space in which **H** and **B** exists. Eq. (2.24) holds true if the magnetized material behaves linearly. For non-linear magnetic material properties, such as the properties of the electrical sheets used for the laminated AMB stators and rotors, the magnetic field strength is a function of the flux density. In this case the permeability is defined as

$$\mu = \frac{\mathbf{B}}{\mathbf{H}(\mathbf{B})} \tag{2.25}$$

Combining Eq. (2.19), Eq. (2.21), and Eq. (2.25), the governing equation for a general three dimensional magneto-static problem with *no* linearity restriction on the **B** - **H** relationship, can be formulated in differential form as

$$\nabla \times \left(\frac{1}{\mu(\mathbf{B})} \nabla \times \mathbf{A} \right) = \mathbf{J} \tag{2.26}$$

The magneto-static problem, formulated in terms of **A** in Eq. (2.26), conveniently condenses all conditions imposed by Eq. (2.19), Eq. (2.21), and Eq. (2.25) into a single expression. Hence, to solve the magneto-static problem, only the solution for **A** is required, and the **B** and **H** -fields can be obtained subsequently by differentiation

of **A**. FEMM features a solver for solving the two dimensional version of the problem defined in Eq. (2.26). The two dimensional version of Eq. (2.26) is given by

$$\nabla \times \left(\frac{1}{\mu(\mathbf{B})} \nabla \times A_z \right) = J_z \tag{2.27}$$

It should be noted that Eq. (2.27) is only valid for two dimensional magneto-static problems (no electrical fields present), furthermore neglecting displacement currents [91] but potentially including material non-linearities. Multiple methods exist for discretizing Eq. 2.27 on a mesh of finite elements, see e.g. [93]. Here it is considered sufficient to state that FEMM discretizes Eq. 2.27 on a triangular mesh of finite elements, approximating the vector potential **A** at the three vertices of the triangles using linear interpolation between nodes. The boundary conditions which are essential to uniquely determine a solution to Eq. (2.27), are not treated in depth here, but generally consists of both Dirichlet and Neumann type boundary conditions [91]. However, it should be mentioned that the boundary condition applied on the outer domain bound are of the asymptotic type, which is imposed to mimic an open solution domain. A thorough review of this type of boundary conditions can be found in [94] and an overview with focus on implementation is found in [91].

Model Setup and Execution

A key feature of FEMM is that it can be accessed through the mathematics software MATLAB. A set of dedicated MATLAB scripting commands allow for defining geometry, assigning material properties and boundary conditions, assigning coil currents, performing simulations and post processing the simulation results. Substantial efforts have been directed towards establishing a MATLAB script that allows for parametrically generating AMB geometries and assigning properties in an automated way. This makes investigating the impact of AMB geometry and property changes easy, as the conventional programming features of MATLAB can be used to loop over design variations changing both geometry and properties iteratively. Additionally, the MATLAB script can be employed to iterate over both control currents and rotor positions which enables FEM based numerical estimation of the force/current and force/displacement factors K_i and K_s, respectively. A visualisation of the 2D AMB geometry defined and assigned with properties in FEMM is seen in Fig. 2.7.

Post Processing

Information on the magnetic flux density is readily available from result plots as the example provided in Fig. 2.8, which depicts the flux density for a completely centred rotor, a bias current of 10A and zero control current. As mentioned previously the flux density can be derived from the solution of Eq. (2.27). The method for obtaining the force exerted on the rotor is introduced below. For an in-depth discussion of how the actual force calculation algorithm is implemented in FEMM, the reader is referred to [91] and [95].

If an object, in this case the rotor, is completely surrounded by air, which is always the case here, the electromagnetic force acting on the object can in the general three dimensional case be determined by integration of the Maxwell stress tensor over a

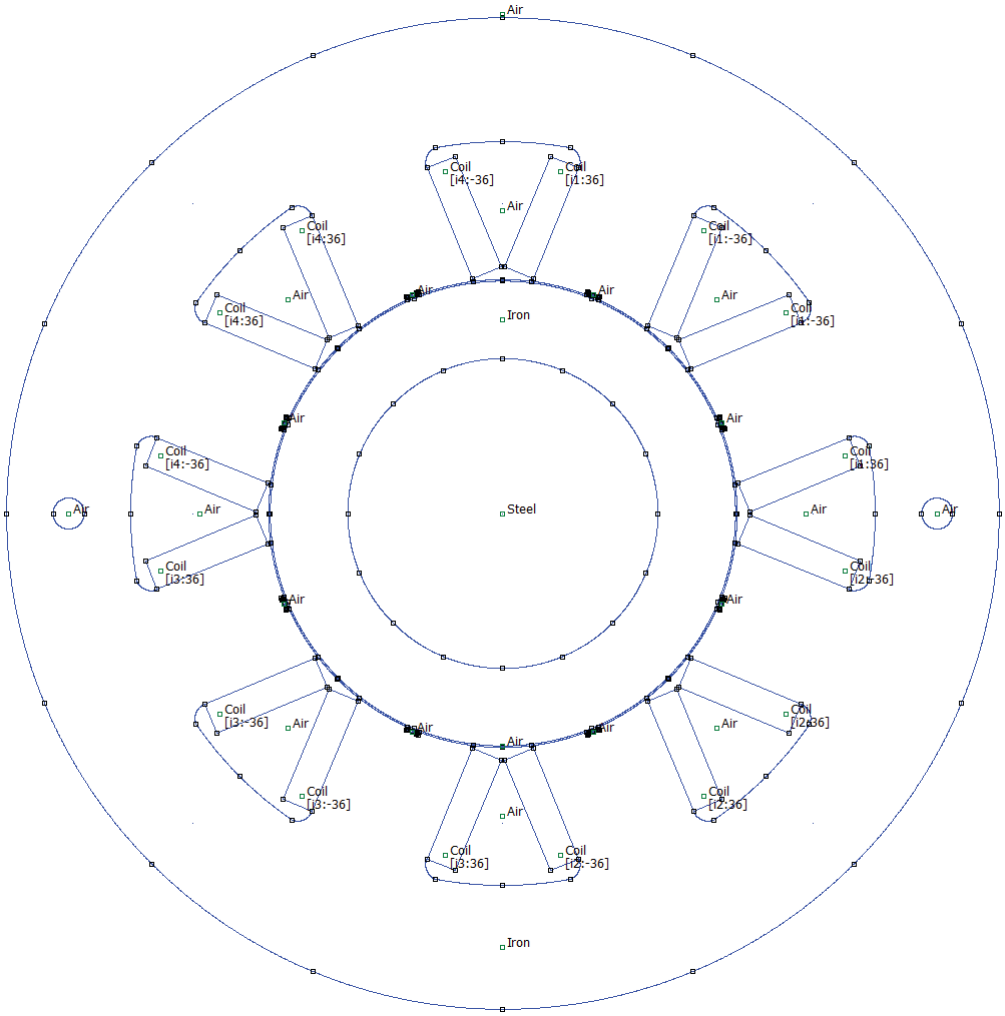

Figure 2.7: AMB geometry defined in FEMM using MATLAB including material and coil current definitions.

surface surrounding the object [96]. This can be expressed as follows, [96]

$$\mathbf{F} = \oint_S \left[\frac{1}{\mu_0} (\mathbf{B} \cdot \mathbf{n}) \mathbf{B} - \frac{1}{2\mu_0} \mathbf{B}^2 \mathbf{n} \right] dS \tag{2.28}$$

in which S is the surface over which integration is performed and $\mathbf{n}$ is an outwards pointing normal vector. Eq. (2.28) is only valid in the absence of an electrical field $\mathbf{E}$, and reveals that conceptually only the $\mathbf{B}$-field and information of the surface normal $\mathbf{n}$ are necessary for evaluation of the force. In the two dimensional case the surface integral is reduced to a line integral of $\mathbf{B}$ around a path enclosing the rotor. Eq. (2.28) needs discretization before the force calculation scheme is applicable which is covered in detail in [95] and will not be treated further here. However, it should be mentioned that FEMM uses a weighted function scheme to average the integration around numerous possible integration paths, and that care must be taken to ensure sufficient element layers in the air gap between rotor and AMB stator [91].

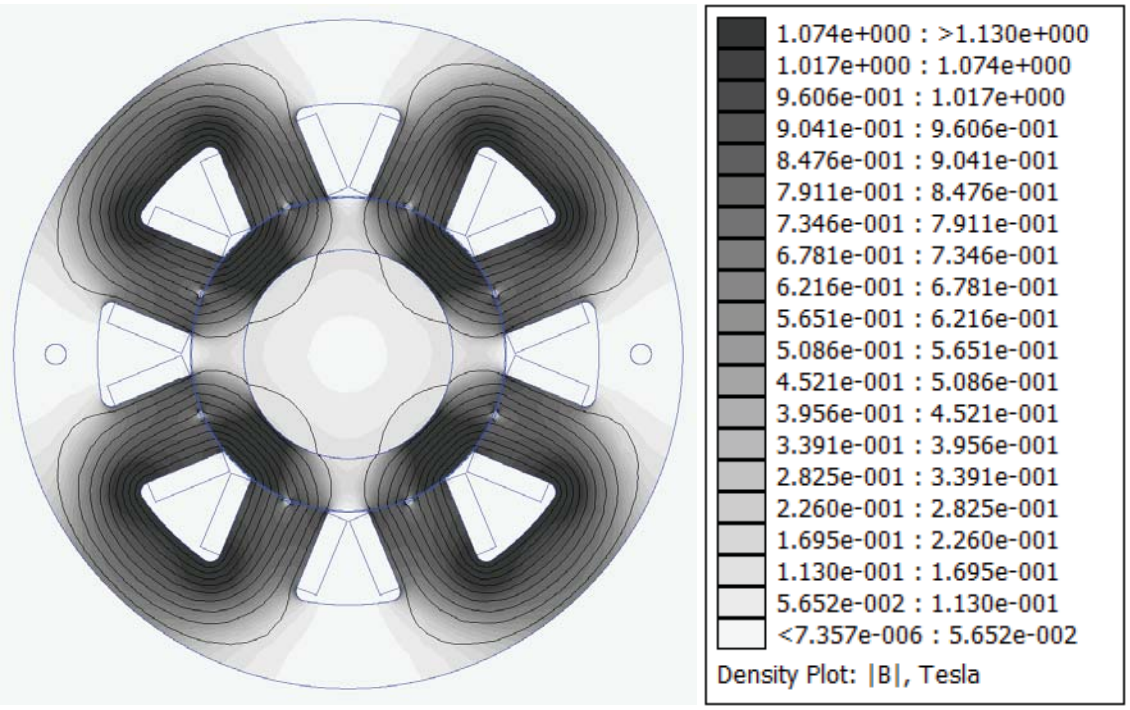

Figure 2.8: Typical visualisation of FEMM simulation results showing a plot of the magnetic flux density and flux paths for a centred rotor. Results presented are for a 10A bias current and zero control current.

Application of FEMM

FEMM has been applied extensively in the design phase of the test facility AMBs. The primary focus has been on determining the AMB geometry such that the static force requirements for the AMBs are met. The force requirements are discussed in section 2.3.1.6. In addition to estimating the force exerted on the rotor, FEMM can be used to estimate K_i and K_s. The numerically estimated K_i and K_s can be valuable as input to a global mathematical model enabling simulation of the system response in the design phase. Furthermore, FEMM has been applied for investigating if the flux for a given combination of bias current and control currents reaches saturation levels in the stator and rotor of the AMB. Ideally the stator and rotor material should reach saturation at the maximum output current of the power amplifiers which is also strongly dependent on the number of turns in the coil. In reality it is a balancing act to arrive at a geometrically compact AMB design that delivers the needed force while avoiding saturation which leads to non-linearities potentially compromising the applicability of the linear control schemes widely applied for AMBs.

Limitations of the AMB FEM Model

Since FEMM is based around a two dimensional solver, it is not capable of quantifying flux variations in the third dimension. For force quantification purposes FEMM uses a depth parameter to scale the resulting force appropriately. In general FEMM is considered appropriate for the application presented here, and the majority of modelling limitations are not considered to be directly related to the numerical implementation or

solution of Maxwell's equations, but to geometrical and material property differences between the FEM model and the physical AMBs. This can be exemplified by considering a variation of the nominal air gap between AMB rotor and stator. Even if the difference between the model and reality is only on the order of a few hundreds of a millimeter, it can lead to significant discrepancies between the numerically estimated force and the force measured through experiments, due to the quadratic dependence of the electromagnetic force on the air gap.

2.3.1.6 Design considerations for AMBs

The overall objective in the AMB design phase is to generate a bearing element that can provide the necessary forces to support the rotor while being able to reject any externally applied disturbances. This imposes strong requirements on the ability of the AMB to exert both static and dynamical forces. Consistently, as is the case here, the available design space is restricted by a multitude of different aspects, such as

- The necessity to insure sufficient stator and rotor heat dissipation capabilities.
- Externally imposed geometric restrictions e.g. from machine enclosure.
- Admissible rotor rotational velocities inherently restricted by the strength of material chosen for the rotor.
- Required rotordynamic system efficiency.
- Available amplifier power.
- System component reliability.
- Design and production time.
- Cost.

All items carry different weight in terms of their impact on the design choices, depending on the application of the AMB based rotordynamic system and the available resources. The AMBs designed for this project are a part of a test vehicle, meaning that some of the above mentioned considerations will have a different impact on the design choices than if the AMBs were designed for e.g. a centrifugal compressor for subsea use. The design of AMBs is an iterative process as the design of each individual element of the AMB will have a strong influence on the design of other elements, making the design process a good candidate for seeking an optimal design through a multi variable optimisation scheme. However, establishing such a design optimisation framework is a considerable task well out the scope for this project, and consequently the strategy employed here follows the classical approach, in which the impact of the design choices on each element is considered in a more holistic fashion. In order to compactly visualise the interdependence of different parameters and aspects of AMB design, a Design Structure Matrix (DSM) is presented in Fig. 2.9. The matrix is not exhaustive and is limited to only include main considerations and parameters. Moreover, it disregards non AMB specific external influences from e.g. the parameters of the rotor. However, the DSM is considered detailed enough for elucidating the main design considerations and how these affect each other. In the following the design considerations are treated sequentially.

		a	b	c	d	e	f	g	h	i	j	k	l	m	n	o	p
Obtainable static force	a	■	x	x			x		x	x	x		x			x	
Magneto motive force	b		■				x						x				
Saturation flux density	c			■					x	x						x	
Formation of eddy current	d				■												x
Necesarry heat dissipation	e				x	■		x									x
Number of coil turns	f						■	x	x								
Coil wire diameter	g						x	■	x				x				
Stator geometry	h						x	x	■	x	x						
AMB rotor geometry	i								x	■							
Nominal air gap size	j								x	x	■						
Inductance	k						x	x	x	x		■					
Maximum amplifier current	l							x					■				
Amplifier bandwidth	m													■			
Obtainable AMB bandwidth	n											x	x	x	■		
Lamination material type	o															■	
Lamination thickness	p																■

Figure 2.9: Design Structure Matrix (DSM) showing dependencies between primary AMB design variables.

Force Considerations

The force that can be generated by an electromagnetic actuator can for design purposes be determined from Eq. (2.11), if the geometric properties of the actuator and the coil current are known. If dynamic variations in the coil current are ignored, inserting the maximum current available from the power amplifiers will yield an estimate of the maximum static force capacity of the electromagnetic actuator. In reality the dynamic performance of the actuator is very important for the operability of AMBs, which is the topic of the subsequent section. For design purposes a good starting point is to consider if the static AMB forces, which can be quantified from Eq. (2.11), can compensate for the loads encountered during operation of the AMB.

To establish the AMB force capabilities needed for a given task, it is necessary to consider the loads that the AMB is required to handle. In general these can be divided into two groups: Static and dynamical loads which in turn can be divided into two additional subgroups: Internal system loads and externally applied loads. The origin and type of the loads relevant for the AMB design is presented in Table 2.1. In the design phase it is assumed that for a sufficiently precise alignment of the coupling and small radial translations of the main rotor, the forces from the flexible coupling linking the main rotor to the intermediate shaft can be neglected. Furthermore, as the rotor is to be balanced to a balancing grade of G2.5, following the ISO standard ISO 1940-1:2003, it is fair to assume that the unbalance force is negligible in comparison to the forces originating from perturbation of the seal flow. The dynamical inertial force load listed in Table 2.1 stems from the fact that the AMBs are required to be able to perturb the rotor during seal testing. At a required perturbation frequency of up to

Table 2.1: Origin and type of design loads.

Origin	Type
Gravitational force on rotor	Static/Internal
Force from misaligned coupling	Static/Internal
Inertia force from perturbing the rotor	Dynamic/Internal
Harmonic force from unbalanced rotor	Dynamic/Internal
Harmonic force from misaligned coupling	Dynamic/Internal
Forces from perturbation of test seal flow	Dynamic/External

200 Hz, the inertial forces can be significant for large perturbation amplitudes. However, as the required perturbation amplitudes are in the order of tenths of micrometers, it is assumed that the inertial forces from accelerating the rotor are negligible for design purposes. This issue will be further addressed in the paragraph describing bandwidth considerations presented later in this section. Consequently, only the gravitational force on the rotor and the forces coming from perturbation of the seal flow will be considered in establishing the necessary force capabilities of the AMB. These are described below:

- The (static) gravitational force on the rotor is determined to approximately 700 N.
- The (dynamic) forces originating from perturbation of the seal flow is determined through a full 3D CFD analysis. To obtain an estimate of the seal forces a simulation similar to that described in [P1] is performed. As the test facility is designed to operate with a mixture of air and water, single phase water is used as the medium for the analysis, in order to establish a worst case scenario for the forces that the AMBs need to be able to exert. Assuming a maximum perturbation amplitude of 10% of the seal clearance of 0.3 mm and a maximum perturbation frequency of 200 Hz a maximum radial force amplitude of 2000 N is determined as the benchmark for the AMBs.

Actuator Bandwidth Considerations

The dynamic force capability of the AMBs is governed by the bandwidth of the electromagnetic actuator consisting of electromagnet and power amplifier. In the present context the discussion is limited to only include aspects relevant for current controlled AMB actuators. The typical dynamic performance of an AMB actuator is illustrated in Fig. 2.10. At relatively low frequencies the full static load capacity of the AMB can be applied dynamically. However, at a certain frequency, here defined as ω_{sat}, the actuator undergoes dynamic saturation, and is no longer capable of delivering the full nominal static load, consequently defining the bandwidth of the actuator. Two factors are of primary importance for the actuator bandwidth:

- The design of the actuator amplifier as well as the power rating of the amplifiers.
- The geometric layout of the AMB stator.

As the test facility AMBs are current controlled the actuator bandwidth is strongly dependent on the speed of the power amplifiers internal feedback loop. In that regard

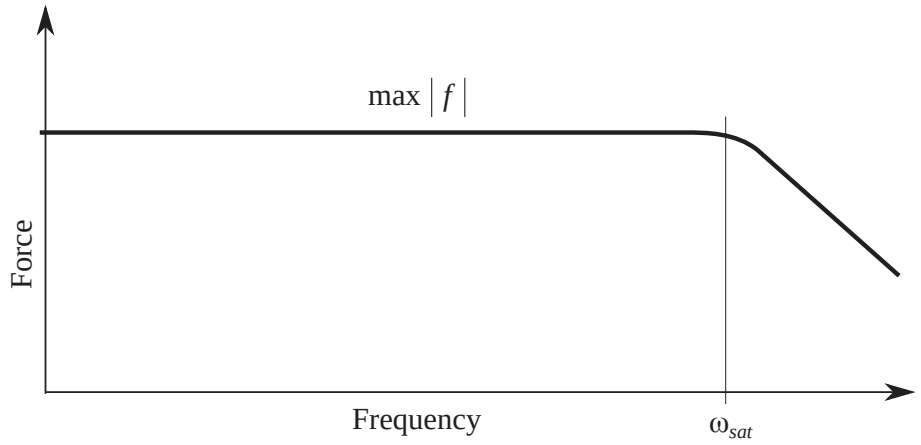

Figure 2.10: Visualisation of typical dynamic performance of an AMB actuator.

it is necessary to insure that the internal feedback loop of the power amplifiers is significantly faster than the wanted dynamic range of the AMB. In addition, the frequency with which the current fed through the coil of the electromagnet can be changed is highly dependent on the geometrical layout of the actuator. Especially the inductance of the actuator, largely governed by the number of turns of the coils, is important. Here it is useful to consider the power amplifier voltage needed to drive current through the coil of the actuator, which can be described by, [69]

$$u = Ri + L\frac{\mathrm{d}i}{\mathrm{d}t} + k_u\frac{\mathrm{d}x}{\mathrm{d}t} \tag{2.29}$$

in which u can be considered to denote the amplifier voltage, R is the resistance of the coil, L is the inductance of the magnetic circuit, i is the coil current, k_u is a coefficient for the velocity induced voltage, and x denotes a generic rotor displacement variable. The velocity induced voltage is considered negligible in the following. Since the resistance R is commonly very small, the first term of Eq. (2.29) is of minor importance. However, the inductance L is of primary importance for the dynamic behaviour of the AMB actuator. It is directly evident from Eq. (2.29) that the magnitude of L needs to be as low as possible to minimise the voltage needed to drive the current through the coil at high current frequencies. As the voltage capability of the power amplifiers are limited by their design, it is necessary to minimise the inductance to avoid requiring excessively large power amplifiers to obtain the desired dynamic AMB actuator performance. The inductance L is in general dependent on the rotor position within the AMB and given by Eq. (2.14), however, imposing simplifying assumptions as discussed in section 2.3.1.2 the inductance can be roughly estimated by Eq. (2.13). From Eq. (2.13) it is seen that the inductance scale quadratically with the number of coil turns and linearly with the pole area of the electromagnet. Additionally, the inductance is inversely proportional to the magnitude of the nominal air gap s.

In addition to the two primary factors discussed above, the formation of eddy currents counteracting the magnetic field generated by the electromagnet can limit the bandwidth as well [97]. However, the influence of eddy currents on the dynamic performance of the actuator is not included in the design considerations, and can to some extent be mitigated by the conventional approach of laminating both the AMB

stator and rotor.

The requirements for the dynamic performance of the AMB actuators are here determined by the desired rotor rotational velocity and rotor perturbation frequency. As the requirement for the perturbation supersedes the rotational velocity requirement the desired perturbation frequency of 200 Hz specifies the minimum actuator bandwidth.

General Performance and Geometrical Considerations

The static and dynamic force capabilities of the AMBs are to some extent mutually competitive. This can be seen by comparing the general expression for the AMB force given by Eq. (2.11) to the expression for the actuator inductance given by Eq. (2.13). It is recalled that increasing the actuator inductance decreases the actuator bandwidth. Increasing the number of turns of the AMB actuator coils increases the force quadratically for the same current, albeit the inductance also increases. A similar, but linear, relationship is found for pole area variations. Furthermore, increasing the pole area without making the AMB stator outer diameter larger generally decreases the available space for the coils entailing that the coils can feature fewer turns without decreasing coil wire diameter. Additional challenges are encountered by including the power amplifiers in the considerations. The thickness of the coil wire dictates the amount of current it can sustain, which makes wire thickness an input for amplifier design. Additionally, the amplifier should be designed so that the AMB stator saturates at the maximum output current of the amplifiers to not waste amplifier capacity which links to the geometrical design of the stator. Moreover, reducing the nominal air gap between AMB rotor and stator will be beneficial both in terms of static and dynamic performance but will imposed stricter manufacturing and assembly tolerances.

For the test facility AMB the starting point of the design process is the wanted rotor diameter which for a specified test seal clearance and seal length implicitly dictates the force that the AMBs have to cope with. Furthermore, the seal rotor diameter, together with the requirement of a rigid rotor and saturation consideration, implicitly specifies the minimum outer diameter of the AMB rotors. In general the AMBs are designed to have a significant safety factor both in terms of static and dynamic force capabilities.

Secondary Design Considerations

The static and dynamic load considerations and the geometrical considerations discussed in the previous paragraphs are considered to be of primary importance to the AMB design. However, other design considerations are shortly introduced and discussed in the following itemised list:

- **Temperature considerations** In the design of the test facility AMBs a simplistic approach to dealing with temperature issues are followed. The current fed through coils is limited by the temperature rating of the wire insulation. Consequently, it should be ensured that the maximum rated current for the chosen coil wire is not superseded. Additionally, current fluctuations generate eddy current in the AMB stator and rotor material which can, to some extent, be mitigated by using laminated electrical steel sheets for these components. Eddy currents

generate heat, which, if excessive, needs to be managed. The design of the test facility AMBs include holes that allow for injecting air into the AMB main housing to convect heat away from the stator assembly if necessary. Additionally, temperature sensors are included in the stator design, so that the temperature can be monitored and the AMBs tripped should the temperature reach critical levels.

- **Speed considerations** For high speed operation centrifugal loads can produce stresses in the rotor above admissible levels. However, within the relative low speeds that the test facility is intended to operate, stresses due to centrifugal loads are not a concern.

- **Loss considerations** For rotating machines employed in the industry losses arising in AMB operation should be minimised to yield energy efficient machines. However, as energy efficiency of the test facility is not particularly important the treatment of AMB operational losses does not receive any further attention in the present documentation.

2.3.1.7 Realised AMB Design

This section contains a description of the realised AMB design. The design parameters are provided in Table 2.2 in which the first entries include references to the geometrical definitions introduced in Fig. 2.6(a).

Fig. 2.11 presents a vertical section view revealing the different components of a test facility AMB. The AMB assembly is divided into three main component groups each given a colour code in Fig. 2.11: The support structure is indicated with a blue hatched pattern, the backup bearing assembly is indicated with a red hatched pattern and the AMB stator assembly is indicated with a green hatched pattern. The three component groups are introduced and discussed sequentially below.

AMB support structure The primary component of the AMB support structure is the main housing which is Computer Numerical Control (CNC) milled out of a solid block of aluminium. The main housing is bolted onto the base block which in turn can be bolted onto the test bed. Two 20 mm thick stainless steel plates are bolted onto each side of the AMB to provide protective cover and transversal stiffness for the AMB assembly. Mounting holes for accelerometers are placed both in the horizontal and vertical centre of the AMB stator. Near the back cover plate threaded holes are included in the design for interfacing with air supply lines. The air supply lines can be used to provide air flow for convective cooling of the stator and coils if necessary. The support structure have been subjected to a FEM based modal analysis campaign to ensure that there are no vertical or lateral modes present in the dynamic operational range of the AMBs.

Backup bearing assembly The backup bearing assembly is indicated with a red hatched pattern on Fig. 2.11. The primary component of the backup bearing assembly is the backup bearing sleeve which is CNC milled from a solid block of stainless steel. The backup bearing sleeve is mounted in the main housing using a fine tolerance sliding fit and held in place by circumferentially distributed bolts. A set of high precision

Table 2.2: AMB design parameters. References are made to Fig. 2.6(a).

Stator pole surface diameter (a)	151	mm
Stator inner diameter (b)	240	mm
Stator outer diameter (c)	300	mm
Nominal radial air gap (S_0)	0.5	mm
Internal stator rounding radius (g)	5	mm
Pole width (p)	40	mm
Stator depth (axial)	80	mm
Number of poles	8	
Winding configuration	N-S-S-N-N-S-S-N	
Lamination thickness	0.35	mm
Number of lamination sheets	228	
Laminate material	SURA M270-35A	
Number of coil windings	36	
Coil wire thickness	2.8	mm
Coil temp. sensor type	PT100	
Number of temp. sensors	4 (one per coil pair)	
Number of Hall sensors	8	
Hall sensor type	F.W. Bell - FH-301	
Hall sensor dimensions ($l \times w \times h$)	$2.54 \times 3.175 \times 0.5$	mm
Number of position sensors per AMB	2	
Position sensor type	VibroMeter TQ402	
Position sensor amplifier	VibroMeter IQS450	
Bias current range	4 to 12.5	A
Max. theoretical static load capacity (per AMB)	7500	N
Theoretical actuator inductance	21	mH

angular contact ball bearings is seated in a compliant ring design and mounted in the backup bearing sleeve. For simplicity the compliant ring is in the present iteration of the AMBs made from aluminium, however the design and material type can be changed in later iterations. The purpose of the compliant ring is to provide energy dissipation in case of a rotor drop. The backup bearings are pre-tensioned using a single turn wave spring and a pre-load ring that is held in place by the backup bearing lid. The pre-load ring can be varied in thickness to obtain different levels of pre-tension. The backup bearings are mounted in a back-to-back configuration to compensate for axial loads during a potential rotor drop. The backup bearing assembly houses the primary AMB sensor system consisting of two high-precision inductive VibroMeter position probes used for feedback control. The backup bearing sleeve is designed to facilitate incorporation of multiple set of position sensors in each bearing. The sensors can be oriented in the vertical and horizontal direction of the global reference frame or tilted 45° to align with the AMB actuator reference frame. Fig. 2.12 presents a rear view of

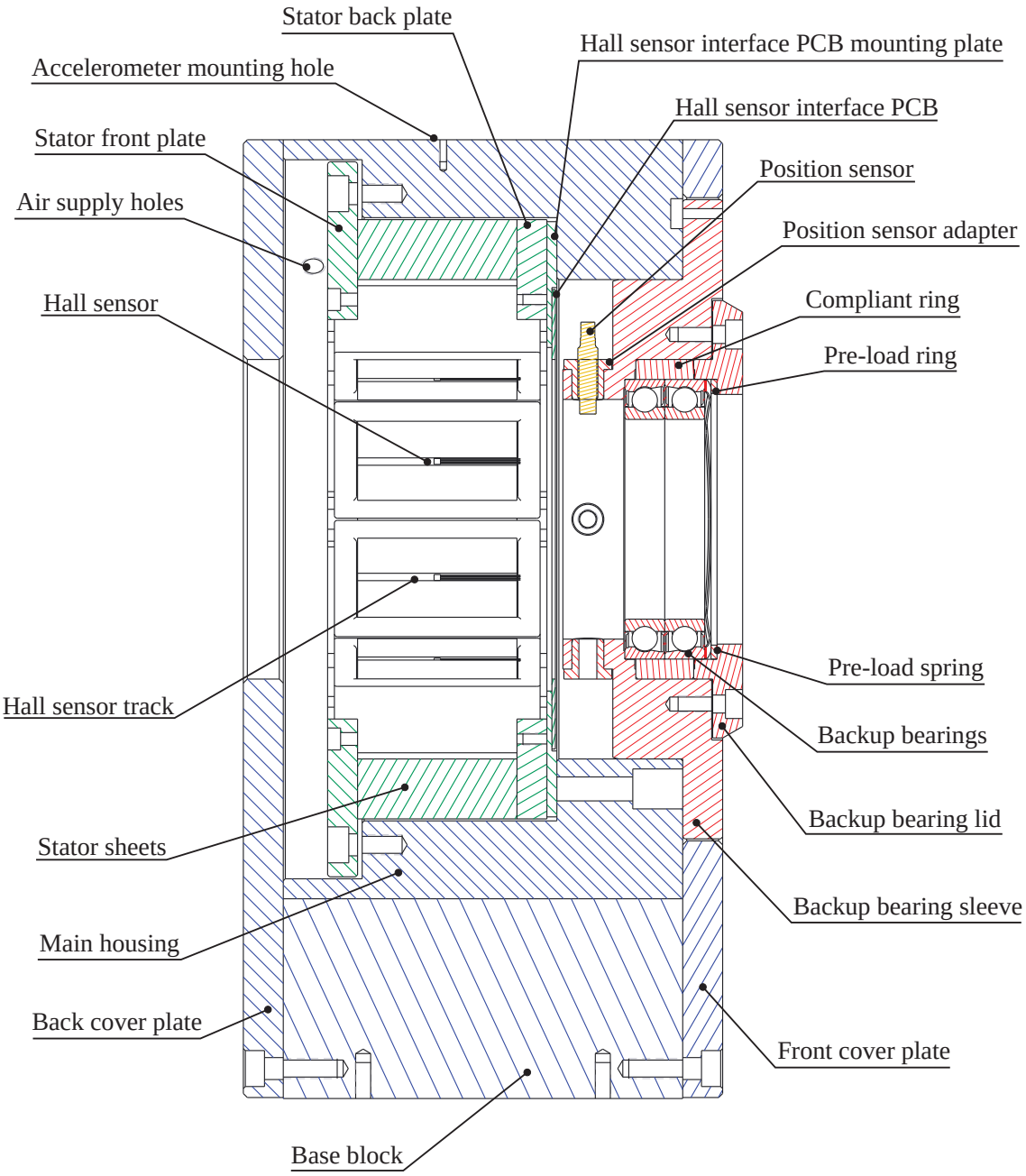

Figure 2.11: AMB section view showing components. Colour scheme indicates component groups.

an AMB without the base block and back and front covers plates mounted. The figure shows the placement of the position sensors.

AMB stator assembly The AMB stator assembly is indicated with a green hatched pattern on Fig. 2.11. The stator sheets are made from SURA M270-35A high quality electrical steel with a high permeability and saturation flux. The sheets are sandwiched in between the stator front and back plates and held together by bolt connections. The orientation of the stator sheets are controlled by guide pins, which also insure precise alignment with the AMB main housing. The stator sheets are coated to electrically isolate them from each other with the aim of reducing formation of eddy currents under

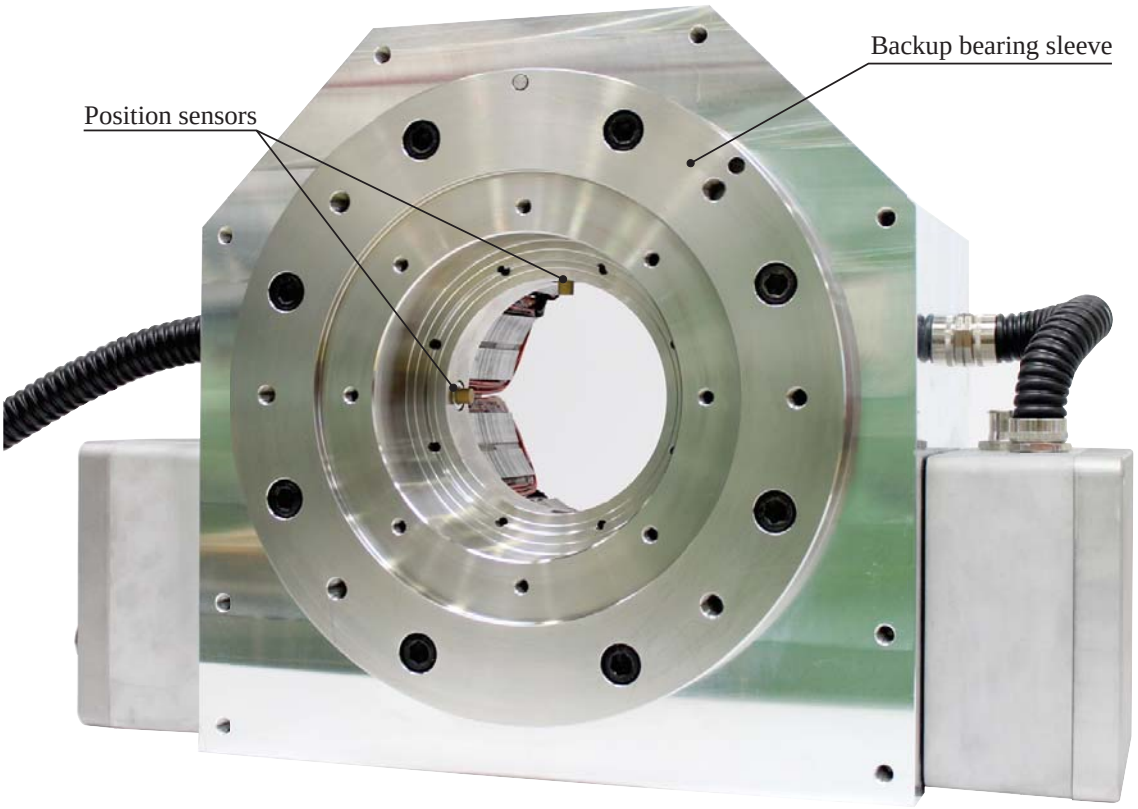

Figure 2.12: Rear view of the AMB presented without the base block and back and front covers plates mounted. The placement of the position sensors in the backup bearing sleeve is indicated. The backup bearing sleeve is shown without the backup bearings and lid.

operation. The stator design adopts the conventional tilted design [69] where the axes of the magnetic bearing actuators are shifted 45° so that two electromagnets can be engaged to account for the gravitational load of the rotor. On the back of the stator assembly the interface Printed Circuit Board (PCB) board for the Hall sensor system is mounted on a dedicated mounting plate. The Hall sensors are cemented into slots in each of the eight pole legs of the stator. The Hall sensors are placed in the vertical centre of the stator sheets. The AMB stator assembly is secured in the AMB main housing by bolts. A front view of the AMB stator mounted in the main housing is shown in Fig. 2.13, in which the AMB assembly is presented without the base block and back and front covers plates. Additionally, Fig. 2.13 shows the placement of the Hall sensor current supplies and amplifiers enclosure as well as the placement of the connection box for the coil power supply lines. The AMB coils are cemented onto the pole leg using a high temperature epoxy compound. Between the coils and the pole legs temperature sensors are mounted to enable monitoring heat development in the stator assembly.

2.3.1.8 Design of the Hall Sensor System

The Hall sensor system is responsible for providing force measurement capabilities to the AMBs. The Hall sensor system has been custom built during this project and consists of the following components

- AMB pole embedded miniature Hall effect sensor.

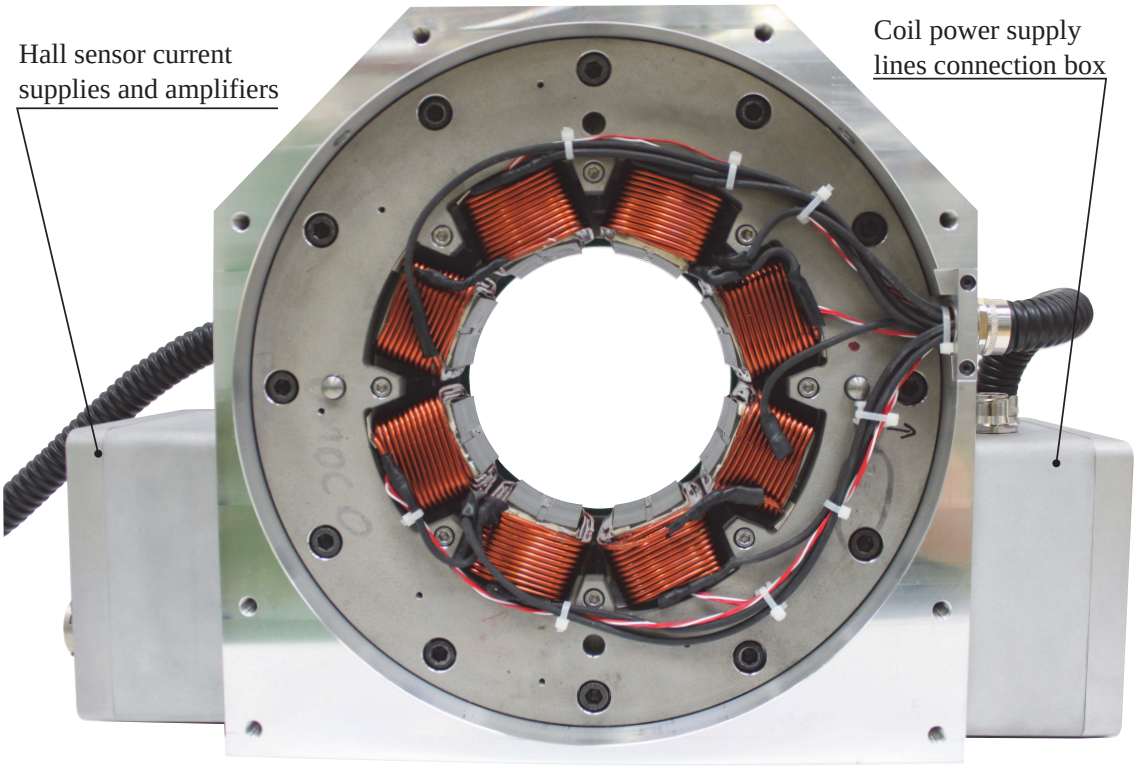

Figure 2.13: AMB front view shown without base block and back and front covers plates. On the figure the placement of the Hall sensor current supplies and amplifiers is indicated together with the placement of the connection box for the coil power supply lines.

- Interface PCB that combines all Hall sensor leads from the eight sensors mounted in each AMB into a single 32 leads cable.
- Current controlled power supplies for each Hall sensor.
- Differential amplifiers employed for amplification of the Hall voltages.

The elements of the Hall sensor system are seen in Fig. 2.14. The Hall sensors are presented in Fig. 2.14(a). The sensors are thin film Indium Arsenide (InAs) semiconductor F.W. Bell FH-301 sensors with dimensions $(l \times w \times h)$ $2.54 \times 3.175 \times 0.5$[mm]. The constant current supplies and the differential amplifiers are based around the PCBs seen Fig. 2.14(b) and Fig. 2.14(c), respectively. Maintaining a constant current supply to the Hall sensors are of paramount importance for the operability of the Hall sensor system, which will become evident in the subsequent section. The interface PCB is shown in Fig. 2.14(d). To minimise the non-amplified signal path for the Hall sensor voltages, the current supplies and amplifiers are contained in an aluminium enclosure mounted on the side of each AMB. The enclosure is seen in Fig. 2.14(e). The placement of the embedded Hall sensors is shown in Fig. 2.15, which additionally shows the placement of the aluminium enclosure containing the current supplies and Hall sensor voltage amplifiers. Embedding the Hall sensors keeps the fragile sensors protected, at the cost of a slightly reduced effective AMB pole area. The reduction in pole area reduces the maximum force generated by the AMBs, however the effect is minimal and has been determined to be in the order of 2% of the maximum load, which is consistent

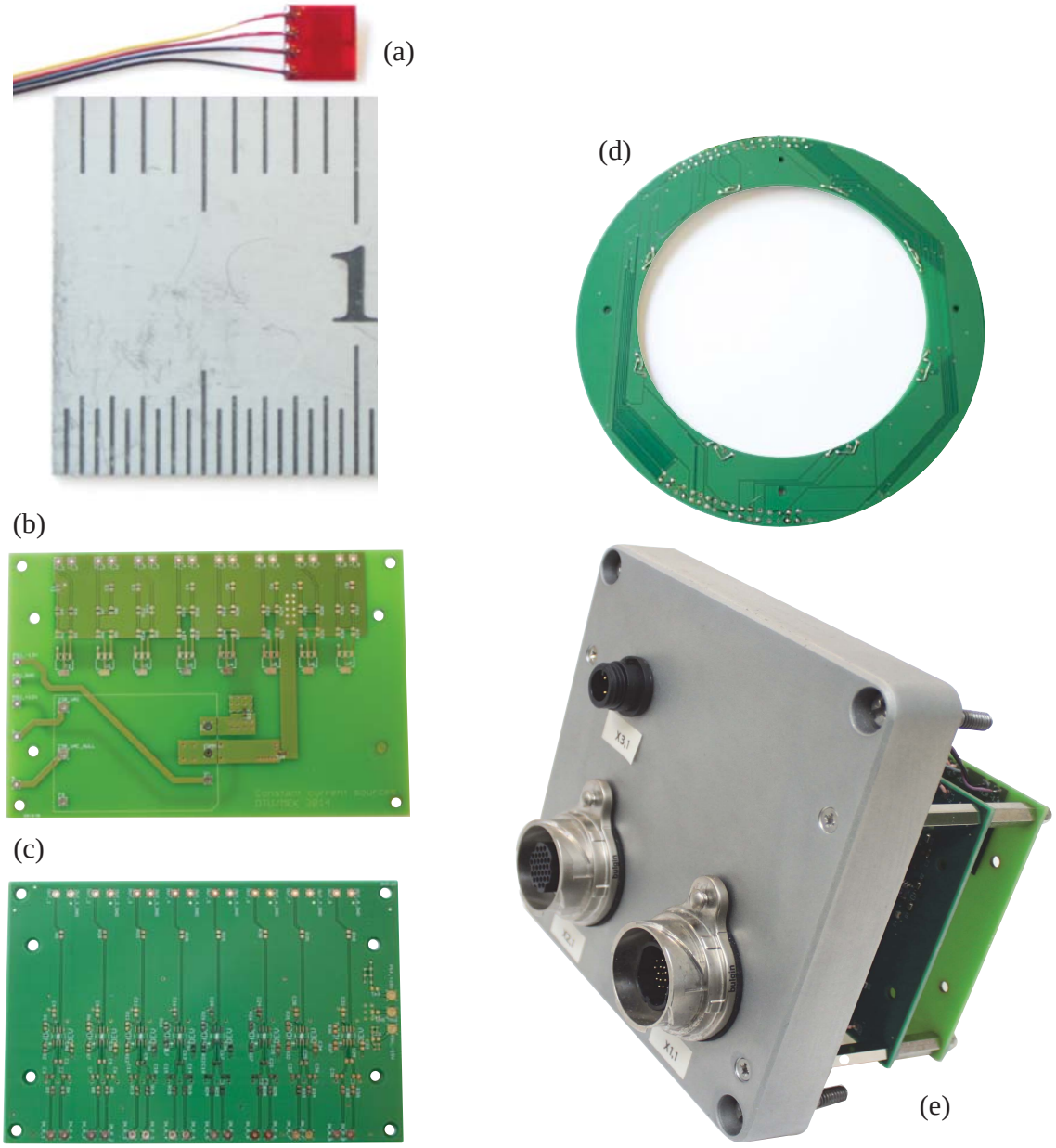

Figure 2.14: Components of the Hall sensor system. (a) Hall sensor, (b) constant current supply PCB, (c) differential voltage amplifier PCB, (d) Hall sensor interface PCB, (e) aluminium enclosure housing the Hall sensor power supplies and amplifiers.

with previous findings [66]. Fig. 2.16 shows a rear view of an AMB without the backup bearings sleeve installed enabling a view of the Hall sensor interface PCB.

Mathematical Model of the Hall Sensor

To relate the Hall voltage to the electromagnetic force exerted by an AMB actuator, a model of the Hall sensor must be obtained. The derivation of the Hall sensor model presented here is adapted from [98].

The definitions used in the following are presented in Fig. 2.17. A current $\mathbf{I}_H$, considered

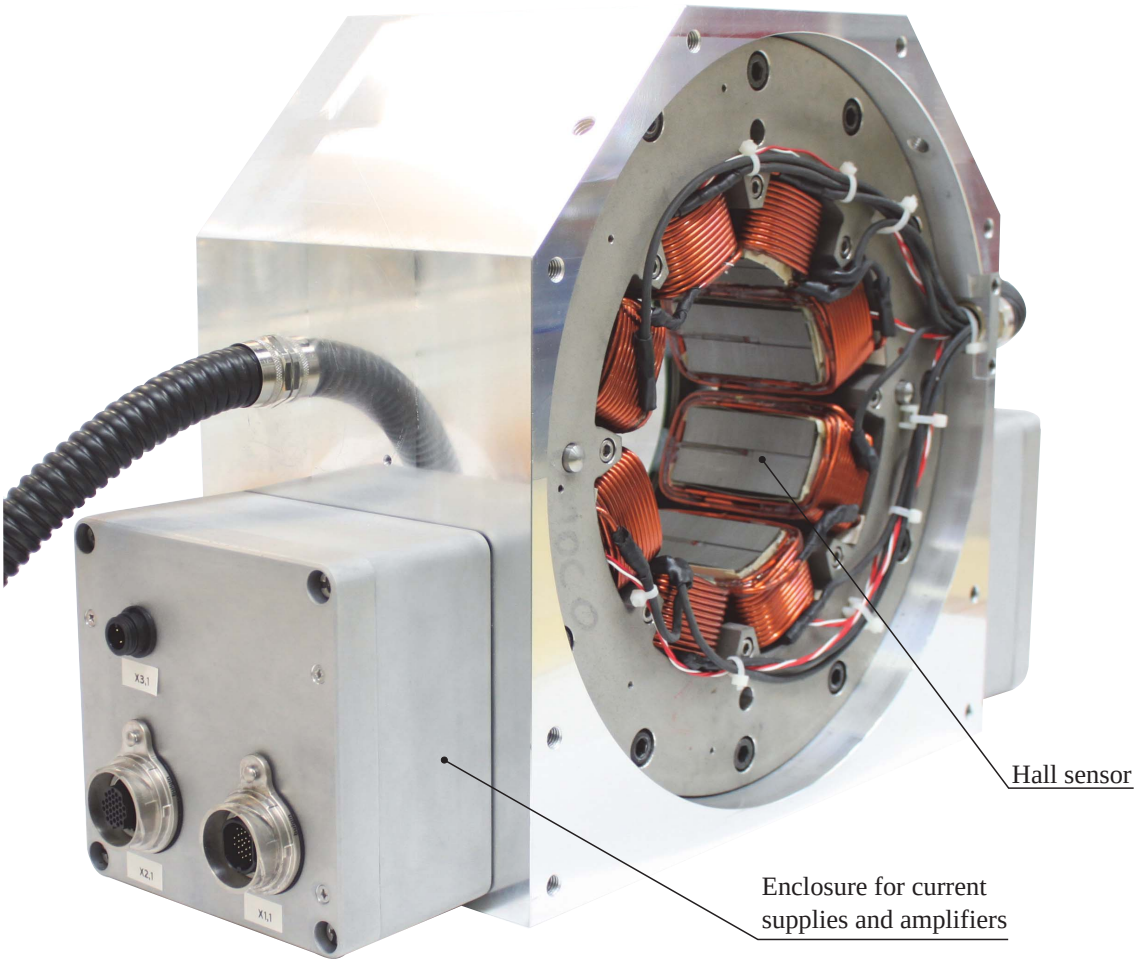

Figure 2.15: Figure shows the placement of the embedded Hall sensors as well as the aluminium enclosure containing the current supplies and Hall sensor voltage amplifiers.

to be consisting of a large number of flowing charge carriers having the charge q_e, runs through the Hall element sketched as a rectangular box in Fig. 2.17. The current density $\mathbf{J}_H = \mathbf{I}_H/A$ parallel to $\mathbf{I}_H$ and normal to the cross section area A can be defined as [84]

$$\mathbf{J}_H \equiv q_e \rho \mathbf{v}_e \tag{2.30}$$

in which q_e is the charge carrier, ρ is the density of the flow of charge carriers and $\mathbf{v}_e$ is the velocity of the charge carriers. The current density $\mathbf{J}_H$ can be thought of as the area normalised current having the same directional orientation as the current $\mathbf{I}_H$. In the presence of a magnetic field, the current carriers are affected by a Lorentz force perpendicular to both the direction of the current density and the imposed field, [84], as illustrated in Fig. 2.17. The magnetic Lorentz force is given as [84]

$$\mathbf{F}_m = q_e \mathbf{v}_e \times \mathbf{B} \tag{2.31}$$

By keeping the vector notation of Eq. (2.30) and (2.31) it is implied that no assumptions about the direction of any vectors displayed in Fig. 2.17 are made. Isolating $\mathbf{v}_e$ in Eq. (2.30) and substituting it into Eq. (2.31) yields

$$\mathbf{F}_m = \frac{1}{\rho} \mathbf{J}_H \times \mathbf{B} \tag{2.32}$$

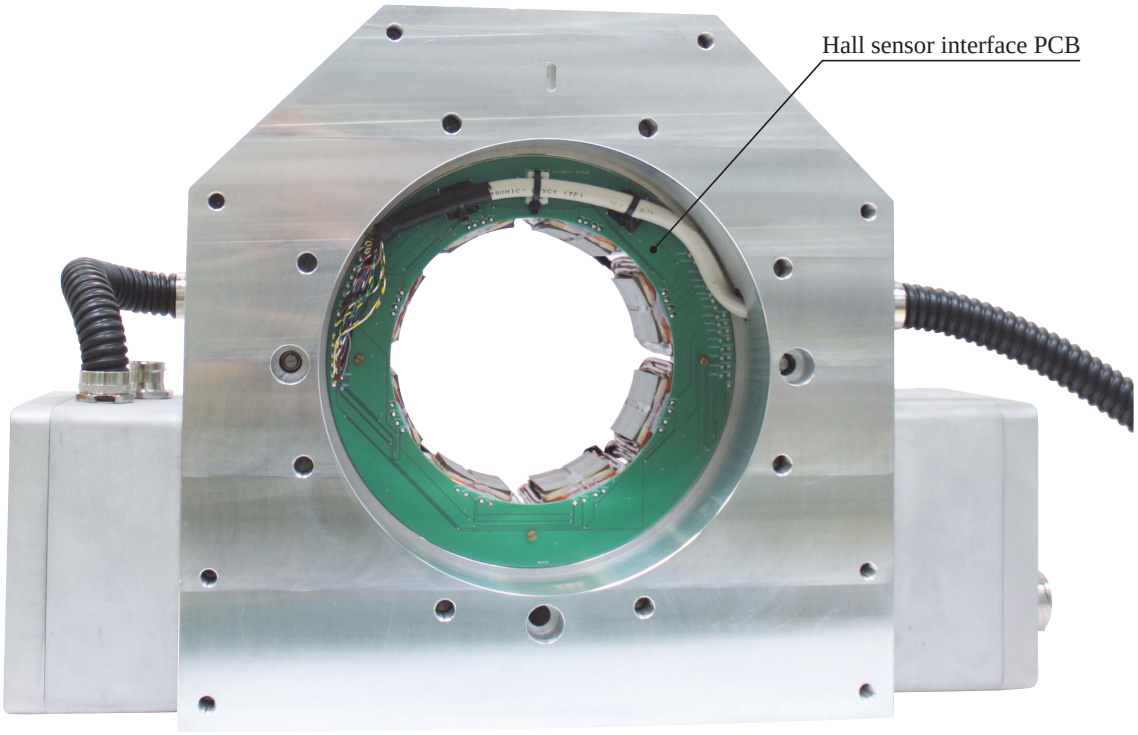

Figure 2.16: Rear view of AMB without the backup bearings sleeve installed revealing the Hall sensor interface PCB.

Considering that $\mathbf{J}_H$ is normal to the surface area A, that $\mathbf{F}_m$ is perpendicular to $\mathbf{J}_H$, and that the potential difference occurs on the sides of the Hall element, it is natural to evaluate $\mathbf{F}_m$ in the x-direction defined in Fig. 2.17. This is done by defining a unit vector $\mathbf{e}_x$ in the x-direction and evaluating the dot-product between $\mathbf{F}_m$ and $\mathbf{e}_x$ as

$$F_{m,x} = \mathbf{F}_m \cdot \mathbf{e}_x \tag{2.33}$$

$$= \frac{1}{\rho}(\mathbf{J}_H \times \mathbf{B}) \cdot \mathbf{e}_x \tag{2.34}$$

$$= \frac{1}{\rho}|\mathbf{J}_H||\mathbf{B}|\sin\eta\cos\theta \tag{2.35}$$

Comparing Fig. 2.17 to Eq. (2.35) reveals that the magnetic force evaluated in the x-direction is a function of the angles with which the magnetic flux density is imposed. The magnetic force exerted on the charge carriers will cause these to accumulate on one side of the Hall element, consequently generating an electric field counteracting this charge distribution. When the electric field reaches a certain strength, known as the Hall field strength [99], a state of equilibrium occurs which can be described as

$$F_{m,x} + F_{e,x} = 0 \tag{2.36}$$

in which $F_{e,x}$ is the counter acting Lorentz force caused by the electric field. The electric field is constant at equilibrium, and the potential energy build-up due to displacement of a charge carrier q_e the distance ∂x in this field can be related to the opposing force $F_{e,x}$ the following way, [99]

$$\frac{F_{e,x}}{q_e} = -\frac{\partial u}{\partial x} \tag{2.37}$$

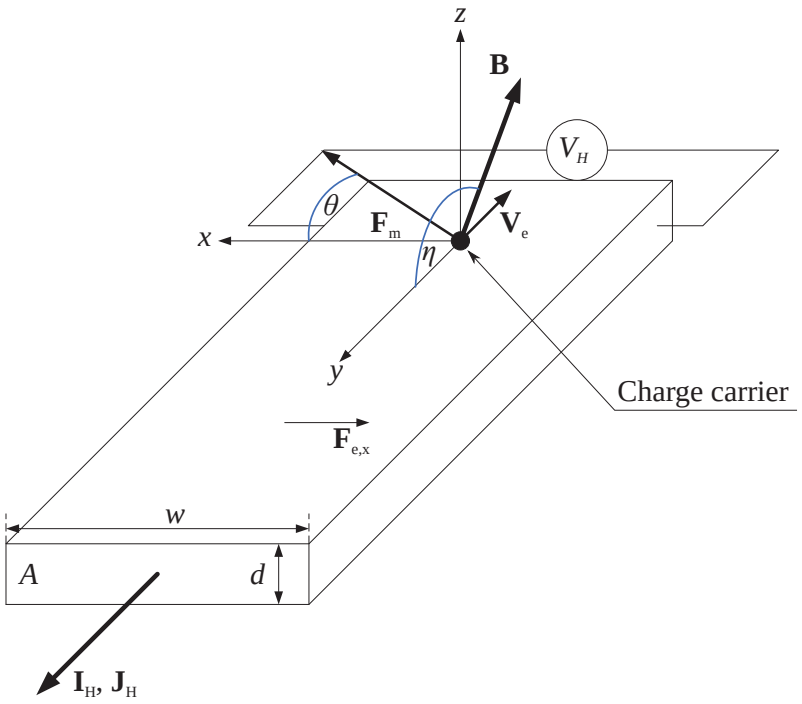

Figure 2.17: Hall element sketch showing definitions used for deriving the Hall sensor governing equation.

where ∂u is the potential difference. It can be shown that [99]

$$\frac{\partial u}{\partial x} \approx \frac{\Delta u}{\Delta x} \tag{2.38}$$

By substituting Δu for the Hall voltage V_H and considering Δx to be the total width of the Hall element w the following is obtained from Eq. (2.38) and (2.37)

$$\frac{F_{e,x}}{q_e} = \frac{-V_H}{w} \tag{2.39}$$

By utilising the equilibrium condition stated in Eq. (2.36), rearranging and implementing Eq. (2.39) into Eq. (2.36) the following is obtained

$$V_H = \frac{w}{q_e}\frac{1}{\rho}|\mathbf{J}_H||\mathbf{B}|\sin\eta\cos\theta \tag{2.40}$$

It should be noted that the charge carrier q_e is assumed to carry electrons with a negative charge of e which explains the direction of $\mathbf{v}_e$ in Fig. 2.17. This assumption implies that the conductor media is most likely a metal. The materials used in the fabrication of modern Hall elements are conventionally semi conducting materials, in which the charge carrier can carry both electrons and positive electron holes [99]. Even though this charge ambiguity is important to the Hall principle, no fault is made by assuming that the charge carriers only carry electrons [99]. Imposing $q_e = -e$, and considering the definition of current density and conductor surface area, Eq. (2.40) can be expressed as

$$V_H = \frac{1}{e\rho d}|\mathbf{I}_H||\mathbf{B}|\sin\eta\cos\theta \tag{2.41}$$

If **B** is assumed to be normal to the upper surface of the Hall element Eq. (2.41) simplifies to

$$V_H = \frac{1}{e\rho d} I_H B \tag{2.42}$$

in which I_H and B are the magnitude of the Hall sensor control current and the magnetic flux density, respectively. This simplification is supported by the fact that the Hall element is generally considered to be much smaller than the magnetic pole surface area, so the field can be considered homogeneous through the Hall element. Eq. (2.42) is seen to be purely scalar and determines V_H as a function of the current magnitude I_H and the magnetic flux density B. Furthermore, Eq. (2.42) reveals the importance of supplying the Hall sensors with a constant current I_H, since variations in the supply current would be interpreted as variations in B ultimately leading to erroneous force measurements.

Hall Sensor Based Force Transducer Model

The Hall sensor model given by Eq. (2.42) relates the magnetic flux density to a measurable quantity, namely the Hall sensor voltage. Additionally, Eq. (2.9) presented in section 2.3.1.2 describes the force exerted by an electromagnet on a magnetisation target as a function of the magnetic flux density. Combining Eq. (2.9) and Eq. (2.42) yields

$$F = KV_H^2 \tag{2.43}$$

in which the coefficient K is defined as

$$\frac{A_g}{2\mu_0}\left(\frac{q_e \rho d}{I_H} Geo\right)^2 \equiv K \tag{2.44}$$

In Eq. (2.44) the factor Geo is introduced which represents all effects related to embedding the Hall sensor in slots in the AMB pole surfaces as opposed to mounting these on the pole surface as implicitly assumed in the derivation of Eq. (2.9) and Eq. (2.42). To enable a precise estimation of the force exerted by the AMB actuators the coefficient K of Eq. (2.43) needs to be quantified experimentally. This is the topic of section 4.2 presenting the calibration procedure for the Hall sensor system.

2.3.2 Rotor Design

The design parameters for the test facility rotor are presented in Table 2.3. The rotor assembly is shown in Fig. 2.18 and consists of two main component groups, namely, the solid rigid shaft and the two AMB rotors. The AMB rotors are composed of three parts. The rotor sheets are sandwiched in between an inner and an outer rotor sleeve which is held together by a bolt connection. The rotor sheets are manufactured from the same material as the AMB stator sheets. The outer sleeve includes the position sensor measurement target surface as well as a backup bearing surface. The AMB rotors are mounted onto the shaft through a conical interference fit between the inner rotor sleeve and the shaft and the assembly is held in place by a locknut. The rotor is designed to be rigid in the entire operational range of the test facility and the first natural frequency corresponding to the first flexible mode is determined theoretically and experimentally to 550 Hz.

Table 2.3: Rotor design parameters.

Rotor length	860	mm
Rotor assembly mass	69	kg
AMB rotor outer diameter	150	mm
Test seal rotor diameter	110	mm
First bending mode @	550	Hz
Lamination thickness	0.35	mm
Number of laminations	228	
Laminate material	SURA M270-35A	
Shaft material	Impax supreme	
AMB rotor outer sleeve material	VCL 140	
AMB rotor inner sleeve material	Aluminium	

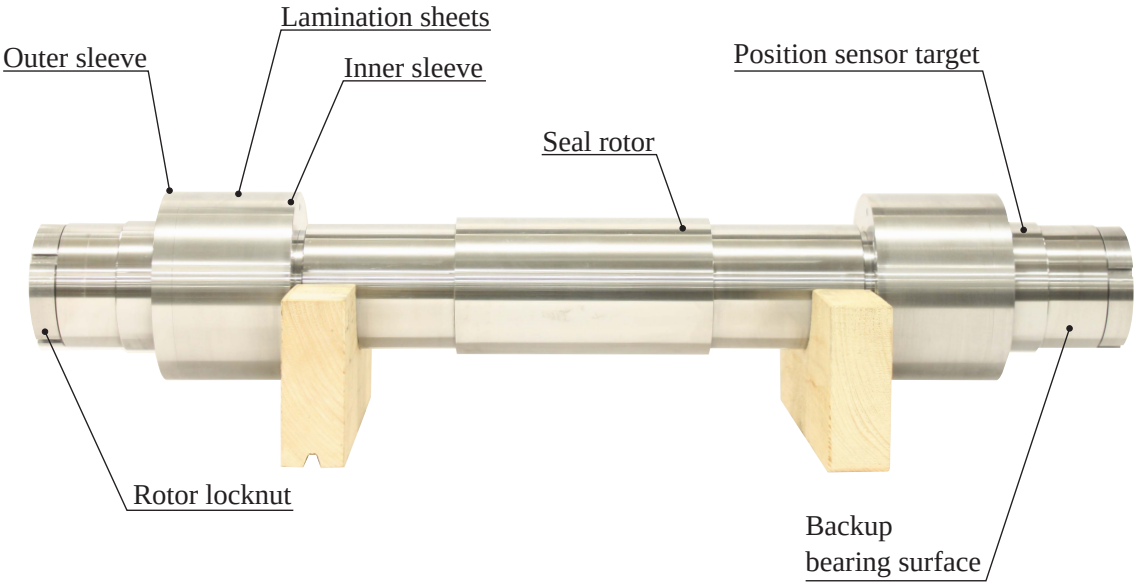

Figure 2.18: Test facility rotor.

2.3.3 Power Amplifiers

The eight power amplifiers supplying current to the coils of the AMBs are commercial available SM120-25D amplifiers from Delta Elektronika with a rated power of 3kW. Commercially available power amplifiers have been chosen to exclude amplifier design from the project scope. The amplifiers are of the switch-mode type capable of delivering 25A at 120V. The amplifiers are programmable through an analogue input, and are controlled via the test facility I/O interface. Between the Input/Output (I/O) interface and the individual amplifiers a galvanic separation point is introduced to avoid ground-loops, potentially disturbing the amplifier command signal. An internal control loop within each amplifier ensures that the amplifier supplies the current requested by the AMB controller.

2.3.4 AMB Controller

Feedback based position control of the rotor is currently achieved through a decentralised discrete Single Input, Single Output (SISO) control structure. The implemented baseline controller is a Proportional-Integral-Derivative (PID) controller which includes an anti-windup scheme for the integrator. A PID controller has been chosen for initial performance assessment of the test facility due to its simplicity. An overview of controller types suitable for AMB control can be found in e.g. [69], which includes a description of the mathematical modelling techniques providing the foundation for controller development. The implemented AMB controller is designed based on a global mathematical model of the AMB-rotor system, however substantial manual tuning has been performed to facilitate rotor levitation and rotation. The controller is implemented using Mathworks Simulink, and runs on the dSPACE system described subsequently in section 2.7.

2.3.5 Drive Unit Design

The drive unit is seen in Fig. 2.19. The drive unit is based on a 7.5 kW asynchronous electric motor which applies driving torque to the main test facility rotor through a timing belt, an intermediate shaft assembly, and a flexible coupling. The motor is controlled by a Variable Speed Drive (VSD) which in turn can be controlled from the test facility control interface, see section 2.7. The rotor speed is measured by an incremental encoder which additionally enables implementing a run-out compensation scheme for the AMB position sensor system. The intermediate shaft is supported by angular contact ball bearings to compensate for any axial loads transmitted from the main rotor through the flexible coupling. Additionally, the intermediate shaft assists in isolating the main rotor from vibrations transmitted by the motor and belt drive. The flexible coupling is rotationally rigid but allows for transversal and axial movement of the main rotor. The pulleys on the motor output shaft and the intermediate shaft can be changed to facilitate different gearing ratios between the motor and main rotor.

2.3.6 Performance Evaluation of Module I

The two AMBs of Module I generally performs as intended and are capable of levitating the rotor and keeping the open loop unstable equilibrium stable for a bias current range of 4 A − 10 A. Additionally, the AMBs facilitate sinusoidal perturbation of the rotor both with the rotor at standstill and while rotating. Rotor perturbation frequencies above 200 Hz have been realised for the rotor at standstill while the full range of perturbation frequencies for the rotating rotor has not been fully explored. Resulting perturbation amplitudes tested are on the order of $10\,\mu$m − $20\,\mu$m, which has proven to be sufficient for retrieving meaningful seal force data, see section 4.5. The drive unit functions as intended and rotational rotor velocities have been realised up to 3000 rpm. The Hall sensor system performs as intended and is capable of quantifying forces acting on the rotor, which is explored in depth in section 4.2. The implemented run-out scheme and the coil temperature sensors functions as intended.

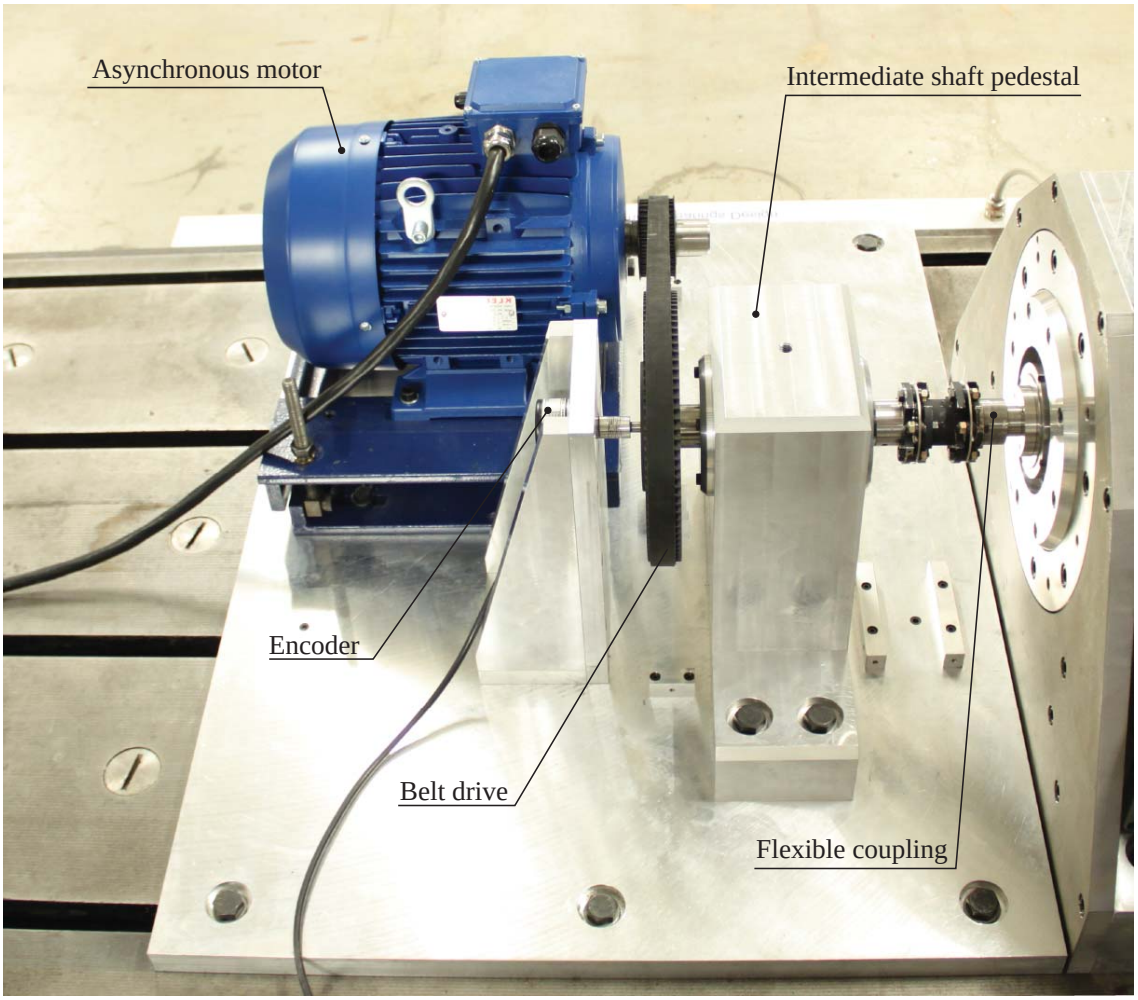

Figure 2.19: Test facility drive unit.

2.4 Module II - Calibration Facility

The calibration facility is primarily intended to be employed in the calibration procedure of the Hall sensor system. The calibration facility consists of the calibration rig seen in Fig. 2.20 and a nylon sleeve, steel clamp mounted on the rotor and a force transducer assembly seen in Fig. 2.21. The calibration facility enables multi-directional application of static forces to the rotor utilising an electronically controlled pneumatic system to control both magnitude and direction of the forces. Module II is designed based on the concept that reference forces exerted during the calibration of the Hall sensor should be able to be applied in an automated sequence with high precision, consequently minimising the potential erroneous quantification of the reference forces. The calibration rig is designed around a heavy-duty u-shape steel frame, which allows the calibration rig to be hoisted onto the test bed and placed over the rotor.

2.4.1 Multi-Directional Force Application

The calibration facility depicted in Fig. 2.20 is designed to exert up to 5 kN per pneumatic actuator at a maximum supply pressure of 7 bar available from the laboratory

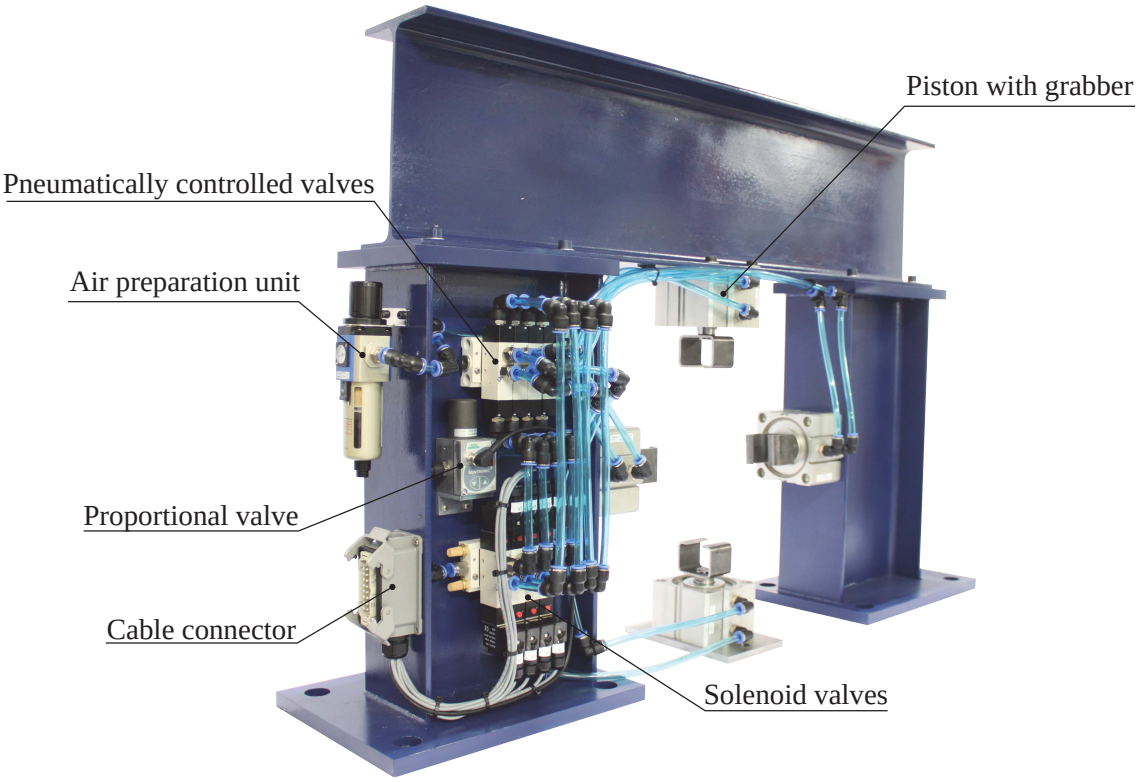

Figure 2.20: Calibration rig with the pneumatic force application system.

central air supply. A schematic presentation of the pneumatic system is included in Appendix A. In the following the functionality of the calibration facility is described. An air preparation unit filters and adds lubrication to the air and additionally allows for manual regulation of the supply pressure. From the air preparation unit the air is led to both the controllable proportional valve and the solenoid valves. The pressure set point for the proportional valve is controlled from the dSPACE system. The pressure set by the proportional valve is ultimately fed to the pneumatic actuators, and consequently the proportional valve controls the magnitude of the force exerted by the pneumatic actuators. The direction of the applied force is controlled by feeding the pressure set by the proportional valve to one of the four pneumatic actuators of the calibration rig. A Programmable Logic Controller (PLC) controlled via an analogue output port of the dSPACE I/O-interface is employed to select the desired pneumatic actuator and thereby the direction of the force exerted on the rotor. Depending on the magnitude of the voltage signal from the dSPACE system the PLC sends a signal to open a specific solenoid valve. When a solenoid valve is activated the resulting pressure opens a pneumatically controlled valve, which in turn lets the pressure set by the proportional valve enter the corresponding pneumatic actuator chamber. Each of the eight solenoid valves activates one of the eight pneumatically controlled valves which correspond to one of the eight chambers in the four pneumatic actuators. Depending on which chamber in the pneumatic actuator is pressurised, the piston either pushes or pulls.

In Fig. 2.21 the nylon sleeve and steel clamp mounted on the rotor are shown. It is noted that the set up in Fig. 2.21 is for illustrative purposes only. The nylon sleeve protects the rotor surface while ensuring that the point of attack for the force applied by

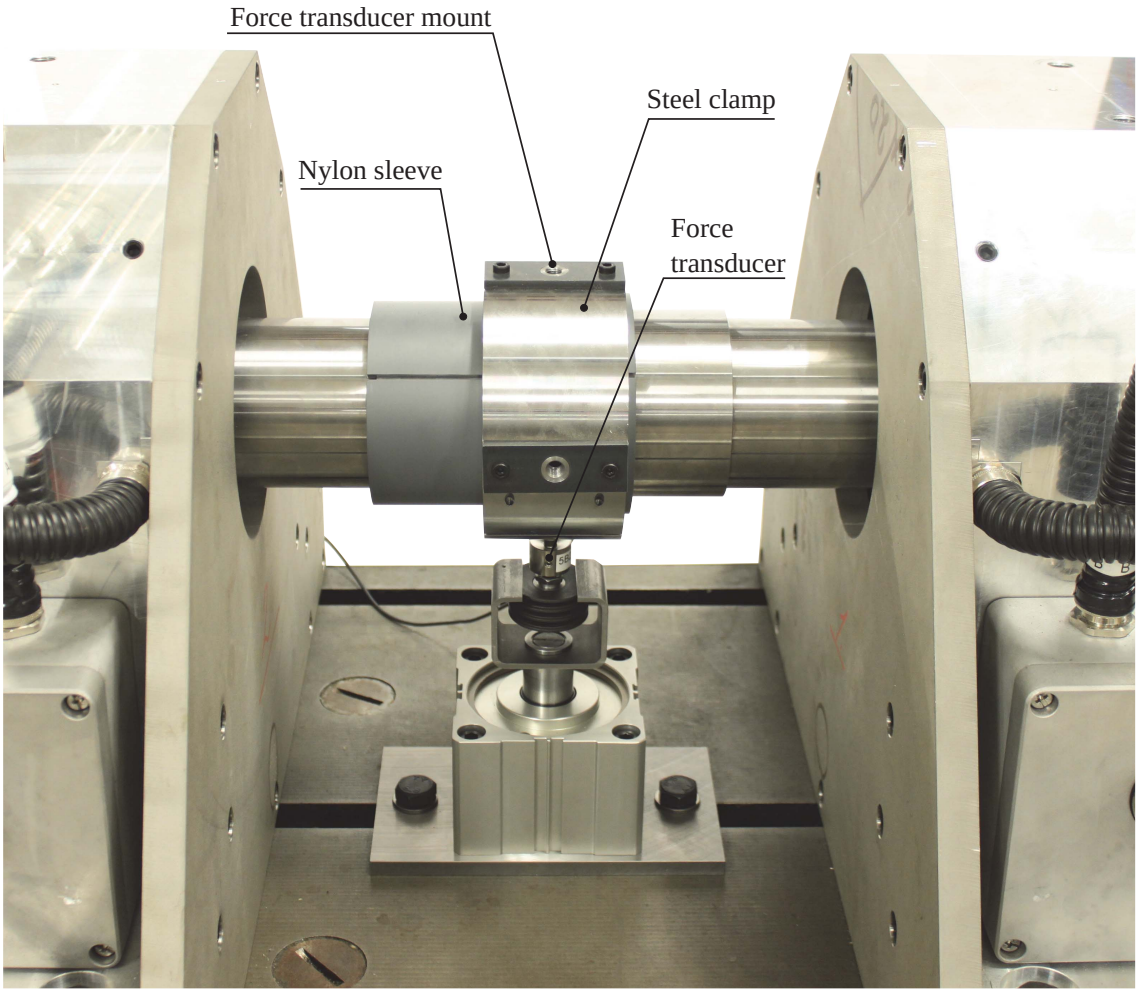

Figure 2.21: The force application sleeves mounted on the rotor. A single force transducer is mounted in the steel clamp together with the Belleville spring setup. A pneumatic actuator with grabbing device is mounted below the rotor.

the calibration module is in the axial centre of the rotor. Below the rotor a pneumatic actuator with a grabbing device is mounted. The pneumatic actuator with the grabbing device is shown in detail in Fig. 2.22. On the steel clamp mounted onto the rotor four force transducers are installed. Each force transducer is mounted with a fitting device that holds seven Belleville springs. The Belleville springs add compliance to the interface between the pneumatic actuators and the rotor, to ensure that the force transducers are not subjected to shocks during the calibration procedure.

The calibration facility is designed such that when the piston of a pneumatic actuator is in the ejected position, the grabber releases the springs, and there is no mechanical contact between grabber and rotor. When the piston of the pneumatic actuator is retracted it grabs the Belleville springs and consequently loads the rotor. The design can accommodate misalignments and hence reduces the risk of having a bending moment over the force transducer, which would lead to erroneous force measurements. During calibration experiments the full calibration module with all four pneumatic actuators and the four force transducers are mounted. The force transducers are 10 kN U9C

Figure 2.22: Close up of the pneumatic actuator and grabbing device. The grabber engages with the Belleville springs when the piston of the pneumatic actuator is retracted.

strain-gauge based multi directional sensors from HBM. A HBM AE301 measuring amplifier is coupled with each of the force transducers. The amplifiers are synchronised with each other to avoid cross-talk and are calibrated to the maximum applied load of 5 kN. The test facility with Module II installed is presented in Fig. 2.23.

2.4.2 Performance Evaluation of Module II

Module II functions as intended. The pneumatic actuators enable exerting a force of up to 5 kN per piston on the rotor. The control system performs as expected enabling the automation functionality necessary for the calibration of the Hall sensor system as discussed in section 4.2.

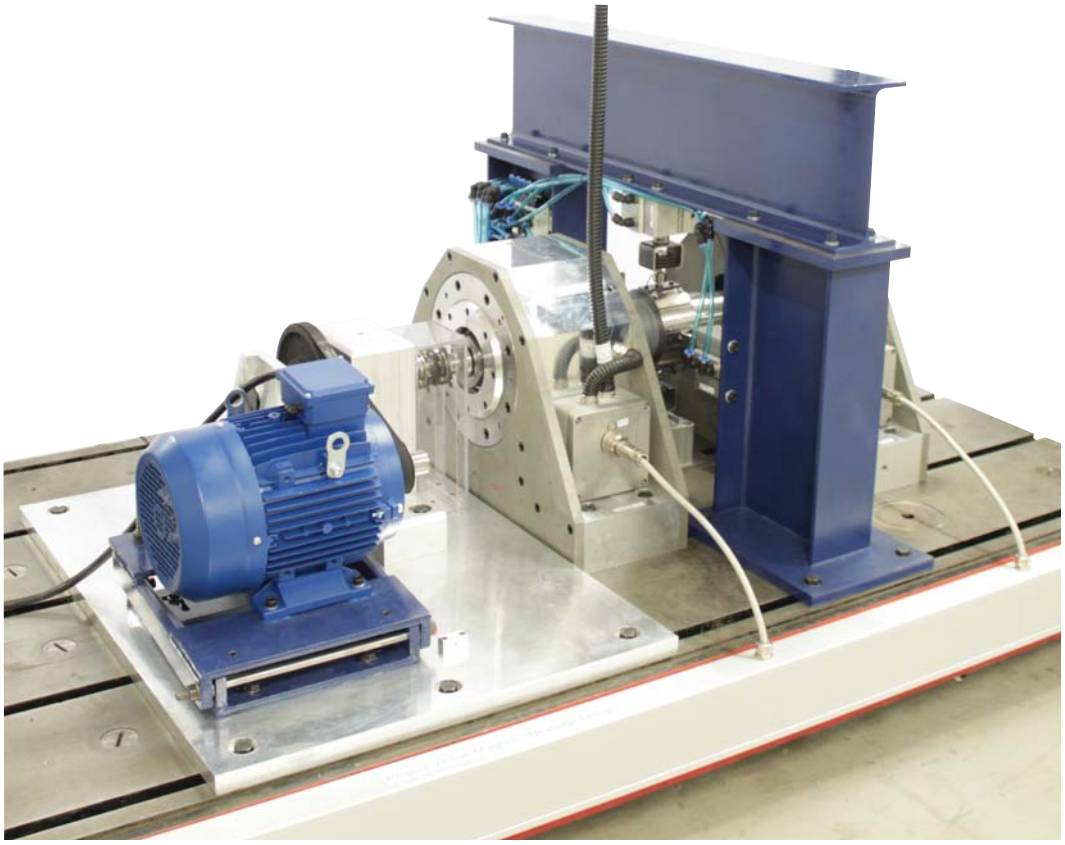

Figure 2.23: Module II installed on the test facility bed.

2.5 Module III - Seal Housing Assembly

The present section contains a description of Module III of the test facility also referred to as the Seal Housing Assembly (SHA). The design of the SHA constitutes a significant task during the project which is partly attributed to the relatively complex geometry of the SHA components, giving rise to manufacturing challenges. The main design considerations for the SHA is

- The overall goal of this research project, spanning outside the work documented in this thesis, is to validate CFD based estimation of rotordynamic coefficients for seals in multiphase flow. To this end smooth annular seals have been chosen as initial test seals as their simple geometry and well known single-phase performance constitutes a good choice for benchmarking the capabilities of the test facility.

- Two test seals mounted in a back to back configuration is used to alleviate axial thrust. Consequently, an axial bearing can be omitted from the design simplifying the overall layout of the test facility.

- The seal housing is designed to replicate seals mounted in a high pre-swirl environment of an industrially applied machine. Preferably the pre-swirl ratio should be modifiable through simple means.

- The SHA should accommodate seal tests with single phase gaseous and liquid fluids as well as multiphase flow. This entails that the SHA must incorporate secondary sealing features capable of completely mitigating leakage flow.
- The operating fluids are air and water, of which air is used for the commissioning of the test facility.
- Pressure and temperature sensors are to be incorporated to provide additional validation data for the CFD simulation results.
- The first design iteration should include considerations for implementing phase mixing devices upstream to the inlet cavity.

2.5.1 Mechanical Design of Seal Housing

A half part of the SHA is presented in Fig. 2.24. The SHA adopts the modular design of the AMBs and is made in a vertically split design to ease assembly. Fig. 2.24 depicts the inlet cavity with a single injection nozzle installed, the outlet feature containing the primary and secondary flow outlets, mounting holes for the pressure transducers, the test seal lands and the SHA support structure. Each half part of the SHA containing the inlet cavity and test seals are CNC milled out of a solid block of aluminium, and constitutes the backbone of the SHA. The outlet features are bolted onto the backbone component. Flow is supplied to the SHA through the four injection nozzles placed in the inlet cavity. From the inlet cavity the supplied flow enters the test seals and exits through the two outlet features. To provide an overview of the internal geometry of the test facility in seal test mode, a horizontal section view is included in Appendix B.

2.5.1.1 Inlet Feature Design

A section view of inlet cavity centre is presented in Fig. 2.25, visualising the symmetric distribution of the four inlet nozzles. Additionally, the mounting holes for the two pressure transducers are visible on the figure. The nozzles are positioned by a fine tolerance fit and a guide pin to ensure proper orientation. The nozzles are held in place by a flow adapter component which is shown in Fig. 2.26 alongside an injection nozzle. The flow adapter interfaces with the flow supply lines and is a relatively simple, and to a large extent axisymmetric, component that can easily and inexpensively be remade to fit a flow mixing device to accommodate multiphase flow testing. In this iteration of the SHA design the pre-swirl is fixed and cannot be adjusted mechanically but only by changing the injection flow velocity through modifying the nozzle geometry. As evident from the tangential injection direction, the SHA is indeed aimed at testing seals in the high pre-swirl range. The inlet cavity and the nozzle design have received substantial attention during the design phase and CFD based analyses have been applied extensively throughout. An exemplifying CFD case study of the nozzle geometry is introduced in section 3.2.2 of chapter 3.

2.5.1.2 Outlet Feature Design

Flow containing a liquid phase fraction can be harmful to various components of the test facility, and even present a potential hazard risk in conjunction with the AMBs, entailing

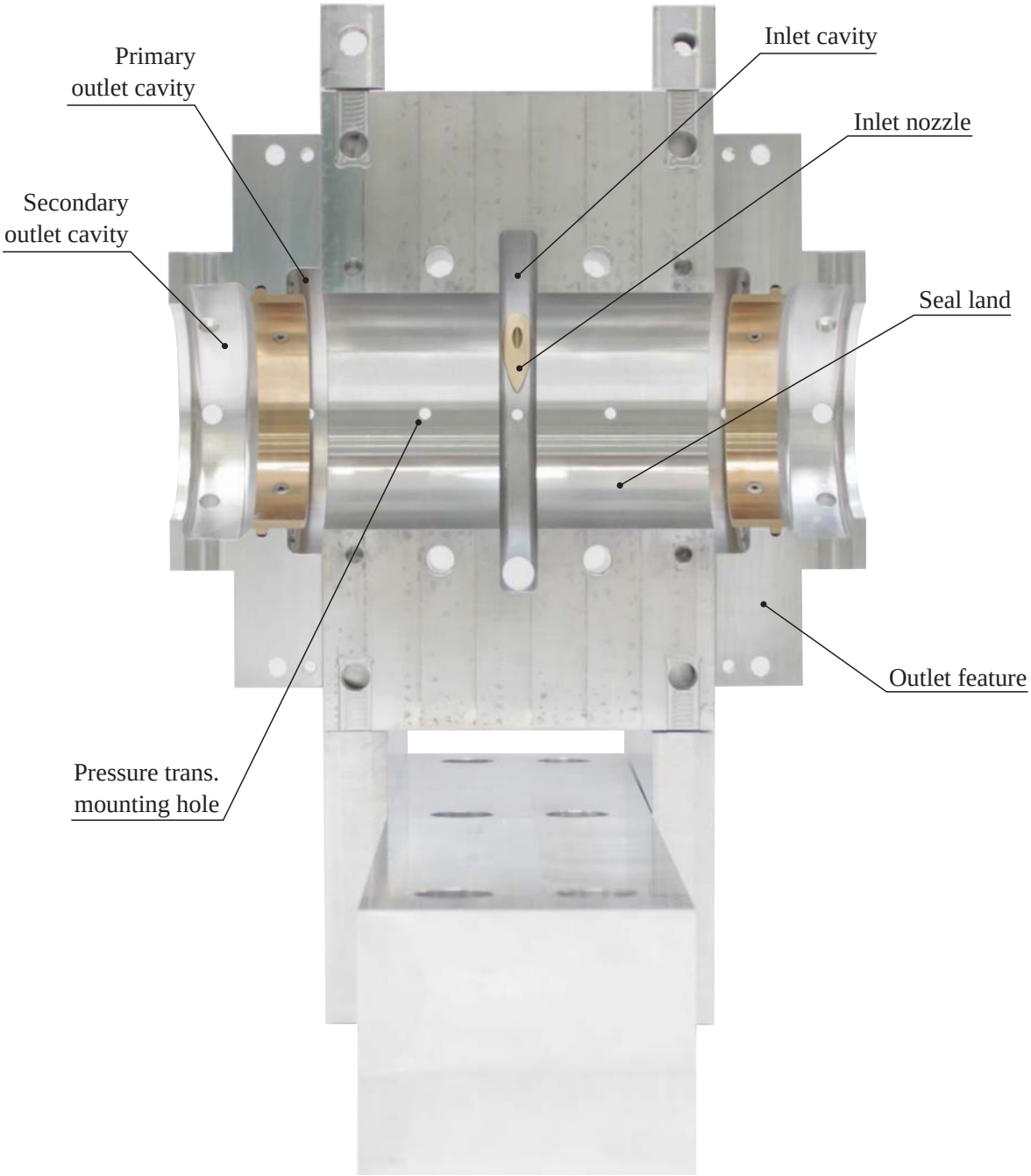

Figure 2.24: Half part of SHA showing inlet and outlet features.

that significant liquid leakage from the SHA cannot be tolerated. To accommodate testing with flows containing a liquid phase fraction secondary rotordynamic sealing functionality is required. The outlet features are intended to provide the necessary secondary sealing functionality which, due to its relative importance to the overall functionality of the test facility, requires special attention. Two requirements for the outlet feature design are imposed. Firstly, the outlet feature should be able to mitigate liquid leakage and secondly the outlet feature sealing should not affect the test results for the test seals adversely. Using conventional secondary sealing elements for the

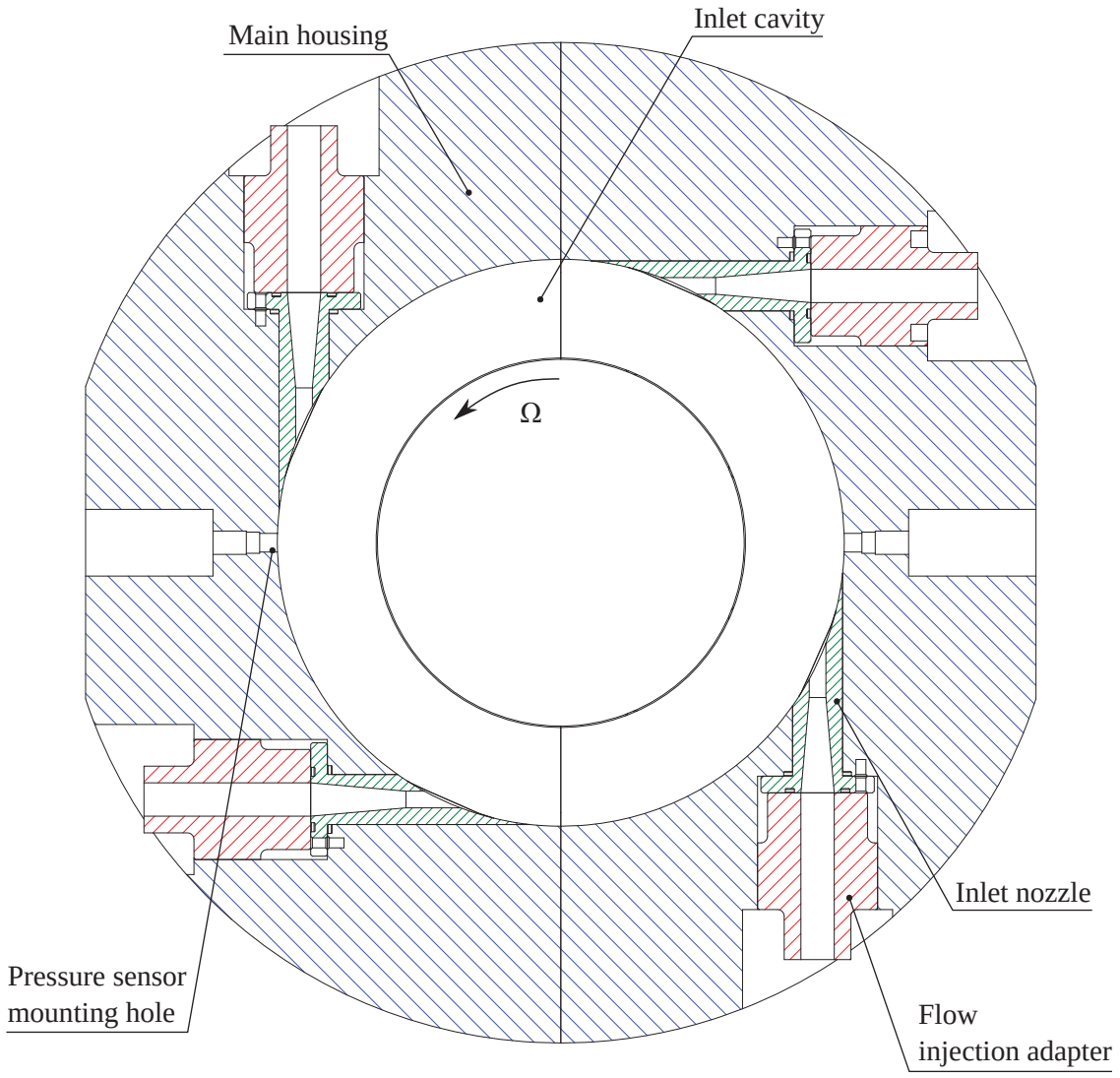

Figure 2.25: Section view of the inlet cavity showing the distribution and orientation of the inlet nozzles as well as the mounting holes for the inlet cavity pressure sensors.

outlet feature, e.g. labyrinth seals, can lead to contamination of the test results as the secondary seals will produce radial forces similarly to the main test seals. The outlet feature incorporated in the test facility aims at avoiding the issue of contaminating radial forces from secondary seals by design.

A schematic visualisation of the test facility outlet feature is presented in Fig. 2.27 and Fig. 2.28 shows a picture of the realised outlet feature in an axially oriented view. The outlet features are complex components from a manufacturing point of view and each half part is CNC milled out of a solid block of aluminium. The outlet feature design includes two sequential outlets referred to as the primary and the secondary outlet, respectively. The primary outlet consists of eight circumferentially distributed outlet ports, four on each outlet feature half part, as shown on Fig. 2.27 and Fig. 2.28. The design concept includes the possibility to mount valves on each of the primary

(a) Flow adapter. (b) Injection nozzle.

Figure 2.26: Picture of inlet feature components.

outlet ports that can be adjusted to apply back-pressure to the test seal flow. However, these are not shown on any of the figures of this section. Any portion of the flow that does not follow the primary flow path through the primary outlet ports, see Fig. 2.27, instead passes through the secondary flow path into the secondary outlet cavity and exits through the secondary outlet ports or leaks along the shaft. The main advantage of the outlet feature design is that sealing takes place between axially oriented surfaces in the secondary flow path between the shaft and the outlet feature lip, see Fig. 2.27. This entails that no contaminating radial forces will arise since all radial clearances in the outlet feature design are kept at least a factor two larger than the test seal clearance. Analysis of the radial clearances necessary to insure minimal radial forces from the secondary radial sealing has been performed using a bulk flow code available from LRC.

To verify performance of the SHA outlet feature design a CFD based performance validation study has been conducted. The study found that for medium to high pressure ratios over the test seals, the flow in the primary flow path creates a Venturi ejector effect when passing the secondary flow path clearance, reversing the flow in the secondary flow path, effectively eliminating leakage flow. This phenomenon has been observed for a back-pressure of up to 10 bar at an inlet pressure of 40 bar for both single-phase water and air conditions. The CFD based analysis methodology applied in the design phase of the SHA is introduced in chapter 3 which also documents a subset of the CFD results obtained for the SHA outlet feature. Fig. 2.29 presents a view of the test facility in the seal testing configuration where the SHA (Module III) is placed between the two test facility AMBs.

2.5.1.3 Seal Housing Instrumentation

The SHA is currently instrumented with two Kistler piezo-resistive absolute pressure sensors of the type 4065B with a pressure range of 0 to 200 bar. The sensors measure

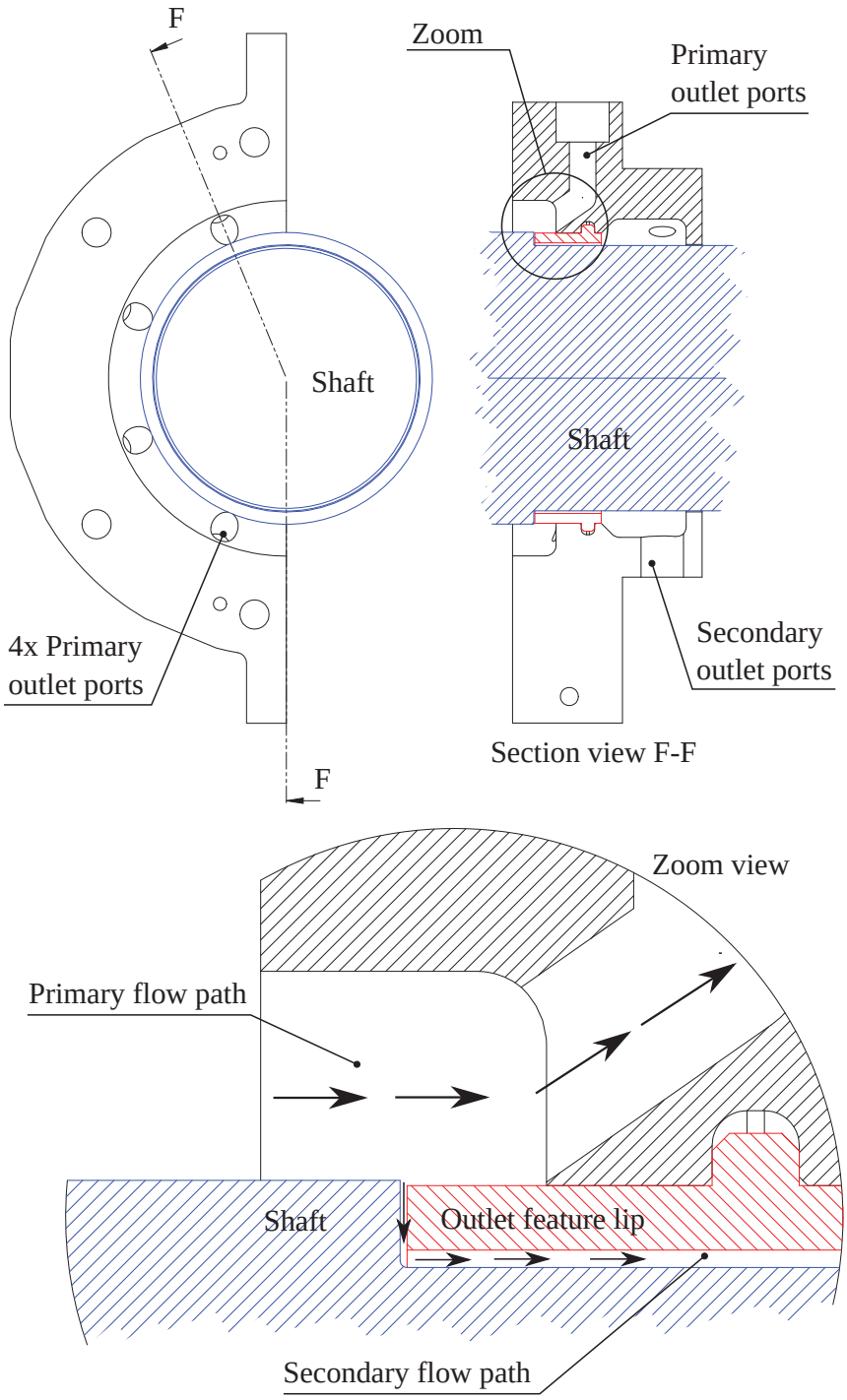

Figure 2.27: Details of the outlet feature.

absolute and dynamic pressure as well as temperature. The SHA can accommodate up to 10 pressure sensors all placed in the horizontal plane of the test facility. The position of the mounting holes for the sensors can be seen in the section view presented in Fig. 2.30, which also provides a schematic overview of the SHA. All pressure sensors are mounted so that their tip is flush with the internal geometry, which is visualised for a sensor mounted in the seal land in Fig. 2.31. In the current SHA configuration, the Kistler

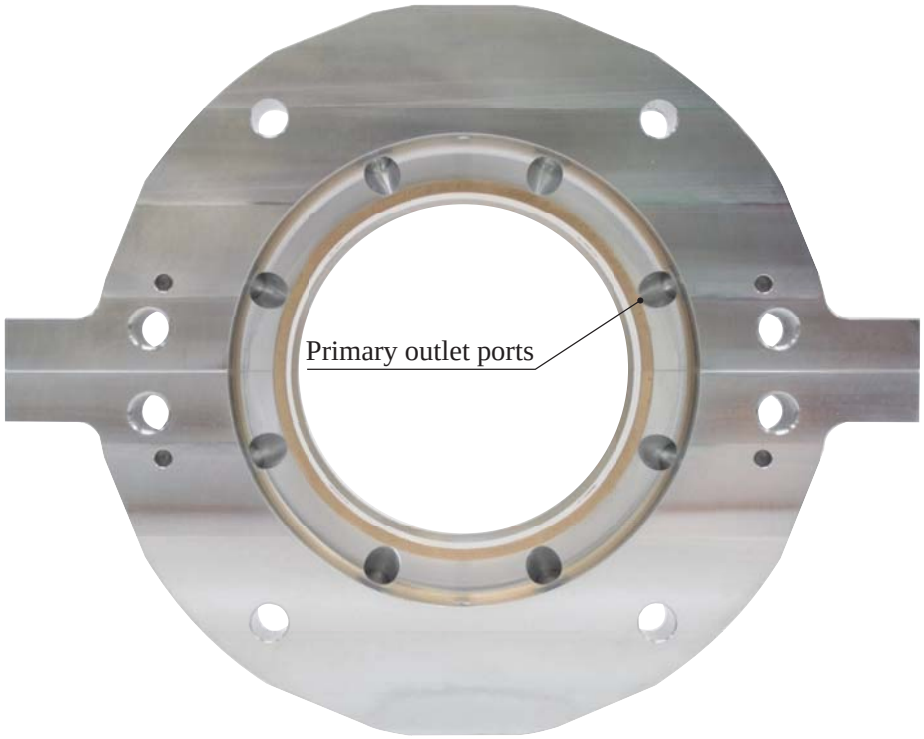

Figure 2.28: Axially oriented view of the outlet feature. The test seal exhaust flow direction is into the paper.

Table 2.4: Design parameters for the SHA.

Inlet cavity diameter	150	mm
Inlet cavity width	18	mm
Nominal radial seal clearance	0.4	mm
Axial length of test seals	83	mm
Axial lip clearance in secondary flow path	0.4	mm
Secondary flow path radial clearance	0.8	mm
Total number of primary outlet ports	16	
Total number of secondary outlet ports	16	
Maximum number of pressure/temp. sensors	10	

probes enable measuring the inlet and outlet cavity pressures and temperatures, as well as the pressure and temperature of the flow within the seal lands. These measurements are valuable for comparison with CFD results. In Table 2.4 key parameters for the SHA are summarised.

2.6 Module IIII - Flow Loop and Phase Mixing Functionality

The test facility is designed to operate with both single phase air and water flows as well as flow containing mixtures of two phases. For commissioning purposes the test

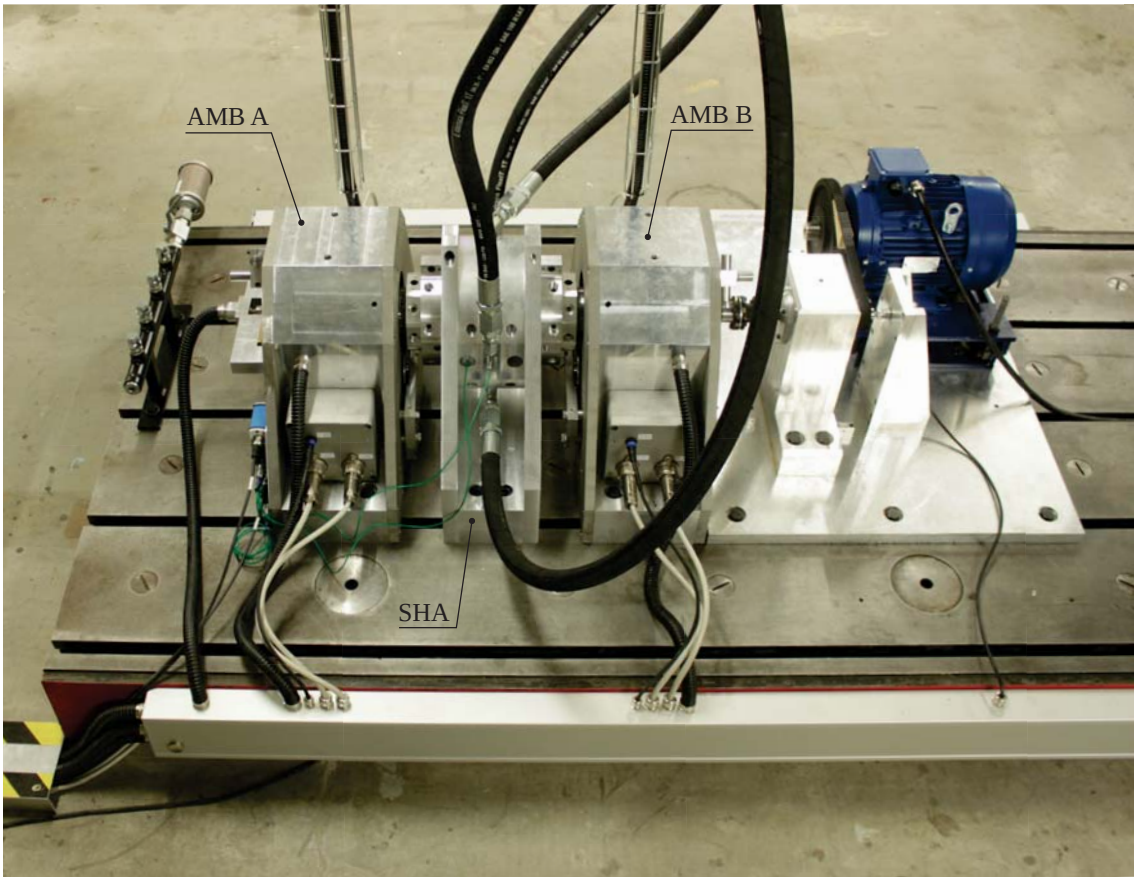

Figure 2.29: Test facility in seal testing configuration with SHA mounted.

facility is supplied with a single-phase air flow. Consequently, the main focus during the design of the flow loop has been oriented at designing a relatively low cost single phase air supply, while considering functionality allowing for a later upgrade of the flow loop to include a liquid phase supply string. A conceptual illustration of the flow loop designed and built during this project is included in Appendix D, Fig. D.1. The air supply string consists of a piston compressor supplying up to 65 bar to a 3 m^3 pressure tank through a series of filters ensuring dry gas conditions. From the tank the flow passes through a single strand pipe section that terminates at a regulator valve. To minimise pressure loss in the flow supply lines running from the air tank to the SHA, the pipes used have an internal diameter of 50.8 mm and the piping layout minimises the number of pipe bends. The supply from the tank to the SHA is controlled by a pressure regulating valve, see Fig. 2.32, capable of maintaining a constant output pressure when the supply pressure drops during tests. From the regulator valve the flow is split into four strands via a custom built manifold, that allows opening and closing individual flow strands using ball valves. Flexible high pressure hydraulic pipes transport the flow from the manifold to the SHA where the flexible pipes interfaces with the SHA through the flow adapter presented earlier in Fig. 3.1(a). The internal diameter of the flexible pipes is 25.4 mm. The flow splitting manifold can be seen in Fig. 2.32.

Integration of a water supply in the flow loop layout is planned to be completed in two iterations. The first is intended to accommodate wet-gas testing for LVFs between 0

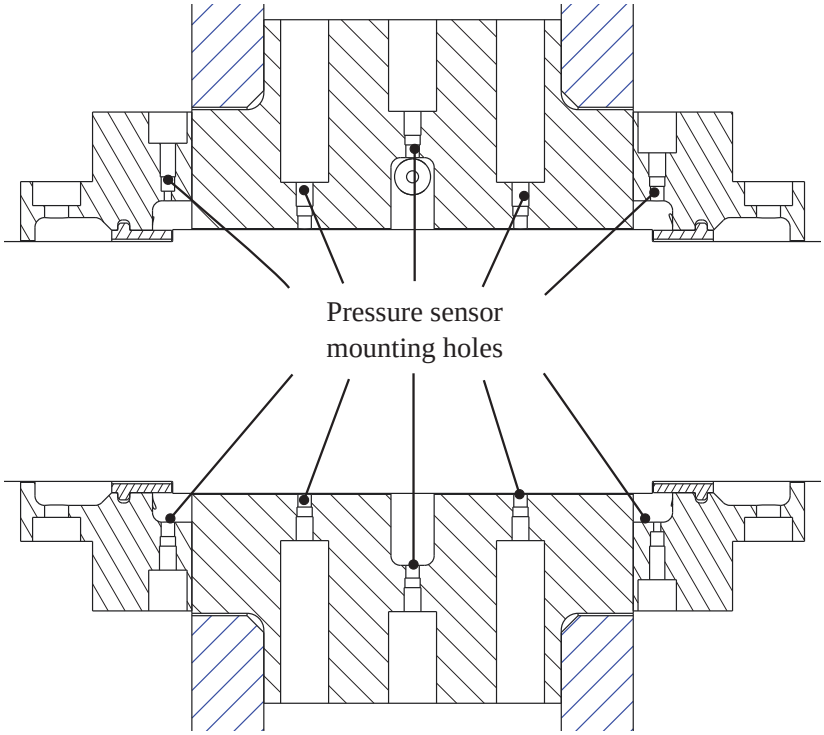

Figure 2.30: Horizontal section view of the SHA showing the mounting holes for the pressure transducers.

% and 5 %, consequently keeping the complexity, size and cost of the water supply to a minimum while still being able to attain the test facility functionality related to multiphase seal testing. The first iteration water supply is based on a high-pressure centrifugal pump, which is capable of matching the pressure of the air supply, albeit for significantly lower flow rates. A conceptual illustration of the flow loop for wet-gas testing can be found in Appendix D, Fig. D.2. For this flow loop iteration the water containing leakage flow can be exhausted directly to a drain, eliminating the need for recycling the water.

The second iteration of the water supply incorporates an upstream water reservoir, filtering units, high capacity pumping system and a separation unit for water recycling. The second iteration is currently in an early stage of the design phase. A conceptual schematic illustration of the second iteration of the flow loop is included in Appendix D, Fig. D.3. For the two later iterations of the flow loop design, the flow supply feeding the SHA will consists of two separate strings for the two fluids. For multiphase operating conditions a mixing device is included upstream to the injections nozzles of the SHA. Different sparger and injection nozzle based mixing devices have been considered for achieving the wanted homogeneous fluid mixtures for a large range of both GVFs and LVFs. An early stage flow mixing and SHA concept is presented in Fig. C.1 of Appendix C. The early concepts are included here for completeness, and it is emphasised that future efforts will ultimately determine the final phase mixing concept(s).

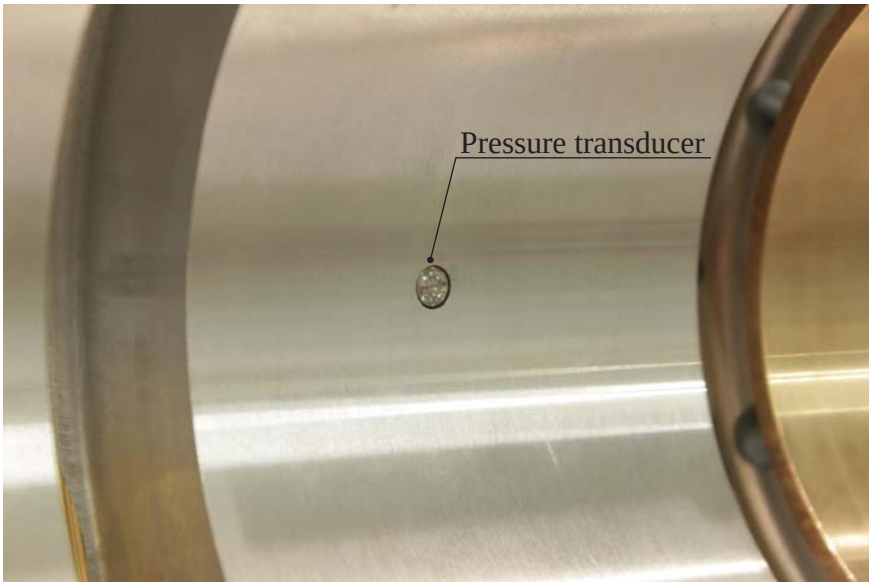

Figure 2.31: Kistler 4065B pressure transducer mounted flush with seal land.

2.6.1 Performance Evaluation of Module III and IIII

The first iteration of the SHA and the single phase flow loop generally perform as intended. The SHA outlet feature performance has been evaluated through tactile and visual inspection which reveals that the air flow, even at very low supply pressures, exists radially through the primary outlet ports. As there is no liquid flow supply at the time of writing this thesis, the ability of the outlet feature to mitigate liquid leakage cannot be assessed, however the indications available from the single phase air test are promising. The regulator valve is capable of maintaining a constant supply pressure as the pressure in the air tank drops during testing. The two pressure sensors mounted in the SHA are capable of measuring both pressure and temperature.

2.7 Test Facility Control Interface

The test facility is controlled from a central processor and I/O interface. The system enables both data acquisition and control tasks, and is based around a DS1006 dSPACE processor board, which is programmable from Simulink. The multi-processor DS1006 board is capable of running multiple tasks with different computational turn-over times and sampling frequencies. This is very useful since it allows the AMB controller to be run with a fast turn-over time, which is necessary for real-time control of the rotor, while processes that does not require high sampling rates and calculation times, such as the Hall sensor system, can be run with lower sampling rates and calculation times. The system can be accessed using a .NET framework that allows manipulating processes running on the processor from a MATLAB scripting environment. Additionally, the .NET framework can facilitate using MATLAB to automate everything from single experiments to full scale test campaigns. This has been used extensively throughout the project, of which the Hall sensor calibration procedure is a good example. The full system features the following I/O capabilities:

Figure 2.32: Picture of the manifold and pressure regulator setup.

- 64 16 bit Analogue/Digital (A/D) channels.
- 12 16 bit Digital/Analogue (D/A) channels.
- 5 24 bit digital encoder channels.

Additionally the I/O setup includes a six channel analogue anti-aliasing filter for the AMB position sensor input. The filters are fourth order butter-worth low pass filters with a cut-off frequency of 5kHz. Control of the DS1006 is achieved via an optical cable connecting the DS1006 to a Personal Computer (PC) which is used for designing controllers, running experiments and visualising the control interface for the test facility.

Chapter 3

Computational Fluid Dynamics Methodology and Results

This chapter contains a review of CFD fundamentals, including aspects relevant for multiphase modelling. Additionally the CFD based methodology used in the analysis of seals during the PhD project is introduced. For all applications of CFD included in this thesis the commercial software package ANSYS CFX is used.

3.1 Fluid Dynamics and General CFD Aspects

The set of equations solved by the CFD software package ANSYS CFX is a modified version of the unsteady Navier-Stokes equations on conservation form. Navier-Stokes equations can be derived from the fundamental principles of conservation of mass, momentum, and energy [100], which will be treated sequentially in the following.

Conservation of Mass

Conservation of mass dictates that the sum of the time rate change of mass within an arbitrary fluid element, and the net mass flow rate through the surfaces of the fluid element is zero. This can be stated in differential form, considering an infinitesimal fluid element, as

$$\frac{\partial \rho}{\partial t} + \frac{\partial (\rho u)}{\partial x} + \frac{\partial (\rho v)}{\partial y} + \frac{\partial (\rho w)}{\partial z} = 0 \tag{3.1}$$

which can be expressed as

$$\frac{\partial \rho}{\partial t} + \nabla \cdot (\rho \mathbf{v}) = 0 \tag{3.2}$$

in which ρ is the fluid density, t denotes time, and $\mathbf{v} = \{u\ v\ w\}$ is the velocity vector.

Conservation of Linear Momentum

The equation governing conservation of momentum is derived by applying Newton's second law to a fluid element which in differential form yields

$$\rho \frac{D\mathbf{v}}{Dt} = \mathbf{f} = \mathbf{f}_{body} + \mathbf{f}_{surface} \tag{3.3}$$

For simplicity the equation is presented on non-conservation form using the substantial derivative. Navigating between the non-conservation and the conservation form can be readily performed using vector identities and employing the continuity equation on conservation form.

The only body forces $\mathbf{f}_{body}$ considered here stem from the external gravity field. Additionally, external stresses give rise to forces acting on the surface of the fluid element. Considering the above Eq. (3.3) can be re-cast as

$$\rho \frac{D\mathbf{v}}{Dt} = \rho \mathbf{g} + \nabla \cdot \tau_{ij} \tag{3.4}$$

which is known as Cauchy's equation, where $\mathbf{g}$ represents gravitational acceleration and $\nabla \cdot \tau_{ij}$ is the divergence of the stress tensor τ_{ij}.

In order to express τ_{ij} in terms of velocity, a relationship between the stress and strain rate tensors is constructed under the assumption of a viscous deformation-rate law. For a Newtonian fluid, the following assumptions must be obeyed

- The fluid is continuous and its stress tensor is at most a linear function of the strain rates.
- The fluid is isotropic, i.e. its properties are independent of direction, and therefore the deformation law is independent of the reference frame in which it is expressed.
- When the strain rates are zero, the deformation law must reduce to the hydrostatic pressure $\tau_{ij} = -p\delta_{ij}$, where δ_{ij} is the Kronecker delta function.

Applying the above, the deformation law for a Newtonian viscous fluid can be expressed as

$$\tau_{ij} = -p\delta_{ij} + \mu_v \left(\frac{\partial u_i}{\partial x_j} + \frac{\partial u_j}{\partial x_i} \right) + \delta_{ij} \lambda div \mathbf{v} \tag{3.5}$$

in which p is the pressure, μ_v is the coefficient of viscosity and λ is the coefficient of bulk viscosity. Substituting the stress relation defined in Eq. (3.5) into Eq. (3.4) yields the compressible Newtonian Navier-Stokes equations, presented below as a single vector equation on non-conservation form

$$\rho \frac{D\mathbf{v}}{Dt} = \rho \mathbf{g} - \nabla p + \frac{\partial}{\partial x_j} \left[\mu_v \left(\frac{\partial v_i}{\partial x_j} + \frac{\partial v_j}{\partial x_i} \right) + \delta_{ij} \lambda div \mathbf{v} \right] \tag{3.6}$$

Conservation of Energy

The first law of thermodynamics describes the increase of energy in an arbitrary system due to work done on system and thermal energy added to the system

$$dE_t = dQ + dW \tag{3.7}$$

where E_t denotes the total energy of the system, Q is the added thermal energy, and W is the work done. Consequently, the time rate of change of the total energy can be expressed as

$$\frac{DE_t}{Dt} = \frac{DQ}{Dt} + \frac{DW}{Dt} \tag{3.8}$$

which can be considered as the non-conservation form of the energy equation for a moving fluid element. The quantities of Eq. (3.8) can be expressed in terms of flow field variables as outlined subsequently. For a fluid element, the total energy E_t will not only include internal energy, denoted e_i in the following, but also kinetic and potential energy. Thus for a fluid element the energy per unit volume can be quantified as

$$\frac{DE_t}{Dt} = \rho\left(\frac{De}{Dt} + \mathbf{v}\frac{D\mathbf{v}}{Dt} - \mathbf{g}\cdot\mathbf{v}\right) \tag{3.9}$$

Here volumetric heating is ignored and consequently only the heat flux due to thermal conduction contributes to the added thermal energy. The heat flux can be modelled by Fourier's law $\mathbf{q} = -k\nabla T$, where k is a proportionality constant and ∇T expresses the local temperature gradients. The added thermal energy can then be expressed as

$$\frac{DQ}{Dt} = -\nabla\cdot\mathbf{q} = \nabla\cdot(k\nabla T) \tag{3.10}$$

The net work done per unit area can be described as the work done by the applied stresses as

$$\frac{DW}{Dt} = \nabla\cdot\left(\mathbf{v}\cdot\tau_{ij}\right) = \rho\left(\mathbf{v}\frac{D\mathbf{v}}{Dt} - \mathbf{g}\cdot\mathbf{v}\right) + \tau_{ij}\frac{\partial u_i}{\partial x_j} \tag{3.11}$$

In Eq. (3.11) the potential and kinetic energy terms in Eq. (3.9) can be identified. Substitution of Eqs.(3.9), (3.10), and (3.11) into Eq. (3.8) yields the first form of the energy equation

$$\rho\frac{De}{Dt} = \nabla\cdot(k\nabla T) + \tau_{ij}\frac{\partial u_i}{\partial x_j} \tag{3.12}$$

It is convenient to recast the energy equation into a form explicitly using enthalpy instead of internal energy. This can be done by splitting the stress tensor into pressure and viscous terms as $\tau_{ij} = \tau'_{ij} - p\delta_{ij}$ thus modifying the last term of Eq. (3.12) to yield

$$\tau_{ij}\frac{\partial u_i}{\partial x_j} = \tau'_{ij}\frac{\partial u_i}{\partial x_j} - p\nabla\mathbf{v} \tag{3.13}$$

From the continuity Eq. (3.2), it is seen that

$$p\nabla \mathbf{v} = -\frac{p}{\rho}\frac{D\rho}{Dt} = \rho\frac{D}{Dt}\left(\frac{p}{\rho}\right) - \frac{Dp}{Dt} \tag{3.14}$$

Combining Eqs. (3.12), (3.13) and (3.14) yields the second form of the energy equation

$$\rho\frac{Dh}{Dt} = \frac{Dp}{Dt} + \nabla\cdot(k\nabla T) + \tau'_{ij}\frac{\partial u_i}{\partial x_j} \tag{3.15}$$

in which h is the enthalpy defined as $h = e_i + p/\rho$.

3.1.1 RANS Equations and Turbulence Modelling

General fluid motion is governed by the Navier-Stokes equations introduced earlier. Laminar flow solutions often exist, however even small perturbations of these solutions can result in a turbulent flow. This is generally the case for flow in turbomachinery seals. Navier-Stokes equations can be solved using different approaches for handling the turbulence quantities. One approach is to solve the discretised equations directly, as these form a closed set of equations, using a Direct Numerical Simulation (DNS) approach. In DNS the spatial and temporal scales of turbulence is resolved from the smallest dissipative scales to the largest integral scales. Thus the mesh and computational requirements are very intensive, as the finest turbulent length scales to be resolved by the mesh are extremely small. This approach is unsuited for dynamic seal analysis even with the current computational capacity of modern supercomputers. In comparison with DNS more suitable approaches exist i.e. using Reynolds Averaged Navier-Stokes (RANS) equations or by employing Large Eddy Simulations (LES). ANSYS CFX solves the RANS equations in which the fundamental governing equations are averaged using the Reynolds decomposition. By applying the Reynolds decomposition it is assumed that the instantaneous flow quantities can be divided into a time averaged and a fluctuating part as exemplified for the velocity component u below

$$u = \overline{u_i} + u' \tag{3.16}$$

in which $\overline{u_i}$ is the time average of the velocity and u' is the fluctuating velocity component. Applying the Reynolds decomposition to all quantities in the Navier-Stokes equations yields the RANS equations. The RANS equations include an additional stress term compared to the instantaneous equations. The additional Reynolds stress term is expressed as $-\rho\overline{u'_i u'_j}$. Due to the additional term the number of unknowns in the set of equations are now higher than the number of equations which constitutes the so-called closure problem of turbulence. In order to close the RANS equations the Reynolds stresses have to be modelled through a turbulence model.

Several types of turbulence models have been developed to amend the closure problems, each having specific strengths and weaknesses, however the $k-\omega$ SST model is used throughout the present study. The $k-\omega$ SST model is a two equation turbulence model which determines the Reynolds stresses using the Boussinesq hypothesis [101] where the turbulent kinetic energy k and the turbulent eddy viscosity μ_t are related to the

Reynolds stresses. In the $k-\omega$ SST model the turbulent viscosity is calculated using the turbulent kinetic energy and the specific turbulent dissipation ω [101], and is suitable for engineering applications [101].

3.1.2 Discretisation Method

To approximate a solution to the RANS equations these are replaced by algebraic approximations which can be solved using a numerical method. ANSYS CFX employs an element-based finite volume method [102]. The fluid domain is descritised into a finite number of small control volumes by a grid. The grid defines the boundaries of the control volumes while the computational node lies at the center of the control volume. The conservation equations are integrated over each control volume and Gauss' Divergence Theorem is applied to convert integrals involving divergence and gradient operators to surface integrals. The net flux through the control volume boundaries is the sum of integrals over the control volume faces. Approximating the integrals requires information of the variable values at locations other than at the computational nodes, i.e. on the control volume faces, which are determined via interpolation. Numerous methods for interpolating the value of the flow field variables at the control volume faces exists. Among these the most common are upwind interpolation, central differencing scheme, and high resolution schemes. ANSYS CFX employs a high resolution scheme as default, which is a second order or higher scheme, using a non-linear recipe to evaluate the face value of an arbitrary fluid property [102]. In flow regions with low gradients a second order accurate discretisation is used and in areas where the flow field changes sharply, a first order accurate numerical discretisation is used to prevent overshoots and undershoots while maintaining robustness [102].

3.1.3 Solution Algorithm

ANSYS CFX employs a coupled solver, which solves the fluid dynamic equations (for u, v, w, p) as a single system [102]. This solution approach uses a fully implicit discretisation of the equations at any given time step. For steady flow problems a pseudo-time step is used to calculate solutions. While this method takes up more memory and solution time per iteration, it also reduces the number of iterations required for convergence to a steady state, or to calculate the solution for each time step [102].

3.1.4 Multiphase Flow Considerations

In the present context the term *multiphase* refers specifically to two phase flow represented by a liquid and a gaseous phase. Furthermore, the flows treated here can generally be classified as *dispersed*, entailing that the flow consists of a continuous phase and a dispersed phase, with a dispersed phase volume fraction below 5%. Considering more than one fluid phase adds considerable complexity to the flow modelling process, and a host of models exist for capturing different aspects of multiphase flow behaviour, albeit these can in general be divided into two sub-groups, introduced subsequently.

Eulerian-Lagrangian Models

Eulerian-Lagrangian models are also referred to as particle transport models [102]. In these models the primary phase is modelled in the Eulerian sense and a secondary phase of discrete particulates are included as a relatively small number of individual particles which are tracked through the flow domain by applying a set of ordinary differential describing particle position, velocity mass and temperature for each particle [102]. The secondary phase representing e.g. water droplets or air bubbles can be included in the models using an Eulerian-Lagrangian approach. The relatively computationally expensive Eulerian-Lagrangian models are appropriate for studying, among others, particle-particle and particle-wall collisions, particle size distribution and detailed modelling of particulate heat and mass transfer. In the present context the objective is to study firstly how the overall multiphase flow characteristics modify the rotordynamic properties of seals and secondly to be able to study flow properties such as homogeneity of the multiphase flow as well as phase volume fraction. For these purposes the Eulerian-Lagrangian modelling framework is considered the sub-optimal choice and consequently it is not used or discussed further. For additional information, the reader is referred to texts on particle transport models, see e.g. [102, 103].

Eulerian-Eulerian Models

In the Eulerian-Eulerian fluid model framework both fluids are modelled as continuous phases, and the Navier-Stokes equations are modified to include terms governing the exchange of mass, momentum and energy between the two phases. Consequently, in the Eulerian-Eulerian modelling framework the effect of the dispersed phase on the continuous phase is approximated without considering the discrete character of the dispersed phase particulates. The primary interest in this project lies in how multiphase flow modifies the rotordynamic properties of seals. To study this, detailed information of how individual particles of the dispersed phase travel through the SHA is not of paramount importance. However, it is relevant to be able to study flow mixing interfaces e.g. at the inlet to the SHA as well as being able to capture and study volume fractions throughout the SHA. Eulerian-Eulerian models are considered appropriate for these purposes, and the framework is applied throughout the results presented in this thesis. Two general sub-models are available for the Eulerian-Eulerian models, namely the homogeneous and the inhomogeneous model. In the homogeneous model the two phases share a common flow field, yielding a simplification of the multiphase flow modelling challenge. In the studies documented here the inhomogeneous model is applied in which the two phases have separate flow fields but share the pressure field. Furthermore, a simplified particle model, in which particles attain a constant mean diameter, is employed to account for phase interfacial transfer of mass, momentum and energy. Inter-phase drag forces for the particle model are quantified using the Schiller-Naumann correlation, assuming that the dispersed phase particles, e.g. drops and bubbles, can be considered spherical. A wide variety of additional models exist, however, as these are not used, it is considered out of the scope to introduce them. For additional information see [102].

3.2 CFD Application and Setup

In the context of the work documented in this thesis CFD is applied for two distinct purposes. Firstly, CFD simulations are used for providing input to, and evaluation of, the SHA design, and secondly CFD is applied for quantifying rotordynamic coefficients for seals subjected to dispersed multiphase flow which is the topic of the paper [P1]. In the paper the CFD based IPM methodology is applied to identify rotordynamic coefficients of a generic smooth annular seal geometry for both liquid and gas dominated dispersed multiphase flows. It should be noted that the seal geometry used in [P1] is not identical to the seal geometry realised in the test facility. The reader is referred to [P1] for details on the CFD setup as well as results for this study. The remainder of this chapter deals with the application of CFD in the design phase of the test facility.

In the design phase of the test facility CFD has mainly been employed for two tasks:

- To quantify the expected radial forces from the seals during experimental testing.
- To investigate the performance of the inlet and outlet features of the SHA.

The two tasks identified above are treated separately in the following. It should be mentioned that the tasks described subsequently are highly iterative in nature and consequently numerous different CFD based analyses have been conducted for the different draft designs. The following subsections are kept relatively short, aiming at outlining only the main elements of the tasks.

3.2.1 Estimation of Seal Forces for AMB Design Input

The forces generated by the seals in the SHA act as important input for the design of the test facility AMBs. In fact, the necessary force capabilities of the AMBs are solely determined based on the dynamic forces occurring during seal testing which need to be estimated before finalising the AMB design. For this to be possible the layout of the SHA needs to be fairly close to its final form, so that the seal forces can be determined, before the design phase of the AMBs is closed. To accommodate this a generic seal geometry close to the final form of the SHA seals is employed as the basis of the investigation. The seal forces are quantified for the generic seal geometry subjected to a worst case scenario flow and operational parameters, specified below

- Single phase water flow is applied in the simulations as the higher density and viscosity, as compared to the properties of single phase air, provides worst-case force estimates.
- The maximum sustainable supply pressure of 40 bar is applied in the simulations.
- An estimated necessary maximum amplitude of the sinusoidal perturbation pattern is applied in the simulations. It should be noted that it is a fairly complicated matter to determine the necessary amplitude of the perturbation, as it is strongly dependent on the force estimation precision, which was unknown at the time of performing the analysis. Here an estimate of the necessary amplitude is chosen to 10% of the radial seal clearance. In the initial part of the design phase the radial seal clearance was set to 0.3 mm.

- The rotor speed is set to the maximum design value of 10krpm.
- The frequency of the sinusoidal perturbation is chosen to 200Hz.

At the time of conducting the worst case force estimation study, no pre-swirl feature was included in the SHA layout. The geometry and general setup used for the initial seal force assessment is identical to that used in [P1].

3.2.2 Design Evaluation of the SHA Input and Output Features

The design of the inlet and outlet features of the SHA is of high importance to the functionality of the test facility, and consequently these features have received significant attention during the design phase of the test facility. A subset of the CFD based analyses performed for the two features is outlined in the following sections which include selected results.

Inlet Feature and Nozzle Design

The inlet feature interfaces with the upstream flow supply and is responsible for ensuring that the flow entering the test seals is properly conditioned in terms of wanted pre-swirl and, in later design iterations, in terms of multiphase flow homogeneity. The flow enters the seal hosing assembly through four discrete inlets leading into an inlet cavity. The inlet cavity is dimensioned to mimic the flow path geometry for industrially applied machinery, e.g. centrifugal compressors, and four inlets are used in order to insure that the flow field is as circumferentially and radially homogeneous as possible when entering the test seals. A pre-requisite for the inlet feature design is that the inlet flow pre-swirl is in the high range, again for the purpose of obtaining a test seal flow pattern similar to that found in conventional turbomachinery. A multitude of different concepts for generating the desired pre-swirl have been identified for which manufacturability, adaptability as well as the resulting flow have been considered. The top concept candidates for generating pre-swirl have been investigated in detail using CFD, however to limit the extent of this section only the realised pre-swirl design is treated here.

The realised SHA inlet design can be seen in Fig. 2.24 and Fig. 2.25 found in section 2.5. The design is based on injecting flow tangentially to the inlet cavity through nozzles. The default nozzles can be interchanged with nozzles with a different flow exit diameter, consequently modifying the exit velocity of the flow. Changing the exit velocity of the flow enables modification of the pre-swirl, as the pre-swirl is defined as the ratio between the circumferential velocity at the fluid inlet and the rotational velocity of the rotor. The study presented here aims at assessing the impact of the two different nozzle geometries on the flow distribution in the inlet cavity. The two nozzle designs are shown in Fig. 3.1. Nozzle design A, conceptually visualised in Fig. 3.1(a), is significantly easier to manufacture and install in the SHA compared to nozzle design B, shown in Fig. 3.1(b). However, the flat exit zone of nozzle A is suspected to generate an unwanted disturbance of the flow as it enters the inlet cavity, and CFD is employed to establish if this is the case.

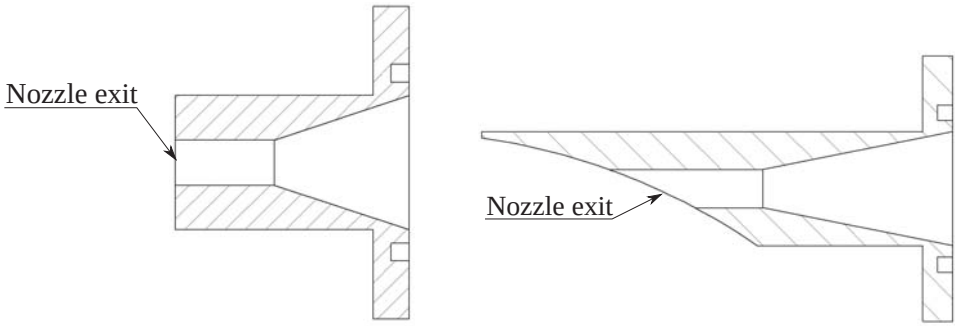

(a) Nozzle design A. (b) Nozzle design B.

Figure 3.1: Conceptual visualisation of the two different injection nozzle designs.

A surface mesh visualisation of one of the two the computational grid used for the nozzle study is shown in Fig. 3.2. The mesh represents the fluid domain of a 90° slice of the 3D seal mesh, and is visualised for the mesh which includes the geometry of the nozzle B design. A zoom view of the mesh for the two different nozzle designs is presented in Fig. 3.3. The boundary conditions used for both computational meshes are indicated in Fig. 3.2 and briefly outlined in the following. As the seal geometry is rotationally symmetric rotational periodicity is specified on the sides of the flow domain as indicated on Fig. 3.2. A symmetry condition is imposed on the axial surface representing a section line through the centre of the inlet cavity, which reduces computational costs. A pressure is specified on the inlet and on both the primary outlet and the leakage outlet an atmospheric pressure Boundary Condition (BC) is imposed. The rotor surface is represented using a rotating wall rotating with the nominal speed of the rotor. All walls are specified as hydraulically smooth no-slip walls. The CFD results presented in section 3.3 are obtained using a steady-state calculation for the following conditions

- Fluid type: single phase water.
- Inlet BC: 40 bar pressure.

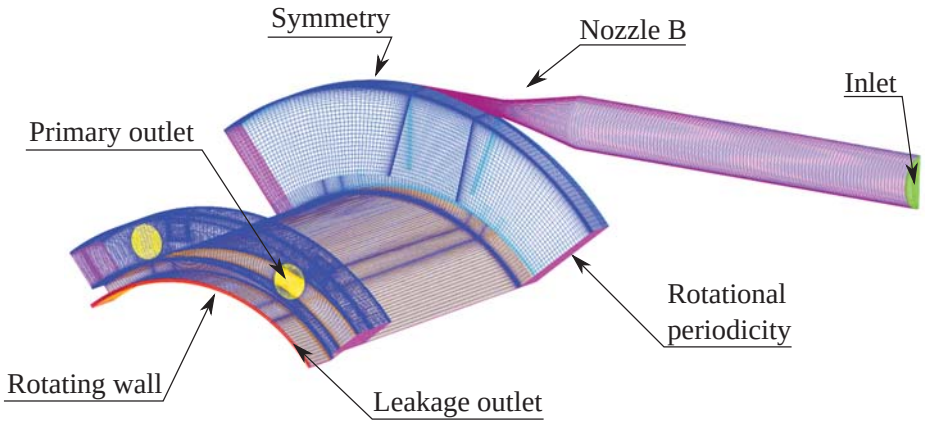

Figure 3.2: Surface mesh for a 90° seal slice showing boundary and symmetry definitions. The mesh includes the geometry of nozzle B.

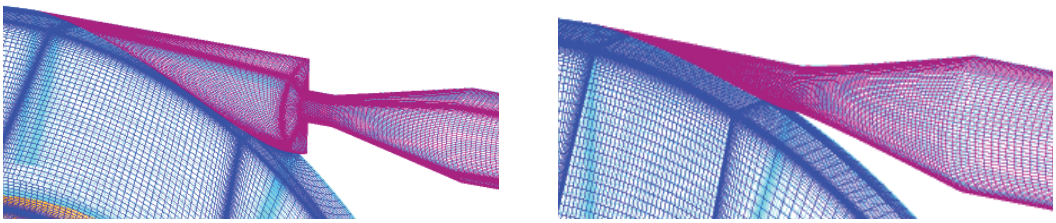

(a) Nozzle design A (b) Nozzle design B

Figure 3.3: Surface mesh for the two nozzle designs.

- Outlet BC: Atmospheric pressure.
- Rotating wall: Rotating at 10krpm.

A significant challenge in the design of the inlet cavity and the nozzles is to ensure homogeneity of the multiphase flow mixture and to avoid phase separation as the multiphase flow enters the inlet cavity through the nozzles. A comprehensive study was performed to investigate the influence of the inlet cavity and nozzle design on the seal flow homogeneity. The study was conducted utilising a Eulerian-Lagrangian multiphase model framework, but is omitted from this documentation for the sake of brevity.

Outlet Feature Design

The outlet feature design has a two-fold functional objective: to mitigate leakage flow while avoiding force contamination from secondary seals. A discussion of how the potentially contaminating forces originating from secondary sealing features can be minimised is presented in section 2.5. The main objective of this section is to verify that the SHA outlet design is capable of preventing liquid flow from exiting through the secondary flow path illustrated in Fig. 2.27 section 2.5. The design process for the seal outlet feature is highly iterative, and for illustrative purposes it is considered sufficient to only present two design iterations here. The slice meshes used for the study are presented in Fig. 3.4. The mesh for the final geometric layout of the outlet feature is presented in Fig. 3.4(b) while Fig. 3.4(a) presents the mesh used for an earlier iteration of the outlet feature design. The difference between the geometry presented in Fig. 3.4(a) and in Fig. 3.4(b) is the axial placement of the primary outlet cavity. In the final version of the outlet feature design the primary outlet cavity is displaced towards the secondary outlet cavity as compared to the position of the primary outlet cavity seen in the earlier design iteration presented in Fig. 3.4(a). Geometrical definitions used in the study are included on Fig. 3.4(a), with reference to Fig. 2.27 of section 2.5. In the present study the inlet is simplified substantially by omitting the nozzle geometry. Instead the inlet BC is imposed on the entire radial inlet cavity outer radius as seen in Fig. 3.4(a). For the investigation of the outlet feature a worst-case scenario is established entailing that a single phase flow of water is supplied at 40bar to the inlet.

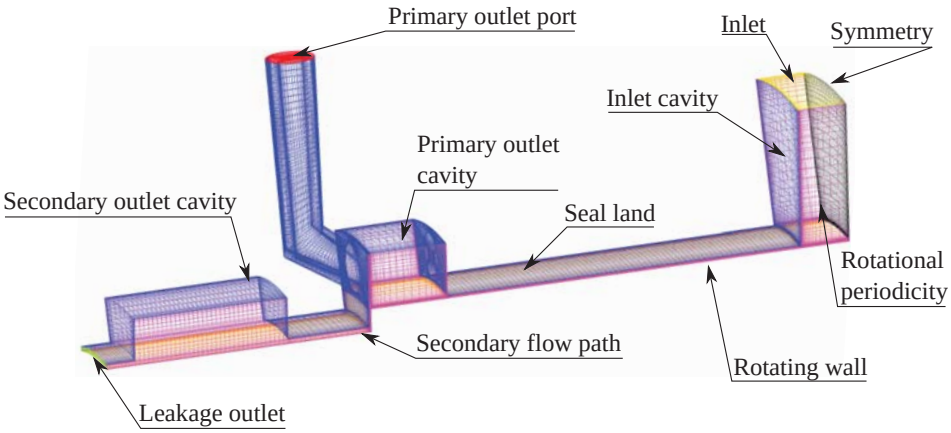

(a) Early iteration of the outlet feature geometry.

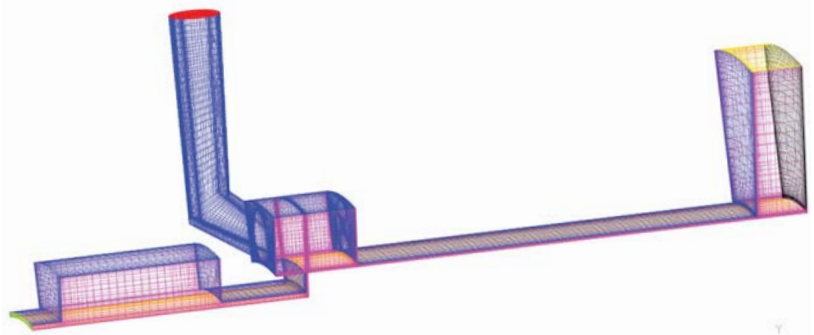

(b) Final form of the outlet feature geometry.

Figure 3.4: Exemplary visualisation of meshes used for investigating the design of the outlet feature.

A 3D version the SHA geometry is introduced in the study to investigate if the simplified representation of the seal inlet and outlet features, used in the iterative study introduced above, impacts the final results. Additionally the 3D model is used to determine the maximum allowable back-pressure and the necessary number of secondary outlets. The 3D mesh for the SHA is presented in Fig. 3.5 which includes definitions used in the investigations.

3.3 CFD Results

The results from the CFD based quantification of rotordynamic coefficients are found in the appended paper [P1]. The paper exemplifies the application of CFD to determine rotordynamic coefficients for smooth annular seals in multiphase flow. The general methodology employed in the paper [P1] has been validated against experimental results for honeycomb and hole-pattern seals subjected to single phase gaseous flow which is presented in [17]. The following two subsections summarise selected CFD results from the test facility design phase.

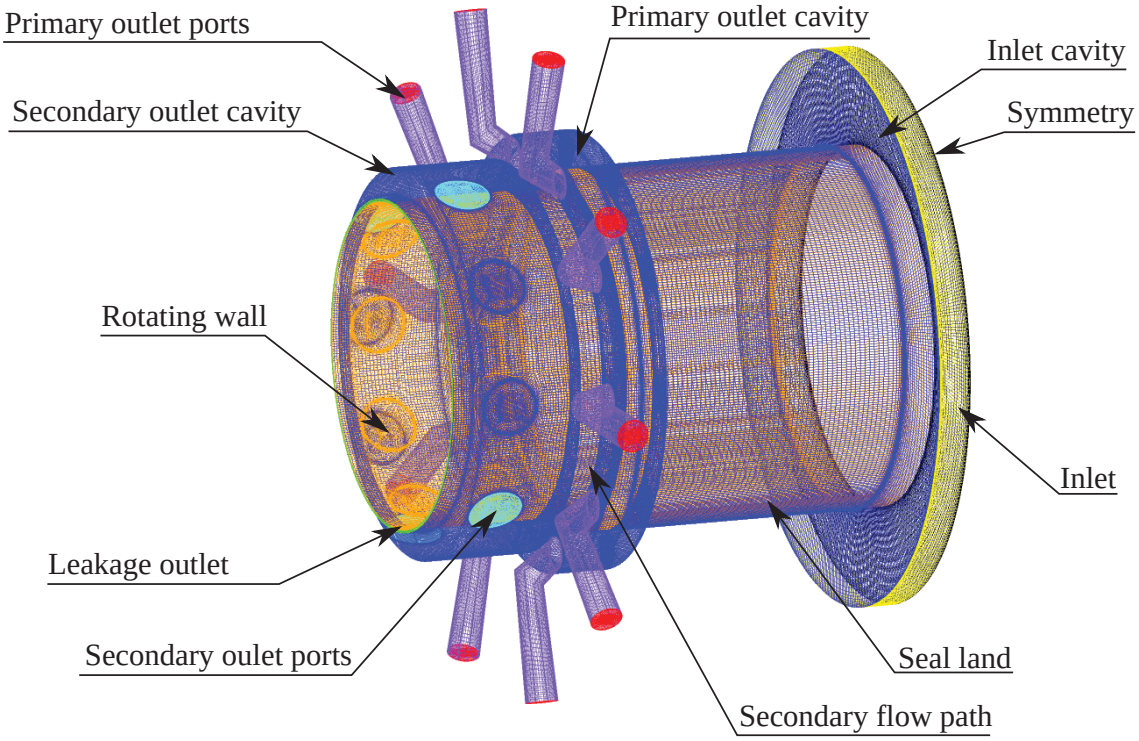

Figure 3.5: Half part of the 3D version of the SHA geometry.

3.3.1 Seal Forces Design Input Results

The resulting forces from the worst-case study conducted to provide input to the design of the test facility AMBs are presented here. The resulting force acting on the rotor is estimated through integration of the pressure and the shear stresses and its maximum amplitude is determined to approximately 2kN, which is used as the minimum requirement for the AMB force capability.

3.3.2 Nozzle Study Results

To assess how the different nozzle designs shown in Fig. 3.1 influence the flow pattern in the inlet cavity streamlines plots will suffice. The streamlines plots are presented in Fig. 3.6. From Fig. 3.6 it is immediately seen that the flow pattern for nozzle B, see Fig. 3.6(b), is significantly smoother near the flow entrance of the inlet cavity as compared to the flow pattern for the nozzle A design seen in Fig. 3.6(b). The flat exit zone of nozzle A creates a notch in the outlet cavity outer radius which disturbs the flow. Additionally, it should be noted that the sudden expansion at the exit zone of nozzle A can potentially lead to unwanted separation of the flow for multiphase flow operating conditions. The notch is eliminated in the design of nozzle B, providing a favourable flow pattern. Consequently, nozzle design B is adopted for the test facility in spite of the increased production complexity requiring CNC milling of the nozzle tip geometry.

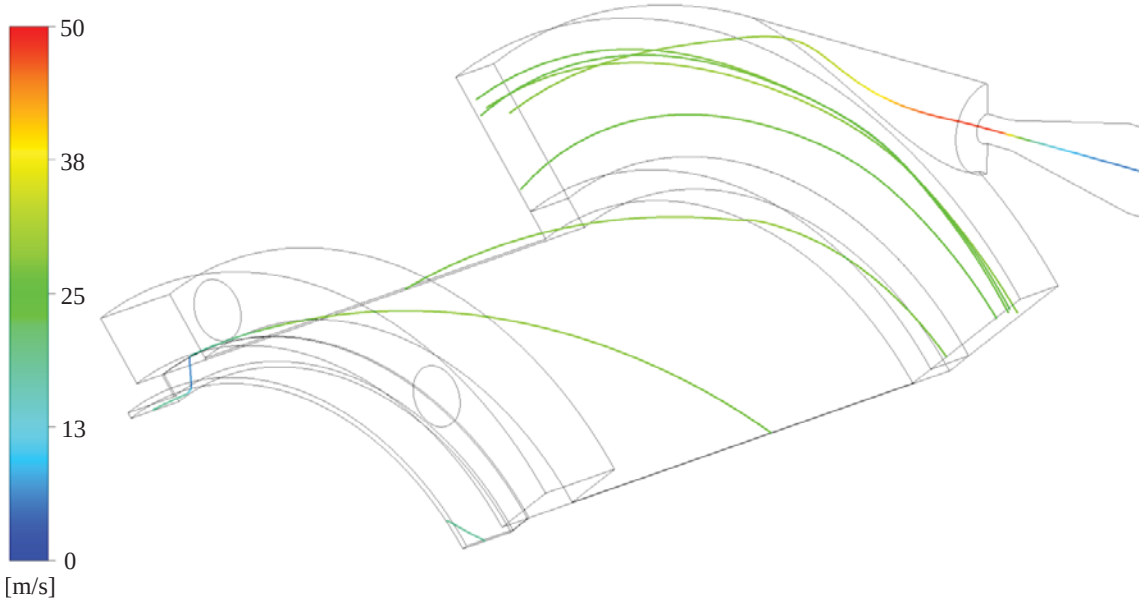

(a) Nozzle design A

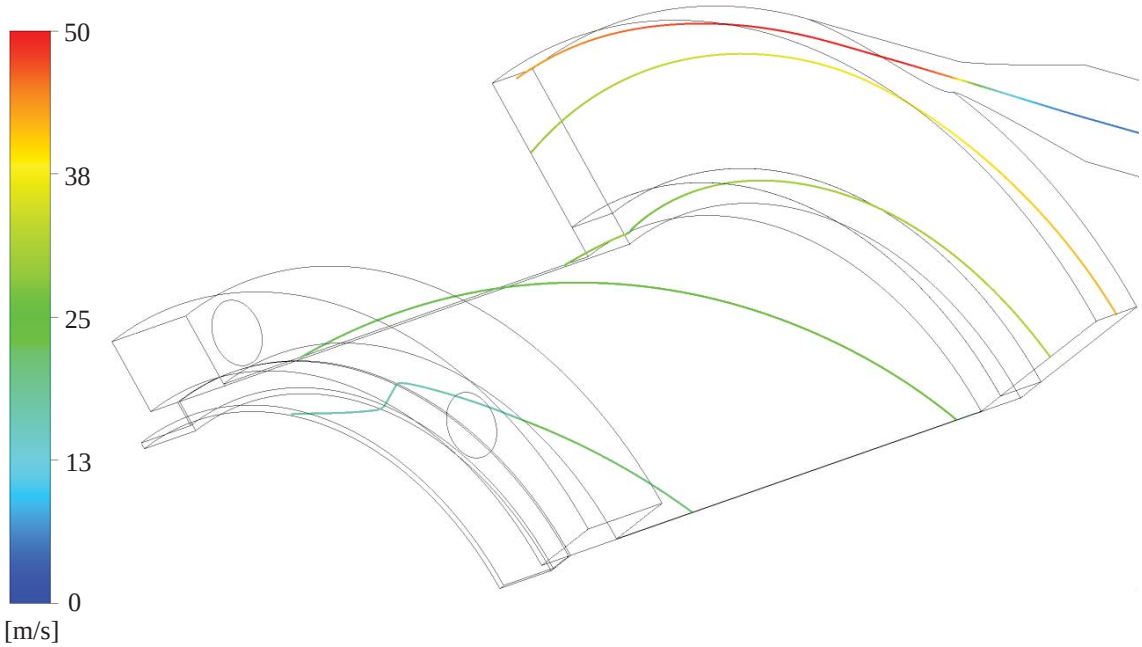

(b) Nozzle design B

Figure 3.6: Streamlines for two different nozzle geometries subjected to a single phase water flow at 40 bar inlet pressure.

3.3.3 Outlet Feature Study Results

The results for the iterative optimization of the primary outlet cavity position are presented in Fig. 3.7. From the combined contour and velocity vector plot of Fig. 3.7 it is seen that the velocity of the flow as it exits the seal clearance is substantial for both outlet cavity configurations. The results for the early iteration depicted in Fig. 3.7(a) show that, in this case, the flow exiting the seal clearance impacts the opposing wall di-

verting the flow both upwards towards the primary outlet channel, and downwards out through the secondary flow path. Fig. 3.7(b) reveals that displacing the primary outlet cavity axially towards the secondary outlet cavity changes the flow field substantially. In this case the high velocity flow exiting the seal clearance passes over the secondary flow path, creating a Venturi ejector effect. The local reduction in pressure in the outlet cavity reverses the direction of the flow in the secondary flow path and consequently leakage is completely mitigated.

Furthermore, the mesh presented in Fig. 3.5, which includes four secondary outlet ports, is used to investigate the leakage flow rates when a back-pressure is applied to the primary outlet ports, and to validate the results from the CFD based analysis conducted with the simplified slice meshes. For zero back-pressure the results obtained using the 3D model agree with the simplified slice models. Additionally, it is found that a zero leakage flow can be maintained for an inlet water pressure of 40 bar, for up to 10 bar back-pressure on the primary outlet ports.

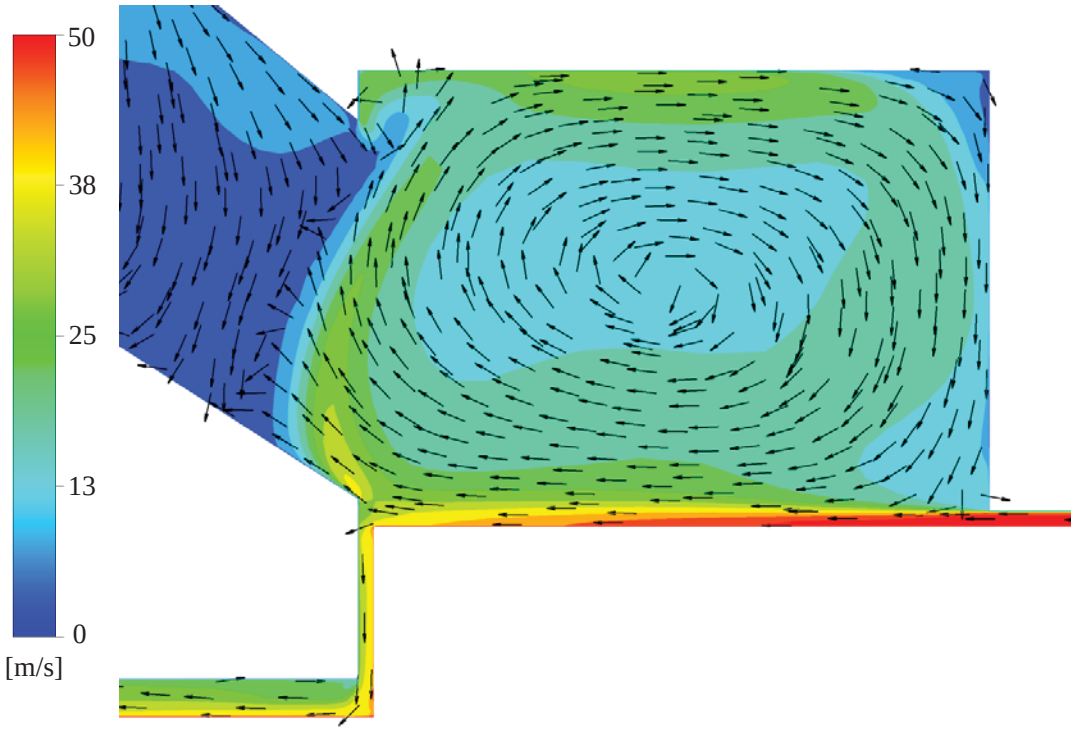

(a) Early iteration of the SHA outlet design

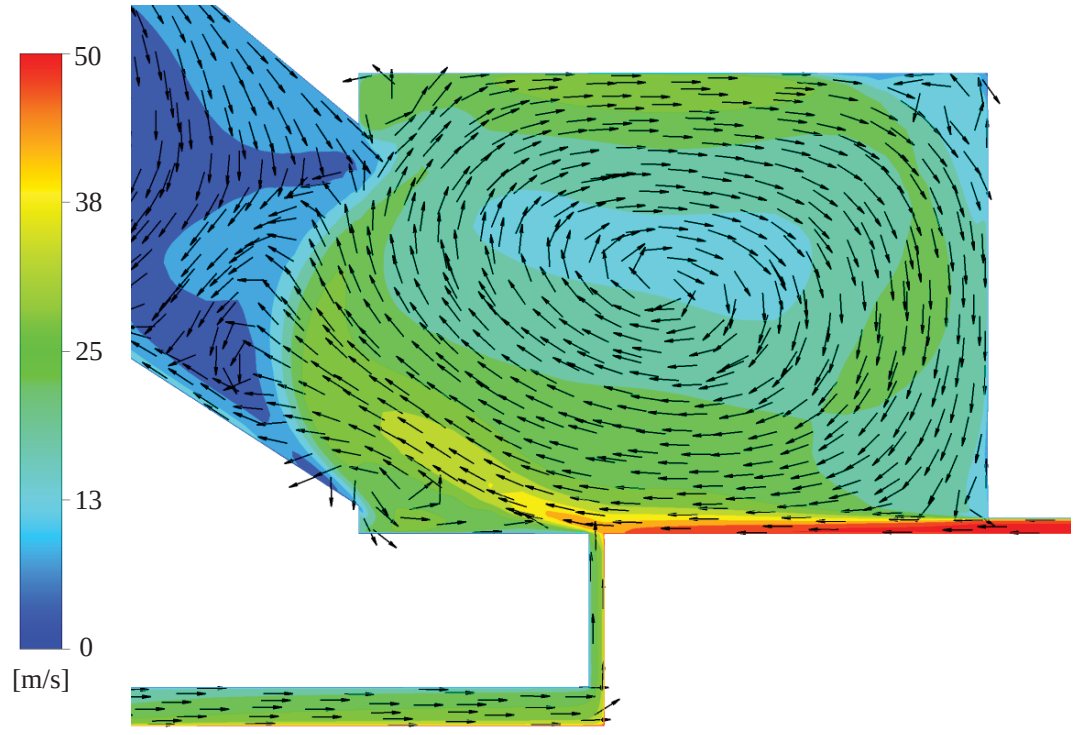

(b) Final version of the SHA outlet design

Figure 3.7: CFD simulation results showing combined contour and velocity vector plots for two different SHA outlet design iterations.

Chapter 4

Preliminary Experimental Methods and Results

This chapter presents the main experimental findings for the work reported in this thesis. Throughout the chapter results are presented for the rotor at standstill and the overall aim here is to investigate the applicability of the test facility for experimental seal analysis.

4.1 Identification of AMB Properties

To gain confidence in the mathematical representation of the AMB-rotor system dynamics, efforts have been directed towards experimental identification of AMB parameters. Discrepancies between theoretical parameter values and experimental values render controller synthesis a largely empiric endeavour, which ultimately leads to potential sub-optimal performance of the AMB-rotor system. A closed loop identification scheme presented in [104] has been applied in this project to identify AMB parameters. The findings are reported in the appended paper [P3].

4.2 Calibration of the Hall Sensor System

A fundamental feature of the test facility is the ability to quantify the forces acting on the rotor. This can be performed using multiple methods as described in section 1.2.3 of the introduction, of which the method of flux measurements using Hall sensors is superior in terms of precision [64, 68]. As mentioned in section 1.2.3 calibration of the Hall sensor system is necessary to obtain the desired force estimation precision. An overview of the Hall sensor system calibration methodology and results are presented in the paper [P2], albeit in compact form. This section provides a detailed description of the in situ calibration procedure and expands on the calibration results presented in [P2].

4.2.1 Calibration Methodology

The principle of the Hall sensor system calibration procedure is based on applying a known force of varying magnitude and direction, while recording the Hall sensor signals. As the applied force is known from the high precision force transducers of Module II, a Least Squares scheme can be employed to experimentally identify a set of Hall sensor calibration coefficients. This is the topic of section 4.2.2.

The calibration procedure is performed for bias currents in the range 4 A—10 A, and configured so that calibration can be performed for multiple rotor positions. The calibration procedure is visualised in the flowcharts presented in Fig. 4.1 and Fig. 4.2. Prior to calibration the operating parameters for the system are chosen along with the range of rotor positions included in the calibration. Additionally, a vector containing the loading directions is constructed. The procedure is fully automated and randomised and consists of three main loops introduced below. All data is recorded with a 500 Hz sampling frequency.

- **Position loop** The calibration loops over the different rotor positions to be included in the calibration. This feature is utilised in the investigation of the potential position dependence of the calibration coefficients for which the results are presented in section 4.2.5. If no variations of the rotor position are to be included the position loop is bypassed.
- **Direction loop** The direction loop controls the direction of the rotor loading force by randomly selecting one of the pneumatic actuators of Module II to engage with the rotor.
- **Loading loop** After a load direction is assigned the force applied onto the rotor is varied by stepwise increasing and decreasing the pressure supplied to the assigned pneumatic actuator using the controllable regulator valve as explained in section 2.4. The variation of the force is controlled by the loading loop shown in Fig. 4.2. Both the number of load steps and the maximum force applied during calibration is dependent on the operating conditions of the test facility. See Table 4.1 in section 4.2.4 for number of load steps and maximum applied force adhering to the results included in this work.

4.2.1.1 Calibration for the $i-s$ Methodology

The calibration procedure introduced above allows for determining a set of calibration coefficients for the $i-s$ based force estimation approach, simply by acquiring the current data vectors during the calibration test. This is utilised to conduct a comparative performance study of the two different force quantification methods, for which the results are included in [P2]. As both the experimental procedure and post processing of the data is very similar for the $i-s$ and the Hall sensor based methodologies, calibration efforts for the $i-s$ approach will not be treated further.

4.2.1.2 Note on Nominal Rotor Position During Calibration

In this documentation, three different nominal rotor positions are relevant. The first is referred to as the geometric centre of the AMBs. This is the rotor position established

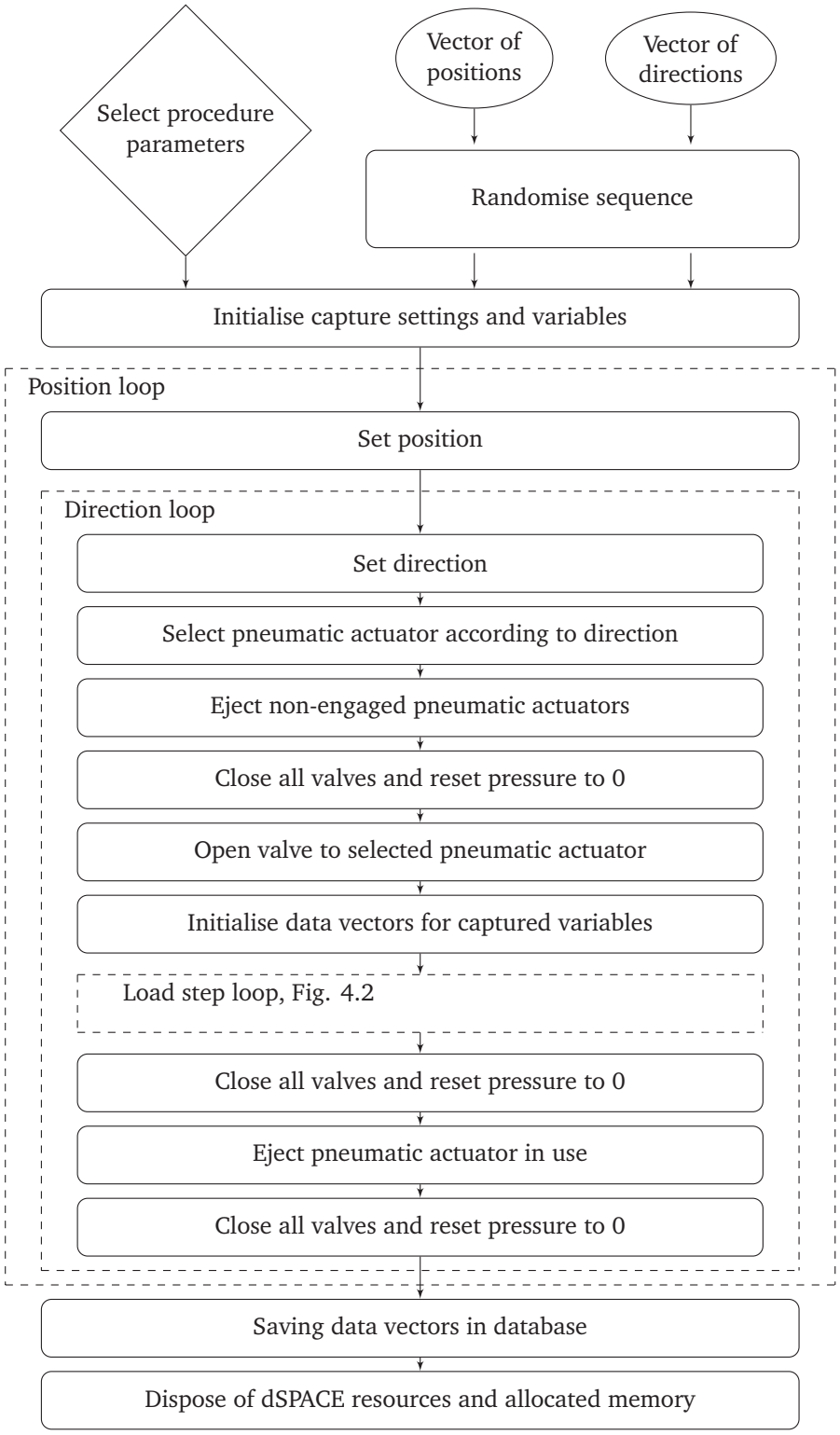

Figure 4.1: Flow chart outlining the automated calibration procedure.

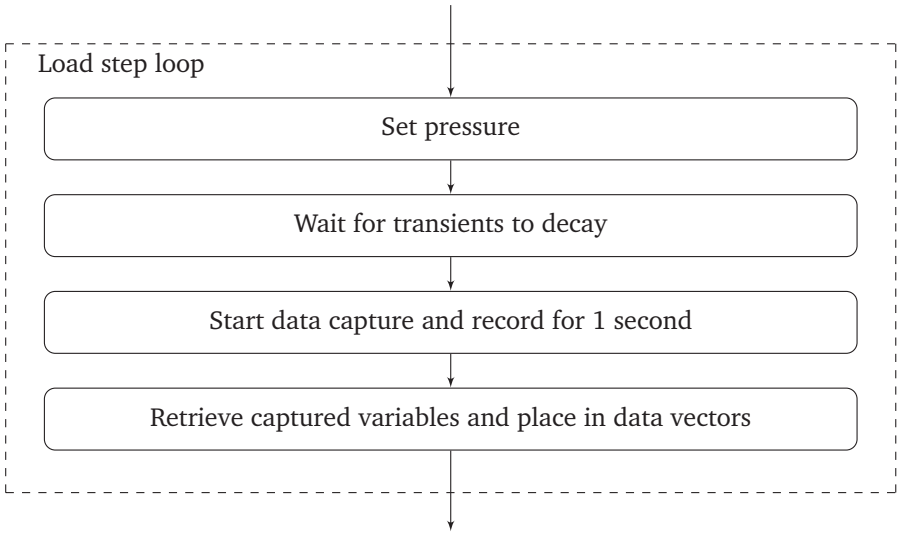

Figure 4.2: Flow chart outlining the load step loop which is a part of the automated calibration procedure presented in Fig. 4.1.

as centred during the alignment phase of Module I. The second is referred to as the effective magnetic centre for the rotor. This rotor position is determined by employing a centring algorithm based on [105]. The algorithm locates the rotor position for which the magnetic properties of the AMB-rotor system are most symmetric, which is beneficial from both an operating and an identification procedure point of view [105]. The third rotor centre is referred to as the seal centre. During assembly the SHA is sought aligned with the rotor placed in the magnetic centre introduced above. As a perfect centring of the SHA around the rotor is not practically possible, the seal centre and the magnetic centre of the rotor deviates from each other. The difference is within a couple of hundredth of a millimetre, however, it is emphasised that the *true* rotor position relative to both the AMB stators and the SHA are appended with uncertainties.

4.2.2 Post Processing of the Calibration Data

A prerequisite for determining the calibration coefficients for the Hall sensor system from experimental data is to establish equilibrium relations that allows the forces acting on the rotor to be determined as a function of the measured Hall voltage signals. With basis in the Free Body Diagram (FBD) shown in Fig. 4.3 the equilibrium equations can be established. Radial and axial forces are considered decoupled and consequently only forces in the two transversal directions are included in the equilibrium equations for the calibration presented below

$$\Sigma F_x = F_{app,x} + F_{A,x} + F_{B,x} + F_{C,x} = 0$$
$$\Sigma F_y = F_{app,y} + F_{A,y} + F_{B,y} + F_{C,y} - F_g = 0$$

in which the subscript A, B, c, and app denotes forces from AMB A, AMB B, the coupling and the externally applied load from Module II, respectively. The gravitational force contribution is denoted F_g. Summing moments around the point of attack for the

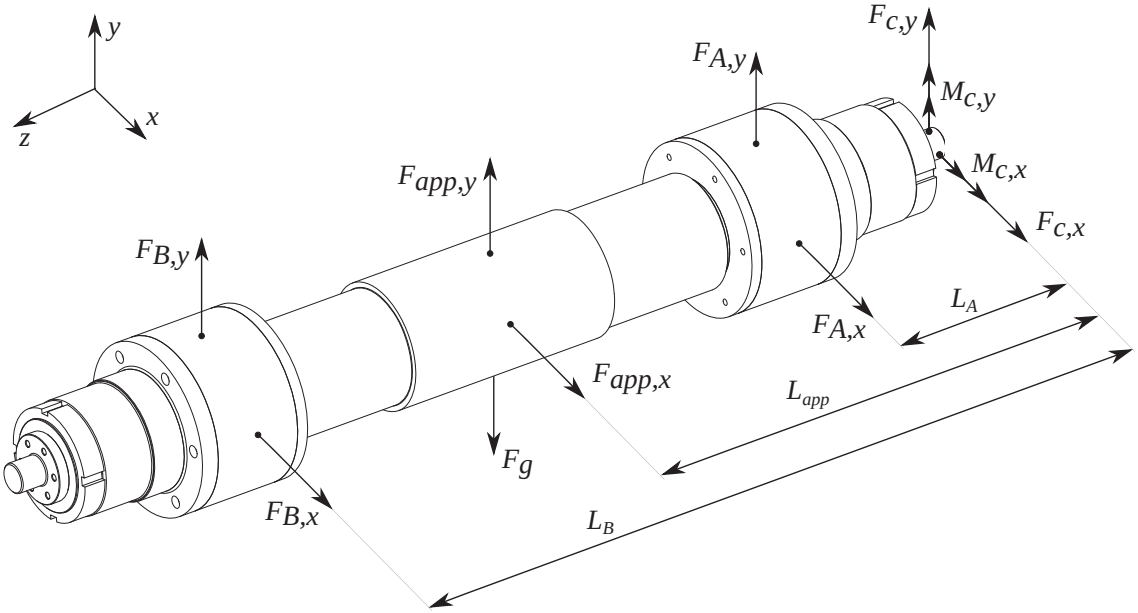

Figure 4.3: Free Body Diagram for the rotor showing geometrical definitions used in the post processing of the calibration data.

coupling forces yields

$$\begin{aligned}\Sigma M_x &= -F_{app,y}L_{app} - F_{A,y}L_A - F_{B,y}L_B + F_g L_g + M_{C,x} = 0\\ \Sigma M_y &= F_{app,x}L_{app} + F_{A,x}L_A + F_{B,x}L_B + M_{C,y} = 0\end{aligned}$$

in which the length L_A, L_B and $L_g = L_{app}$ are defined in Fig. 4.3. Considering only *changes* in force contributions yields

$$\begin{aligned}\Sigma\Delta F_x &= \Delta F_{app,x} + \Delta F_{A,x} + \Delta F_{B,x} + \cancelto{0}{\Delta F_{C,x}} = 0\\ \Sigma\Delta F_y &= \Delta F_{app,y} + \Delta F_{A,y} + \Delta F_{B,y} + \cancelto{0}{\Delta F_{C,y}} - \cancelto{0}{\Delta F_g} = 0\\ \Sigma\Delta M_x &= -\Delta F_{app,y}L_{app} - \Delta F_{A,y}L_A - \Delta F_{B,y}L_B + \cancelto{0}{\Delta F_g L_g} + \cancelto{0}{\Delta M_{C,x}} = 0\\ \Sigma\Delta M_y &= \Delta F_{app,x}L_{app} + \Delta F_{A,x}L_A + \Delta F_{B,x}L_B + \cancelto{0}{\Delta M_{C,y}} = 0\end{aligned} \tag{4.1}$$

Here the fact that neither the gravitational force acting on the rotor nor the rotor position changes during a single calibration loop is used. The orientation of the AMB actuators are visualised in Fig. 4.4 from which it is seen that the actuators are rotated 45° with respects to the global reference system depicted in both Fig. 4.3 and 4.4. From the definitions of Fig. 4.4 the AMB forces can be expressed in the global reference as

$$\Delta F_{A,x} = \frac{\sqrt{2}}{2}\left(\Delta F_{A,act1} + \Delta F_{A,act2}\right) \quad , \quad \Delta F_{A,y} = \frac{\sqrt{2}}{2}\left(\Delta F_{A,act1} - \Delta F_{A,act2}\right)$$
$$\Delta F_{B,x} = \frac{\sqrt{2}}{2}\left(\Delta F_{B,act1} + \Delta F_{B,act2}\right) \quad , \quad \Delta F_{B,y} = \frac{\sqrt{2}}{2}\left(\Delta F_{B,act1} - \Delta F_{B,act2}\right)$$

Relating the Hall sensor measurements to the AMB force requires that the AMB forces are expressed in terms of the individual electromagnets of each AMB, respectively. From

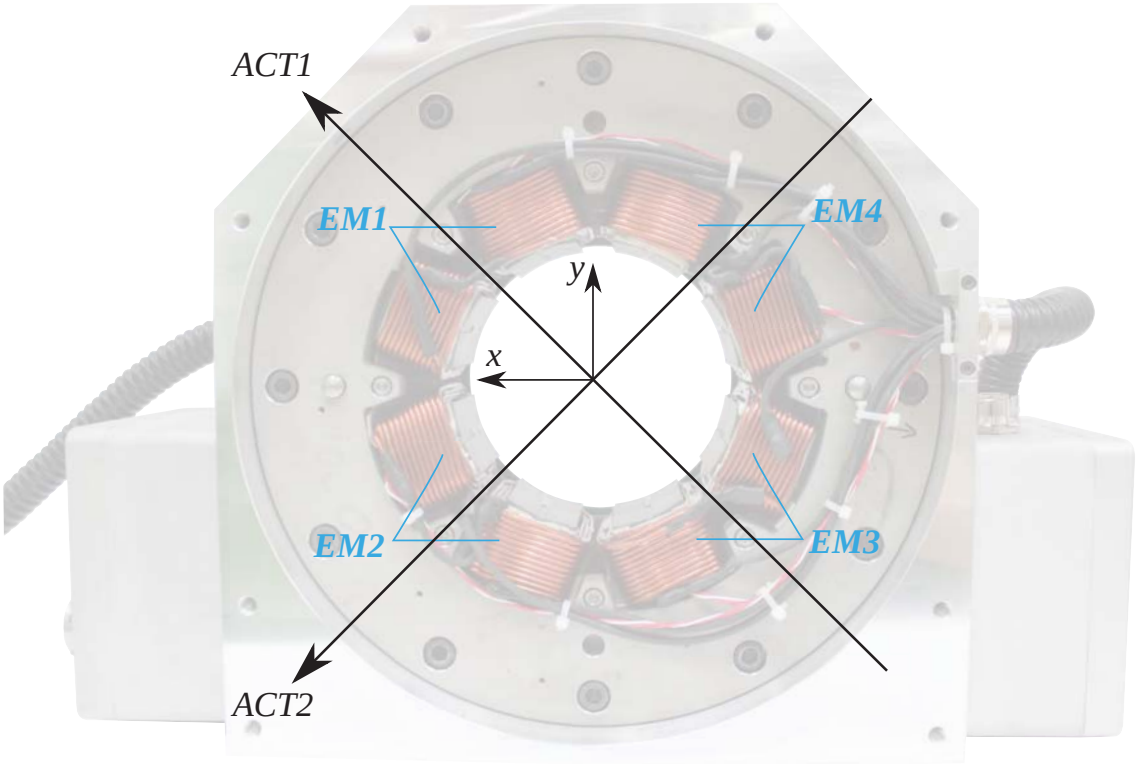

Figure 4.4: Stator layout showing definition of actuator and global reference frame alongside definitions of the individual electromagnets.

the definitions in Fig. 4.4 the AMB force components in the global reference frames, expressed as a function of the individual electromagnets (EM), are

$$\begin{aligned}
\Delta F_{A,x} &= \frac{\sqrt{2}}{2}\left[\left(\Delta F_{A,EM1}-\Delta F_{A,EM3}\right)+\left(\Delta F_{A,EM2}-\Delta F_{A,EM4}\right)\right] \\
\Delta F_{A,y} &= \frac{\sqrt{2}}{2}\left[\left(\Delta F_{A,EM1}-\Delta F_{A,EM3}\right)-\left(\Delta F_{A,EM2}-\Delta F_{A,EM4}\right)\right] \\
\Delta F_{B,x} &= \frac{\sqrt{2}}{2}\left[\left(\Delta F_{B,EM1}-\Delta F_{B,EM3}\right)+\left(\Delta F_{B,EM2}-\Delta F_{B,EM4}\right)\right] \\
\Delta F_{B,y} &= \frac{\sqrt{2}}{2}\left[\left(\Delta F_{B,EM1}-\Delta F_{B,EM3}\right)-\left(\Delta F_{B,EM2}-\Delta F_{B,EM4}\right)\right]
\end{aligned} \tag{4.2}$$

Expressing the electromagnetic force in terms of the Hall voltage as described in Eq. (2.43) of section 2.3.1.8 allows the forces from the AMBs to be determined from Hall sensor voltage measurements. The relation between Hall voltage and force from a electromagnet is re-stated here for completeness

$$F_{EM} = K_H V_H^2 \tag{4.3}$$

in which F_{EM} is the electromagnetic force from an arbitrary single electromagnet, K_H is a coefficient to be determined through calibration, and V_H represents an equivalent Hall sensor voltage determined as

$$V_H = \frac{|V_{H,N}|+|V_{H,S}|}{2} \tag{4.4}$$

where N and S denotes the north and south pole of the electromagnet, respectively. See Fig. 2.3 for details. Averaging two Hall sensor voltage signals is motivated by the fact that for small rotor displacements, i.e. neglecting the changes in flux due to displacement of the rotor, the two Hall sensors mounted on the same electromagnet should *theoretically* measure the same flux with a different sign. Additionally, averaging will reduce uncertainties imposed by random noise on the Hall sensor voltage signals. Combining Eqs. (4.1), (4.2), (4.3) and (4.4) allows the equilibrium equations to be cast in $\mathbf{Ax} = \mathbf{b}$ form with

$$\mathbf{A} = \begin{bmatrix} \Delta V_{H,A,1}^2 & \Delta V_{H,A,2}^2 & -\Delta V_{H,A,3}^2 & -\Delta V_{H,A,4}^2 & \Delta V_{H,B,1}^2 & \Delta V_{H,B,2}^2 & -\Delta V_{H,B,3}^2 & -\Delta V_{H,B,4}^2 \\ \Delta V_{H,A,1}^2 & -\Delta V_{H,A,2}^2 & -\Delta V_{H,A,3}^2 & \Delta V_{H,A,4}^2 & \Delta V_{H,B,1}^2 & -\Delta V_{H,B,2}^2 & -\Delta V_{H,B,3}^2 & \Delta V_{H,B,4}^2 \\ r_A \Delta V_{H,A,1}^2 & -r_A \Delta V_{H,A,2}^2 & -r_A \Delta V_{H,A,3}^2 & r_A \Delta V_{H,A,4}^2 & r_B \Delta V_{H,B,1}^2 & -r_B \Delta V_{H,B,2}^2 & -r_B \Delta V_{H,B,3}^2 & r_B \Delta V_{H,B,4}^2 \\ r_A \Delta V_{H,A,1}^2 & r_A \Delta V_{H,A,2}^2 & -r_A \Delta V_{H,A,3}^2 & -r_A \Delta V_{H,A,4}^2 & r_B \Delta V_{H,B,1}^2 & r_B \Delta V_{H,B,2}^2 & -r_B \Delta V_{H,B,3}^2 & -r_B \Delta V_{H,B,4}^2 \end{bmatrix}$$

and

$$\mathbf{x} = \begin{bmatrix} K_{H,A,1} \\ K_{H,A,2} \\ K_{H,A,3} \\ K_{H,A,4} \\ K_{H,B,1} \\ K_{H,B,2} \\ K_{H,B,3} \\ K_{H,B,4} \end{bmatrix}, \quad \mathbf{b} = \begin{bmatrix} \Delta F_{app,x} \\ \Delta F_{app,y} \\ \Delta F_{app,y} \\ \Delta F_{app,x} \end{bmatrix}$$

The length parameters r_A and r_B found in the matrix $\mathbf{A}$ are defined as $r_A = L_A/L_{app}$, $r_B = L_B/L_{app}$. The Hall sensor coefficients contained in the vector $\mathbf{x}$ are readily approximated from the experimental calibration data using a Least Squares scheme. Here a constrained Least Squares scheme is used, which entails that the two Hall sensor coefficients adhering to the respective AMB actuators are considered equal. Specifically

$$\begin{aligned} K_{H,A,1} &= K_{H,A,3}, \quad K_{H,A,2} = K_{H,A,4} \\ K_{H,B,1} &= K_{H,B,3}, \quad K_{H,B,2} = K_{H,B,4} \end{aligned} \tag{4.5}$$

which is motivated by the fact that the Hall sensor coefficients belonging to an actuator are theoretically equal. The post processing procedure for the calibration data is presented in the flow chart of Fig. 4.5.

4.2.3 Uncertainty Analysis

Aspects of the following section are adapted from [90]. To gain confidence in the estimated force the uncertainty on the force is investigated in the present section. A relatively simple approach based on [106] is utilised which employs the Root-Sum-Squared (RSS) methodology to *estimate* uncertainties. Conceptual errors originating e.g. from the design of the test facility are ignored, implicitly assuming that variables are measured correctly but have an appended uncertainty originating from the measurement system. Defining the error u_i of a true value x_i as

$$u_i = \mid x_i - x_{measured,i} \mid \tag{4.6}$$

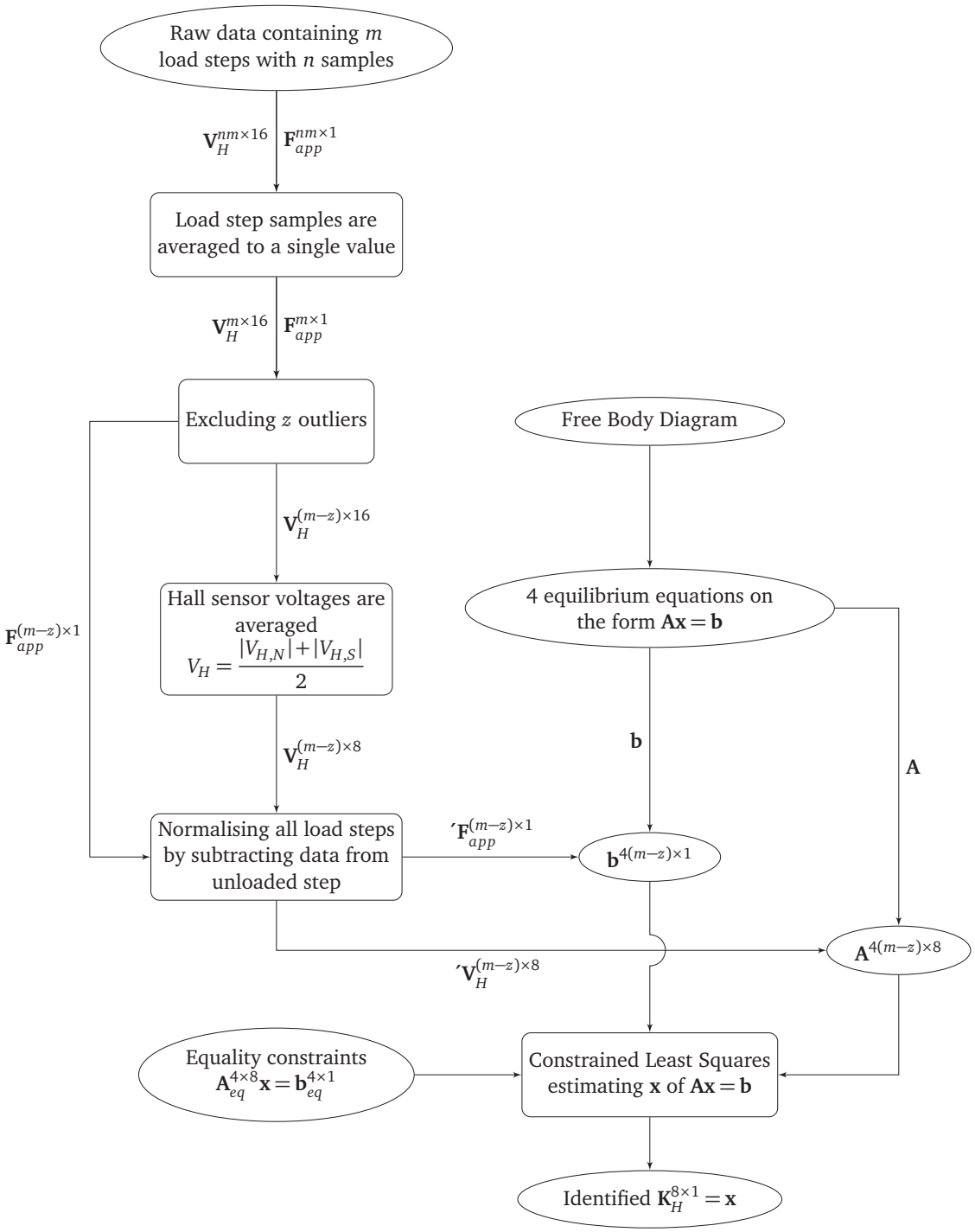

Figure 4.5: Flow chart outlining the post processing procedure for the Hall sensor calibration data.

allows the uncertainty of an arbitrary quantity R to be determined as [106]

$$u_R = \left[\left(\frac{\partial R}{\partial x_1} u_1 \right)^2 + \left(\frac{\partial R}{\partial x_2} u_2 \right)^2 + \cdots + \left(\frac{\partial R}{\partial x_n} u_n \right)^2 \right]^{1/2} \tag{4.7}$$

in which n denotes the number of variables affecting R. The error u_i is considered to be comprised of two contributions as indicated below [106]

$$u_i = \left[\left(u_{i,fixed} \right)^2 + \left(u_{i,random} \right)^2 \right]^{1/2}$$

where $u_{i,fixed}$ denotes a fixed or systematic error that does not vary during an experiment and $u_{i,random}$ represents a random error that does [106]. Assuming that $u_{i,random}$ is normally distributed, and employing a 95 % confidence interval, allows the random error on a measured variable x_i to be determined as

$$u_{i,random} = 2\sigma_i \tag{4.8}$$

in which σ_i is the standard deviation of the envelope of N measured points given by

$$\sigma_i = \left(\frac{1}{N-1} \sum_{j=1}^{N} \left(x_{i,j} - \langle x_i \rangle \right)^2 \right)^{1/2}$$

where

$$\langle x_i \rangle = \frac{1}{N} \sum_{j=1}^{N} x_{i,j}$$

In an effort to reduce the complexity of the analysis while still retaining the key factors contributing to the overall uncertainty on the estimated force, it is assumed that the force quantified by the Hall sensor system can be represented by the simple generic relation

$$F_{Hall} = K_H V_H^2 \tag{4.9}$$

Consequently, two groups of uncertainties are considered in the following: Uncertainties that adhere to the Hall sensor calibration coefficients, and uncertainties adhering to the measurement of the Hall sensor signals themselves.

Uncertainties Related to the Hall Sensor Signals

The uncertainty on the Hall sensor signals are assumed not to be influenced by any fixed errors and are therefore considered to be of a purely random nature. The uncertainty is estimated experimentally by conducting a baseline noise test which entails recording Hall sensor signals with the rotor placed in the backup bearings and no current running through the AMB coils. The results are presented in Fig. 4.6 where the classical bell curve shaped histogram plot is seen in Fig. 4.6(b) confirming that the data is normal distributed. The results presented for Hall sensor AH3 are representative for all Hall sensors. Based on the data the random error can be determined as

$$u_{H,rand.} = 2\sigma = 2.1\,\text{mV}$$

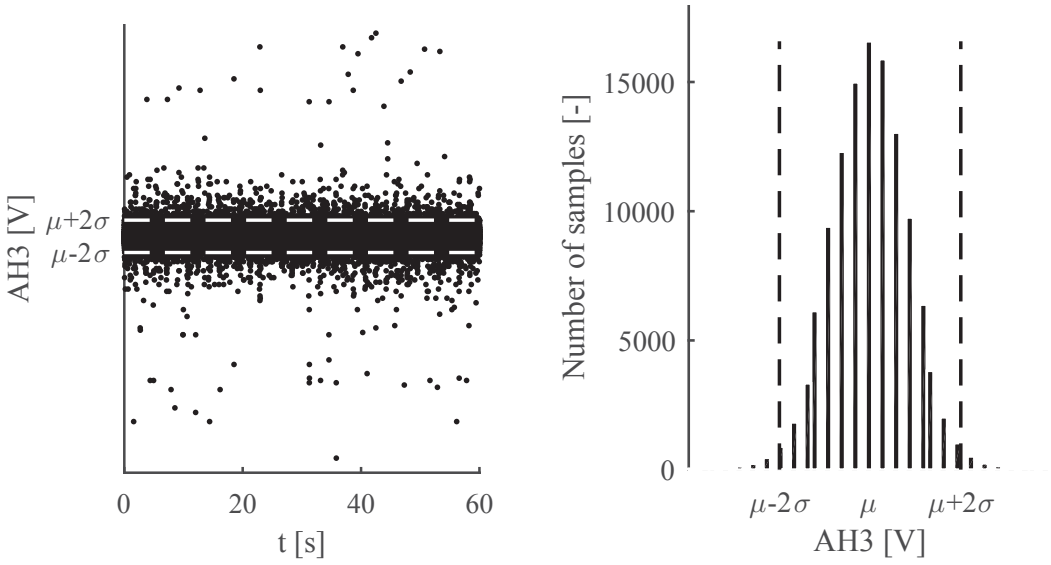

(a) Time series data (b) Histogram

Figure 4.6: Data from noise measurement for Hall sensor AH3.

Additionally, the Hall sensor signals are subjected to a fixed error originating from the finite resolution of the data acquisition system ADCs. The ADCs have a 16 bit resolution over a voltage range of ±10 V resulting in a discretisation error of

$$u_d = \frac{20\,\mathrm{V}}{2^{16}} = 0.31\,\mathrm{mV}$$

The total error is estimated as

$$u_H = \left[u_{H,rand.}^2 + u_d^2\right]^{1/2}$$

Uncertainties Related to the Hall Sensor Calibration Coefficients

Three main contributors to the overall uncertainty related to the identification of the Hall sensor calibration coefficients are considered. These are shortly described below.

- **Goodness of fit** The largest contributor to the error on the calibration coefficient stems from fitting the experimental data to the mathematical representation of the AMB force using a Least Squares scheme. In this context the error can be quantified as the difference between the reference force imposed by the pneumatic actuators of Module II and the force quantified based on the Hall sensor measurements. The method introduced here is applied throughout the result sections of the thesis and is based on determining the Mean Absolute Error (MAE) between a reference force and the force measured using the Hall sensor system. The MAE is defined as

$$MAE = \frac{1}{N}\sum_{j=1}^{N}|u_j|$$

in which n denotes the number of samples in the measurement envelope and u_j is the local estimation error, here defined as

$$u_j = F_{app,j} - F_{Hall,j}$$

where $F_{app,j}$ is the force applied by the pneumatic actuators of Module II and $F_{Hall,j}$ is the force estimated using the Hall sensor system. In the present context the MAE is considered a fixed error for a given calibration coefficient K_H and is renamed here as

$$u_{fit} = MAE = \frac{1}{N}\sum_{j=1}^{N}|u_j|$$

- **Reproducibility** The coefficients are appended with an error related to the reproducibility of the coefficients for repeated calibration experiments. To assess the reproducibility repeated calibrations are performed for a subset of operating conditions. The coefficients are found to vary within two percent of their maximum value between calibrations. The error is considered fixed and estimated as two percent of the average of all identified coefficients $\overline{K_H}$ for a given bias current. Consequently

$$u_{rep} = 0.02\overline{K_H}$$

- **Force transducer error** The force transducers employed to measure the reference force introduces an error on the estimated calibration coefficients. This error, which is fixed, is estimated on the basis of the manufacturers guidelines and data sheet, and found to be

$$u_{trans} = 0.48\,\mathrm{N}$$

The overall uncertainty on the force quantified by the Hall sensor system can then, from Eq. (4.7) and the errors identified above, be approximated as

$$u_{F_{Hall}} = \left[\left(u_{fit}\right)^2 + (u_{trans})^2 + \left(\frac{\partial F_{Hall}}{\partial K_H}u_{rep}\right)^2 + \left(\frac{\partial F_{Hall}}{\partial V_H}u_H\right)^2\right]^{1/2} \tag{4.10}$$

Invoking Eq. (4.9) allows Eq. (4.10) to be expanded to

$$u_{F_{Hall}} = \left[\left(u_{fit}\right)^2 + (u_{trans})^2 + \left(V_H^2 u_{rep}\right)^2 + (K_H u_H)^2\right]^{1/2} \tag{4.11}$$

To obtain a simple but useful fixed uncertainty estimate V_H and K_H in Eq. (4.11) needs to be assigned meaningful values. Here it is chosen to estimate V_H as the average of the maximum variation of all Hall sensor voltages recorded during a calibration cycle. Consequently V_H in Eq. (4.11) is redefined as $V_H = \overline{\Delta V}_{H,max}$. This is considered to yield a conservative uncertainty estimate. Likewise, in the interest of obtaining a conservative uncertainty estimate, K_H is assigned the maximum value of the four coefficients identified in a calibration cycle. Consequently K_H in Eq. (4.11) is redefined as $K_H = K_{H,max}$. Using the above, Eq. (4.11) can be restated as

$$u_{F_{Hall}} = \left[\left(u_{fit}\right)^2 + (u_{trans})^2 + \left(\overline{\Delta V}^2_{H,max}u_{rep}\right)^2 + \left(K_{H,max}u_H\right)^2\right]^{1/2} \tag{4.12}$$

The overall uncertainty on the force quantified by the Hall sensor system can be estimated using Eq. (4.12), and should be done so for each choice of bias current in the calibration envelope. The uncertainty estimated using (4.12) is dominated by u_{fit} and u_{rep}, while the fixed error u_{trans} from the force transducer and the random uncertainty u_H from the Hall sensor signals only have minor influence.

4.2.4 Calibration Results: Coefficients

The content presented in this section expands the results published in [P2]. Specifically the calibration results for the full range of AMB bias currents are presented. The calibration coefficients identified are presented as a function of the bias current in Fig. 4.7. Generally, the coefficients are seen to decrease as the bias current is increased, which is attributed to the increase in nominal flux density measured by the Hall sensor system. The coefficients identified for AMB B are larger than those belonging to AMB A, which is primarily a consequence of geometrical and electrical differences between the two AMBs. The calibration coefficients adhering to the two orthogonal actuators of each AMB, respectively, are seen to differ in magnitude, with the largest deviation found for AMB A. This suggests that the AMB stators are not completely rotationally symmetric, with the geometrical and electrical non-symmetry being significantly more pronounced for AMB A.

The quality of the calibration is assessed by comparing the force quantified using the test facility Hall sensor system to the force applied during calibration. This procedure is equivalent to estimating the quality of fit for the Least Squares curve fitting approach employed in the post processing of the calibration data. The MAE results are shown in Table 4.1. The table includes the maximum resulting force applied in the calibration for each bias current $F_{res,max}$. Additionally, the maximum estimation errors for all bias currents are presented. The MAE in percent of $F_{res,max}$ is on the order of 1 % for all bias currents which is comparable to results from the literature [65, 68] and

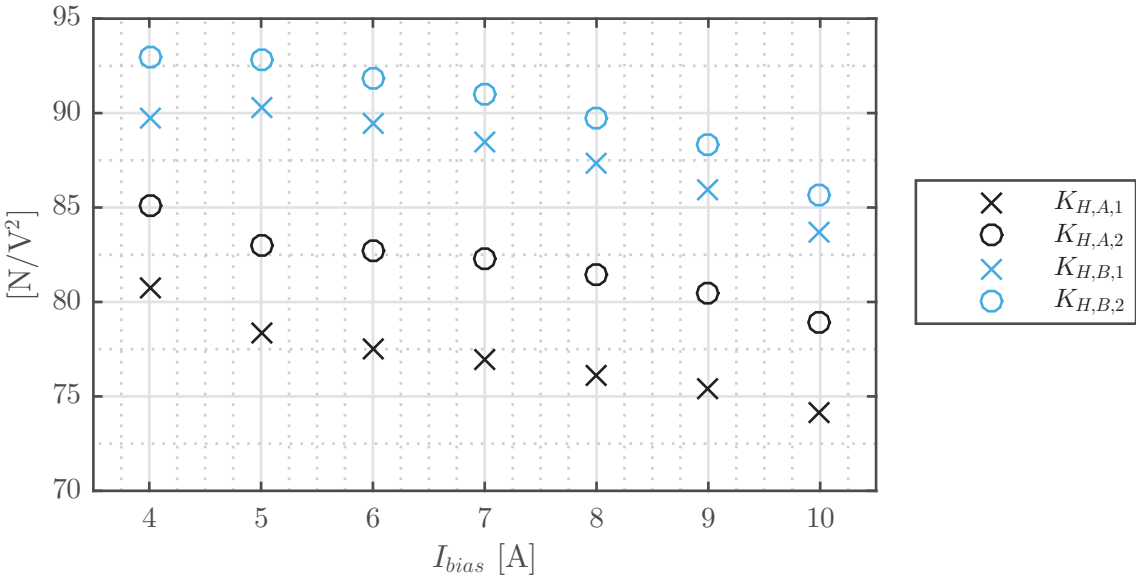

Figure 4.7: Calibration coefficients visualised as a function of AMB bias current.

Table 4.1: Calibration results for all bias currents.

Bias current	[A]	4	5	6	7	8	9	10
Number of load steps	[-]	11	9	17	21	25	29	33
$F_{res,max}$	[N]	500	1000	2000	2500	3000	3500	4000
MAE	[N]	5.9	9.8	17	18	20	25	32
MAE/$F_{res,max}$	[%]	1.2	0.95	0.82	0.74	0.68	0.72	0.79
Max. error	[N]	35.9	37.6	57.6	56.3	64.3	81.6	146
Max. error/$F_{res,max}$	[%]	7.2	3.8	2.9	2.3	2.1	2.3	3.7
Uncertainty	[N]	6.02	9.91	17.3	18.3	20.3	25.3	32.2

considered satisfactory. A static and a dynamic validation of the Hall sensor system force quantification performance is presented in sections 4.3 and 4.4, respectively.

A Note on the Quadratic Versus a Linear Force Relation

In [P4] it was found that exchanging the quadratic relation between force and measured Hall voltage for a simpler linear relation entailed an increase in the force estimation precision under certain circumstances. The study was performed using an experimental setup featuring a four pole MBE. In the calibration phase of the test facility developed during the PhD project the linear force relation was found to produce inferior force estimations compared to the quadratic force relation. Consequently the quadratic force relation is applied throughout the work documented here.

4.2.5 Calibration Results: Investigation of Position Dependence of the Hall Sensor Calibration Coefficients

Motivated by the findings presented in [P4], which indicates that calibration coefficients for an embedded Hall sensor system could be dependent on the rotor position, the potential position dependence of the Hall sensor calibration coefficients is investigated. The paper [P2] includes a detailed investigation of the Hall sensor calibration coefficient position dependence for the rotor centred in the geometric centre of the AMBs. As the rotor is nominally positioned in the seal centre during seal test, the position dependence study presented in [P2] is repeated for the rotor positioned in the SHA centre. The study presented here includes a circular manifold of 13 rotor positions distributed within a position range from $\{-50;50\}$ μm in the y and x-direction as shown on Fig. 4.8, where $(0,0)$ indicates a centred rotor. The investigating of position dependence is conducted for two choices of bias current namely 5 A and 10 A.

To determine the variation the difference between the minimum and the maximum value of each coefficient is quantified in percent. The resulting variations are summarised in Table 4.2. Coefficient variation data for two different rotor position variation limits, namely 50μm and 100μm, is included in Table 4.2. Variations are seen to be more pronounced for the 5 A bias current case than for the 10 A bias current case. For the 100 μm rotor position variation limit the change in coefficient magnitudes are

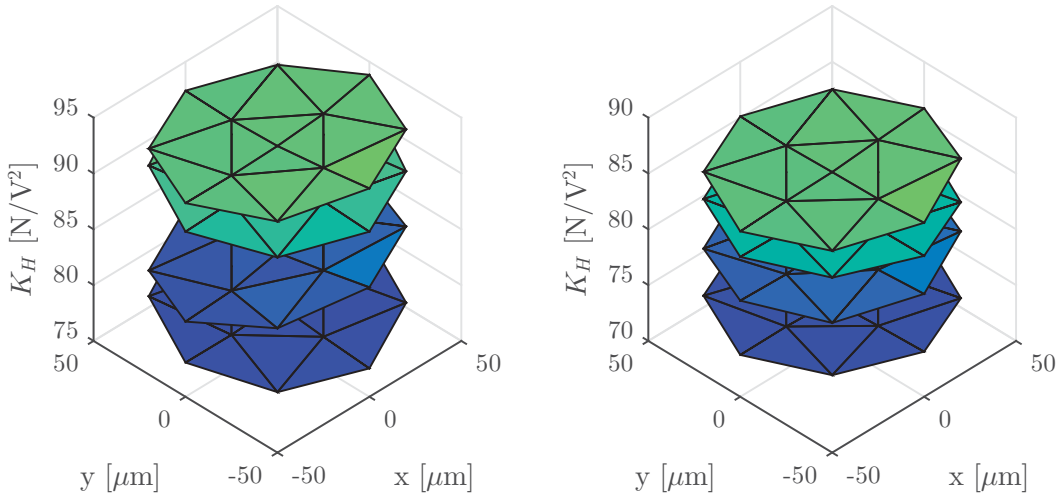

(a) Results for a bias current of 5 A

(b) Results for a bias current of 10 A

Figure 4.8: Calibration coefficients for different rotor positions. The individual coefficients are represented using a triangular surface plot for which nodes correspond to a coefficient determined at a specific position. The four coefficients are organised from bottom to top in the following sequence: $K_{H,A,1}$, $K_{H,A,2}$, $K_{H,B,1}$ and $K_{H,B,2}$.

Table 4.2: Percentile variation of the Hall sensor coefficients for two bias currents, induced by variation of the rotor position.

Bias current	[A]	5		10	
$F_{res,max}$	[N]	1000		4000	
Max. Δ pos.	[μm]	50	100	50	100
$\Delta K_{H,A,1}$	[%]	1.6	3.3	0.4	0.9
$\Delta K_{H,A,2}$	[%]	2.1	4.6	0.6	1.9
$\Delta K_{H,B,1}$	[%]	1.1	3.3	0.4	0.8
$\Delta K_{H,B,2}$	[%]	0.7	1.8	0.6	1.7

below 4.6 % for 5 A bias current and below 1.9 % for 10 A bias current. Decreasing the rotor position variation limit to 50μm, expectedly results in smaller variations of the calibration coefficients. For the 50 μm limit the change in the coefficients are below 2.1 % for 5 A bias current and below 0.6 % for 10 A bias current. The variations are considered small enough to be neglected for seal experiments.

4.2.6 Frequency Dependence of the Hall Sensor Coefficients

For the static calibration of the Hall sensor system to be useful for dynamic force quantification purposes, the identified calibration coefficients must be frequency independent. This was treated in the paper [P4] in which the findings indicated that the Hall sensor calibration constants are indeed frequency independent, thus a static calibration will suffice even for dynamic force measurement purposes.

4.3 Static Validation of Hall Sensor System Performance

The precision with which the forces acting on the rotor can be determined has to be rigorously assessed. This is performed by employing both a dynamic and a static validation scheme, where the latter is the focus of this section. It should be noted that the dynamic validation scheme, presented in section 4.4 is only conducted for a 5 A bias current.

4.3.1 Test Methodology

The test methodology employed here mirrors that used for the calibration of the Hall sensor system, and is based on applying a force of varying and known magnitude and direction to the rotor via Module II. The main difference between the calibration and the static validation procedures is that in the validation study forces are also applied in non-horizontal and non-vertical directions. This is done in order to ensure that the Hall sensor system can capture force applied in directions not included in the calibration procedure with sufficient precision.

Forces are employed in non-horizontal and non-vertical directions by engaging two pneumatic actuators of Module II simultaneously. Consequently the resulting force can be determined by a simple projection of the forces measured by the force transducers of Module II. The loading directions included in the static validation test are shown in Table 4.3 where the force direction angle α is introduced. The definition of α is presented in Fig. 4.9.

Similarly to the calibration experiments the force on the rotor is in the static validation experiments increased and decreased incrementally for each loading direction, albeit here in nine steps. The validation experiment is performed for four choices of bias currents, namely 5 A, 6 A, 8 A, and 10 A, respectively. For the 5 A bias current the rotor is positioned in the seal centre, while the rotor is positioned in the magnetic centre for the 6 A, 8 A, and 10 A bias current cases. To ensure that the rotor is not pulled out of equilibrium for the off-axis loading cases, the maximum force applied to the rotor in the validation experiments is reduced to 75 % of the maximum force applied in the calibration experiments.

Table 4.3: Applied load directions for the static Hall sensor system performance validation tests.

α [°]	Load direction
0	$(-x)$
45	$(-x,+y)$
90	$(+y)$
135	$(+x,+y$
180	$(+x)$
225	$(+x,-y)$
270	$(-y)$
315	$(-x,-y)$

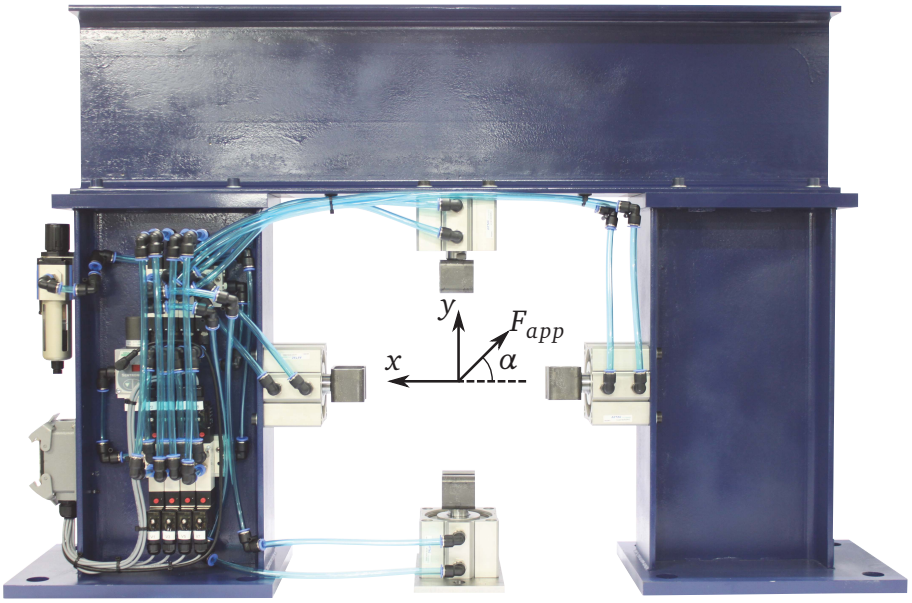

Figure 4.9: Calibration facility with direction of applied force indicated.

4.3.2 Post Processing of the Experimental Data

Post processing of the static validation data is very similar to the methodology used for the calibration data. The procedure is presented in the flow chart shown in Fig. 4.10. Ultimately the post processing of the experimental data enables a comparison of the force quantified using the force transducers of Module II and the force determined by the Hall sensor system. The results are presented in section 4.3.3.

4.3.3 Test Results and Discussion

The results from the static validation of the Hall sensor performance is summarised in Table 4.4. The table includes the results presented in paper [P2] expanded by the 5 A bias current case. Again the force estimation error is quantified using the MAE approach introduced in section 4.2.2. The MAE in percent of the maximum applied force are seen to be below 1 % for all bias current cases, which is comparable in magnitude to the results obtained for the calibration data. The results are considered to provide affirmation that the Hall sensor system performs satisfactory, even for off-axis loading cases.

The force estimation precision for the Hall sensor system is compared to the widely applied $i-s$ methodology for the 6 A, 8 A, and 10 A bias current cases. The results are presented in [P2] which confirms that the Hall sensor system outperforms the $i-s$ based methodology as expected [64, 68].

4.4 Dynamic Validation of the Hall Sensor System Performance

This section presents the underlying method for the dynamic validation of the Hall sensor based force measurement system, as well as the validation results. The dynamic validation study is based on comparing the force experimentally quantified using the

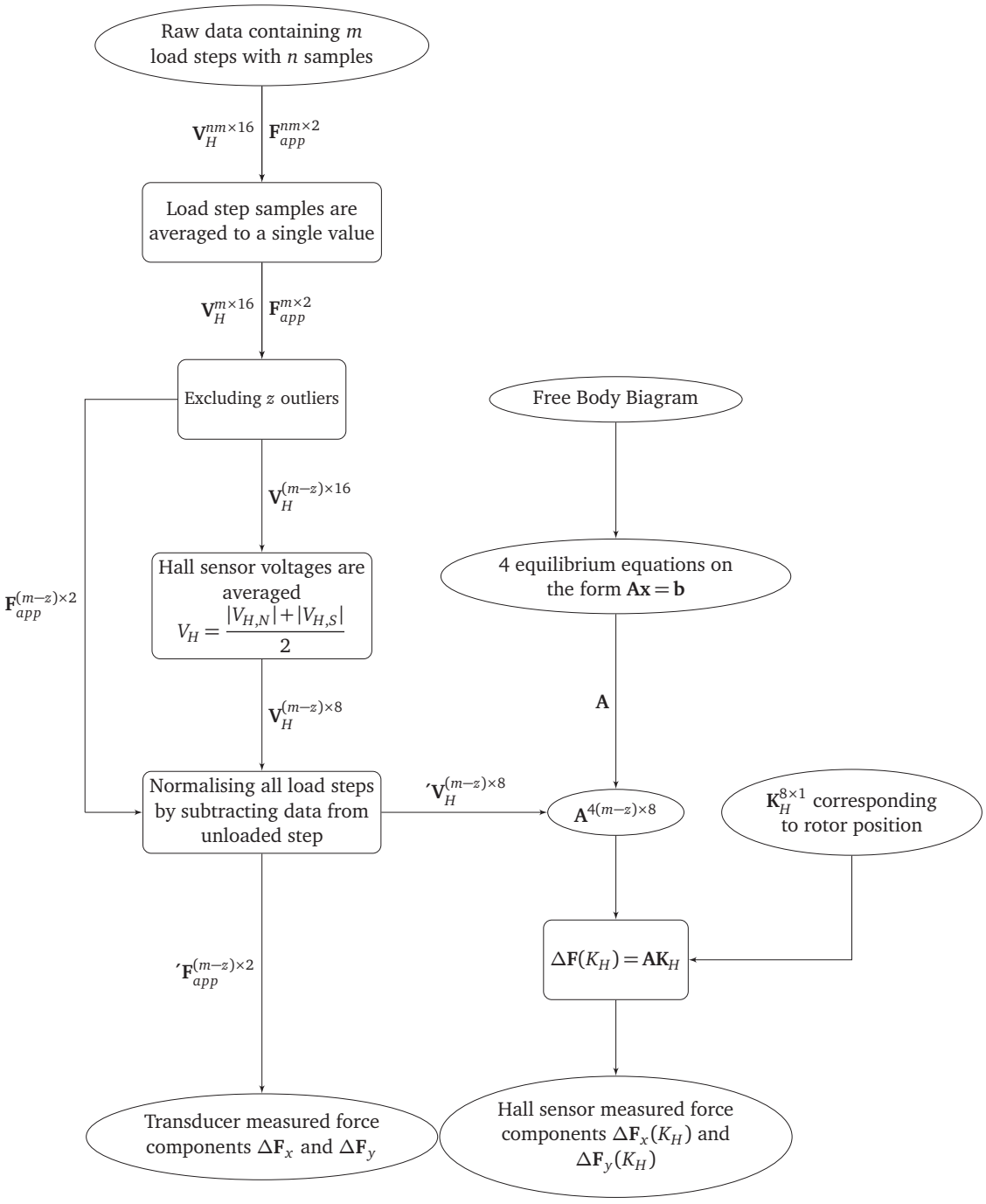

Figure 4.10: Flow chart for the post processing of the static validation data.

Table 4.4: Results for the static validation of the Hall sensor system calibration. It is noted that the results for the 5 A bias current case are for the rotor placed in the seal centre, while the remaining data is for the rotor centred in the geometric centre of the AMBs. See section 4.2.1.2 for details.

Bias current	[A]	5	6	8	10
$F_{res,max}$	[N]	1000	1500	2250	3000
MAE	[N]	8.4	12	18	26
MAE/$F_{res,max}$	[%]	0.84	0.77	0.78	0.86
Max. error	[N]	17.4	34.2	65.3	61.1
Max. error/$F_{res,max}$	[%]	1.7	2.3	2.9	2.0

Hall sensor system to the force determined from the dynamic response of the rotor. The general methodology used in the validation experiments are conceptually similar to the methodology used in the seal experiments described in section 4.5.1.

4.4.1 Test Methodology

In the dynamic validation experiments the rotor is excited by imposing a single frequency sinusoidal current perturbation on the AMB control currents resulting in 1D harmonic motion of the rotor. The perturbation of the AMB control currents applied simultaneously to both test facility AMBs can be defined as

$$i_x := i_{x,n} + i_{x,\delta} \quad \wedge \quad i_y := i_{y,n} + i_{y,\delta} \tag{4.13}$$

in which $i_{x,n}$ and $i_{y,n}$ denotes the nominal actuator control currents determined by the AMB controller. It is recalled that the actuators are tilted 45° with respects to the global reference frame. The perturbation of the nominal control currents are in Eq. (4.13) denoted $i_{x,\delta}$ and $i_{y,\delta}$, and can take any arbitrary form. For the purpose of the validation experiment and the seal test it is sufficient to define the current perturbations as

$$i_{x,\delta} := A_x \sin \omega t \quad \wedge \quad i_{y,\delta} := A_y \sin \omega t \tag{4.14}$$

in which A_x and A_y are the amplitudes of the harmonic current perturbations in Amperes, and ω is the perturbation frequency. It should be noted that the current perturbation scheme can be adapted by tuning a set of gains to facilitate resulting sinusoidal rotor displacement in any arbitrary direction in the $x-y$ plane of the global reference frame. The strategy of perturbing the control currents is chosen over imposing a sinusoidal position reference for the rotor as the AMB PID controllers implemented is not optimised for reference tracking. Experience has shown that control current perturbation is sufficient to obtain a useful perturbation of the rotor motion. The perturbation currents defined in Eq. (4.14) are used for both AMBs, and an example of a resulting perturbation pattern for $A_x = A_y = 50$ mA and $\omega = 5$ Hz is shown in Fig. 4.11(a). The figure shows the expected resulting displacement in the vertical direction of the global reference frame, with negligible disturbance of the rotor position in the horizontal direction. It is observed that the motion of the rotor measured at the two bearing locations are in phase. However, the displacement amplitude at AMB A is significantly reduced compared to the

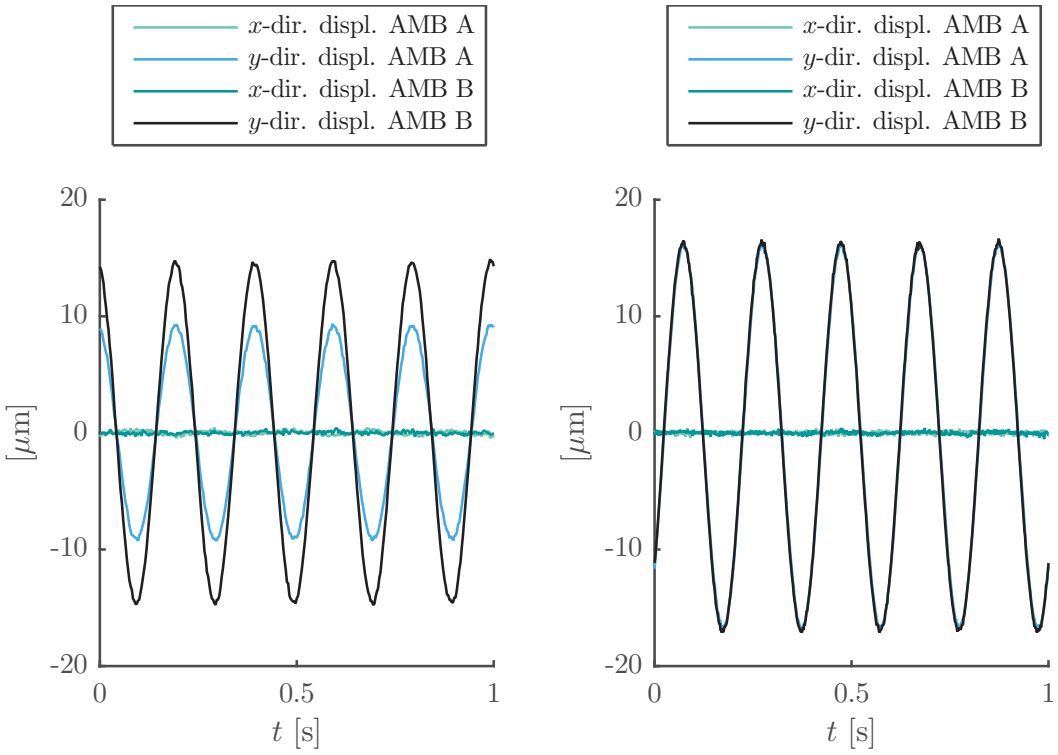

(a) Before tuning (b) After tuning

Figure 4.11: Adjustment of 1D vertical current perturbation pattern for the test facility AMBs.

displacement in AMB B. This is primarily due to the transversal stiffness of the flexible coupling situated near AMB A and secondarily to mechanical and electrical differences between the two bearings. The differences in amplitude result in an unwanted tilting motion of the rotor which should be minimised. This can be achieved through tuning of a set of gains, which ultimately results in different A_x and A_y values between the two AMBs. Fig. 4.11(b) shows the rotor perturbation pattern after tuning where close to identical rotor displacements in the two AMBs are seen ensuring purely transversal motion of the rotor during tests.

An outline of the experimental procedure is presented in Fig. 4.12. The validation test is repeated for multiple frequencies between 0 Hz and 80 Hz, while the amplitude of the rotor motion is kept constant at 10 μm for all frequencies in the test. Additionally, the experiment is performed for rotor motion in both the x and y -direction of the global reference frame, respectively. A sampling frequency of 2.5 kHz is used for acquiring force and position data and the AMBs are operated with a bias current of $i_{bias} = 5$ A throughout the tests.

4.4.2 Post Processing of the Experimental Data

Post processing the experimental data is done in a number of steps outlined in the following and summarised in the pseudo flowchart presented in Fig. 4.13. Firstly, the forces acting on the rotor are quantified from the measured raw Hall sensor signals as

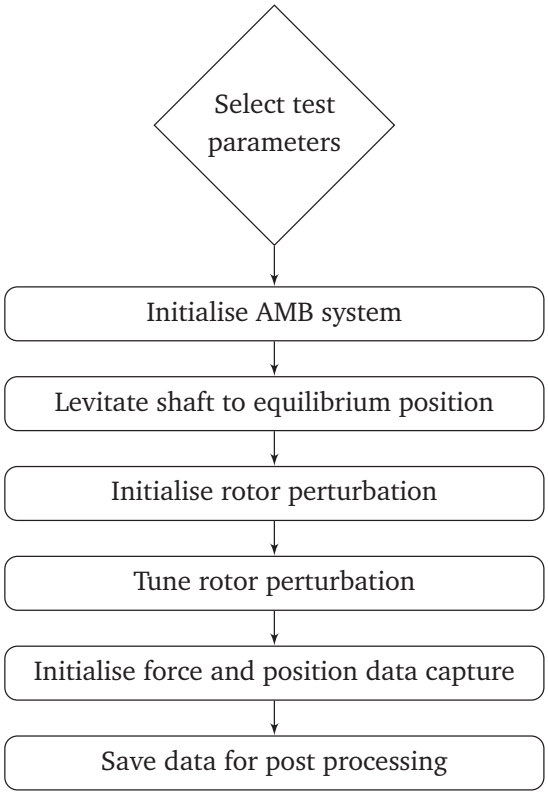

Figure 4.12: Pseudo flow chart outlining the experimental procedure for the dynamic validation tests.

described in section 4.2. Subsequently the displacement time series of the centre of the rotor is determined by averaging the position data from each AMB as

$$x_c = (x_\mathrm{A} + x_\mathrm{B})/2, \qquad y_c = (y_\mathrm{A} + y_\mathrm{B})/2$$

in which x_c and y_c denotes the two DOFs of the rotor mass centre described in the global reference frame and x_A, x_B, y_A, and y_B denotes the x and y -directional displacements measured at AMB A and AMB B, respectively. Averaging the displacements in the AMBs is allowed as the motion of the shaft is purely translational and equal in both AMBs as exemplified in Fig. 4.11(b). Additionally, averaging greatly simplifies further treatment of the experimental data, as the motion of the rotor can now be described by two DOFs, namely x_c and y_c. It is noted that x_A, x_B, y_A, y_B, x_c and y_c as well as the forces quantified using the Hall sensor system $F_{Hall,x}$ and $F_{Hall,y}$ are all data vectors. However, for simplicity they are treated and presented here as time dependent scalars, while the explicit time argument is dropped to further simplify notation.

Theoretical sine functions are fitted to the experimentally quantified displacement and force data and the sinusoidal functions are on the following form

$$\xi_j = A_j \sin \omega t + \phi_j \quad , \quad j = \{1..4\} \tag{4.15}$$

in which A_j is the fitted amplitude, ω is the perturbation frequency, ϕ_j is the phase and j is an index used to denote the different time series in the dataset as follows: $\xi_1 = x_c$, $\xi_2 = y_c$, $\xi_3 = F_{Hall,x}$, $\xi_4 = F_{Hall,y}$, where F_x and F_y is the x and y -directional

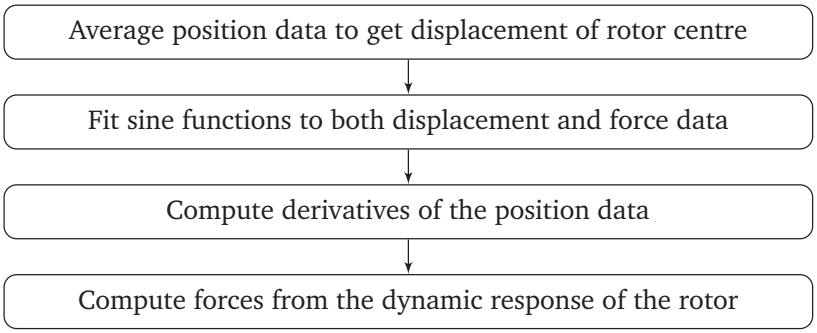

Figure 4.13: Pseudo flow chart outlining the post processing procedure for the experimental data acquired during the dynamic validation experiments.

force components measured in the global reference frame. Time series data fitting is motivated by the purely single frequency sinusoidal form of the raw data and performed in order to remove noise and ease further post processing, thus only retaining essential information from the data. A similar result would be obtained by averaging over blocks of data. Representative examples of experimental data with appertaining fits can be found in Appendix F. Estimating the forces acting on the rotor based on the dynamic response to an external perturbation requires that the acceleration of the rotor is determined. Additionally, as discussed later in section 4.5.2 estimating the velocity is necessary for determining seal damping coefficients, and consequently the procedure of obtaining the velocity is included here for completeness. The first and second order time derivatives of the displacements which attain the harmonic form presented in Eq. (4.15) can be determined analytically as

$$\frac{\mathrm{d}\xi_j}{\mathrm{d}t} = \omega A_j \cos\omega t + \phi_j \quad , \quad j = \{1,2\} \tag{4.16}$$

$$\frac{\mathrm{d}^2\xi_j}{\mathrm{d}t^2} = -\omega^2 A_j \sin\omega t + \phi_j \quad , \quad j = \{1,2\} \tag{4.17}$$

From the expressions introduced in Eq. (4.16) and Eq. (4.17) it is straight forward to compute the velocity and acceleration of the rotor centre of mass. Computing the velocity and acceleration from analytical expressions altogether avoids noise amplification commonly encountered when performing numerical differentiation based on conventional finite-difference schemes of non-exact discreet data [107–109].

During validation tests the imposed AMB forces result in a periodic motion of the rotor, and for each point on the path traced out by the rotor the forces acting on the rotor must fulfil the following vectorial equilibrium requirement

$$\sum \mathbf{F} = \mathbf{F}_{AMB} + \mathbf{F}_C + \mathbf{F}_I = \mathbf{0} \tag{4.18}$$

in which $\mathbf{F}_{AMB}$ is the AMB force, $\mathbf{F}_C$ represents the coupling forces and $\mathbf{F}_C$ denotes the rotor inertia forces. It is emphasised that no seal forces are present during the validation study. Furthermore, as a direct consequence of the calibration procedure presented in section 4.2.1, the Hall sensor system quantifies forces externally applied to the rotor, such that the forces determined on the basis of the Hall sensor measurements are in

the direction of the applied load. This can be stated as

$$\mathbf{F}_{Hall} = \mathbf{F}_{ext} \tag{4.19}$$

in which $\mathbf{F}_{Hall}$ is the force vector quantified using the Hall sensor system, and $\mathbf{F}_{ext}$ is a vector containing the components of an arbitrary externally applied force. Here the externally applied force is the AMB force such that Eq. (4.19) yields $\mathbf{F}_{Hall} = \mathbf{F}_{AMB}$, which enables restating Eq. (4.18) as

$$\mathbf{F}_{Hall} = -\mathbf{F}_C - \mathbf{F}_I \tag{4.20}$$

The right hand side of Eq. (4.20) presents an opportunity to quantify the forces acting on the rotor through its dynamic response. This can be realised by expanding Eq. (4.20) to yield

$$\mathbf{F}_{Hall} = \begin{Bmatrix} F_{Hall,x} \\ F_{Hall,y} \end{Bmatrix} = \begin{bmatrix} k_{C,x} & 0 \\ 0 & k_{C,x} \end{bmatrix} \begin{Bmatrix} x_c \\ y_c \end{Bmatrix} - \begin{bmatrix} m & 0 \\ 0 & m \end{bmatrix} \begin{Bmatrix} \ddot{x}_c \\ \ddot{y}_c \end{Bmatrix} \tag{4.21}$$

Consequently, if the coupling stiffness $\{k_{C,x}, k_{C,y}\}$, the rotor mass m, and the rotor displacements $\{x, y\}$ and accelerations $\{\ddot{x}, \ddot{y}\}$ are known, then the forces acting on the rotor subjected to an arbitrary excitation pattern can be determined as

$$\mathbf{F}_{calc} = \begin{Bmatrix} F_{calc,x} \\ F_{calc,y} \end{Bmatrix} = \begin{bmatrix} k_{C,x} & 0 \\ 0 & k_{C,x} \end{bmatrix} \begin{Bmatrix} x_c \\ y_c \end{Bmatrix} - \begin{bmatrix} m & 0 \\ 0 & m \end{bmatrix} \begin{Bmatrix} \ddot{x}_c \\ \ddot{y}_c \end{Bmatrix} \tag{4.22}$$

in which the rotor mass is known and the coupling stiffness $k_{C,x}, k_{C,y}$ is obtained experimentally in situ using the Hall sensor system. The coupling stiffness identification procedure and results are presented in appendix E. The displacements x_c, y_c are given by Eq. (4.15) and the accelerations $\ddot{x}_c, \ddot{y}_c$ are determined employing Eq. (4.17).

4.4.3 Uncertainty Analysis

The uncertainty on the force estimated by the Hall sensor system was addressed in section 4.2.3, however here it is relevant to quantify the uncertainty appended to the force estimated from the dynamic response of the rotor. The general methodology outlined in section 4.2.3 is applied again here. To simplify the analysis, the force determined based on the dynamic response of the rotor presented in Eq. (4.22) is restated here in an equivalent generic scalar form as

$$F_{calc} = k_c x - m\ddot{x} \tag{4.23}$$

Employing Eq. (4.7) from section 4.2.3 the total uncertainty affecting F_{calc} can be estimated by

$$\begin{aligned} u_{F_{calc}} &= \left[\left(\frac{\partial F_{calc}}{\partial k_c} u_{k_c} \right)^2 + \left(\frac{\partial F_{calc}}{\partial x} u_x \right)^2 + \left(\frac{\partial F_{calc}}{\partial m} u_m \right)^2 + \left(\frac{\partial F_{calc}}{\partial \ddot{x}} u_{\ddot{x}} \right)^2 \right]^{1/2} \\ &= \left[\left(x u_{k_c} \right)^2 + \left(k_c u_x \right)^2 + \left(-\ddot{x} u_m \right)^2 + \left(-m u_{\ddot{x}} \right)^2 \right]^{1/2} \end{aligned} \tag{4.24}$$

The individual errors are defined below

- **Coupling stiffness error** The error on the identified coupling stiffness u_{k_c} is estimated to be within 5 % of the maximum nominal stiffness component estimated in appendix E, thus

$$u_{k_c} = 0.05 k_{c,x}$$

  It is noted that the identification of the coupling stiffness is affected by the error on the force estimated by the Hall sensor system. However, for simplicity the above defined error is assumed appropriate and representative. The error is fixed.

- **Rotor position error** The fixed error u_x on the measured rotor position is obtained from the position sensor data sheet and is given as $u_x = 2.5\,\mu$m. As the displacement signals are always fitted by harmonic functions, the random error for the measurement system can be neglected. Furthermore, the fitting error is considered small compared to the fixed error provided by the sensor manufacturer and therefore neglected.

- **Rotor mass estimation error** The fixed error u_m is provided by the manufacturer of the scale used to measure the rotor mass. The error on u_m is within 0.1 kg.

- **Acceleration estimation error** The acceleration data is derived from rotor displacement measurements and here assumed to have an appended error of 2 % of the maximum acceleration value observed for a given test. For rotor perturbation with a single frequency the error is considered fixed.

4.4.4 Test Results and Discussion

The results from the dynamical validation of the Hall sensor system performance are presented here. Fig. 4.14 shows a plot of the maximum force acting on the rotor as measured by the Hall sensor system and additionally as determined using Eq. (4.22), as a function of the perturbation frequency. Both Fig. 4.14(a) and Fig. 4.14(b) includes uncertainty estimates determined as described in section 4.2.3 for F_{Hall} and 4.4.3 for F_{calc}, respectively. Very good agreement between the two methods is found for both perturbation directions, over the entire frequency range included in the study. At $\omega = 0$, the rotor is statically displaced 10 μm and the force exerted by the AMBs on the rotor is identical in magnitude to the force from the coupling F_c. As ω is increased the inertia forces rapidly dominates the combined force on the rotor. As the perturbation displacement is kept constant throughout the frequency range, the inertia force is expected to increase proportionally to ω^2. This second order tendency is clearly seen in Fig. 4.14, and is captured well by both force quantification approaches.

The difference between the two force estimation methods can be assessed using the MAE approach introduced in section 4.2.3, where it is assumed that the force quantified using the dynamic response is the true estimate. To visualise the differences between the two force estimation methods, the local MAE in percentage determined for each frequency step, respectively, is plotted in Fig. 4.15. Fig. 4.15 includes a plot of the average of the local MAEs and the findings are summarised in Table 4.5. Table 4.5 shows that the average difference in percent between the two methods is below 1 % for both direction, and a maximum local deviation of 5 % is found in the y-direction for

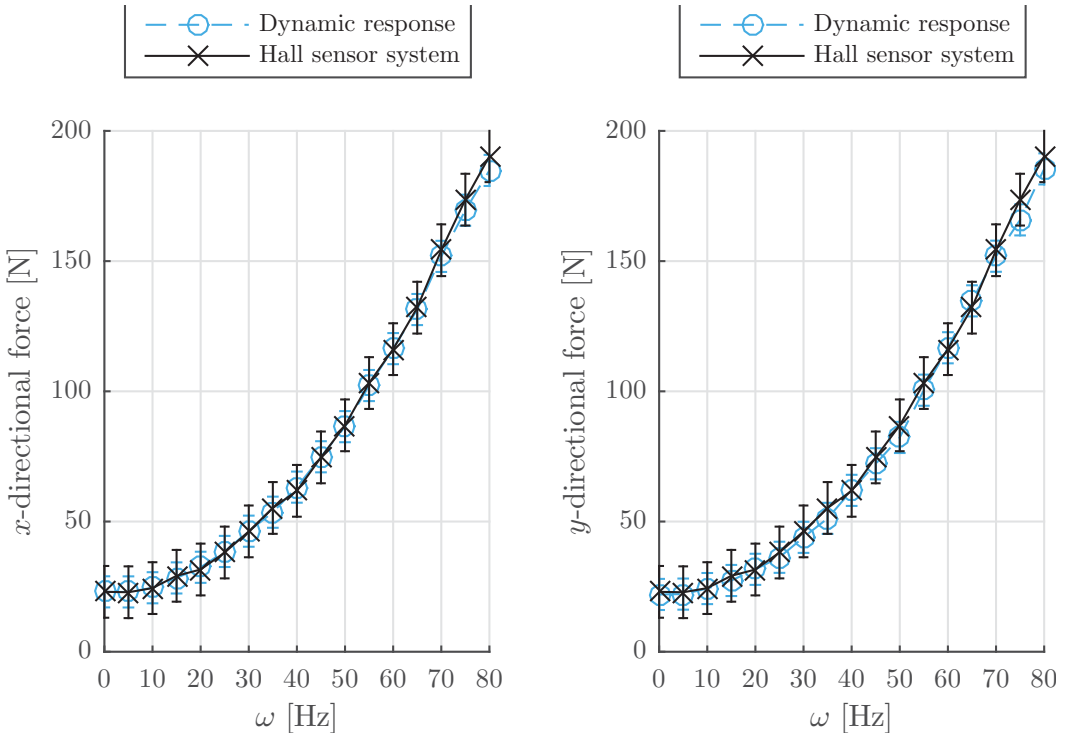

(a) x-directional forces as a function of perturbation frequency.

(b) y-directional forces as a function of perturbation frequency.

Figure 4.14: Comparison of dynamic forces quantified using the Hall sensor system and estimated from the dynamic response of the rotor. The plotted data reflects maximum amplitude values of the forces for a given frequency.

$\omega = 30$ Hz as seen in Fig. 4.15(b).

The goal here is primarily to validate the performance of the Hall sensor system, i.e. to ensure that the force quantified using the Hall sensor system measures the force correctly in applications where dynamic forces are encountered. The term validation implies that the force obtained through the Hall sensor system is compared to a true benchmark reference, i.e. a reference for which the force is known within specified and minimal uncertainty bounds. Here the benchmark reference is the force determined based on the dynamic response of the rotor. As can be seen in Fig. 4.14, the uncertainties on $F_{calc,x}$ and $F_{calc,y}$ are indeed lower than the uncertainties on the force estimated using the Hall sensor system. However, the good correspondence between the results of the two force estimation methodologies can also be considered as mutually validating both approaches, providing important confidence in the performance of the entire rotor-AMB system.

4.5 Single Phase Seal Results

The following sections outline the main experimental methods and results for the introductory investigation of the test seals. The results presented here are analysed with the objective of assessing if the test facility fulfils the general functionality requirements

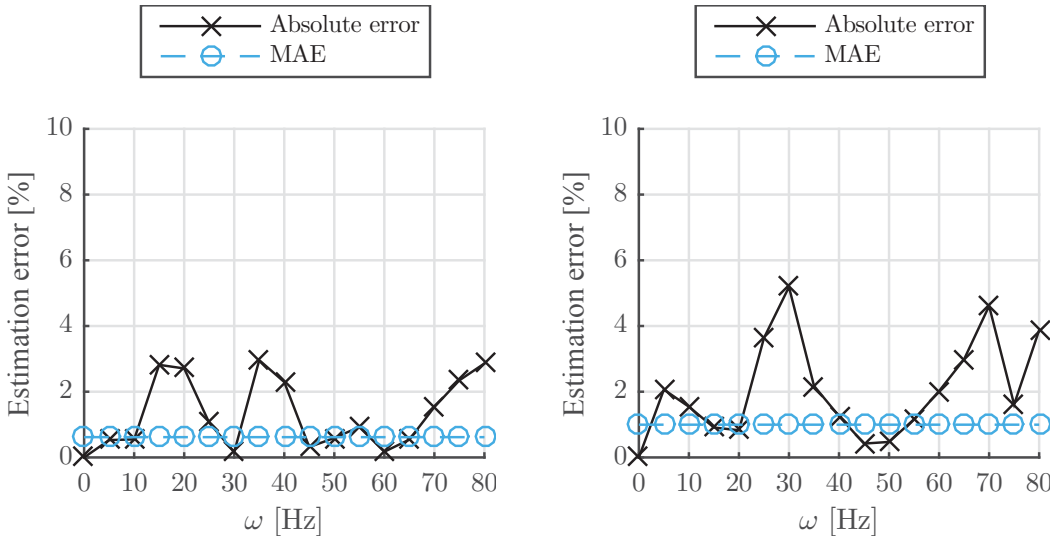

(a) Absolute estimation error in % for the x-directional forces as a function of perturbation frequency.

(b) Absolute estimation error in % for the y-directional forces as a function of perturbation frequency.

Figure 4.15: Estimation errors for the dynamic validation results.

Table 4.5: Dynamic validation MAE. The presented data is an average of the local MAEs for each frequency in the test envelope.

Force direction	MAE [N]	MAE [%]
F_x	1.2	0.62
F_y	1.9	0.98

stated in chapter 2, and as such is suited for a future full scale seal testing program. For the initial test campaign single phase air flow is used exclusively, as the multiphase functionality of the flow loop has not been realised at the conclusion of this PhD project.

4.5.1 Test Methodology

The seals testing procedure presented here is relatively simple in nature and is conducted with the rotor at standstill. The general methodology employed in the test campaign conceptually mirrors the approach used in the IPM method described in [P1], in which the seal flow is perturbed by moving the rotor in a predefined pattern while capturing information of the rotor position and the force acting on the rotor. However, differences between the numerical and experimental efforts exist. In the CFD simulations the rotor position follows a predefined sinusoidal pattern, but in the experiments the rotor is moved through enforcing a perturbation on the control currents of the AMB actuators, as described in section 4.4.1. An overview of the test procedure is provided in the flowchart presented in Fig. 4.16. For the purpose of identifying seal coefficients it is necessary to obtain data for perturbations in at least two directions. This entails that the experiment outlined in Fig. 4.16 is repeated for current perturbations resulting in rotor displacements in both the x and y -direction. There are multiple test parameters

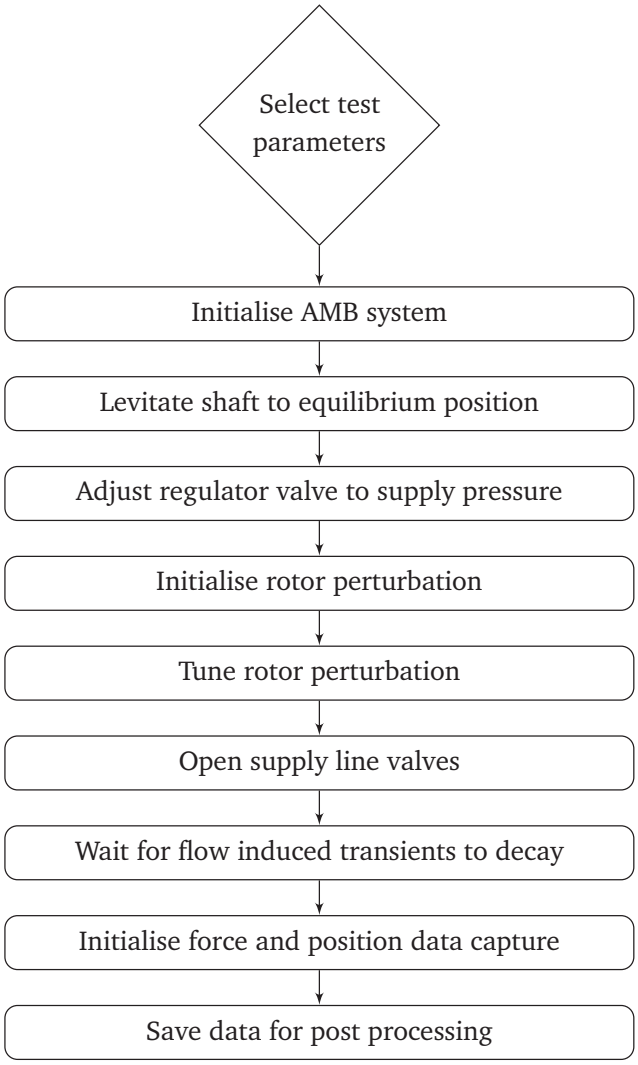

Figure 4.16: Pseudo flow charts outlining the experimental procedure for the initial seal tests.

to be chosen before initialising a test. These are listed below:

- Flow loop related parameters: Supply pressure and number of SHA inlets used. The flow supply pressure is throughout the test presented in this section chosen to yield an inlet pressure of 2.5 bar, i.e. in the low end of the available supply pressures. The SHA outlets are configured for zero back pressure, entailing that the flow exits to atmospheric conditions.

- Operational parameters for the AMB system: Bias current, perturbation frequency, direction of perturbation, and nominal rotor position. All experiments presented here are performed with the rotor centred relative to the SHA and with a bias current of 5 A. Two distinct perturbation frequencies are included in the study: $\omega = 5\,[\mathrm{Hz}]$ and $\omega = 10\,[\mathrm{Hz}]$.

4.5.2 Post Processing of the Experimental Data

Post processing the experimental seal data follows the procedure outlined in section 4.4.2. However, the force data quantified using the Hall sensor system now contains the force acting on the rotor from the perturbation of the seal flow. This can be described by expanding the imposed equilibrium condition presented in Eq. (4.18) of section 4.4.2 as follows

$$\sum \mathbf{F} = \mathbf{F}_{AMB} + \mathbf{F}_C + \mathbf{F}_I + \mathbf{F}_S = \mathbf{0} \tag{4.25}$$

in which $\mathbf{F}_S$ denotes the forces from the perturbed seal flow. Applying similar considerations that yielded Eq. (4.20) in section 4.4.2 for the case where seal forces are present produces

$$\mathbf{F}_{Hall} = -\mathbf{F}_C - \mathbf{F}_I - \mathbf{F}_S \tag{4.26}$$

For the purpose of identifying the rotordynamic seal coefficients the seal forces need to be isolated. This entails subtracting the force contribution from the flexible coupling $\mathbf{F}_C$ and the rotor inertia $\mathbf{F}_I$ from the force quantified using the Hall sensor system. As described in section 4.4.2 the combined coupling and inertia forces can be determined from the dynamic response of the rotor as

$$\mathbf{F}_{calc} = \begin{Bmatrix} F_{calc,x} \\ F_{calc,y} \end{Bmatrix} = \begin{bmatrix} k_{C,x} & 0 \\ 0 & k_{C,x} \end{bmatrix} \begin{Bmatrix} x_c \\ y_c \end{Bmatrix} - \begin{bmatrix} m & 0 \\ 0 & m \end{bmatrix} \begin{Bmatrix} \ddot{x}_c \\ \ddot{y}_c \end{Bmatrix}$$

The seal forces can then be determined as

$$\mathbf{F}_{Hall} - \mathbf{F}_{calc} = -\mathbf{F}_S$$

The ultimate goal of the seal test campaign is to experimentally determine the rotordynamic coefficients of the seal reaction force model restated below for completeness

$$-\mathbf{F}_S = \begin{bmatrix} K_{xx}(\omega) & -K_{xy}(\omega) \\ K_{yx}(\omega) & K_{yy}(\omega) \end{bmatrix} \begin{Bmatrix} x_c \\ y_c \end{Bmatrix} + \begin{bmatrix} C_{xx}(\omega) & -C_{xy}(\omega) \\ C_{yx}(\omega) & C_{yy}(\omega) \end{bmatrix} \begin{Bmatrix} \dot{x}_c \\ \dot{y}_c \end{Bmatrix} \tag{4.27}$$

The time domain identification method used for extracting the stiffness and damping coefficients requires that the velocity of the rotor is determined. This is done following the approach presented in Eq. (4.16) of section 4.4.2. For identification purposes it is convenient to re-cast (4.27) into the following form

$$\begin{bmatrix} \Delta x_c & \Delta y_c & 0 & 0 & \Delta \dot{x}_c & \Delta \dot{y}_c & 0 & 0 \\ 0 & 0 & \Delta x_c & \Delta y_c & 0 & 0 & \Delta \dot{x}_c & \Delta \dot{y}_c \end{bmatrix} \begin{Bmatrix} K_{xx} \\ K_{xy} \\ K_{yx} \\ K_{yy} \\ C_{xx} \\ C_{xy} \\ C_{yx} \\ C_{yy} \end{Bmatrix} = \begin{Bmatrix} \Delta F_{S,x} \\ \Delta F_{S,y} \end{Bmatrix} \tag{4.28}$$

in which $\Delta F_{S,x}$ and $\Delta F_{S,y}$ denotes the x and y components of the seal force vector, respectively. As indicated only variations in the displacements, velocities and forces are

considered. It is important to note that all coefficients in this formulation of Eq. (4.27) are assumed positive for identification purposes. Eq. (4.28) is required to be valid for all n samples in the test data envelope, which enables Eq. (4.28) to be expanded to yield

$$\underbrace{\begin{bmatrix} \Delta x_{c,1} & \Delta y_{c,1} & 0 & 0 & \Delta \dot{x}_{c,1} & \Delta \dot{y}_{c,1} & 0 & 0 \\ 0 & 0 & \Delta x_{c,1} & \Delta y_{c,1} & 0 & 0 & \Delta \dot{x}_{c,1} & \Delta \dot{y}_{c,1} \\ \Delta x_{c,2} & \Delta y_{c,2} & 0 & 0 & \Delta \dot{x}_{c,2} & \Delta \dot{y}_{c,2} & 0 & 0 \\ 0 & 0 & \Delta x_{c,2} & \Delta y_{c,2} & 0 & 0 & \Delta \dot{x}_{c,2} & \Delta \dot{y}_{c,2} \\ \vdots & \vdots & \vdots & \vdots & \vdots & \vdots & \vdots & \vdots \\ \Delta x_{c,n} & \Delta y_{c,n} & 0 & 0 & \Delta \dot{x}_{c,n} & \Delta \dot{y}_{c,n} & 0 & 0 \\ 0 & 0 & \Delta x_{c,n} & \Delta y_{c,n} & 0 & 0 & \Delta \dot{x}_{c,n} & \Delta \dot{y}_{c,n} \end{bmatrix}}_{\mathbf{A}} \underbrace{\begin{Bmatrix} K_{xx} \\ K_{xy} \\ K_{yx} \\ K_{yy} \\ C_{xx} \\ C_{xy} \\ C_{yx} \\ C_{yy} \end{Bmatrix}}_{\mathbf{x}} = \underbrace{\begin{Bmatrix} \Delta F_{S,x,1} \\ \Delta F_{S,y,1} \\ \Delta F_{S,x,2} \\ \Delta F_{S,y,2} \\ \vdots \\ \Delta F_{S,x,n} \\ \Delta F_{S,y,n} \end{Bmatrix}}_{\mathbf{b}} \tag{4.29}$$

As indicated Eq. (4.29) attains the form $\mathbf{Ax} = \mathbf{b}$, and the rotordynamic coefficients contained in the vector $\mathbf{x}$ are readily approximated using a Least Squares scheme. To obtain a unique solution for the rotordynamic coefficients the matrix $\mathbf{A}$ in Eq. (4.29) must be of sufficient rank. This entails that $\mathbf{A}$ and $\mathbf{b}$ must contain data from experiments in which the rotor is perturbed in both the x and the y -direction, respectively. Additionally, it is noted that as the raw experimental data has been post processed by fitting theoretical sine functions to the data, all available information is contained in one period of the respective data vectors.

4.5.3 Test Results and Discussion

The experimentally obtained rotor displacement patterns and resulting seal forces are visualised for a perturbation frequency of $\omega = 5$ Hz in the $x-y$ plots of Fig. 4.17 and in the time series plot of Fig. 4.18. Fig. 4.17(a) depicts the displacement and force for a perturbation in the x-direction, while Fig. 4.17(b) depicts the displacement and force for a perturbation in the y-direction. For the data presented here an inlet cavity pressure of 2.5 bar is imposed, resulting in a pressure drop over the seals of $\Delta p = 2.5$ bar. Fig. 4.17(a) shows that when air is supplied to the SHA, the rotor displacements shifts from being completely horizontal before air is supplied, to a displacement pattern that has an inclined offset from the horizontal axis. A similar tendency can be seen for the vertical perturbation in Fig. 4.17(b). This skewness in the displacement patterns results from the high level of pre-swirl generated by the tangential inlet flow direction of the SHA, see Fig. 2.25 in chapter 2. The fluid forces impose a shift in the dominating displacement direction of the rotor and this strong cross-coupling effect also dominates the forces acting on the rotor. The absolute displacement amplitudes as measured in the direction of the resulting displacements are low, approximately 18 μm, which constitutes 4.5 % of the test seal clearance.

From the time series of Fig. 4.18 the directional correlation between the rotor displacement and the resulting force acting on the rotor can be elucidated for both perturbation directions. To ease interpretation, the information has been included on Fig. 4.18. In Fig. 4.18 the position point marked with an "a" generates a resulting force in the direc-

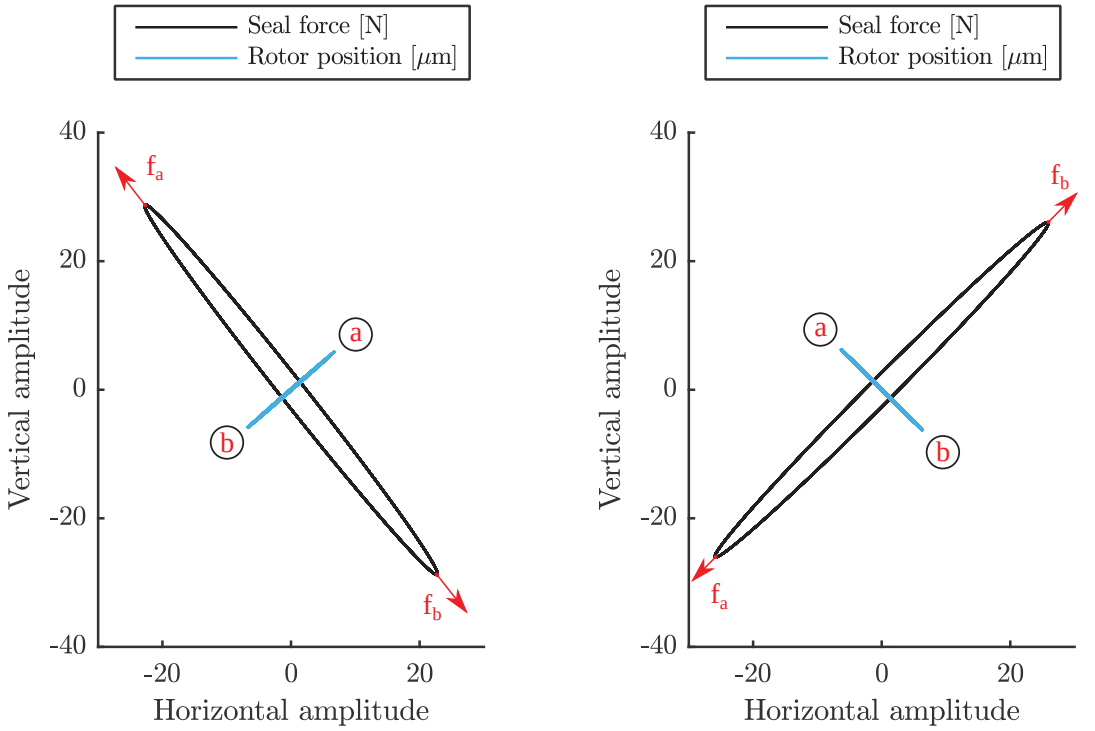

(a) x-directional current perturbation.

(b) y-directional current perturbation.

Figure 4.17: Seal rotor displacements and forces for a perturbation frequency of $\omega = 5$ Hz and an inlet cavity pressure of 2.5 bar.

tion indicated "f_a" and likewise for the position point "b". It is seen that the fluid force generated by displacing the rotor is almost completely perpendicular to the direction of the displacements, with very small force components in the direction of the rotor displacement.

The stiffness and damping coefficients are determined as described in section 4.5.2. The resulting coefficients are presented in Fig. 4.19 for a centred rotor at standstill. It is recalled that the SHA assembly contains two smooth annular test seals, why the resulting coefficients have to be divided by two to get the coefficients for a single seal. Results are presented for two different perturbation frequencies for an inlet cavity pressure of 2.5 bar.

As expected from the data visualised in Fig. 4.17 and Fig. 4.18, the direct stiffness coefficients are an order of magnitude smaller than the cross-coupling stiffness as seen in Fig. 4.19(a). Additionally, the cross-coupling stiffness coefficients K_{xy} and K_{yx} are close to identical in magnitude but with opposite signs, thus approximately obeying $K_{xy} = -K_{yx}$. The direct stiffness is numerically small but positive, which is attributed to the Lomakin effect [110] which generates restoring forces due to circumferential variations in the axial pressure drop across the seal, [5]. Minimal frequency dependence of the stiffness coefficients is seen when comparing results for the 5 Hz and the 10 Hz

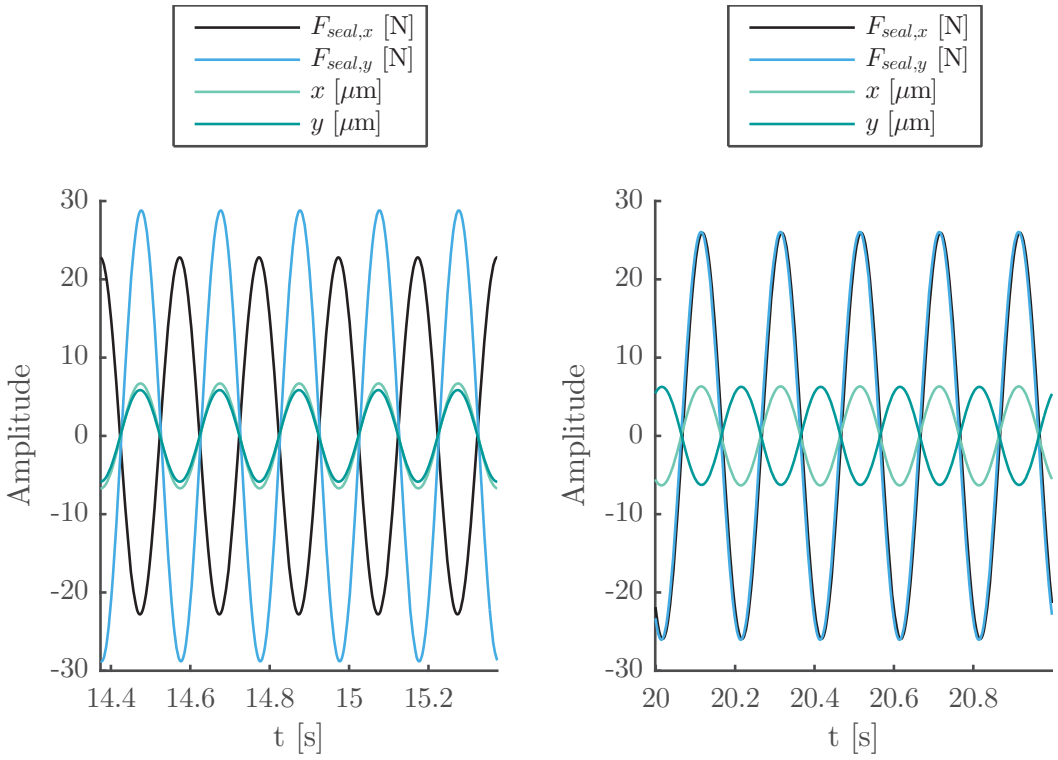

(a) x-directional perturbation.

(b) y-directional perturbation.

Figure 4.18: Time series plot of rotor displacements and forces during seal testing for a perturbation frequency of $\omega = 5$ Hz and an inlet cavity pressure of 2.5 bar.

case, which is in line with results reported in the literature [5]. The damping coefficients are presented in Fig. 4.19(b) from which it is seen that they are all relatively low in magnitude. The direct damping coefficients C_{xx} and C_{yy} are negative and close to equal with their numerical value being significantly higher than the cross-coupling damping coefficients C_{xy} and C_{yx}. The cross-coupling damping coefficients follow the tendencies of the cross-coupling stiffness coefficients where $C_{xy} = -C_{yx}$ is a good approximation for both the 5 Hz and the 10 Hz case.

It is well documented that high pre-swirl can have an adverse impact on the stability margins of rotating machines [3, 47, 111, 112] which originally motivated the incorporation of swirl brakes in the design of rotating machines. Under certain conditions pre-swirl reduces the effective damping below zero, thus generating destabilising forces acting on the rotor. The effective damping is given as the sum of the direct damping coefficient and the cross coupling stiffness, for skew symmetric cross coupling stiffness coefficients $\left(K_{xy} = -K_{yx}\right)$, divided by the excitation frequency, [5]. The effective damping captures information of the direction and magnitude of the forces acting normal to the displacement of the rotor, and if these become large enough, so that they exceed the stabilising restoring forces of the overall rotordynamic system, the otherwise stable rotor equilibrium becomes unstable. Consequently, for the case investigated here where the pre-swirl is high, it is expected that the seal forces will, for certain operating conditions, induce instability of the rotor equilibrium position.

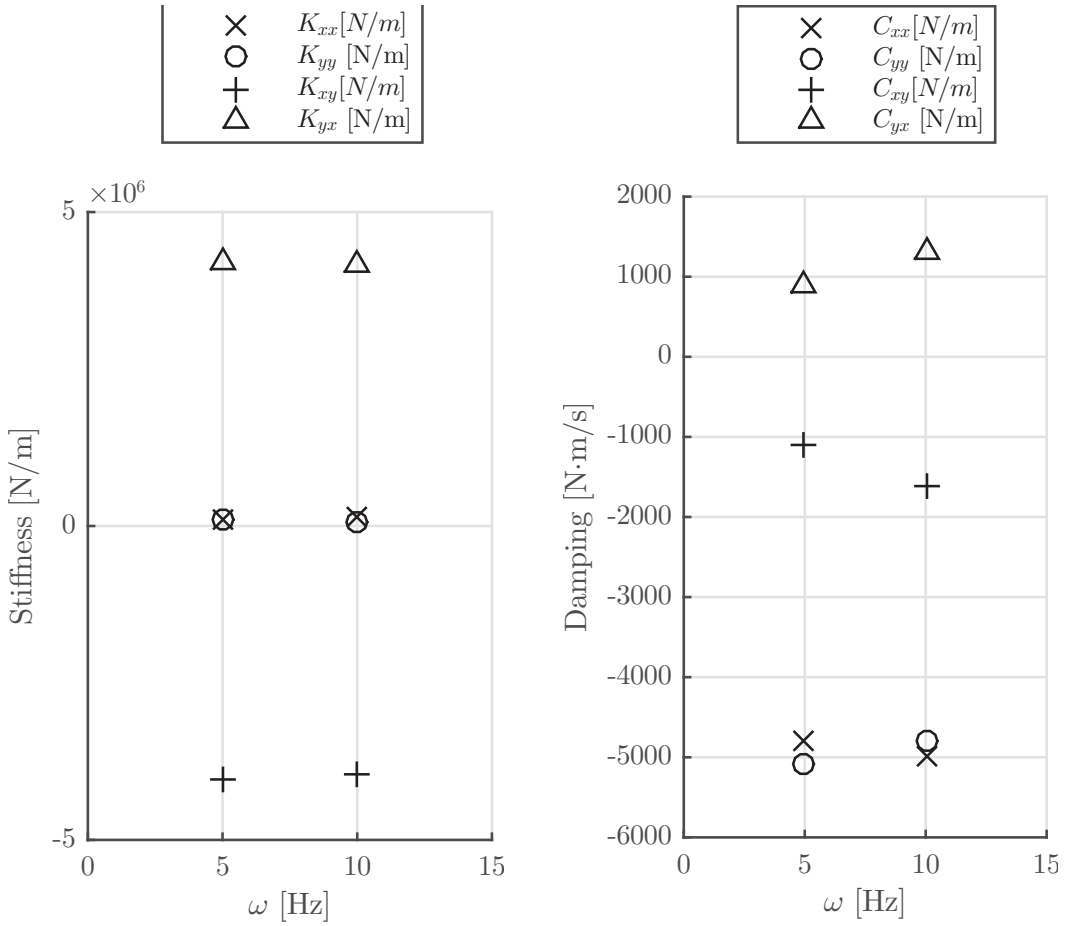

(a) Direct and cross coupled stiffness.

(b) Direct and cross coupled damping.

Figure 4.19: Rotordynamic coefficients for a 2.5 bar inlet cavity pressure and zero rotational velocity plotted as a function of the perturbation frequency.

4.6 Rotordynamic Instability

The fluid forces generated by the seal flow can, even at moderate supply pressures, render the static equilibrium of the rotor supported by the AMBs unstable. The relatively large anti-symmetric cross-coupling force components from the test seals combined with the negative direct damping coefficients requires balancing from the AMBs. By careful tuning of the force capacity of the AMBs, different stability regions can be experimentally realised. The purpose of the experiment documented in this section is to portray how the adaptability of the AMB based test facility can be used to investigate important rotordynamic phenomena, out of reach for non AMB based test vehicles.

4.6.1 Test Methodology

The test methodology is straight forward as illustrated in Fig. 4.20, and is based on varying the bias current for the test facility AMBs, thus changing their effective force capacity, for a constant supply pressure. This entails that the test outlined in Fig. 4.20 is repeated for three choices of bias currents, namely 4 A, 5 A and 6 A. In these tests

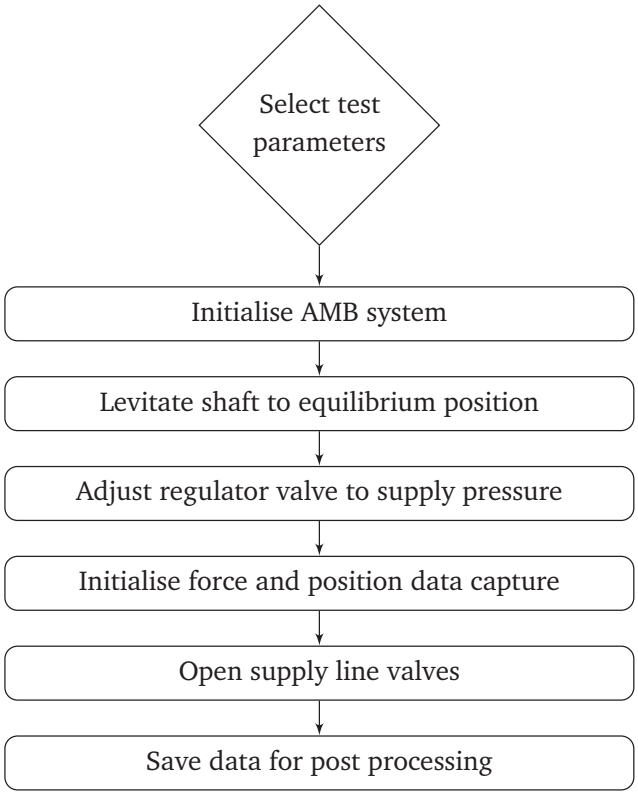

Figure 4.20: Pseudo flow charts outlining the experimental procedure for the initial seal tests.

the rotor is not perturbed, thus the AMBs are only employed to stabilise the rotor in the seal centre. Additionally, the PID controller gains remain constant throughout the three tests. The supply pressure for these tests is adjusted to yield a seal inlet cavity pressure of 3 bar, which is slightly higher than for the seal tests described in the previous section.

4.6.2 Post Processing

The post processing of the experimental data is straight forward and only requires determining the forces from the Hall sensor measurements and averaging the displacement signals to determine the rotor centre of mass displacements as described in section 4.4.2. The forces presented in the result section are the sum of all the forces acting on the system as measure by the Hall sensor system.

4.6.3 Test Results and Discussion

The test results are presented in Fig. 4.21 which includes $x-y$ plots of the rotor displacements and the force as well as time series plots of the rotor displacements for the three choices of bias currents. Varying the bias current changes the characteristics of the AMBs by modifying the force/current factor k_i and the force/displacement factor k_s, identified in Eq. (2.18) of section 2.3.1.3. The force/current factor k_i increases proportionally to the bias current i_0, while k_s increases proportionally to i_0^2. Increasing k_i effectively increases the force gain on the control current signal determined by the AMB controller. This entails that the damping forces provided through the PID feedback

control scheme are amplified as well, which has a significant impact on the results presented subsequently.

For a bias current of 6 A, the positive damping produced by the AMB controller compensates for the destabilising seal forces, resulting from the negative direct damping coefficients and the large skew symmetric cross-coupling stiffness identified in section 4.5.3. For a bias current of 6 A the rotor equilibrium is stable which is evident from the left most column of plots in Fig. 4.21 where the rotor displacement is driven towards zero and generally variation are closed to the inherent noise level of the position sensors. The measurements contain spikes in the force signals which cannot be contributed to noise contamination, coupling or inertia forces. These spikes are attributed to the AMBs working to compensate for the fluctuating unsteady flow forces.

The centre column of Fig. 4.21 shows results for a bias current of 5 A. The rotor equilibrium is in this case rendered marginally stable as the damping forces provided by the AMBs diminish by the decrease in bias current as compared to the 6 A case. As a consequence the rotor oscillates in both coordinates with small amplitudes at the natural frequency of the first rigid body mode of the system, creating the displacement and force orbits seen in the centre column of Fig. 4.21.

For a bias current of 4 A the effective damping forces produced by the AMBs does not balance the destabilising seal forces, and as the air supply lines are opened the rotor equilibrium becomes unstable. This is seen clearly in the data presented in the leftmost column of Fig. 4.21, where the rotor displacement and the force acting on the rotor spirals outwards.

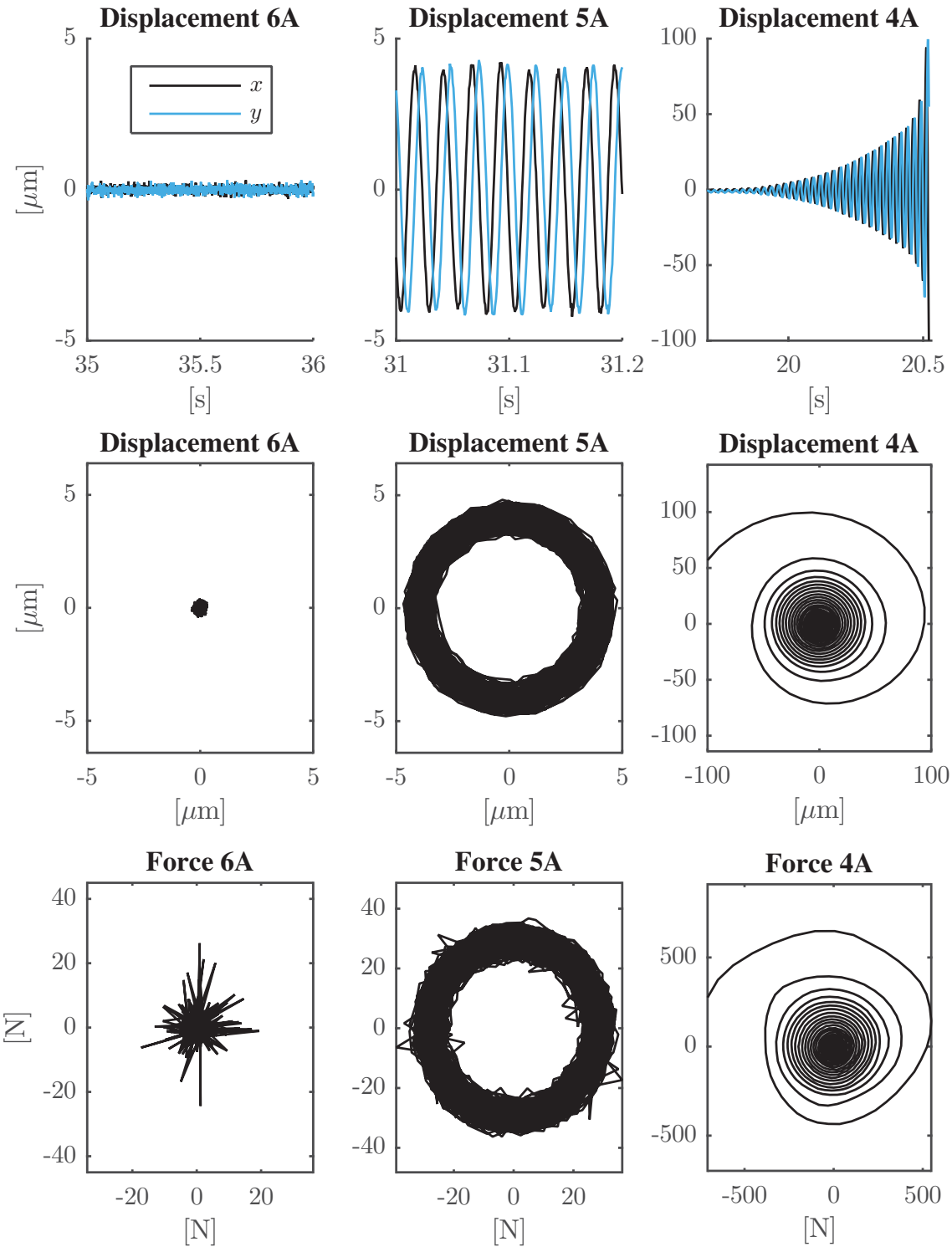

Figure 4.21: Results for the instability tests, conducted for a constant seal inlet cavity pressure of 3 bar for three choices of AMB bias currents without rotor perturbation. The figure includes $x-y$ plots of the rotor displacements and the force as well as time series plots of the rotor displacements.

Chapter 5

Conclusions

The pronounced lack of experimental data available for benchmarking predictive numerical tools for turbomachinery seals subjected to multiphase flow conditions imposes serious limitations on their usability. While this statement is universally applicable to the engineering sciences the importance of seals for overall rotordynamic performance of costly rotating machines merits a particularly strong effort directed towards experimental validation of multiphase seal models.

This thesis documents the efforts related to establishing an industrial scale test facility for investigating rotordynamic properties of seals subjected to both single phase and multiphase flow conditions. The title of the thesis includes the phrasing *towards identification of rotordynamic properties for seals in multiphase flow* which signifies that, while the majority of the necessary infrastructure for testing seals in multiphase flow is in place, test facility functionality has been assessed with single phase air flow and *no* multiphase seal experiments have been conducted within the scope of the presently documented PhD project.

The test facility constitutes the first AMB based rotordynamic system that allows full radial magnetic suspension of a rigid shaft at DTU. The global novelty of the test facility is attributed to the fact that both AMBs are instrumented with an *embedded* Hall sensor system allowing for precise measurement of radial rotordynamic forces. The research project documented here can be considered a frontrunner project for future ventures into experimentally quantifying rotordynamic properties of turbomachinery seals subjected to multiphase flow conditions. Generally speaking the test facility performs as intended and enables the seal flow perturbation, rotor displacement measurement, and force measurement functionality needed for future seal testing campaigns.

The important ability of the embedded Hall sensor system to quantify forces exerted by AMBs has received significant attention during the PhD study. The paper [P4] employed a test facility based on a four-pole MBE with an embedded Hall sensor system for investigating potential frequency dependence of the Hall sensor calibration coefficients, which was found to be non-existent in a range of 0 Hz to 200 Hz. Consequently, it

was concluded that a static calibration of embedded Hall sensors is sufficient even for dynamic force measurement applications. The same paper found force estimation precision improvements by using a linear force relation compared to the fundamental quadratic force relation. These improvements were *not* replicable for the seal test facility for which the quadratic force relation outperformed the linear version which consequently was abandoned. Finally, the paper [P4] investigated the Hall sensor system force estimation error as a function of rotor offset from a centred position. The results of the presented numerical study indicated that the force estimation error increases with the eccentricity. As a consequence the potential rotor eccentricity, or position, dependence of the Hall sensor coefficients was studied in the paper [P2] employing the seal test facility.

The controllable calibration facility allows determining calibration coefficients for multiple rotor positions in an automated procedure which was utilised in [P2] to quantify Hall sensor coefficients mapped over a grid of rotor positions. The study found only a minor degree of rotor position dependence for the range of AMB bias currents investigated which was confirmed by the results included in section 4.2.5 where the range of rotor positions was expanded. It was concluded that the force can be precisely estimated using Hall sensor calibration coefficients determined for a centric rotor position, as long as the rotor displacement does not exceed $\pm 50\,\mu$m in both the horizontal and vertical direction.

The ability of the Hall sensor system to precisely quantify forces exerted onto the rotor was investigated through both a static and dynamic validation procedure. Results from the static validation procedure were included in [P2] showing MAE below 1% of the maximum applied load in the validation experiments. Low MAE was reported for the full range of bias currents included in the study. The results reported for the dynamic validation study showed excellent agreement between the two compared methodologies for quantifying the dynamic force. Based on the results it was concluded that the Hall sensor system can be utilised for high precision dynamic force quantification.

The paper [P1] documents the application of a commercial CFD software package to identify rotordynamic properties for seals subjected to multiphase flow conditions. A generic seal geometry was utilised as the basis of the study to determine the applicability of the commercial CFD software to multiphase seal problems. It was found that the commercial CFD software could indeed be applied for the purpose of determining rotordynamc coefficients of seals in multiphase flow. Additionally, the study found a mild influence of low LVF and GVF values on the rotordynamic coefficients. For wet gas compression conditions (low LVF), increasing the LVF caused a general increase in direct stiffness and damping, as well as cross-coupling stiffness. For multiphase pumping conditions (low GVF) an increase in GVF entailed a decrease in direct damping, while the direct and cross-coupling stiffness revealed a more complex behaviour in the frequency domain.

The paper [P3] presents the application of a closed loop parameter identification scheme to the test facility AMBs. The paper documents the efforts directed towards validating the performance of the identification scheme by comparing $\mathbf{K}_i$ obtained using the identification scheme and through employing a static loading procedure enabled by the calibration facility. Good agreement between $\mathbf{K}_i$ obtained by the different methods

was found, and consequently it was concluded that the closed loop identification scheme works as intended.

5.1 Suggestions for Future Work

The test facility is to a large extent ready to be applied for multiphase seal testing, however some tasks still remain. The second iteration of the flow loop should be realised to accommodate a liquid phase fraction in the seal flow. At the time of concluding this thesis infrastructure consisting of water reservoir, motor and VSD, gearbox and pump have been acquired and awaits assembly. Additionally, the work done on the design of multiphase mixing functionality should be continued and the existing design suggestions for different mixing devices should be refined and ultimately matured for production.

To reach the full potential of the test facility additional work should be done on the AMB controller, and it is expected that more advanced control strategies will greatly improve the performance of the rotordynamic test bench. Along the same lines, the AMB power amplifiers should be replaced by a suitable alternative to avoid dynamic performance bottlenecks stemming from under-performing AMB amplifiers.

Additionally, it is recommended to perform a dynamic validation of the Hall sensor system performance considering a rotating rotor. This has been done by previous authors [65] and revealed only minor deterioration of the force estimation precision.

The work carried out on CFD simulations for seals in multiphase flow can be expanded. However, final evaluation and benchmarking of the CFD tools has to await multiphase test results, and is consequently considered to be of secondary importance.

References

[1] I. F. Santos and F. H. Russo, "Tilting-Pad Journal Bearings With Electronic Radial Oil Injection," *Journal of Tribology*, **120**(3), pp. 583–594, 1998, ISSN: 07424787.

[2] I. Santos and R. Nicoletti, "THD Analysis in Tilting-Pad Journal Bearings Using Multiple Orifice Hybrid Lubrication," *October*, **121**(October), pp. 892–900, 1999.

[3] D. Childs, *TURBOMACHINERY ROTORDYNAMICS: PHENOMENA, MODELING, AND ANALYSIS*. John Wiley & Sons, Inc., Hoboken, New Jersey, 1993.

[4] D. Childs and J. Vance, "Annular Gas Seals and Rotordynamics of Compressors and Turbines," *Proceedings of the Twenty-Sixth Turbomacinery Symposium*, 1997, pp. 201–220.

[5] J. M. Vance, F. Y. Zeidan, and B. Murphy, *MACHINERY VIBRATION AND ROTORDYNAMICS*. John Wiley & Sons, Inc., Hoboken, New Jersey, 2010, ISBN: 9780471462132.

[6] A. Picardo and D. W. Childs, "Rotordynamic Coefficients for a Tooth-on-Stator Labyrinth Seal at 70 Bar Supply Pressures: Measurements Versus Theory and Comparisons to a Hole-Pattern Stator Seal," *Journal of Engineering for Gas Turbines and Power*, **127**(4), pp. 843–855, 2005, ISSN: 07424795.

[7] T. Soulas and L. S. Andres, "A Bulk Flow Model for Off-Centered Honeycomb Gas Seals," *Journal of Engineering for Gas Turbines and Power*, **129**(1), pp. 185–194, 2007, ISSN: 07424795.

[8] J. K. Scharrer, "Theory Versus Experiment for the Rotordynamic Coefficients of Labyrinth Gas Seals: Part I—A Two Control Volume Model," *Proc. ASME 11th Biennial Conference on Mechanical Vibration and Noise, Rotating Machinery Dynamics Volume Two*, 1987, pp. 411–426.

[9] T. Iwatsubo, "Evaluation of Instability Forces of Labyrinth Seals in Turbines or Compressors," *Proc. Rotordynamic Instability Problems in High Performance Turbomachinery,NASA CP-2133, Texas A&M University*, 1980, pp. 139–167.

[10] K. T. Millsaps and M. Martinez-sanchez, "DYNAMIC FORCES FROM SINGLE GLAND LABYRINTH SEALS : Part 1 - IDEAL AND VISCOUS DECOMPOSITION," *Journal of Turbomachinery*, **116**(4), p. 686, 1994.

[11] J. J. Moore, "Three-Dimensional CFD Rotordynamic Analysis of Gas Labyrinth Seals," *Journal of Vibration and Acoustics*, **125**(4), pp. 427–433, 2003, ISSN: 07393717.

[12] T. Hirano, Z. Guo, and R. G. Kirk, "Application of Computational Fluid Dynamics Analysis for Rotating Machinery—Part II: Labyrinth Seal Analysis," *Journal of Engineering for Gas Turbines and Power*, **127**(4), pp. 820–826, 2005, ISSN: 07424795.

[13] R. Kirk, "Evaluation of Aerodynamic Instability Mechanisms for Centrifugal Compressors—Part II: Advanced Analysis," *ASME J. Vibr. Acoust.*, (110), pp. 207–212, 1988.

[14] O. Marquette, D. W. Childs, and S. G. Philips, "Theory Versus Experiments for Leakage and Rotordynamic Coefficients of Circumferetially- Grooved Liquid Annular Seals with L/D of 0.45," *Proceedings of the 1997 ASME Fluids Engineering Division Summer Meeting*, 1997, ASME Paper No. FED SM97–3333.

[15] D. W. Childs and J. K. Scharrer, "An Iwatsubo Based Solution for Labyrinth Seals: A Comparison to Experimental Results," *ASME J. Eng. Gas Turbines Power*, (108), pp. 325–331, 1986.

[16] O. R. Marquette, D. W. Childs, and L. S. Andres, "Eccentricity Effects on the Rotordynamic Coefficients of Plain Annular Seals: Theory Versus Experiment," (96), pp. 443–447, 1997.

[17] K. K. Nielsen, K. Jønck, and H. Underbakke, "Hole-Pattern and Honeycomb Seals Rotordynamic Forces: Validation of CFD Based Prediction Techniques," 2012.

[18] G. Vannini, M. Bertoner, K. K. Nielsen, R. Stronach, P. Iudiciani, and M. Bertoneri, "Experimental Results and CFD Simulations of Labyrinth and Pocket Damper Seals for Wet Gas Compression," *Journal of Engineering for Gas Turbines and Power*, **138**(May), pp. 052 501–1, 2016, ISSN: 0742-4795.

[19] M. M. Athevale, A. J. Przekwas, R. C. Hendricks, and A. Liang, "SCISEAL: A 3D CFD Code for Accurate Analysis of Fluid Flow and Forces in Seals," *Proceedings of the Advanced ETO Propulsion Conference*, NASA Marshall Space Flight Center, May, Huntsville, AL, 1994, pp. 337–345.

[20] J. J. Moore and A. B. Palazzolo, "CFD Comparison to 3D Laser Anemometer and Rotordynamic Force Measurements for Grooved Liquid Annular Seals," *ASME J. Tribol.*, **121**(2), pp. 307–314, 1999.

[21] N. Kim and D. L. Rhode, "A New CFD-Perturbation Model For The Rotordynamics of Incompressible Flow Seals," *ASME International Gas Turbine and Aeroengine Congress and Exposition*, 2000.

[22] R. Nordmann and F. J. Dietzen, *Finite Difference Analysis of Rotordynamic Seal Coefficients For An Eccentric Shaft Position*, 1988.

[23] D. L. Rhode, S. J. Hensel, and M. J. Guidry, "Labyrinth Seal Rotordynamic Forces Using a Three-Dimensional Navier-Stokes Code," *ASME J. Tribol.*, (114), pp. 683–689, 1992.

[24] L. T. Tam, A. J. Przekwas, A. Muszynska, R. C. Hendricks, M. J. Braun, and R. L. Mullen, "Numerical and Analytical Study of Fluid Dynamic Forces in Seals and Bearings," *ASME J. Vibr. Acoust.*, **110**, pp. 315–325, 1988.

[25] K. K. Nielsen, D. W. Childs, and C. M. Myllerup, "Experimental and Theoretical Comparison of Two Swirl Brake Designs," *Journal of Turbomachinery*, **123**(2), p. 353, 2001, ISSN: 0889504X.

[26] K. K. Nielsen, C. M. Myllerup, and R. A. Van den Braembussche, "Parametric Study of the Flow in Swirl Brakes by Means of a 3D Navier- Stokes Solver," *Transactions of the Third European Conference on Turbomachinery*, 1999, pp. 489–498.

[27] K. K. Nielsen, R. Van den Braembussche, and C. Myllerup, "Optimization of swirl brakes by means of a 3D Navier-Stokes solver," *The 1998 International Gas Turbine & Aeroengine Congress & Exhibition*, Stockholm, Sweden, 1998, p. 7.

[28] N. Wagner, K. Steff, R. Gausmann, and M. Schmidt, "Investigations on the Dynamic Coefficients of Impeller Eye Labyrinth Seals," *Proceedings of the Thirty-eighth Turbomacinery Symposium*, 2009.

[29] J. A. Kocur, J. C. Nicholas, and C. C. Lee, "Surveying Tilting Pad Journal Bearing and Gas Labyrinth Seal Coefficients and Their Effect on Rotor Stability," *Proceedings of the 36th Turbomachinery Symposium*, College Station, Texas, 2007, pp. 1–10.

[30] P. A. Beatty and W. F. Hughes, "Turbulent Two-Phase Flow in Annular Seals," *A S L E Transactions*, **30**(1), pp. 11–18, 1987, ISSN: 0569-8197.

[31] P. a. Beatty and W. F. Hughes, "Stratified Two-Phase Flow in Annular Seals," *Journal of Tribology*, **112**(April), p. 372, 1990, ISSN: 07424787.

[32] G. L. Arauz and L. San Andrés, "Analysis of Two-Phase Flow in Cryogenic Damper Seals— Part I: Theoretical Model," *Journal of Tribology*, **120**(2), p. 228, 1998, ISSN: 07424787.

[33] G. L. Arauz and L. S. Andres, "Analysis of Two-Phase Flow in Cryogenic Damper Seals—Part II: Model Validation and Predictions," *Journal of Tribology*, **120**(April), pp. 228–233, 1998.

[34] M. Arghir, Z. Abdelmalik, and P. Gérard PINEAU, "Rotordynamic Analysis of Textured Annular Seals With Multiphase (Bubbly) Flow," *Incas Bulletin*, **3**(3), pp. 3–13, 2011, ISSN: 20668201.

[35] L. S. Andrés, "Rotordynamic Force Coefficients of Bubbly Mixture Annular Pressure Seals," *Proceedings of ASME Turbo Expo 2011*, **60**, pp. 1–10, 2011.

[36] G. Vannini, M. Bertoneri, G. D. Vescovo, and M. Wilcox, "Centrifugal Compressor Rotordynamics in Wet Gas Conditions," *Proceedings of 43rd Turbomachinery Symposium, Huston, Texas*, 2014.

[37] T. Iwatsubo and T. Nishino, "An Experimental Study on the Static and Dynamic Characteristics of Pump Annular Seals," *7th Workshop on Rotordynamic Instability Problems in High Performance Turbomachinery*, Texas A&M University, College Station, Texas, May 10-12., 1993.

[38] L. S. Andrés, X. Lu, and Q. Liu, "Measurements Of Flowrate And Force Coefficients In A Short Length Annular Seal Supplied With A Liquid/Gas Mixture (Stationary Journal)," *Tribology Transactions*, **2004**(November), pp. 00–00, 2015, ISSN: 1040-2004.

[39] T. W. Dimond, P. N. Sheth, P. E. Allaire, and M. He, "Identification methods and test results for tilting pad and fixed geometry journal bearing dynamic coefficients - A review," *Shock and Vibration*, **16**(1), pp. 13–43, 2009, ISSN: 10709622.

[40] R. Tiwari, A. W. Lees, and M. I. Friswell, "Identification of Dynamic Bearing Parameters: A Review," *The Shock and Vibration Digest*, **36**(2), pp. 99–124, 2004, ISSN: 05831024.

[41] E. Storteig, "Dynamic characteristics and leakage performance of liquid annular seals in centrifugal pumps," PhD thesis, Norwegian University of Science and Technology, 1999.

[42] D. W. Childs, L. E. Rodriguez, V. Cullotta, A. Al-Ghasem, and M. Graviss, "Rotordynamic-Coefficients and Static (Equilibrium Loci and Leakage) Characteristics for Short, Laminar-Flow Annular Seals," *Journal of Tribology*, **128**(2), pp. 378–387, 2006, ISSN: 07424787.

[43] C. R. Carter, D. W. Childs, and L. T. Jordan, "Gt2008-50069 Measurements Versus Predictions for the Rotordynamic," *Asme & Gt*, pp. 1–11, 2008.

[44] A. M. Al-Ghasem and D. W. Childs, "Rotordynamic Coefficients Measurements Versus Predictions for a High-Speed Flexure-Pivot Tilting-Pad Bearing (Load-Between-Pad Configuration)," *Journal of Engineering for Gas Turbines and Power*, **128**(4), pp. 896–906, 2006, ISSN: 07424795.

[45] T. Dimond, A. Younan, and P. Allaire, "A review of tilting pad bearing theory," *International Journal of Rotating Machinery*, **2011**, 2011, ISSN: 1023621X.

[46] T. W. Dimond, A. A. Younan, and P. Allaire, "Comparison of Tilting-Pad Journal Bearing Dynamic Full Coefficient and Reduced Order Models Using Modal Analysis (GT2009-60269)," *Journal of Vibration and Acoustics*, **132**(5), p. 051 009, 2010, ISSN: 07393717.

[47] D. W. Childs and J. M. Vance, *Annular gas seals and rotordynamics of compressors and turbines*, 1997.

[48] Y.-S. Shin and D. W. Childs, "The Impact of Real Gas Properties on Predictions of Static and Rotordynamic Properties of the Annular Gas Seals for Injection Compressors," *Journal of Engineering for Gas Turbines and Power*, **130**(4), p. 042 504, 2008, ISSN: 07424795.

[49] J. W. Lund and K. K. Thomsen, "A CALCULATION METHOD AND DATA FOR THE DYNAMIC COEFFICIENTS OF OIL-LUBRICATED JOURNAL BEARINGS," *Topics in fluid film bearing and rotor bearing system design and optimization: Proc. ASME Design Engineering Conference*, S. Rohde, P. Allaire, and C. Maday, Eds., Chicago, 1978, pp. 1–28.

[50] K. Brockwell, D. Kleinbub, and W. Dmochowski, "Measurement and calculation of the dynamic operating characteristics of the five shoe, tilting pad journal bearing," *Tribology transactions*, 1990.

[51] W. Dmochowski and K. Brockwell, "Dynamic testing of the tilting pad journal bearing," *Tribology transactions*, 1995.

[52] R. TIWARI, A. W. LEES, and M. I. FRISWELL, "Identification of Speed-Dependent Bearing Parameters," *Journal of Sound and Vibration*, **254**(5), pp. 967–986, 2002, ISSN: 0022-460X.

[53] A. Delgado and L. San Andrés, "Nonlinear Identification of Mechanical Parameters in a Squeeze Film Damper With Integral Mechanical Seal," *Journal of Engineering for Gas Turbines and Power*, **131**(4), p. 042 504, 2009, ISSN: 07424795.

[54] B. H. Ertas, A. Delgado, and G. Vannini, "Rotordynamic Force Coefficients for Three Types of Annular Gas Seals with Inlet Preswirl and High Differential Pressure Ratio," *Proceedings of ASME Turbo Expo 2011: Power for Land, Sea and Air*, (518), pp. 1–12, 2011.

[55] J. Li, R. Aguilar, L. S. Andrés, and J. M. Vance, "Dynamic Force Coefficients of a Gas Damper Seal : Test Results and Predictions," *Journal of Tribology*, **122**(January), pp. 317–322, 2000.

[56] J. Glienicke, "Experimental Investigation of the Stiffness and Damping Coefficients of Turbine Bearings and Their Application to Instability Prediction," *Proceedings of the Institution of Mechanical Engineers, Conference Proceedings*, **181**(2), pp. 116–129, 1965, ISSN: 0367-8849.

[57] H. Ulbrich, "New Test Techniques Using Magnetic Bearings," *1st International Symposium on Magnetic Bearings*, pp. 281–288, 1988.

[58] J. D. Knight, Z. Xia, and E. B. McCaul, "Forces in Magnetic Journal Bearings : Nonlinear Computation and Experimental Measurement," *3rd International Symposium on Magnetic Bearings*, pp. 441–450, 1992.

[59] Z. S. Zutavern and D. W. Childs, "Fiber-Optic Strain Gauge Calibration and Dynamic Flexibility Transfer Function Identification in Magnetic Bearings," *Volume 4: Turbo Expo 2005*, pp. 757–762, 2005.

[60] S. G. Raymer and D. W. Childs, "Force Measurements in Magnetic Bearings Using Fiber Optic Strain Gauges," *ASME Turbo Expo 2001: Power for Land, Sea, and Air*, 2001.

[61] Z. S. Zutavern and D. W. Childs, "Identification of Rotordynamic Forces in a Flexible Rotor System Using Magnetic Bearings," *Journal of Engineering for Gas Turbines and Power*, **130**(2), p. 022 504, 2008, ISSN: 07424795.

[62] C. Gähler and P. Förch, "A Precise Magnetic Bearing Exciter for Rotordynamic Experiments," *4th International Symposium on Magnetic Bearings*, (August), pp. 193–200, 1994.

[63] C. Gähler, "Dynamic Testing and Control with Active Magnetic Bearings," (12718), p. 178, 1998.

[64] M. Aenis, E. Knopf, and R. Nordmann, "Active Magnetic Bearings for the Identification and Fault Diagnosis in Turbomachinery," *Mechatronics*, **12**, pp. 1011–1021, 2002.

[65] E. Knopf and R. Nordmann, "ACTIVE MAGNETIC BEARINGS FOR THE IDENTIFICATION OF DYNAMIC CHARACTERISTICS OF FLUID BEARINGS—CALIBRATION RESULTS," *Proceedings of the Fourth International Symposium on Magnetic Bearings*, 1994, pp. 52–61.

[66] K. Kjolhede and I. F. Santos, "Experimental Contribution to High-Precision Characterization of Magnetic Forces in Active Magnetic Bearings," *Journal of Engineering for Gas Turbines and Power*, **129**(2), p. 503, 2007, ISSN: 07424795.

[67] M. Kasarda, J. Marshall, and R. Prins, "Active magnetic bearing based force measurement using the multi-point technique," *Mechanics Research Communications*, **34**(1), pp. 44–53, Jan. 2007, ISSN: 00936413.

[68] P. Förch, C. Gähler, and R. Nordmann, "AMB System for Rotordynamic Experiments: Calibration Results and Control," *Fifth International Symposium on Magnetic Bearings*, Kanazawa, Japan, 1996, pp. 171–178.

[69] H. Bleuler, M. Cole, P. Keogh, R. Larsonneur, E. Maslen, Y. Okada, G. Schweitzer, and A. Traxler, *MAGNETIC BEARINGS THEORY, DESIGN, AND APPLICATION TO ROTATING MACHINERY*, S. G. and M. E., Eds. Dordrecht New York: Springer, 2009.

[70] J. M. Sorokes, T. A. Soulas, J. M. Koch, and J. L. G. R., "Full-Scale Aerodynamic and Rotordynamic Testing for Large Centrifugal Compressors," *Proceedings of the Thirty-eighth Turbomacinery Symposium*, (1998), 2009.

[71] K. Kwanka, "DYNAMIC COEFFICIENTS OF STEPPED LABYRINTH GAS SEALS," *Journal of Engineering for Gas Turbines and Power*, **122**(3), p. 473, 2000.

[72] P. Argumugam, S. Swarnamani, and B. S. Prabhu, "Experimental Identification of Linearized Oil Film Coefficients of Cylindrical and Tilting Pad Bearings," *Journal of Gas Turbines and Power*, **117**(July), pp. 593–599, 1995, ISSN: 04021215.

[73] N. G. Wagner and W. D. Pietruszka, "Identification of Rotordynamic Parameters on a Test Stand with Active Magnetic Bearings," *Magnetic Bearings*, pp. 289–299, 1989.

[74] N. Wagner and K. Steff, "Dynamic Labyrinth Coefficients from a High-Pressure Full-Scale Test Rig Using Magnetic Bearings," *Rotordynamic Instability Problems in High-Performance Turbomachinery, NASA Conference Publication 3344*, 1996, pp. 95–112.

[75] N. G. Wagner, *Reliable Rotor Dynamic Design of High-Pressure Compressors Based on Test Rig Data*, 2001.

[76] R. Nordmann and M. Aenis, "Fault Diagnosis in a Centrifugal Pump Using Active Magnetic Bearings," *The International Journal of Rotating Machinery*, **10**(3), pp. 183–191, 2004, ISSN: 1023-621X.

[77] G. Vannini, S. Cioncolini, V. Calicchio, and F. Tedone, "Development of a high pressure rotordynamic test rig for centrifugal compressors internal seals characterization," *Proceedings of the 40th Turbomachinery Symposium*, Huston, Texas, 2011, pp. 46–59.

[78] M. Athavale, A. Przekwas, and R. Hendricks, "A Finite Volume Numerical Method to Calculate Fluid Forces and Rotordynamic Coefficients in Seals," *28th Joint Propulsion Conference and Exhibit*, 1992.

[79] G. Chochua and T. Soulas, "Numerical modeling of rotordynamic coefficients for deliberately roughened stator gas annular seals," *Journal of tribology*, 2007.

[80] X. Yan, J. Li, and Z. Feng, "Investigations on the Rotordynamic Characteristics of a Hole-Pattern Seal Using Transient CFD and Periodic Circular Orbit Model," *Journal of Vibration and Acoustics*, **133**(4), p. 041 007, Aug. 2011, ISSN: 07393717.

[81] S. Earnshaw, "On the nature of the molecular forces which regulate the constitution of the luminiferous ether," *Trans. Camb. Phil. Soc*, **7**, pp. 97–112, 1842.

[82] S. B. Andersen, S. Enemark, and I. F. Santos, "Dynamics and stability of rigid rotors levitated by passive cylinder-magnet bearings and driven/supported axially by pointwise contact clutch," *Journal of Sound and Vibration*, **332**(25), pp. 6637–6658, 2013, ISSN: 0022460X.

[83] G. Schweitzer, "Active magnetic bearings - chances and limitations," *IFToMM Sixth International Conference on Rotor Dynamics, Vol. 1*, Sydney, Australia, 2002, pp. 1–14.

[84] Matthew N. O. Sadiku, *ELEMENTS OF ELECTROMAGNETICS*, Third edit. Oxford University Press, 2001.

[85] E. C. Stoner, "Ferromagnetism," *Reports on Progress in Physics*, **11**, pp. 43–112, 1947, ISSN: 1098-6596. arXiv: `arXiv:1011.1669v3`.

[86] R. Bozorth, *FERROMAGNETISM*. IEEE Press, 1993, ISBN: 978-0780310322.

[87] E. C. Stoner and E. P. Wohlfarth, "A Mechanism of Magnetic Hysteresis in Heterogeneous Alloys," *Philosophical Transactions of the Royal Society of London. Series A, Mathematical and Physical Sciences*, **240**(826), pp. 599–642, 1948.

[88] J. L. Kirtley Jr., *Electromagnetic Energy: From Motors to Lasers - Supplemental Class Notes -Energy Method for Finding Forces*, 2010. [Online]. Available: `http://ocw.mit.edu/courses/electrical-engineering-and-computer-science/6-007-electromagnetic-energy-from-motors-to-lasers-spring-2011/readings/MIT6%7B%5C_%7D007S11%7B%5C_%7Dforces.pdf` (visited on 02/19/2016).

[89] D. Meeker, *Finite Element Method Magnetics*, 2011. [Online]. Available: `http://www.femm.info`.

[90] A. J. Voigt, "Calibration of Active Magnetic Bearings with Embedded Hall Sensors: Theory and Experiment," Master Thesis, The Technical University of Denmark, 2011.

[91] D. Meeker, *Finite Element Method Magnetics - User's Manual*, 2010. [Online]. Available: `http://www.femm.info/Archives/doc/manual42.pdf` (visited on 03/28/2011).

[92] M. N. O. Sadiku, *ELEMENTS OF ELECTROMAGNETICS*, Third Edit. Oxford University Press, 2001.

[93] J. Jin, *THE FINITE ELEMENT METHOD IN ELECTROMAGNETICS*, 2nd. John Wiley and Sons, 2002.

[94] Q. Chen and A. Konrad, "A review of finite element open boundary techniques for static and quasi-static electromagnetic field problems," *IEEE Transactions on Magnetics*, **33**(1), pp. 663–676, 1997, ISSN: 0018-9464.

[95] S. McFee, J. P. Webb, and D. A. Lowther, "A tunable volume integration formulation for force calculation in finite-element based computational magnetostatics," *IEEE Transactions on Magnetics*, **24**(1), pp. 439–442, 1988, ISSN: 19410069.

[96] M. Antila, E. Lantto, and A. Arkkio, "Determination of Forces and Linearized Parameters of Radial Active Magnetic Bearings by Finite Element Technique," **34**(3), pp. 684–694, 1998.

[97] J. J. Feeley and D. J. Ahlstrom, "A New Eddy Current Model for Magnetic Bearing Control System Design," *4th NASA Symposium on VLSI Design*, 1992, pp. 2.1.1–2.1.8.

[98] A. J. Voigt, "Development of a Contact Free Excitation Device for Testing the Dynamics of Magnetically Supported Rotors: Theory, Experiment and Application," Bachelor Thesis, The Technical University of Denmark, 2008.

[99] N. Jonassen, *ELEKTRO MAGNETISME*. Polyteknisk Forlag, 2004.

[100] J. D. Anderson, *COMPUTATIONAL FLUID DYNAMICS: THE BASICS WITH APPLICATIONS*. New York: McGraw-Hill, 1995.

[101] F. R. Menter, "Two-Equation Eddy-Viscosity Turbulence Models for Engineering Applications," *AIAA Journal*, **32**(8), pp. 1598–1605, 1994.

[102] ANSYS, *ANSYS CFX-SOLVER THEORY GUIDE*. ANSYS Inc, 2011.

[103] C. E. Brennen, *FUNDAMENTALS OF MULTIPHASE FLOWS*. Cambridge University Press, 2005.

[104] J. S. Lauridsen, K. Sekunda, I. F. Santos, and H. Niemann, "Identifying parameters in active magnetic bearing system using LFT formulation and Youla factorization," pp. 2–7,

[105] R. J. Prins, M. E. F. Kasarda, and S. C. Bates Prins, "A System Identification Technique Using Bias Current Perturbation for Determining the Effective Rotor Origin of Active Magnetic Bearings," *Journal of Vibration and Acoustics*, **129**(3), p. 317, 2007, ISSN: 07393717.

[106] R. J. Moffat, "Describing the uncertainties in experimental results," *Experimental Thermal and Fluid Science*, **1**(1), pp. 3–17, 1988, ISSN: 08941777.

[107] H. J. Woltring, "On optimal smoothing and derivative estimation from noisy displacement data in biomechanics," *Human Movement Science*, **4**(3), pp. 229–245, 1985, ISSN: 01679457.

[108] A. Savitzky and M. J. E. Golay, "Smoothing and Differentiation of Data by Simplified Least Squares Procedures," *Analytical Chemistry*, **36**(8), pp. 1627–1639, 1964, ISSN: 00032700.

[109] R. Chartrand, "Numerical Differentiation of Noisy, Nonsmooth Data," *ISRN Applied Mathematics*, **2011**(1), pp. 1–11, 2011, ISSN: 2090-5572.

[110] A. A. Lomakin, "Calculation of critical speed and securing of dynamic stability of the rotor of hydraulic high pressure machines with reference to forces arising in the seal gaps [in Russian]," *Energomashinostroenie*, **4**, pp. 1–5, 1958.

[111] B. Ertas and J. Vance, "The Influence of Same-Sign Cross-Coupled Stiffness on Rotordynamics," *Journal of Vibration and Acoustics*, **129**(1), p. 24, 2007, ISSN: 07393717.

[112] H. Kanki and S. Morit, "Destabilizing force of labyrinth seal," *NASA. Lewis Research Center Rotordynamic Instability Problems in High-Performance Turbomachinery*, 1986, pp. 205–223.

[113] J. Lagarias, J. Reeds, H. Wright, and P. Wright, "Convergence properties of the Nelder–Mead simplex method in low dimensions," *Journal of Optimization*, **9**(1), pp. 112–117, 1998, ISSN: 1052-6234.

Appendix A

Module II - Pneumatic Control

The schematics for the calibration facility pneumatic control scheme are included here. The schematics visualise one out of four pneumatics actuation circuits.

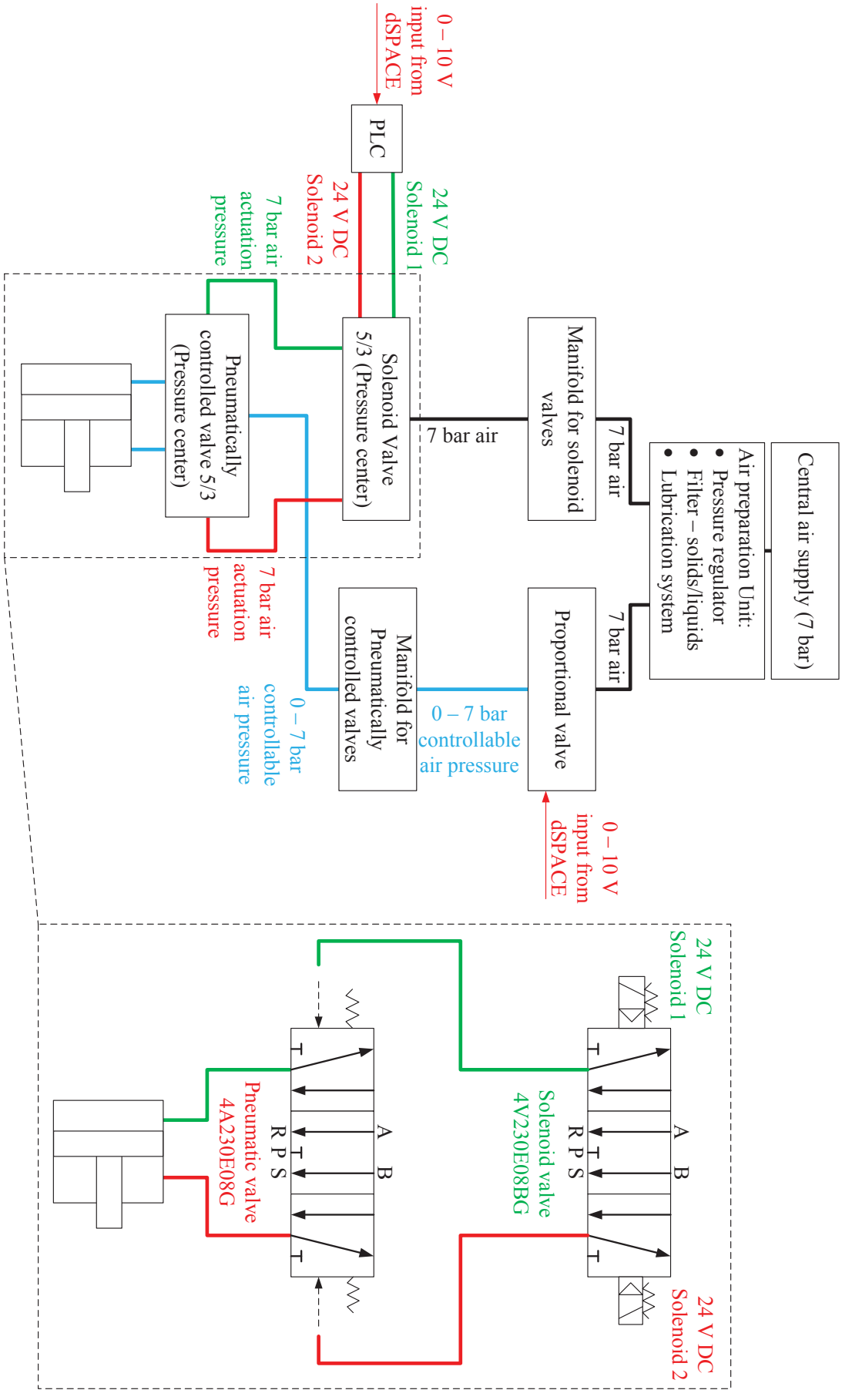

Figure A.1: Schematics of the pneumatic control scheme for the calibration facility

Appendix B

Module I and III - Section View

A horizontal section view of the complete test facility in seal test configuration is included here. Only main component groups are included for clarity.

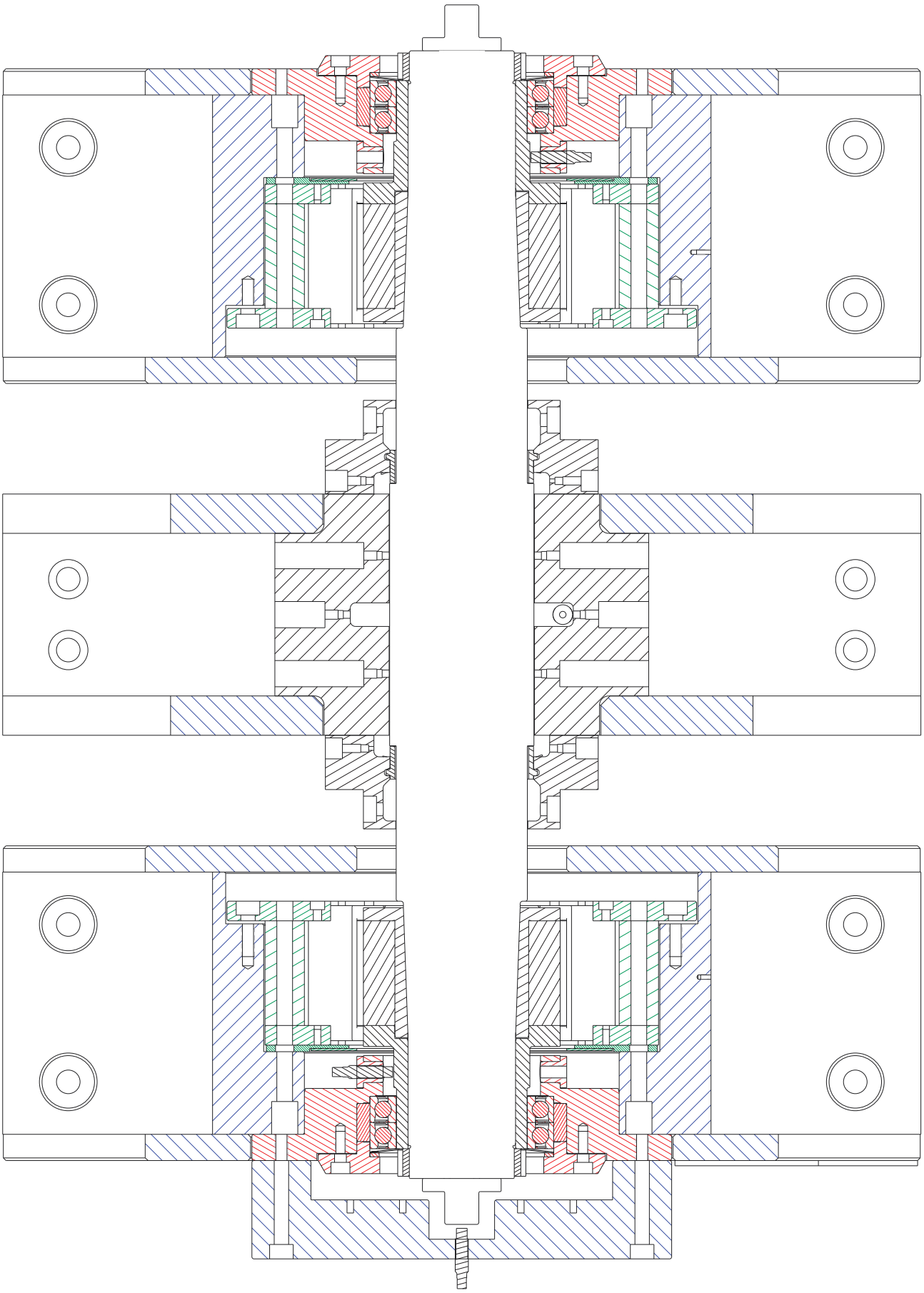

Figure B.1: Horizontal section view of the complete test facility.

Appendix C

Module III - Early Phase Mixing Concept

An early stage flow mixing and SHA concept is presented in Fig. C.1. The SHA concept shown in Fig. C.1(b) is presented without the test seal elements designed for this SHA iteration. The mixing device concept is to be mounted directly onto the SHA and has three separate inlets as seen in Fig. C.1 intended to enable generating multiphase flow mixtures for a large range of GVFs and LVFs. Inlet 1 and 2 are symmetrically distributed and titled 45° with respect to the centre axis of the mixing device, while inlet 3 is perpendicular to the centre axis of the mixing device. Blocking inlet 3 and supplying water and air at the same pressure through inlet 2 and 3, respectively, should be able to provide multiphase flow in the centre range of GVFs and LFVs. Injecting either air or water through inlet 3 while supplying the SHA with the other phase through inlet 1 and/or 2 is intended for seal testing in the dispersed flow regime.

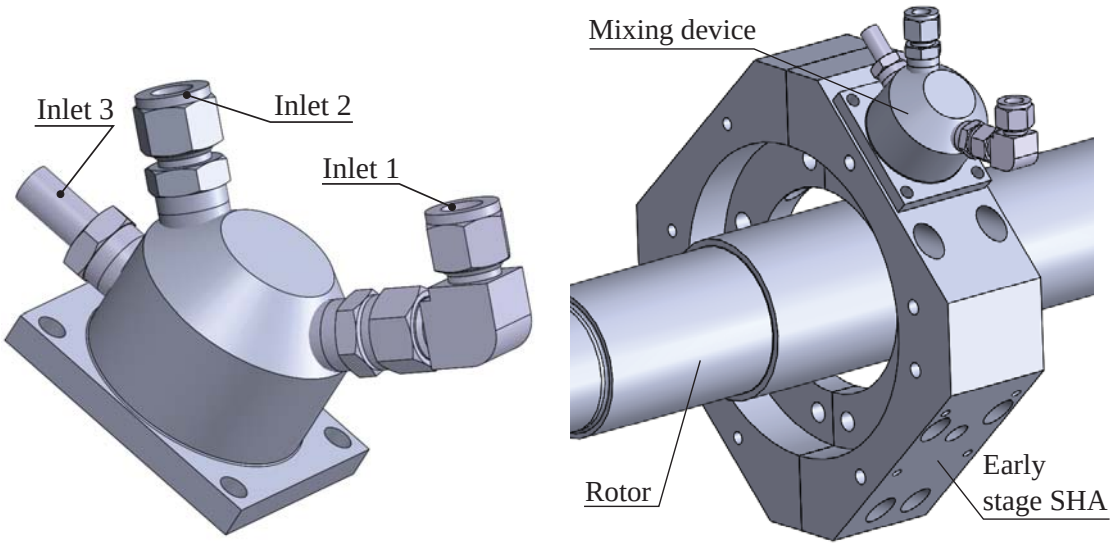

(a) Mixing device. (b) SHA

Figure C.1: Early stage SHA and flow mixer concepts.

Appendix D

Module IIII - Flow Loop Layouts

Appendix contains conceptual schematics for the different flow loop layouts.

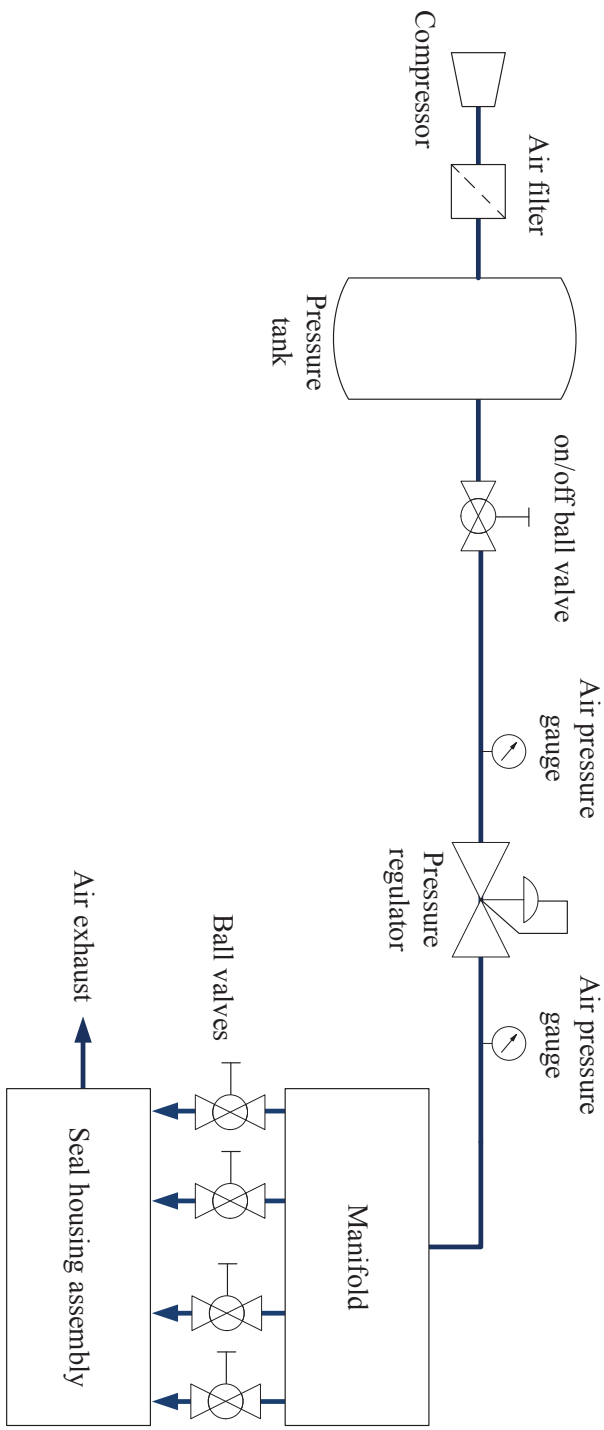

Figure D.1: Conceptual schematic for the layout of the realised flow loop.

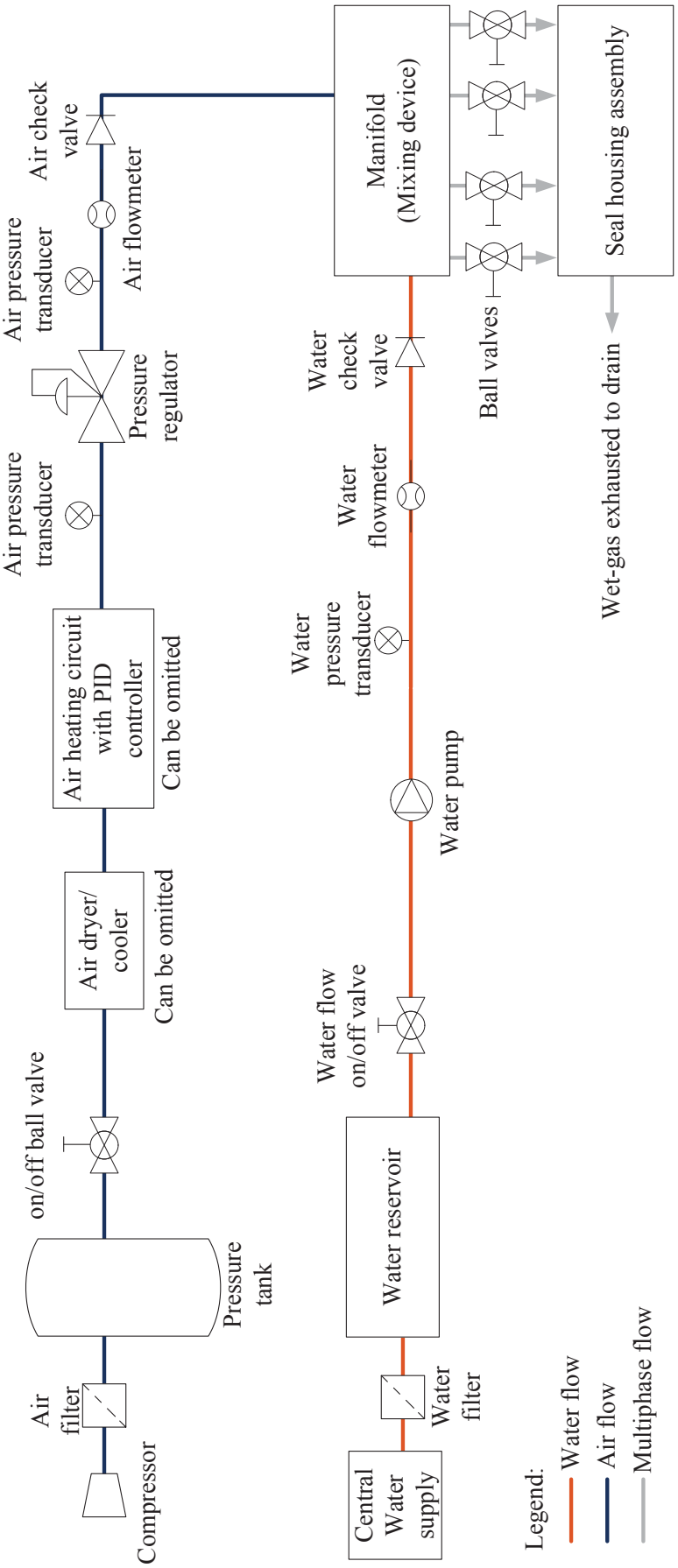

Figure D.2: Conceptual schematic for the layout of the flow loop intended for wet-gas seal testing.

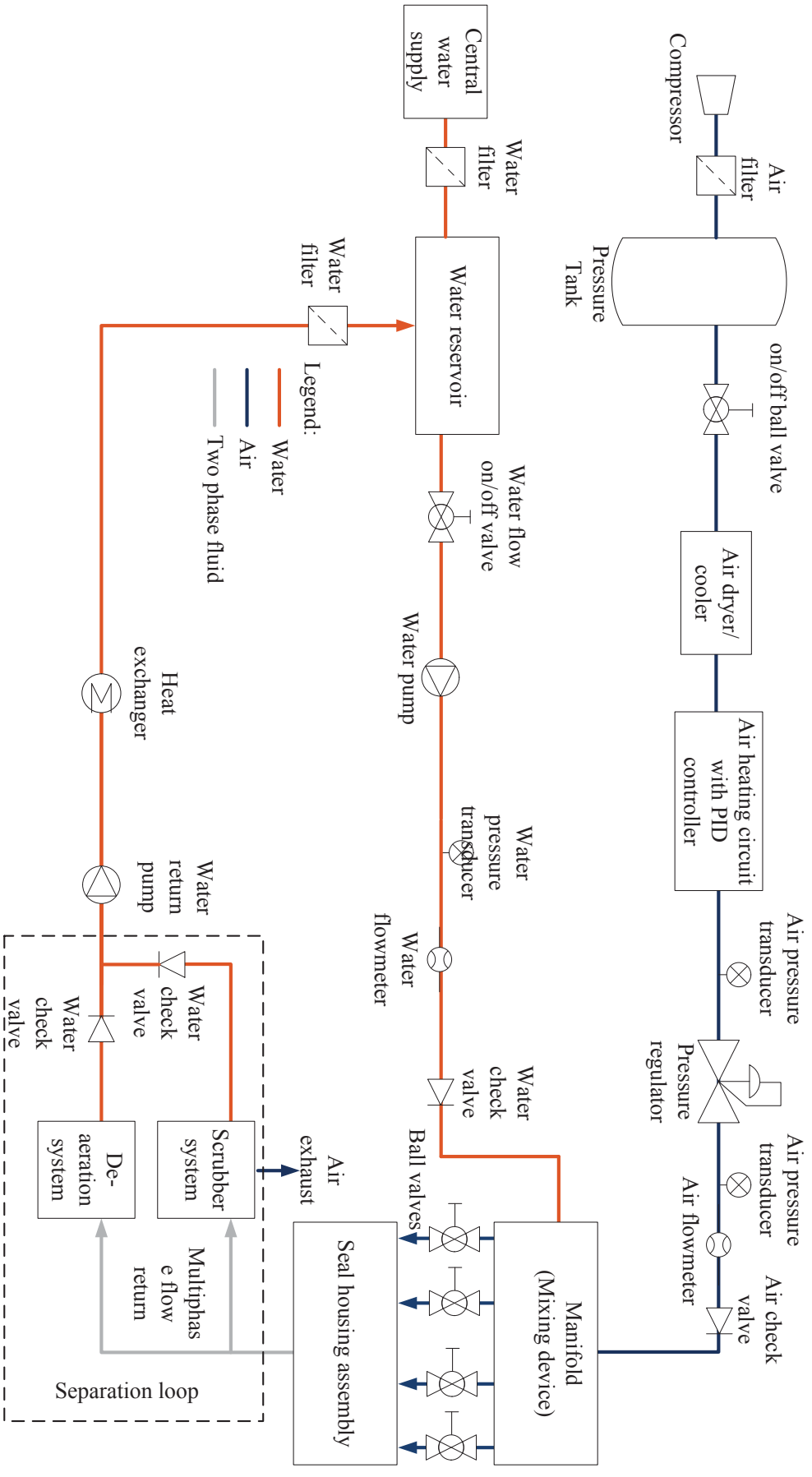

Figure D.3: Conceptual schematic for the layout of the complete flow loop intended to facilitate full range multiphase seal testing.

Appendix E

Identification of the Coupling Stiffness

Here the procedure for identifying the stiffness of the flexible coupling is presented alongside the identified stiffness coefficients. For identifying the stiffness from the flexible coupling, the rotor is displaced in discrete steps while both the force required to displace the rotor and the displacement is recorded. Separate experiments are conducted the vertical y-direction and the horizontal x-direction in the global reference frame, in order to identify a coupling stiffness coefficient in both direction. Time series of the displacement for the two experiments are shown in Fig. E.1, revealing the staircase pattern including both positive and negative displacements in both the x and y -direction, respectively. Including both positive and negative displacements, allows for identifying any potential hysteresis phenomena. The experiments are conducted in the seal centre reference frame. Displacement-force plots for the x and y -direction are presented in Fig. E.2 along with a first order polynomial data fit, used to extract the actual stiffness coefficients. Fig. E.2 visually reveals the expected linearity of the displacement-force correlation with minimal hysteresis, and good coherence between data and fit. The identified stiffness coefficients are presented in Table E.1 along with the MAE in percent of the maximum applied force in the respective stiffness identification experiment. The MAE is defined in section 4.2, and it is noted that here the MAE is calculated in Newton as the mean of the absolute error between the force raw data and the force estimated by the data fit, for each discrete displacement. The x and y -directional coefficients are close to identical with $k_{C,x}$ being $\sim 3.9\,\%$ larger than $k_{C,y}$.

Table E.1: Experimentally identified coupling stiffness

Stiffness coefficient	Value [N/m]	MAE [N]	MAE [%]
$k_{C,x}$	$2.39 \cdot 10^6$	1.08	0.9
$k_{C,y}$	$2.30 \cdot 10^6$	1.59	1.3

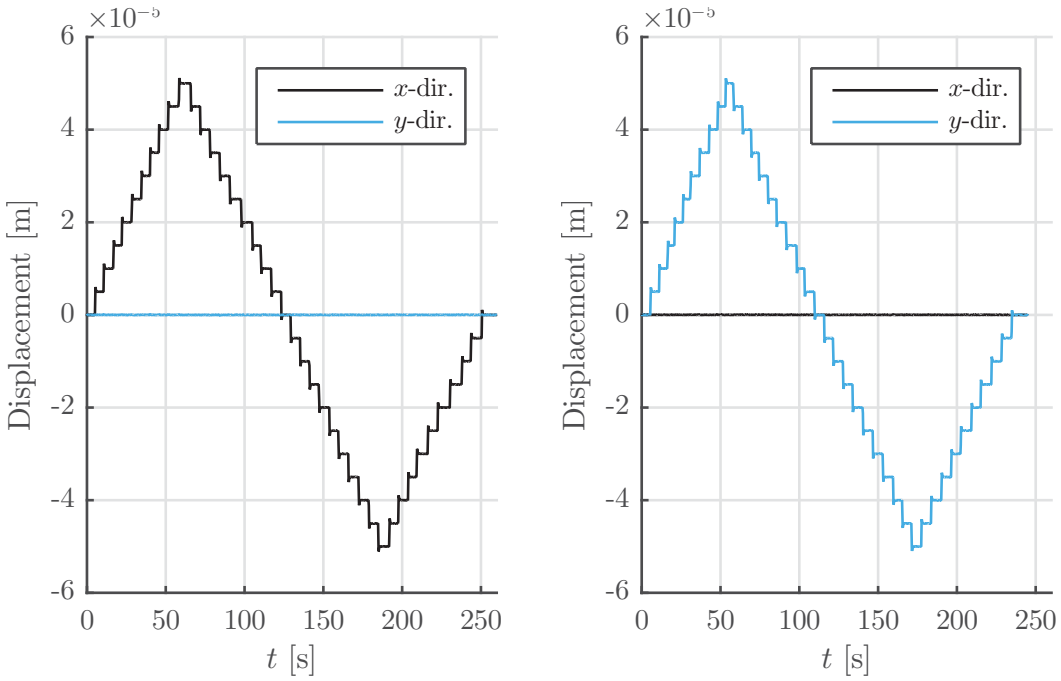

(a) Rotor displaced in the x-direction. (b) Rotor displaced in the y-direction.

Figure E.1: Time series plot of the rotor displacements during coupling stiffness experiment.

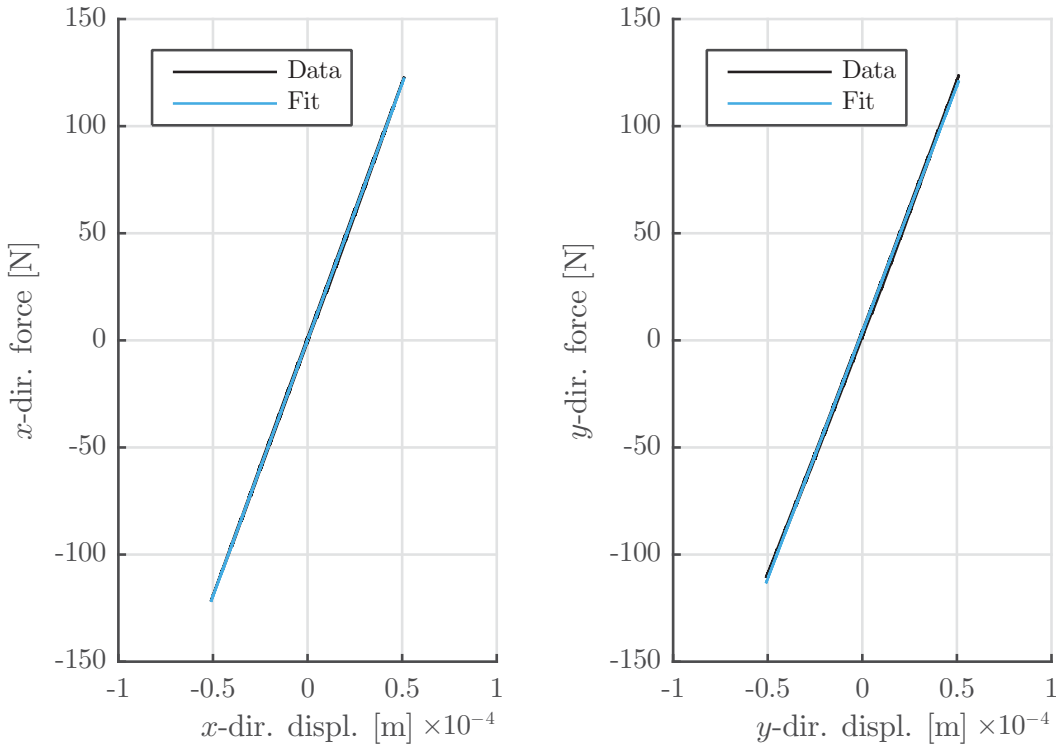

(a) Rotor displaced in the x-direction. (b) Rotor displaced in the x-direction.

Figure E.2: Force-displacements curves used for identification of the coupling stiffness. The figure shows both raw data and data fit.

Appendix F

Post Processing of Experimental Data: Representative Data Fitting Examples

This appendix serves to present representative illustrations of the data fitting procedure used in post processing of raw experimental data. All data fits are made using an unconstrained non-linear optimization method available through the MATLAB function `fminsearch` which does not utilise analytical or numerical gradients [113]. Here `fminsearch` is applied to fit the experimental data to a discrete time domain single frequency sinusoidal function on the form

$$A_i \sin \omega_i t + \phi_i$$

in which A_i denotes the identified amplitude, ω_i the known frequency, and ϕ_i the identified phase of the experimentally obtained time series data with index i. The discrete data time vector is denoted t. In Fig. F.1 raw position and force data samples are plotted along with the correlated fit for a forced 5 Hz sinusoidal perturbation of the rotor in the y-direction. The x-direction data is not visualised here, however it is included in the estimation quality results presented in Table F.1. All data presented here is acquired with a 2.5 kHz sampling frequency.

Good qualitative agreement between the raw data and the fit are seen in Fig. F.1. The displacement data presented in F.1(a) reveals a very low level of noise, however, significantly more noise are seen on the force data in Fig. F.1(b), which are largely attributed to random noise in the unfiltered Hall sensor signals. Again the quality of the data fit can be assessed using the MAE approach introduced in section 4.2. The resulting MAEs and the MAEs in percent of the maximum applied displacement and force, respectively, are presented in Table F.1. Table F.1 shows the expected very small MAEs between raw and fitted data for the position data. The MAEs on the force data is significantly larger due to noise contamination, however still within tolerable bounds.

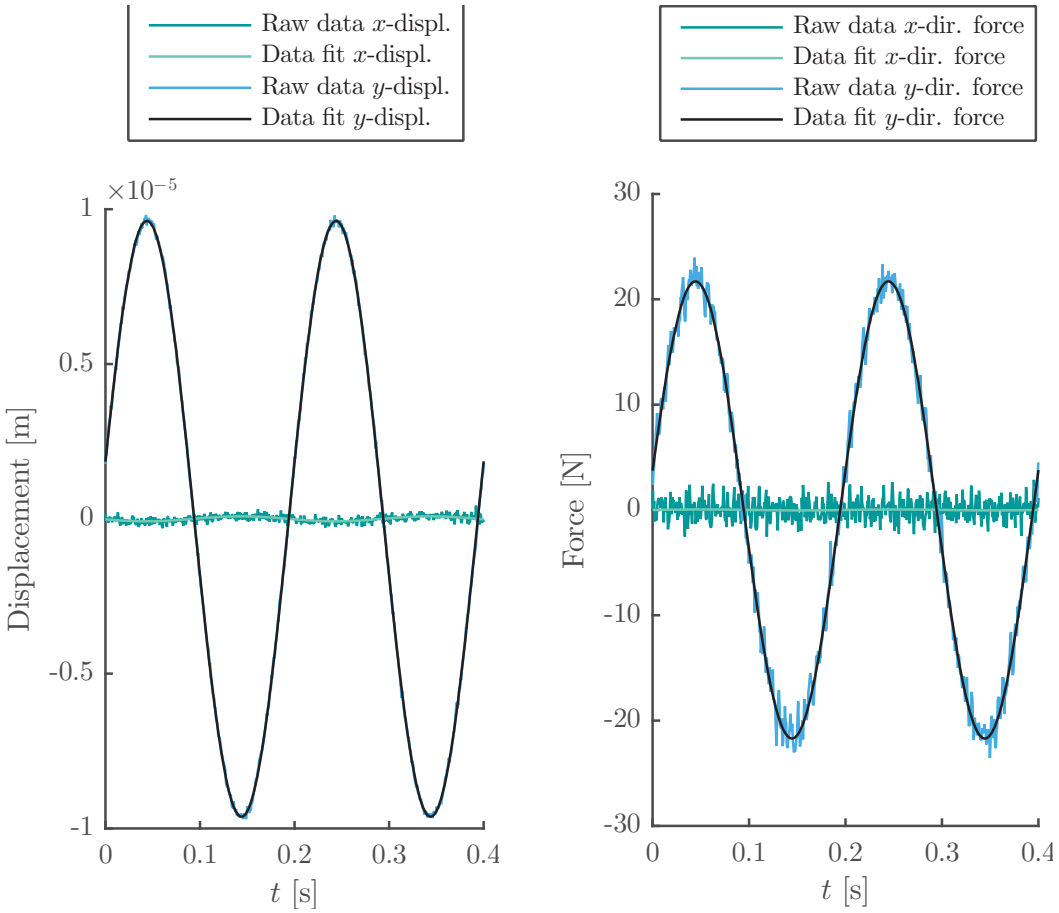

(a) Rotor displaced in the x-direction.

(b) Rotor displaced in the y-direction.

Figure F.1: Time series plot of the rotor displacements during coupling stiffness experiment.

Generally the signal-to-noise ratio are good for both displacement and force data.

Table F.1: Assessment of MAE for representative data fits of position and force data.

Data type	MAE	MAE [%]
Displacement x data fit	0.082 μm	0.85
Displacement y data fit	0.077 μm	0.80
Force x data fit	0.78 N	3.4
Force y data fit	0.93 N	4.2

Publication P1

CFD Applied for the Identification of Stiffness and Damping Properties for Smooth Annular Turbomachinery Seals in Multiphase Flow

---

Paper published in the proceedings of ASME Turbo Expo 2016.

Proceedings of ASME Turbo Expo 2016: Turbomachinery Technical Conference and Exposition
GT2016
June 13-17, 2016, Seoul, South Korea

GT2016-57905

CFD APPLIED FOR THE IDENTIFICATION OF STIFFNESS AND DAMPING PROPERTIES FOR SMOOTH ANNULAR TURBOMACHINERY SEALS IN MULTIPHASE FLOW

Andreas Jauernik Voigt
Department of Mechanical Engineering
Technical University of Denmark/
Lloyd's Register Consulting
Copenhagen, Denmark
Email: ajavo@mek.dtu.dk

Piero Iudiciani
Lloyd's Register Consulting
Copenhagen, Denmark
Email: piero.iudiciani@lr.org

Kenny Krogh Nielsen*
Lloyd's Register Consulting
Copenhagen, Denmark
Email: kenny.krogh-nielsen@lr.org

Ilmar F. Santos
Department of Mechanical Engineering
Technical University of Denmark
Copenhagen, Denmark
Email: ifs@mek.dtu.dk

ABSTRACT

This paper presents a first venture into quantifying stiffness and damping coefficients for turbomachinery seals in multiphase flow using Computational Fluid Dynamics (CFD). The study focusses on the simplest seal type: the smooth annular seal. The investigation is conducted for both wet-gas and bubbly flow regimes in which the primary phase is gas (air) and liquid (water), respectively. For the wet gas regime three different Liquid Volume Fraction (LVF) conditions are included in the study; 5%, 3% and 0%. Similarly for the bubbly flow regime three Gas Volume Fractions (GVF) conditions are included; 5%, 3% and 0%. An Eulerian-Eulerian modelling approach is taken, applying an inhomogeneous model, where the primary phase is treated as continuous and the secondary phase is included as dispersed. The Instationary Perturbation Method (IPM) is applied to identify the rotordynamic coefficients, in which the rotor is harmonically perturbed, and forces acting on the rotor are quantified through integration of the pressure and shear stresses. The perturbation is repeated for different frequencies to uncover any frequency dependence. The results presented in this paper are intended as an initial comparison basis for the experimental results to be obtained by applying the multiphase seal test facility currently in development, as part of a collaboration between Lloyd's Register Consulting, the Technical University of Denmark, OneSubsea, TOTAL and Statoil.

INTRODUCTION

High pressures, small clearances, and high rotational velocities in compressors and pumps ensure high productivity for the oil and gas industry. However, the obtainable rotational velocities are limited by the stability margins of the rotating machinery, specifying the operable range of these. It is well known that the rotordynamic forces generated by the interaction of process fluid, rotor and seals are of primary importance for the rotordynamic stability [1, 2], making them an important subject to study.

*Address all correspondence to this author.

Rotordynamic codes are used to assess overall machine stability and performance information. These codes rely on precise modelling of individual components in the machines. A wealth of theoretical and experimental investigations have been performed to establish reliable component level models.

The oil and gas industry continues to move towards production from fields at greater sea depths and in the Arctic regions. The production from many of these fields requires compression and pumping to take place on the sea floor where the possibility of performing liquid and gas separation on the well stream is limited. The increase in the application of pumps and compressors that are required to handle unseparated well streams motivates developing and refining predictive tools for rotordynamic analysis of machines subdued to multiphase flow.

As an alternative to bulk flow seal codes developed in the past [1, 3–6], the use of Computational Fluid Dynamics (CFD) for seal modelling has advanced within recent years, as the available computational power has increased [7, 8]. CFD-based commercial tools are now an integral part of the toolbox available for Original Equipment Manufacturers (OEMs) design engineers and consultants dealing with the complex rotor-fluid interaction in seals.

In contrast to bulk flow seal codes a CFD-based mathematical model does not rely heavily on empirical corrections [9] in order to represent experimental results in a satisfactory manner [6–8, 10–12] and can handle complex geometries out of reach for bulk flow codes. Additionally, CFD can be used to investigate flow details such as local volume fractions, separation regions, and local flow velocities which is especially advantageous for studying seal multiphase flows [13]. CFD is however much more computational expensive and not likely to replace bulk flow codes but simply supplement these. CFD models have been implemented with success by multiple authors through discretization of the (simplified) Navier-Stokes equations [7–9, 14–23].

Predictive bulk flow or CFD-based models for single phase seals are relatively mature as indicated above, yet the need for a continued effort was emphasised in the 2007 study presented by Kocur, et al. [24]. The subject of expanding these models to include multiphase flow conditions is largely untouched in comparison, however, some work has been done. In the late 1980's and early 1990's models to predict liquid-vapor leakage flow in smooth annular seals were presented [25, 26], however this did not treat multiphase flow impact on rotordynamic seal coefficients. Arauz and San Andrés presented a bulk flow model for a cryogenic damper seal subdued to a liquid-vapor multiphase flow [27, 28]. This work presented theoretical prediction of rotordynamic seal coefficients. Recently, Arghir et al. published an analysis of textured annular seals subdued to multiphase (bubbly) flow [29]. In this work a bulk flow code was used to calculate rotordynamic seal coefficients, and found these to be dependent on the excitation frequency. Similar findings were reported by San Andrés [30], in a study where a bulk flow code was applied to investigate a smooth annular seal, in this case for varying LVFs between 0 and 100%. In a very recent paper by Vannini et al. [13] a CFD based study was conducted to investigate the impact of both a tooth on stator labyrinth and a pocket damper balance piston seal design on the overall rotordynamic performance of a centrifugal compressor subdued to wet gas conditions (0 to 3% LVF). The paper offered a physical explanation of sub-synchronous vibrations found in a previously conducted experimental campaign [31], however rotordynamic seal coefficients were not determined.

A major constraint on the development of valid predictive models that are able to precisely evaluate multiphase flow impact on rotordynamic seal coefficients, is the scarcity of experimental data. Iwatsubo and Nishino [32] were the first to publish a data set for seals in multiphase flow albeit this was practically unusable for validation purposes, since many details were omitted. San Andrés et al. recently published experimental data for a short length smooth annular seal subdued to wet gas conditions (0 to 4% LVF) with a stationary journal [33]. The paper reports an increase in the direct damping coefficients with increasing LVF, but no clear tendencies are evident in the stiffness data.

From the above it is clear that there is a pronounced need for additional high quality multiphase validation data combined with a continued focus on developing predictive tools for seals in multiphase flow. This paper is a first presentation of applying CFD to explicitly determine the rotordynamic coefficients of seals subdued to multiphase flow for a range of LVFs. The simplest possible seal geometry, the smooth annular seal, is chosen as the subject of study, in an attempt to focus on the seal flow physics and rotordynamic tendencies rather than complex geometries, such as labyrinth or honeycomp seals, that intentionally influences the flow patterns within the seal.

This paper provides a theoretical contribution to the field of studying multiphase seals. In conjunction with a newly developed multiphase seal test facility [34] designed and manufactured in a joint venture between the Technical University of Denmark, Lloyd's Register Consulting, OneSubsea, TOTAL and Statoil, the underlying work is a part of the ongoing effort aiming to establishing a flexible, well rounded, and experimentally validated tool for multiphase seal analysis.

DETERMINING ROTORDYNAMIC COEFFICIENTS USING CFD

The conventional rotordynamic model employed to quantify gas seal forces, assuming small motion around a concentric rotor position is presented in Eqn. (1), [1]. Here all coefficients are assumed frequency dependent and added mass effects are neglected.

$$-\begin{Bmatrix} F_z \\ F_y \end{Bmatrix} = \begin{bmatrix} K(\Omega) & k(\Omega) \\ -k(\Omega) & K(\Omega) \end{bmatrix} \begin{Bmatrix} Z \\ Y \end{Bmatrix} + \begin{bmatrix} C(\Omega) & c(\Omega) \\ -c(\Omega) & C(\Omega) \end{bmatrix} \begin{Bmatrix} \dot{Z} \\ \dot{Y} \end{Bmatrix} \quad (1)$$

The IPM is based on an unsteady CFD simulation of a full 360° model of the fluid domain defined by the seal geometry. In the simulation the rotor surface boundary is virtually perturbed in a periodic fashion. The perturbation is imposed by deforming the fluid domain mesh, meaning that no time consuming re-meshing is required. The reaction forces acting on the rotor due to the rotor displacement are obtained by integrating the pressure and shear stresses predicted in the CFD simulation. The reaction forces have the same frequency as the prescribed rotor movement but are shifted in phase.

The rotor position is perturbed using a uni-directional harmonic function presented in Eqn. (2), where the amplitude A is typically defined as a fraction of the radial clearance, and the excitation frequency Ω is chosen as a fraction of the rotational velocity of the rotor. In this study the amplitude is fixed to 10% of the 0.3 mm nominal seal clearance.

$$Y = A\sin(\Omega t) \quad (2)$$

The uni-directional lateral perturbation normal to the rotation axis is visualized in Fig. 1, in which the displacement of the rotor and the seal clearance are exaggerated for visualization purposes.

The rotordynamic coefficients can be determined based on a quantification of the forces resulting from the prescribed harmonic excitation. The procedure will be outlined in the following. Initially Eqn. (1) is expanded to yield (the argument (Ω) is dropped for simplicity)

$$-F_z = KZ + kY + C\dot{Z} + c\dot{Y} \quad (3)$$
$$-F_y = -kZ + KY - c\dot{Z} + C\dot{Y} \quad (4)$$

As rotor displacement is only prescribed in the y direction, lateral movement in the z direction is enforced to be 0 at all times.

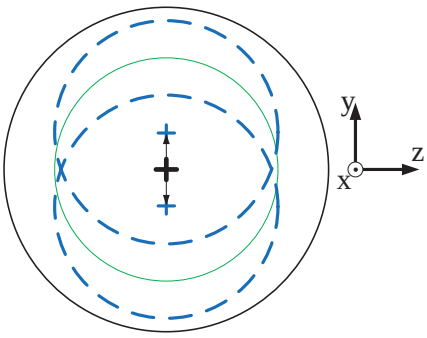

FIGURE 1: VISUALISATION OF PERTURBATION PATTERN

Considering this, Eqn. (3) and Eqn. (4) can be simplified to yield

$$-F_z = kY + c\dot{Y} \quad (5)$$
$$-F_y = KY + C\dot{Y} \quad (6)$$

It is convenient to re-introduce the harmonic excitation expressed using a complex exponential the following way

$$Y = Ae^{i\Omega t} \quad (7)$$

Inserting Eqn. (7) and its time-derivative into Eqn. (5) and (6) and recalling that the reaction forces resulting from the imposed displacement will be a harmonic force with the same frequency but with a phase lag, yields

$$-f_z e^{i(\Omega t+\phi_1)} = kAe^{i\Omega t} + i\Omega cAe^{i\Omega t}$$
$$-f_y e^{i(\Omega t+\phi_2)} = KAe^{i\Omega t} + i\Omega CAe^{i\Omega t}$$

in which ϕ_1 and ϕ_2 are the (positive or negative) phase lag between the rotor displacement and the reaction forces and f_z and f_y denotes the amplitude of the harmonic z and y -directional reaction forces. Rewriting the exponentials on the left hand side using $e^{i(\Omega t+\phi)} = e^{i\Omega t}e^{i\phi}$, and dividing through by $Ae^{i(\Omega t)}$ yields:

$$\frac{-f_z}{A}e^{i\phi_1} = k + i\Omega c \quad (8)$$
$$\frac{-f_y}{A}e^{i\phi_2} = K + i\Omega C \quad (9)$$

Redefining the left hand side of Eqn. (8) and Eqn.(9) using $-f_z e^{i\phi_1} = -F_z$ and $-f_y e^{i\phi_2} = -F_y$ yields a simple expression for the complex impedance functions

$$\frac{-F_z}{A} = k + i\Omega c \tag{10}$$

$$\frac{-F_y}{A} = K + i\Omega C \tag{11}$$

The frequency dependent rotordynamic force coefficients can then simply be obtained by separating the impedance functions into their real and imaginary parts as follows (argument (Ω) is re-introduced)

$$Re(-F_z/A) = k(\Omega) \tag{12}$$

$$Im(-F_z/A) = c(\Omega)\Omega \tag{13}$$

$$Re(-F_y/A) = K(\Omega) \tag{14}$$

$$Im(-F_y/A) = C(\Omega)\Omega \tag{15}$$

To be able to apply the above for the identification of the rotordynamic coefficients, the forces F_y and F_z have to be cast into complex form. This is straightforward and requires identification of the phase lag ϕ between the rotor position and the two force components. This is done by measuring the peak-to-peak time delay ΔT between the harmonic position and force data series resulting from the CFD simulations. This can then be turned into a phase lag using $\phi = 2\pi\Omega\Delta T$. The amplitudes of the forces f_z and f_y can be quantified as the mean of the maximum values of the peaks in a force data series.

GEOMETRY AND OPERATING CONDITIONS

The seal geometry used in the numerical investigations presented in this paper is based on a simplified representation of the smooth annular test seals found in the multiphase seal test facility presented in [34]. A picture of the test facility vertically split seal housing assembly design can be seen in Fig. 2. As evident from Fig. 2 the seals in the test facility are mounted in a back-to-back configuration to alleviate axial thrust. This setup is adopted in the CFD analysis presented here. Additionally, the operating conditions imposed in the CFD analysis reflect a subset of the operating conditions under which the physical test facility can be used to identify rotordynamic coefficients for the test seals. Table 1 lists the geometrical dimensions of the seal as well as the operating parameters.

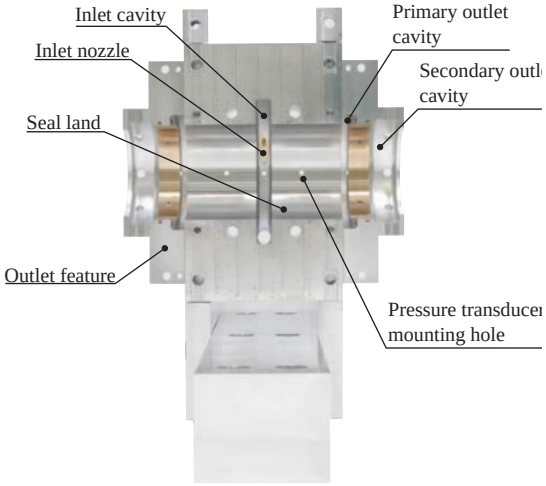

FIGURE 2: HALF PART OF SEAL HOUSING ASSEMBLY SHOWING INLET AND OUTLET FEATURES

TABLE 1: GEOMETRICAL AND OPERATING PARAMETERS

Parameter	Value
Seal Length [mm]	83
Rotor Diameter [mm]	110
Clearance (constant) [mm]	0.3
Rotor Speed [rpm]	10000
Inlet pressure [barg]	20.0
Outlet pressure [barg]	10.0
Inlet temperature [C]	20
Preswirl	0

The operating conditions listed in Table 1 are the same for all simulations presented in this paper. Six different cases are investigated, the only difference between the cases being the inlet LVF, and GVF values. Table 2 presents the six aforementioned cases. The first three cases are relevant for wet gas compression (one fully dry case and two low LVF conditions); the last three cases are relevant for multiphase pumping (one fully liquid case and two low GVF conditions). Corresponding Liquid Mass Fraction (LMF) and Gas Mass Fraction (GMF) are also listed in Table 2. To capture any frequency dependence of the rotordynamic coefficients, several simulations are performed over a range of frequencies. For each of the cases in Table 2, four exci-

TABLE 2: INVESTIGATED CASES

Case	LVF (%)	GVF (%)	LMF (%)	GMF (%)
Low LVF conditions				
Case 1	0	100	0	100
Case 2	3	97	54.95	45.05
Case 3	5	95	67.48	32.52
Low GVF conditions				
Case 4	100	0	100	0
Case 5	97	3	99.87	0.13
Case 6	95	5	99.92	0.08

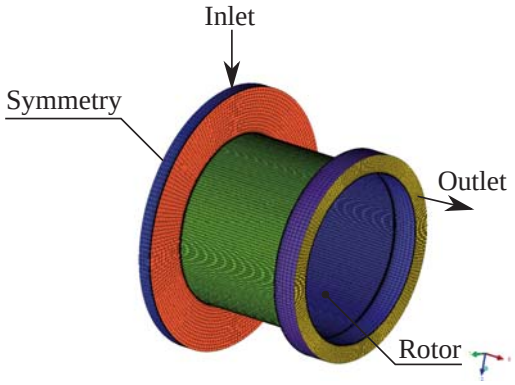

FIGURE 3: CFD MODEL OF THE SMOOTH SEAL

tation frequencies Ω are investigated. The used set of frequencies is detailed in Eqn. 16, in which $\Omega_{rot} = 166.67\,\text{Hz}$ corresponds to the rotational velocity of the shaft.

$$\Omega = [0.25, 0.50, 0.75, 1.00] \cdot \Omega_{rot} \tag{16}$$

CFD SETUP

A full view of the implemented CFD model is presented in Fig. 3 which reflects one half part of two seals placed in a back-to-back configuration, sharing an inlet cavity. As seen in Fig. 3, the model includes the radial inlet cavity, the smooth seal and the outlet cavity.

The calculations were performed using the commercial CFD solver ANSYS CFX. The fluids modelled in this study were atmospheric air for the gaseous phase and water for the liquid phase. The gaseous phase was modelled under the assumption of a calorically perfect ideal gas, i.e. using an ideal gas equation of state with a constant specific heat capacity. Using an ideal gas formulation incorporates the compressibility of the gas. The viscosity was assumed to be constant. Constant properties were assumed for the liquid phase. Table 3 presents the properties of the fluids used in the simulations.

TABLE 3: FLUID PROPERTIES

Gaseous phase (air)		
Molecular Weight	28.96	$[kg\,kmol^{-1}]$
Dynamic Viscosity	1.831	$[kg\,m^{-1}s^{-1}]\cdot 10^{-5}$
Specific Heat	1.004	$[J\,kg^{-1}K^{-1}]\cdot 10^{3}$
Liquid phase (water)		
Density	997	$[kg\,m^{-3}]$
Dynamic Viscosity	8.899	$[kg\,m^{-1}s^{-1}]\cdot 10^{-4}$
Specific Heat	4.182	$[J\,kg^{-1}K^{-1}]\cdot 10^{3}$

Boundary conditions were assigned as follows: At the inlet the total pressure was assigned and the flow direction was specified to be normal to the surface (zero preswirl). At the outlet the static pressure was assigned. No slip conditions were imposed at the walls and all surfaces are considered hydraulically smooth. This implies that the model surfaces are similar to physical surfaces machined to a level at which they are sufficiently smooth, such that the roughness of these does not extend beyond the viscous sublayer. The rotor is assigned the rotating speed of 10000 rpm, see Table 1. The rotor perturbation was achieved using a mesh deformation technique where a transient displacement was specified. The perturbation amplitude was chosen to 10% of the radial clearance i.e. 0.03 mm. A zero preswirl ratio was chosen for simplicity and because the effects of preswirl is not the main interest of this study. Symmetry conditions are applied at the backplane of the radial inlet cavity.

An Eulerian-Eulerian method was used to model the multiphase flow. An inhomogeneous model was selected, i.e. the phases share the pressure field but they have different velocity fields. For both cases, the phase with the highest volume fraction was modelled as continuous and the other phase as dispersed droplets or bubbles of the same size, respectively. The droplets/bubbles are assumed to be 0.003 mm, i.e. $1/100$th of the seal clearance, as in a previous work from the same authors [13].

A $k-\omega$ SST turbulence model was used throughout the simulations. The near-wall modelling was done using scalable

TABLE 4: MESH DETAILS

No. of nodes parameter	Coarse	Medium	Fine
a	11	16	23
b	14	21	30
c	6	11	16
d	64	105	147
e	2	3	5
Total No. of nodes	71100	328500	1580000

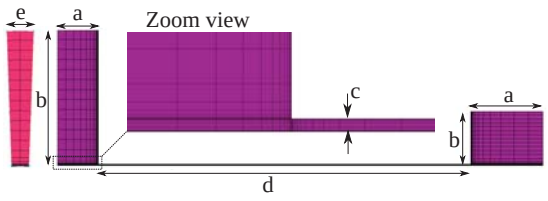

FIGURE 4: MESH NODES PARAMETER SPECIFICATION. THE MAIN VIEW PRESENTS A SINGLE SIDED SECTION OF THE MEDIUM MESH IN THE X,Y PLANE. THE LEFT VIEW IS INCLUDED TO VISUALISE THE NODE PARAMETER e, AND SHOWS AN AXIAL CROSS SECTION OF THE 4° MESH SLICE

wall functions which prescribe a velocity distribution in the part of the near wall region that is too narrow to be fully discretized with the chosen mesh densities.

A structured block mesh created using ANSYS ICEM CFD was used. The mesh consisted of approximately 330000 grid nodes. The used mesh was compared to a coarser and a finer version to ensure mesh independence of the results. The number of nodes for the three meshes used in the mesh independence study are listed in Table 4. The node parameters listed in Table 4 refer to the number of nodes on a given mesh coordinate, as specified in Fig. 4. Fig. 4 visualises the medium mesh for a four degree slice of the complete 360° mesh, and includes a zoom view of the seal land inlet zone, as well as an axial cross section of the inlet cavity.

The number of timesteps used for the calculations was varied with perturbation frequency. This is due to the differences between the rotational and perturbational time scales and the need to sufficiently resolve both features. Between 40 and 360 timesteps per period of the harmonic perturbation were typically used with increasing values for perturbation at lower frequencies. Typically the IPM analyses reach convergence within four simulated periods. Fig. 5 shows the perturbation

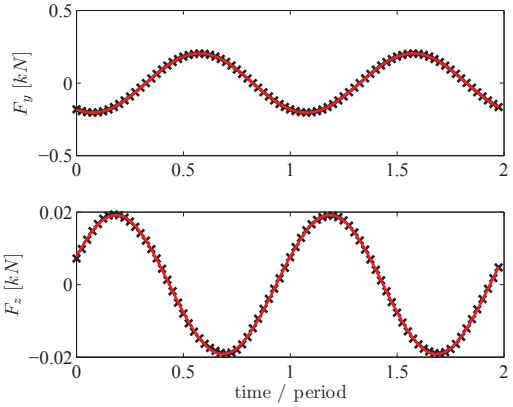

FIGURE 5: EXAMPLE OF REACTION FORCES. LVF=0%. $\Omega = \Omega_{rot} = 166.67\,\text{Hz}$

function and an example of the simulated reaction forces acting on the rotor, as a function of time. The example presented in Fig. 5 is for Case 1 with LVF=0%, and depicts only the last two periods. The crosses represent the computed forces from the IPM simulation, while the solid red line is the closest sinusoidal fit computed during post-processing. From the figure it is possible to see how the forced exerted on the rotor, due to the perturbation of the seal flow, displays a perfectly periodic behaviour.

MESH INDEPENDENCE STUDY

A mesh independence study was performed for Case 1 (LVF=0%). Calculations were performed using the same perturbation frequency ($\Omega = \Omega_{rot} = 166.67\,\text{Hz}$) for the three different mesh sizes indicated in Table 4. Fig. 6 shows the amplitude of the normal forces acting on the rotor as a function of the number of nodes in the mesh. Both the y and z directional forces show small variations with the number of nodes. The force in z direction is slightly more affected and the force calculated using the Medium mesh is closer to that quantified using the Fine mesh. Fig. 7 shows the rotordynamic coefficients computed via Eqns. (12), (13), (14), and (15). It can be seen that no significant change in terms of rotordynamic coefficients is observed with the number of nodes.

RESULTS: LEAKAGE

Table 5 lists the predicted leakage flows for the various cases. It is noticed that for an increasing LVF the total leakage

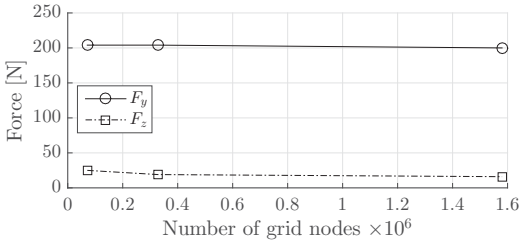

FIGURE 6: FORCES VS NO. OF NODES. LVF= 0%. $\Omega = \Omega_{rot} = 166.67\,\text{Hz}$

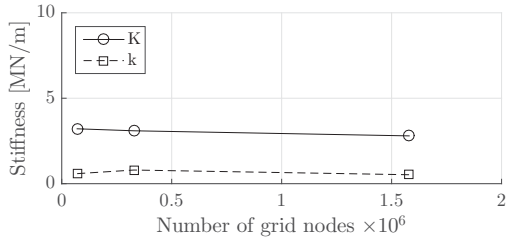

(a) STIFFNESS

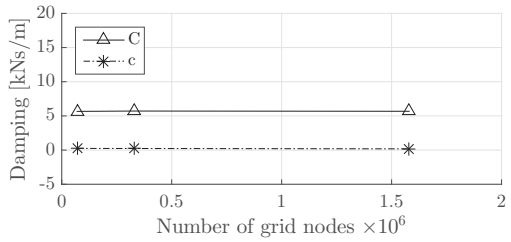

(b) DAMPING

FIGURE 7: ROTORDYNAMIC COEFFICIENTS VS NO. OF NODE. LVF= 0%. $\Omega = \Omega_{rot} = 166.67\,\text{Hz}$

rate is increasing. For increasing GVF the total leakage rate decreases monotonously, however at a lower rate than for the LVF cases. These findings are in qualitative agreement with results reported in [30].

RESULTS: LOW LVF CONDITIONS

In this section the effect of the low LVF on the rotordynamic coefficients will be shown. Cases $1-3$ are considered, i.e. with conditions relevant for wet gas compression. It should be noted

TABLE 5: LEAKAGE RATES

Case no.	Case	Air [kg/s]	Water [kg/s]	Total [kg
1	LVF = 0%	0.283	0	0.283
2	LVF = 3%	0.197	0.243	0.440
3	LVF = 5%	0.168	0.353	0.521
4	GVF = 0%	0	1.451	1.451(
5	GVF = 3%	0.0011	1.449	1.4501
6	GVF = 5%	0.0019	1.444	1.4459

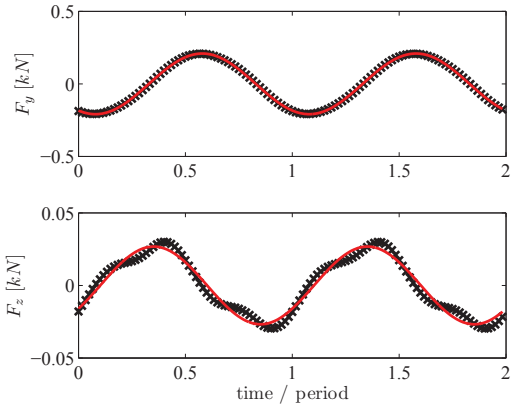

FIGURE 8: EXAMPLE OF REACTION FORCES. LVF= 5%, 125 Hz $\Omega = 0.75\Omega_{rot}$

that while for Case 1 (LVF= 0%) and Case 2 (LVF= 3%) the sinusoidal behaviour of the forces could be precisely represented as a single harmonic as in the example shown in Fig. 5, the behaviour in the z direction for Case 3 (LVF= 5%) was not perfectly periodical. An example (at the excitation frequency of 125 Hz, $\Omega = 0.75 \times \Omega_{rot}$) is shown in Fig. 8. It is possible to see that higher harmonics are observed in the response in the z direction. Consequentially, an underestimation of the force in z direction may result for the cases at LVF= 5%. It is noted that the response in the z direction is approximately one order of magnitude smaller than the response in the direction of the excitation, i.e. y. This was observed throughout all the cases at low LVF (Cases $1-3$). Fig. 9 shows the rotordynamic coefficients obtained via IPM analysis for the cases at low LVF conditions. The coefficients do not vary significantly with the perturbation frequency and increasing liquid content in the flow increases the direct stiffness and the direct damping. The increase is monotonous with

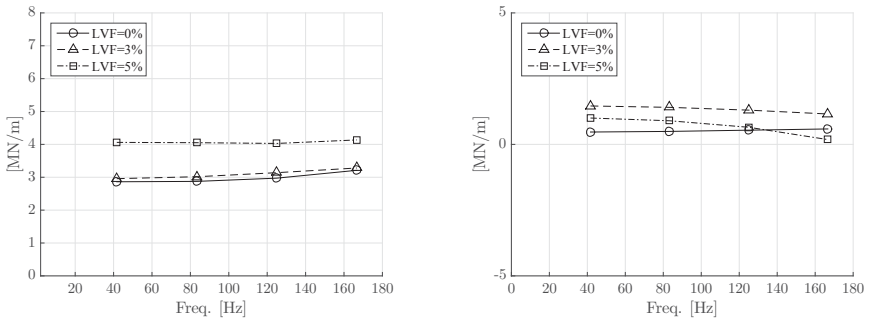

(a) DIRECT STIFFNESS

(b) CROSS COUPLED STIFFNESS

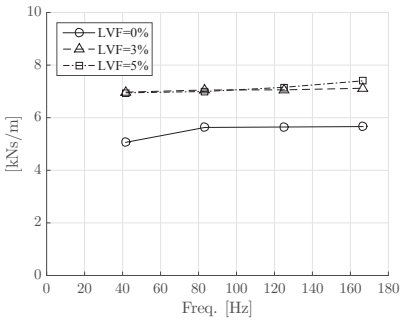

(c) DIRECT DAMPING

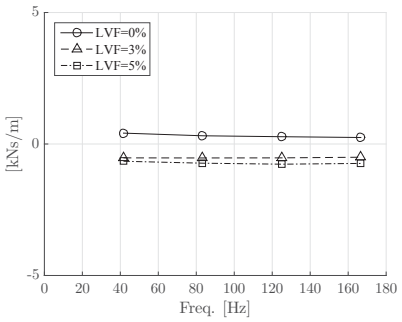

(d) CROSS COUPLED DAMPING

FIGURE 9: ROTORDYNAMICS COEFIICIENTS: LOW LVF CONDITIONS.

the LVF and the increase in direct damping is in agreement with that found by [29] and [30] by means of bulk flow codes. The increase is however mild compared to the tenfold increase in direct damping recently found experimentally by [33] in a case with a non rotating shaft. Increasing the LVF mildly increases the cross-coupled stiffness coefficients, which is in contrast with results reported in [29]. In that study the cross coupled coefficients were decreasing with increasing LVF. This increase is however not monotonous: The cross coupled stiffness for LVF=5% is in between the LVF=0% case and the LVF= 3% case, with one outlier at $\Omega = \Omega_{rot}$ in which it is even lower than in the LVF=0% case. This could be due to the underestimation of the forces in z direction as shown in Fig. 8. The cross coupled damping decreases monotonously towards negative values for increasing LVF, and is generally lower than the direct damping.

RESULTS: LOW GVF CONDITIONS

In this section the effect of the low GVF on the rotordynamic coefficients will be shown. Cases $4-6$ are considered, i.e. with conditions relevant for multiphase pumping and Fig. 10 shows the rotordynamic coefficients obtained via IPM analysis. At high liquid content (low GVF) the coefficients show a stronger dependency on frequency, due to the added mass effect. The effect of increasing GVF on the direct stiffness seems to be frequency dependent, with lower stiffness at high frequency and higher stiffness at low frequency. The direct damping instead decreases with increasing GVF. This was also observed in [30]. It should be noted that for all low GVF cases it proved difficult to obtain a sinusoidal response of the forces at low frequency, i.e. the excitation frequency of $41.67\,\text{Hz}$, $\Omega = 0.25 \times \Omega_{rot}$. An example is shown in Fig.with 11, for Case 6 (GVF=5%). It can be seen that the response in the y direction is not perfectly periodical. It is also noted that the response in the z direction is of the same order of magnitude as the response in the direction

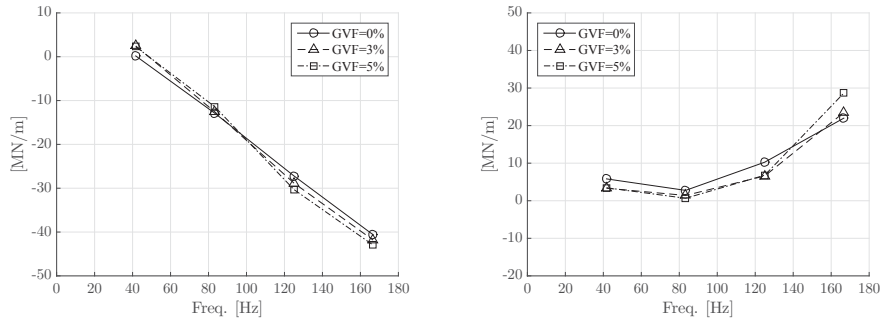

(a) DIRECT STIFFNESS (b) CROSS COUPLED STIFFNESS

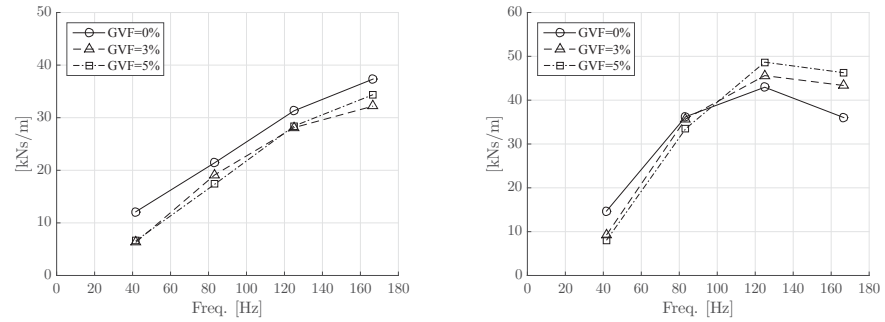

(c) DIRECT DAMPING (d) CROSS COUPLED DAMPING

FIGURE 10: ROTORDYNAMICS COEFIICIENTS: LOW GVF CONDITIONS

of the excitation, i.e. y. This was observed throughout all the cases at low GVF (Cases $4-6$). The cross coupled stiffness and damping show a rather complex behaviour with increasing GVF and frequency, and it should keep in mind that the low frequency data might be affected by the non perfect periodicity of the force response, depicted in Fig. 11. Surprisingly, the cross coupled damping coefficients are larger in magnitude than the direct damping coefficients. In general, the impact of increasing GVF on the coefficients is rather mild.

CONCLUSION

This paper presents the first attempt to apply CFD simulations to explicitly determine the rotordynamic coefficients of seals subdued to multiphase flow conditions. Low LVFs and low GVFs are analysed, making the study relevant for wet gas compression as well as for multiphase pumping. The study showed a mild influence of low values of LVF and GFV on the rotordynamic coefficients. For wet gas compression conditions, increasing the LVF corresponds to a general increase in direct stiffness and damping, as well as cross coupled stiffness. For multiphase pumping conditions an increase in GVF entailed a decrease in direct damping, while the direct and cross coupled stiffnesses showed a more complex frequency dependent behaviour.

The CFD based study presented here outlines the theoretical component of the twofold effort employed to establish a validated predictive tool for multiphase seal analysis. The near future completion of the planned multiphase seal testing experimental campaign, will provide the much needed data for benchmarking the theoretical tools.

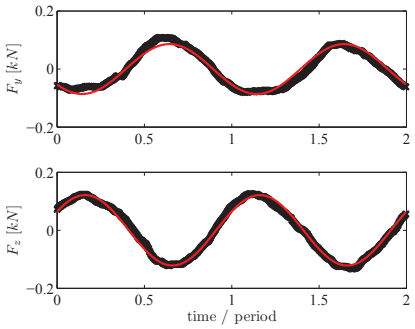

FIGURE 11: EXAMPLE OF REACTION FORCES. GVF= 5%, 41.67 Hz $\Omega = 0.25\Omega_{rot}$

NOMENCLATURE

Ω	Excitation frequency [Hz]
Ω_{rot}	Rotational velocity of the rotor [rpm]
Y, Z	Lateral rotor coordinates [mm]
K	Direct seal stiffness [N/m]
k	Cross coupling seal stiffness [N/m]
C	Direct seal damping [Ns/m]
c	Cross coupling seal damping [Ns/m]
F_y, f_y, F_z, f_z	Seal reaction force components [N]
A	Excitation amplitude [mm]
i	Complex unit
CFD	Computational Fluid Dynamics
GVF	Gas Volume Fraction
LVF	Liquid Volume Fraction
IPM	Instationary Perturbation Method
OEM	Original Equipment Manufacturer

REFERENCES

[1] Childs, D., 1993. *Turbomachinery Rotordynamics: Phenomena, Modeling, and Analysis*. John Wiley & Sons, Inc., Hoboken, New Jersey.

[2] Childs, D., and Vance, J., 1997. "Annular Gas Seals and Rotordynamics of Compressors and Turbines". In Proceedings of the Twenty-Sixth Turbomacinery Symposium, pp. 201–220.

[3] Picardo, A., and Childs, D. W., 2005. "Rotordynamic Coefficients for a Tooth-on-Stator Labyrinth Seal at 70 Bar Supply Pressures: Measurements Versus Theory and Comparisons to a Hole-Pattern Stator Seal". *Journal of Engineering for Gas Turbines and Power,* ***127***(4), pp. 843–855.

[4] Soulas, T., and Andres, L. S., 2007. "A Bulk Flow Model for Off-Centered Honeycomb Gas Seals". *Journal of Engineering for Gas Turbines and Power,* ***129***(1), pp. 185–194.

[5] Scharrer, J. K., 1987. "Theory Versus Experiment for the Rotordynamic Coefficients of Labyrinth Gas Seals: Part IA Two Control Volume Model". In Proc. ASME 11th Biennial Conference on Mechanical Vibration and Noise, Rotating Machinery Dynamics Volume Two, pp. 411–426.

[6] Iwatsubo, T., 1980. "Evaluation of Instability Forces of Labyrinth Seals in Turbines or Compressors". In Proc. Rotordynamic Instability Problems in High Performance Turbomachinery,NASA CP-2133, Texas A&M University, pp. 139–167.

[7] Hirano, T., Guo, Z., and Kirk, R. G., 2005. "Application of Computational Fluid Dynamics Analysis for Rotating MachineryPart II: Labyrinth Seal Analysis". *Journal of Engineering for Gas Turbines and Power,* ***127***(4), pp. 820–826.

[8] Moore, J. J., 2003. "Three-Dimensional CFD Rotordynamic Analysis of Gas Labyrinth Seals". *Journal of Vibration and Acoustics,* ***125***(4), pp. 427–433.

[9] Nielsen, K. K., Jønck, K., and Underbakke, H., 2012. Hole-Pattern and Honeycomb Seals Rotordynamic Forces: Validation of CFD Based Prediction Techniques.

[10] Kirk, R., 1988. "Evaluation of Aerodynamic Instability Mechanisms for Centrifugal CompressorsPart II: Advanced Analysis". *ASME J. Vibr. Acoust.*(110), pp. 207–212.

[11] Marquette, O., Childs, D. W., and Philips, S. G., 1997. "Theory Versus Experiments for Leakage and Rotordynamic Coefficients of Circumferetially- Grooved Liquid Annular Seals with L/D of 0.45". In Proceedings of the 1997 ASME Fluids Engineering Division Summer Meeting, pp. ASME Paper No. FED SM97–3333.

[12] Childs, D. W., and Scharrer, J. K., 1986. "An Iwatsubo Based Solution for Labyrinth Seals: A Comparison to Experimental Results". *ASME J. Eng. Gas Turbines Power*(108), pp. 325–331.

[13] Vannini, G., Bertoner, M., Nielsen, K. K., Stronach, R., Iudiciani, P., and Bertoneri, M., 2016. "Experimental Results and CFD Simulations of Labyrinth and Pocket Damper Seals for Wet Gas Compression". *Journal of Engineering for Gas Turbines and Power,* ***138***(May), pp. 052501–1.

[14] Athevale, M. M., Przekwas, A. J., Hendricks, R. C., and Liang, A., 1994. "SCISEAL: A 3D CFD Code for Accurate Analysis of Fluid Flow and Forces in Seals". In Proceedings of the Advanced ETO Propulsion Conference, pp. 337–345.

[15] Moore, J. J., and Palazzolo, A. B., 1999. "CFD Comparison to 3D Laser Anemometer and Rotordynamic Force Measurements for Grooved Liquid Annular Seals". *ASME J. Tribol.,* ***121***(2), pp. 307–314.

[16] Kim, N., and Rhode, D. L., 2000. "A New CFD-Perturbation Model For The Rotordynamics of Incompressible Flow Seals". In ASME International Gas Turbine and Aeroengine Congress and Exposition.

[17] Nordmann, R., and Dietzen, F. J., 1988. Finite Difference Analysis of Rotordynamic Seal Coefficients For An Eccentric Shaft Position.

[18] Rhode, D. L., Hensel, S. J., and Guidry, M. J., 1992. "Labyrinth Seal Rotordynamic Forces Using a Three-Dimensional Navier-Stokes Code". *ASME J. Tribol.*(114), pp. 683–689.

[19] Tam, L. T., Przekwas, A. J., Muszynska, A., Hendricks, R. C., Braun, M. J., and Mullen, R. L., 1988. "Numerical and Analytical Study of Fluid Dynamic Forces in Seals and Bearings". *ASME J. Vibr. Acoust.,* ***110***, pp. 315–325.

[20] Nielsen, K. K., Childs, D. W., and Myllerup, C. M., 2001. "Experimental and Theoretical Comparison of Two Swirl Brake Designs". *Journal of Turbomachinery,* ***123***(2), p. 353.

[21] Nielsen, K. K., Myllerup, C. M., and Van den Braembussche, R. A., 1999. "Parametric Study of the Flow in Swirl Brakes by Means of a 3D Navier- Stokes Solver". In Transactions of the Third European Conference on Turbomachinery, pp. 489–498.

[22] Nielsen, K. K., Van den Braembussche, R., and Myllerup, C., 1998. "Optimization of swirl brakes by means of a 3D Navier-Stokes solver". In The 1998 International Gas Turbine & Aeroengine Congress & Exhibition, p. 7.

[23] Wagner, N., Steff, K., Gausmann, R., and Schmidt, M., 2009. "Investigations on the Dynamic Coefficients of Impeller Eye Labyrinth Seals". *Proceedings of the Thirty-eighth Turbomacinery Symposium*.

[24] Kocur, J. A., Nicholas, J. C., and Lee, C. C., 2007. "Surveying Tilting Pad Journal Bearing and Gas Labyrinth Seal Coefficients and Their Effect on Rotor Stability". In Proceedings of the 36th Turbomachinery Symposium, pp. 1–10.

[25] Beatty, P. A., and Hughes, W. F., 1987. "Turbulent Two-Phase Flow in Annular Seals". *A S L E Transactions,* ***30***(1), pp. 11–18.

[26] Beatty, P. a., and Hughes, W. F., 1990. "Stratified Two-Phase Flow in Annular Seals". *Journal of Tribology,* ***112***(April), p. 372.

[27] Arauz, G. L., and San Andres, L., 1998. "Analysis of Two-Phase Flow in Cryogenic Damper Seals Part I: Theoretical Model". *Journal of Tribology,* ***120***(2), p. 228.

[28] Arauz, G. L., and Andres, L. S., 1998. "Analysis of Two-Phase Flow in Cryogenic Damper SealsPart II: Model Validation and Predictions". *Journal of Tribology,* ***120***(April), pp. 228–233.

[29] Arghir, M., Abdelmalik, Z., and Gérard PINEAU, P., 2011. "Rotordynamic Analysis of Textured Annular Seals With Multiphase (Bubbly) Flow". *Incas Bulletin,* ***3***(3), pp. 3–13.

[30] Andrés, L. S., 2011. "Rotordynamic Force Coefficients of Bubbly Mixture Annular Pressure Seals". *Proceedings of ASME Turbo Expo 2011,* ***60***, pp. 1–10.

[31] Vannini, G., Bertoneri, M., Vescovo, G. D., and Wilcox, M., 2014. "Centrifugal Compressor Rotordynamics in Wet Gas Conditions". *Proceedings of 43rd Turbomachinery Symposium, Huston, Texas*.

[32] Iwatsubo, T., and Nishino, T., 1993. "An Experimental Study on the Static and Dynamic Characteristics of Pump Annular Seals". In 7th Workshop on Rotordynamic Instability Problems in High Performance Turbomachinery.

[33] Andrés, L. S., Lu, X., and Liu, Q., 2015. "Measurements Of Flowrate And Force Coefficients In A Short Length Annular Seal Supplied With A Liquid/Gas Mixture (Stationary Journal)". *Tribology Transactions,* ***2004***(November), pp. 00–00.

[34] Voigt, A. J., Mandrup-Poulsen, C., Nielsen, K. K., and Santos, I. F., 2016. "Design and Calibration of a Full Scale Active Magnetic Bearing Based Testing Facility for Investigating Rotordynamic Properties of Turbomachinery Seals in Multiphase Flow". In Accepted for publication in the proceedings of the ASME Turbo Expo 2016 and recommended for journal publication.

Publication P2

Design and Calibration of a Full Scale Active Magnetic Bearing Based Testing Facility for Investigating Rotordynamic Properties of Turbomachinery Seals in Multiphase Flow

---

Paper published in the proceedings of ASME Turbo Expo 2016. Additionally, the paper has been accepted for journal publication in the ASME Journal of Engineering for Gas Turbines and Power.

Proceedings of ASME Turbo Expo 2016: Turbomachinery Technical Conference and Exposition
GT2016
June 13-17, 2016, Seoul, South Korea

GT2016-57893

DESIGN AND CALIBRATION OF A FULL SCALE ACTIVE MAGNETIC BEARING BASED TEST FACILITY FOR INVESTIGATING ROTORDYNAMIC PROPERTIES OF TURBOMACHINERY SEALS IN MULTIPHASE FLOW

Andreas Jauernik Voigt
Lloyd's Register Consulting/
Department of Mechanical Engineering
Technical University of Denmark
Copenhagen, Denmark
Email: andreas.voigt@lr.org

Christian Mandrup-Poulsen
Department of Mechanical Engineering
Technical University of Denmark
Copenhagen, Denmark
Email: cman@mek.dtu.dk

Kenny Krogh Nielsen
Lloyd's Register Consulting
Copenhagen, Denmark
Email: kenny.krogh-nielsen@lr.org

Ilmar F. Santos*
Department of Mechanical Engineering
Technical University of Denmark
Copenhagen, Denmark
Email: ifs@mek.dtu.dk

ABSTRACT

The recent move towards subsea oil and gas production brings about a requirement to locate process equipment in deepwater installations. Furthermore, there is a drive towards omitting well stream separation functionality, as this adds complexity and cost to the subsea installation. This in turn leads to technical challenges for the subsea installed pumps and compressors that are now required to handle multiphase flow of varying gas to liquid ratios. This highlights the necessity for a strong research focus on multiphase flow impact on rotordynamic properties and thereby operational stability of the subsea installed rotating machinery. It is well known that careful design of turbomachinery seals, such as interstage and balance piston seals, is pivotal for the performance of pumps and compressors. Consequently, the ability to predict the complex interaction between fluid dynamics and rotordynamics within these seals is key. Numerical tools offering predictive capabilities for turbomachinery seals in multiphase flow are currently being developed and refined, however the lack of experimental data for multiphase seals renders benchmarking and validation impossible. To this end, the Technical University of Denmark and Lloyd's Register Consulting are currently establishing a purpose built state of the art multiphase seal test facility, which is divided into three modules. Module I consists of a full scale Active Magnetic Bearing (AMB) based rotordynamic test bench. The internally designed custom AMBs are equipped with an embedded Hall sensor system enabling high-precision non-contact seal force quantification. Module II is a fully automatised calibration facility for the Hall sensor based force quantification system. Module III consists of the test seal housing assembly. This paper provides details on the design of the novel test facility and the calibration of the Hall sensor system employed to measure AMB forces. Calibration and validation results are presented, along with an uncertainty analysis on the force quantification capabilities.

*Address all correspondence to this author.

NOMENCLATURE

$\mathbf{B}$	Magnetic flux density [T]
Δy	Rotor displacement from rotor offset [m]
Ω	Rotational velocity of shaft [rpm]
C	Direct seal damping [Ns/m]
c	Cross coupling seal damping [Ns/m]
EM	Electromagnet
F_{act}	AMB actuator forces [N]
$F_{app,y}$,$F_{app,z}$	Calibration forces [N]
$F_{A,y}$,$F_{A,z}$	AMB A force components [N]
$F_{B,y}$,$F_{B,z}$	AMB B force components [N]
$F_{c,y}$,$F_{c,z}$	Coupling force components [N]
F_{K_H}	Force estimated by Hall sensor system [N]
F_y,F_z	Seal reaction force components [N]
I_{bias}	AMB bias current [A]
K	Direct seal stiffness [N/m]
k	Cross coupling seal stiffness [N/m]
K_a,K_b,K_c,K_d	Hall sensor calibration constants [N/V]
M	Direct seal inertia [kg]
m	Cross coupling seal inertia [kg]
u	Error
$M_{c,y}$,$M_{c,z}$	Coupling moment components [Nm]
V_H,$V_{H,N}$,$V_{H,S}$	Hall voltage signal [V]
AMB	Active Magnetic Bearing
CFD	Computational Fluid Dynamics
FBD	Free Body Diagram
GVF	Gas Volume Fraction
LVF	Liquid Volume Fraction
I/O	Input/Output
IPM	Instationary Perturbation Method
MAE	Mean Absolute Error
PCB	Printed Circuit Board
PID	Proportional-Integral-Derivative
PWM	Pulse-Width Modulation
SISO	Single-Input Single-Output
VSD	Variable Speed Drive

INTRODUCTION

The energy sector is dependent on high pressures, small clearances, and high rotational velocities in compressors and pumps to ensure a high productivity. However, the range of rotational velocities is restricted by the stability margins of the rotating machinery [1, 2]. It is well known that the rotordynamic forces generated by the interaction of process fluid, rotor and seals are of primary importance for the rotordynamic stability and thereby operability and life span of the rotating machinery employed in the energy sector today [3, 4], rendering seals a very important subject of study.

A significant amount of research has been done over the last 40 years to identify the rotordynamic properties of seals subdued to single-phase flows, both theoretically and experimentally, in order to ensure the very important predictive capabilities for seal dynamics through mathematical modelling [4–27]. However, as highlighted in the survey presented by Kocur, et al. [28], there is still work to be done. Kocur, et al. found, among other, very large variations in rotordynamic coefficients for gas labyrinth seals predicted by survey participant from both academia and industry.

As oil and gas reserves presently in production deplete, the global oil and gas industry continues to move towards production from fields at greater sea depth and in the Arctic regions. The production from many of these fields requires compression and pumping to take place on the sea floor where the possibility of performing liquid and gas separation on the well stream is very limited. Consequently, the subsea installed pumps and compressors have to cope with streams that cannot be considered single-phase. Multiphase fluid mixture will have significantly different fundamental properties [29] as compared to single-phase fluids, and therefore the modelling of the multiphase seal flow impact on rotordynamics requires special treatment.

As indicated above the research on single-phase seal rotordynamics is well established. However, the research on multiphase seal rotordynamics is presently only in its infancy [30–34]. The experimental validation of existing mathematical models is in particular insufficient. An improved understanding of the underlying assumptions and limitations of these models is necessary to further justify their usage, which only rigorous experimental testing and comparison with theoretical results will provide. The focus of this paper is to present a newly developed test facility for testing seals subdued to both single- and multiphase flow conditions. The paper contains a presentation of the different modules of the test facility as well as a calibration of the main functionality of the test facility. The underlying work presents the status of the experimental research branch of the ongoing collaboration between the Technical University of Denmark (DTU), Lloyd's Register Consulting (LRC), OneSubsea, TOTAL and Statoil. This research venture was initiated to ensure validated predictive capabilities through state of the art Computational Fluid Dynamics (CFD) benchmarked using high quality experimental data. The state of the art regarding determination of rotordynamic coefficients for seals in multiphase flow using CFD can be found in [35].

BASELINE FUNCTIONALITY CONSIDERATIONS FOR THE TEST FACILITY DESIGN

The multiphase seal test facility is designed to enable component level experimental identification of rotordynamic properties of turbomachinery seals. The test results are to be used for benchmarking and performance evaluation of Computational Fluid Dy-

namics (CFD) based numerical tools as well as bulk flow models used for theoretical prediction of seal properties. The functional principle of the test facility adheres to the group conventional parameter identification schemes for rotordynamic components, which is based on frequency dependent time domain perturbation of the seal flow. The goal of the identification scheme is to extract stiffness, damping, and where relevant, inertia properties of seals subdued to both single- and multiphase flow. For rotordynamic modelling purposes it is conventional to cast the seal model in the following form [3], assuming frequency dependent coefficients and neglecting inertia effects

$$-\begin{Bmatrix} F_z \\ F_y \end{Bmatrix} = \begin{bmatrix} K(\Omega) & k(\Omega) \\ -k(\Omega) & K(\Omega) \end{bmatrix} \begin{Bmatrix} z \\ y \end{Bmatrix} + \begin{bmatrix} C(\Omega) & c(\Omega) \\ -c(\Omega) & C(\Omega) \end{bmatrix} \begin{Bmatrix} \dot{z} \\ \dot{y} \end{Bmatrix} \quad (1)$$

The test facility is designed to be able to mirror the Instationary Perturbation Method (IPM) applied for numerical estimation of seal properties using CFD. This method is described in detail in [26, 35–38], and relies on perturbing the seal flow by moving the shaft in a prescribed 1D sinusoidal pattern with a constant amplitude and for multiple frequencies. Acquiring information on the reaction forces exerted on the seal rotor allows the coefficients of Eqn. 1 to be determined by applying simple time domain identification techniques [26]. Active Magnetic Bearings (AMBs) are very well suited to provide the necessary perturbation functionality, and it should be mentioned that the AMBs allow for much more sophisticated perturbation patterns and thereby identification techniques, than the baseline functionality discussed above.

The forces exerted on the seal rotor from perturbing the seal flow need to be quantified with high precision and reliability to allow for identification of the rotordynamic seal properties. The AMB readily facilitates force estimation through measurement of the AMB coil currents and knowledge of the shaft position within the AMB. This method is referred to as the $(i-s)$ methodology in the literature [39]. However, it has been shown that higher force estimation precision can be achieved by employing Hall sensors mounted in the pole surface areas of the AMBs [40, 41] as compared to the $(i-s)$ method. Additionally, low force estimation errors have been reported using fiber optic strain gauges [42–44], giving merit to a continued research effort. However, the relatively low level of experience with this method reported in the literature, and the fact that it is susceptible to calibration drift [42], makes it less proven than the two previously outlined force estimation approaches.

Conventional placement of Hall sensors in AMB poles requires enlargement of the air gap between rotor and stator in the AMBs consequently reducing the load bearing capacity of the AMB system. To accommodate this the test facility have been designed with a Hall sensor system where the Hall sensors are completely embedded into the pole surface, a method previously employed with success in stand-alone AMBs used for excitation purposes [41, 45]. This test facility is the first to feature a shaft completely radially supported by two AMBs with embedded Hall sensors. To achieve the desired precision needed to perform experimental identification of seal rotordynamic properties it is of paramount importance that the Hall sensor system is calibrated in-situ, which is the focus of the last part of this paper. Additionally, it is essential for identification purposes that the relative motion of the seal rotor to the seal stator is precisely determined. High-precision position data (uncertainty including noise below $1\,\mu$m) is readily available from the AMBs, as these inherently features position sensors needed for feedback control. Calibration of the position sensors are not discussed further in this paper.

MULTIPHASE SEAL TEST FACILITY

The test facility is comprised of three modules: (1) An AMB based rotordynamic test bench, (2) a calibration module for the Hall sensor system, and (3) a test seal housing assembly and multiphase flow loop. It should be mentioned that the calibration module and the seal housing assembly replaces each other, and cannot be installed on the test bench simultaneously. The individual modules are introduced in the following sections.

MODULE I

A picture of the test facility in its calibration configuration is presented in Fig. 1, in which both Module I and II are visible. The picture shows the main elements of Module I, namely: The two radial AMBs, the shaft assembly, the asynchronous motor, the intermediate shaft pedestal, and the flexible coupling. The main shaft is supported radially by the AMBs and axially by the intermediate shaft through a flexible disc coupling. The intermediate shaft sits in high-speed angular contact ball bearings within the intermediate shaft pedestal. The 7.5 kW three-phase asynchronous motor is controlled through a Variable Speed Drive (VSD) unit and drives the intermediate shaft, and thereby the main shaft, through a timing belt interface. The timing belt pulleys on the motor and intermediate shaft can be changed to achieve the wanted rpm range for the main shaft. At the motor end of the intermediate shaft an encoder is attached through a flexible multibeam coupling (not visible on Fig. 1). The encoder provides precise information on shaft speed and angular position, the latter being important for runout compensation purposes. The main shaft assembly parameters are summarized in Table 1. The shaft is symmetric and can be considered rigid within the operational frequency range of the test facility with its first bending mode at 550 Hz. The main component of the AMB rotor assemblies are made from laminated electrical steel

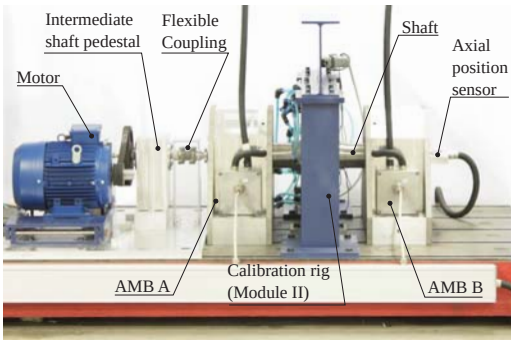

FIGURE 1: TEST FACILITY IN THE CALIBRATION CONFIGURATION

sheets identical to that of the AMB stators, and the assemblies are mounted onto the main shaft through an interference fit.

The hub component of Module I is the radial eight pole heteropolar AMB depicted in Fig. 2 without its cover plates to reveal the internal layout. The AMB design parameters are presented in Table 2. Each AMB features three main component groups visualized in a section view on Fig. 3: (1) The support structure is indicated with a blue hatched pattern in Fig. 3. The support structure consists of a main aluminium body bolted onto an aluminium base and two 20 mm thick stainless steel plates bolted onto each side of the AMB to provide transversal stiffness to the assembly. (2) The backup bearing assembly is indicated with a red hatched pattern on Fig. 3. The backup bearing assembly features a set of grease lubricated high-precision high-speed angular contact ball bearings. These are mounted in a back-to-back configuration to account for axial loads during a potential shaft drop. The backup bearings are seated in a compliant ring design that facilitates dissipation of energy during a shaft drop. The backup bearing assembly also houses the primary AMB sensor system consisting of two high-precision inductive VibroMeter position probes used for feedback control. (3) The AMB stator assembly, which is indicated with a green hatched pattern on Fig. 3. The stator laminates, made from SURA M270-35A high quality electrical steel, are sandwiched in between two retention plates and held together by bolt connections. The stator design adopts the conventional tilted design [39] where the axes of the magnetic bearing actuators are shifted 45° so that two electromagnets can be engaged to account for the gravitational load of the shaft. On the back of the stator assembly the interface Printed Circuit Board (PCB) board for the Hall sensor system is positioned. The Hall sensors are cemented into tracks in each of the eight

TABLE 1: MAIN SHAFT PARAMETERS

Shaft length	860	mm
Shaft assembly mass	69	kg
AMB rotor outer diameter	150	mm
Test seal rotor diameter	110	mm
First bending mode @	550	Hz
Lamination thickness	0.35	mm
Number of laminations	228	
Laminate material	SURA M270-35A	

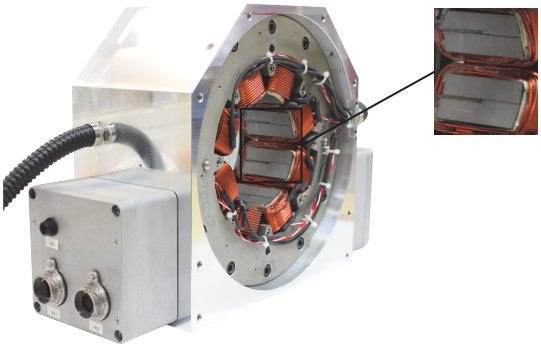

FIGURE 2: A VIEW OF THE TEST FACILITY AMB DESIGN SHOWING THE EMBEDDED HALL SENSOR PLACEMENT IN A ZOOM VIEW

pole legs of the stator. The Hall sensor placement can be seen on the zoom view of Fig. 2. Embedding the Hall sensors keeps the fragile sensors protected, at the cost of a slightly reduced effective pole area. This reduces the maximum force obtainable from the AMBs, however the effect is minimal and has been determined to be in the order of 2%, which is consistent with previous findings [45]. The Hall sensor supply and signal leads are soldered onto the interface PCB board from which the Hall sensor signal is fed to the signal amplifier situated on the side of the AMB main housing. Amplification and signal conditioning of the Hall sensor signals close to the sensor helps keep noise contamination of the signals to a minimum and thereby the signal to noise ratio high. Both the Hall sensor constant current supply and the amplification circuits have been custom built for the test facility.

The AMBs are designed to be operated in differential mode [39] and feedback based position control of the shaft is currently

TABLE 2: AMB DESIGN PARAMETERS

Stator outer diameter	300	mm
Stator inner diameter	151	mm
Nominal radial air gap	0.5	mm
Pole width	40	mm
Pole depth (axial)	80	mm
Number of poles	8	
Winding configuration	N-S-S-N-N-S-S-N	[-]
Lamination thickness	0.35	mm
Number of laminations	228	
Laminate material	SURA M270-35A	
Number of coil windings	36	
Coil wire thickness	2.8	mm
Max. load capacity (per AMB)	7500	N
Bias current range	4 to 10	A
Coil temp. sensor type	PT100	
Number of temp. sensors	4 (one per coil pair)	
Number of Hall sensors	8	
Hall sensor type	F.W. Bell - FH-301	
Hall sensor dimensions ($l \times w \times h$)	$2.54 \times 3.175 \times 0.5$	mm

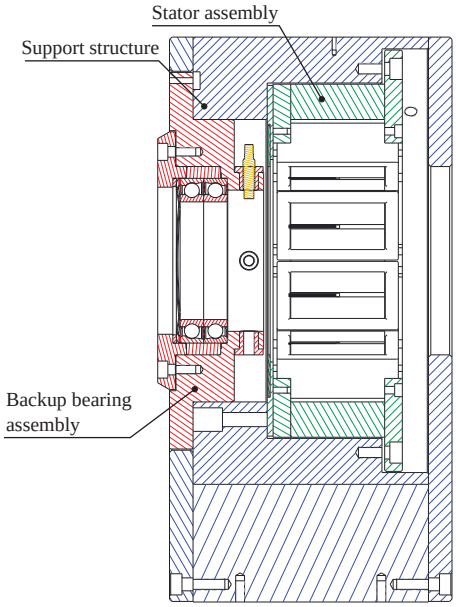

FIGURE 3: SECTION VIEW OF AMB SHOWING THREE MAIN COMPONENT GROUPS

achieved through a decentralized Single-Input Single-Output (SISO) control structure. The baseline controller is a conventional Proportional-Integral-Derivative (PID) controller, however the system can also be operated using a robust H_∞ controller. The controllers are embedded on a modular dSPACE I/O system that facilitates control and data acquisition for the entire test facility. The AMBs are supplied by eight 3 kW high-speed Pulse-Width Modulation (PWM) mode power amplifiers from Delta-Elektronika. The high level of controllability enables the AMBs to support the shaft, while perturbing the lateral motion of the shaft in an arbitrary pattern, which is needed for seal parameter identification.

MODULE II

The calibration facility consists of two features: (1) The calibration rig shown in Fig. 4 and (2) the calibration clamp seen on Fig. 5. The calibration clamp is clamped around the shaft, and while mounted, the rotation of the shaft is restricted. The calibration facility enables applying a controllable multi-directional load onto the shaft, which is accomplished through a set of four pneumatic pistons. Each individual piston can be electronically controlled through the dSPACE I/O interface both in terms of actuation direction and force magnitude. The magnitude of the applied force is controlled using a PD regulated proportional valve. The force from the pistons is transferred to the shaft by a grabbing device engaging with a set of Belleville springs that transfers the force to a high-precision HBM U9C force transducer in order to measure the imposed load. The grabbing device, seen in Fig. 5, is designed such that when a piston is parked in its most extended position, there is no contact between the calibration rig and the shaft, thus reducing force contamination in the calibration procedure. Additionally the grabbing device allows for misalignments thus reducing bending moments over the force transducer and thereby reducing erroneous force measurements during calibration. The highly controllable calibration facility enables complete automation of the calibration procedure for multiple load directions and shaft positions.

MODULE III

Module III is comprised of two main parts: the seal housing assembly and the multiphase flow loop, treated separately in the following.

Seal housing assembly The seal housing assembly is presented in Fig. 6 showing the inlet cavity and nozzles, the outlet feature containing the primary and secondary flow outlets,

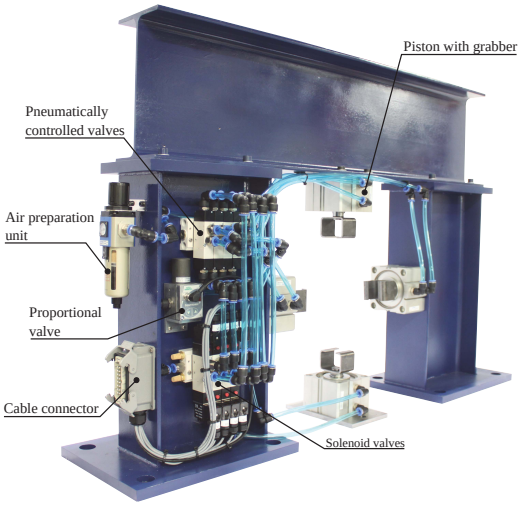

FIGURE 4: CALIBRATION RIG SHOWING PNEUMATIC PISTONS, GRABBING DEVICE AND CONTROL FEATURES

mounting holes for the pressure transducers, the test seal lands, and the support structure. The seal housing assembly adopts the modular design of the AMBs and is made in a split design to ease assembly. The flow medium is injected into the seal housing assembly through nozzles placed in the centre of the seal housing assembly and enters the two symmetrical test seals machined from a solid block of aluminium in a back-to-back configuration to alleviate axial thrust. After the flow has passed the seal lands, it exits in a controlled manner through two outlet features. Smooth annular seals have been chosen as initial test seal configurations since their simple geometry and well known single-phase performance constitutes a good choice for benchmarking the capabilities of the test facility initially.

A section view of the centre of the inlet cavity is presented in Fig. 7, which shows the symmetrical distribution of the four inlet nozzles as well as the two mounting holes for the inlet pressure transducers. In this initial iteration of the seal housing assembly design the pre-swirl is fixed and cannot be adjusted mechanically but only by changing injection flow velocity through modifying the nozzle geometry. As evident from the almost tangential injection direction, the seal housing assembly is aimed at testing seals in the high pre-swirl range. The nozzles are held in place by a flow adapter component, which additionally interfaces with the flow supply lines.

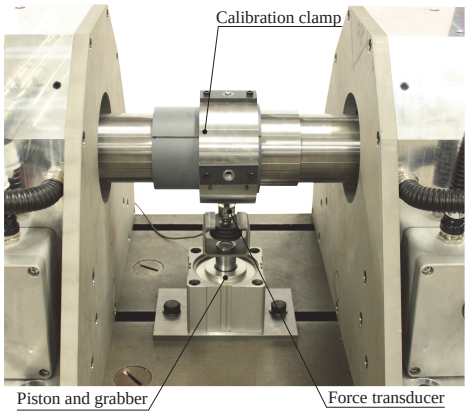

FIGURE 5: SIMPLIFIED CALIBRATION SETUP SHOWING CALIBRATION CLAMP, SINGLE PISTON WITH GRABBER, AND FORCE TRANSDUCER

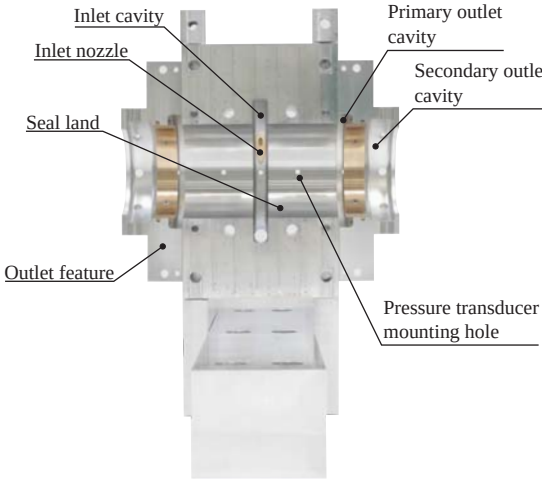

FIGURE 6: HALF PART OF SEAL HOUSING ASSEMBLY SHOWING INLET AND OUTLET FEATURES

Since the test facility is designed to handle both pure gaseous, pure liquid and multiphase flows, the seal housing assembly outlet features require special attention, as it cannot be assumed that the flow can be exhausted to atmospheric conditions. Additionally, the wish to be able to run the test facility with

significant back-pressures entails that secondary sealing capabilities should be included in the design. Using conventional secondary seals for the outlet, e.g. labyrinth seals, gives rise to potential contamination of the test results as the secondary seals will produce radial forces similarly to the main test seals. The outlet feature design aims at avoiding the issue of contaminating radial forces from secondary seals.

The test facility outlet feature is shown in Fig. 8. The outlet feature has two sequential outlets, referred to as the primary and the secondary outlet, respectively. The primary outlet consists of eight circumferentially distributed outlet ports, four on each outlet feature half part, as shown on Fig. 8. Valves on the primary outlet ports can be adjusted to apply back-pressure to the seal flow (not shown). Any flow that does not follow the primary flow path passes through the secondary flow path into the secondary outlet cavity and exits through the secondary outlet ports or as leakage flow along the shaft. The main advantage of the outlet design is that sealing takes place between axially oriented surfaces in the secondary flow path between the shaft and the outlet feature lip, see Fig. 8. This entails that there will be no contaminating radial forces from the outlet feature since all radial clearances are kept at least a factor of two larger than the test seal clearance. To verify performance of the outlet feature design a full 3D Computational Fluid Dynamic (CFD) based performance validation study was conducted. The study found that for medium to high pressure ratios over the test seals, the flow in the primary flow path creates a Venturi ejector effect when passing the secondary flow path clearance, reversing the flow in the secondary flow path, effectively eliminating leakage flow. This phenomenon has been observed for a back-pressure of up to 10 bar at an inlet pressure of 40 bar for both single-phase water and air conditions.

The seal housing assembly is instrumented with Kistler piezo-resistive absolute pressure sensors of the type 4065B. These sensors measure absolute and dynamic pressure as well as temperature of the flow in the range from 0 to 200 bar. The mounting holes for the sensors can be seen in Fig. 9, along with an overview of the seal housing assembly main components in its seal testing configuration. The Kistler probes enable measuring the inlet and outlet cavity pressures and temperatures, as well as the pressure and temperatures of the flow within the seal lands. These measurements are valuable for comparison with simulated CFD results in the validation phase. In Table 3 key parameters for the seal housing and the test facility in general are summarized.

Flow loop The test facility is designed to operate with air and water flows. For run-in purposes the test facility will be supplied with a single-phase air flow in order to benchmark the rotordynamic seal properties identification capabilities of the test facility. The flow supply for the seal housing assembly consists of two separate supply strings for the two fluids. For multiphase operating conditions a mixing device is included upstream to the inlet injections nozzles of the seal housing assembly. Different sparger and injection nozzle based mixing devices are considered able to achieve homogeneous fluid mixtures for a large range of both Gas Volume Fractions (GVFs) and Liquid Volume Fractions (LVFs). The air supply string consists of a piston compressor supplying up to 65 bar to a 3 m^3 pressure tank through a series of filters ensuring dry gas conditions. The supply from the tank to the seal housing assembly is controlled by a regulator valve, capable of maintaining a stable output pressure though a supply pressure drop is experienced during tests. The water supply is designed in two iterations. The first accommodates wet gas testing for LVFs between 0 and 5 %, keeping the complexity, size and costs of the water supply to a minimum while still being able to attain multiphase seal test functionality of the test facility. For this setup the leakage flow containing water can be exhausted directly to a drain, eliminating the need for a separation unit and recycling of the water. The water supply for the first iteration is based around a high-pressure centrifugal pump, which matches the pressure of the air supply. The second iteration of the water supply incorporates upstream water reservoir, filtering units, high capacity pumping system and de-aeration unit for water recycling. The second iteration is currently in the design phase.

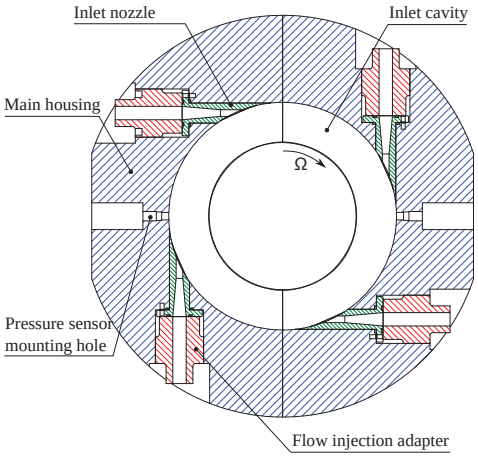

FIGURE 7: SECTION VIEW OF THE CENTRE OF THE INLET CAVITY SHOWING INLET NOZZLE DISTRIBUTION AND ORIENTATION AS WELL AS PRESSURE SENSOR MOUNTING HOLES

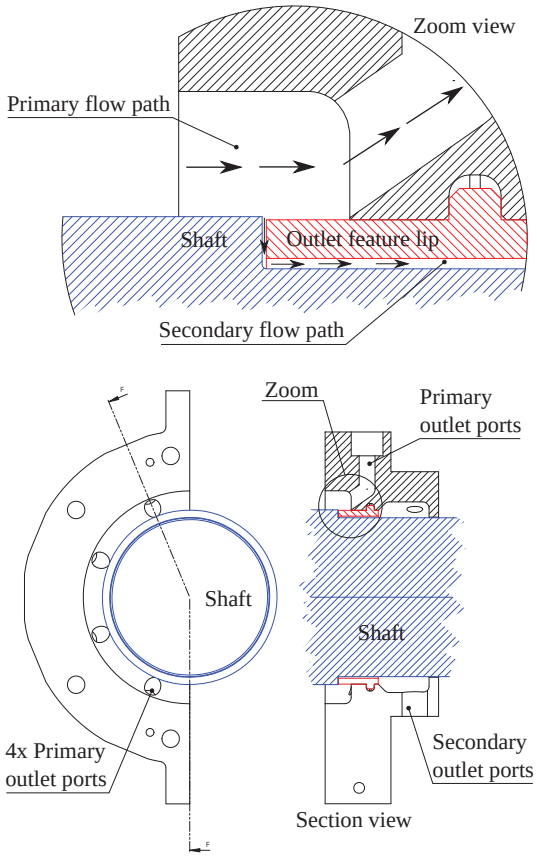

FIGURE 8: VISUALIZATION OF OUTLET FEATURE DETAILS

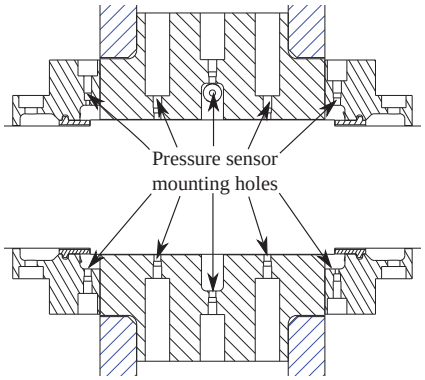

FIGURE 9: HORIZONTAL SECTION VIEW OF THE SEAL HOUSING ASSEMBLY

TABLE 3: SEAL HOUSING AND OVERALL TEST FACILITY KEY PARAMETERS

Inlet cavity diameter	150	mm
Inlet cavity width	18	mm
Nominal radial seal clearance	0.4	mm
Seal axial length	83	mm
Axial lip clearance in secondary flow path	0.4	mm
Secondary flow path radial clearance	0.8	mm
Total number of primary outlet ports	16	
Total number of secondary outlet ports	16	
Maximum number of pressure/temp. sensors	10	
Rotational velocity range	$0-10$	krpm
Perturbation frequency range	$0-250$	Hz
Calibrated force measurement range	$0-4$	kN
Air (single-phase) max. supply pressure	65	bar
Water (single-phase) max supply pressure	–	

HALL SENSOR CALIBRATION METHODOLOGY

The basic principle of the calibration procedure is to apply a known load to the centre of the shaft using the pneumatic pistons of the calibration facility and record the Hall sensor signals from all sensors. In addition to the Hall sensor signals the current signals, shaft position, and applied load are recorded simultaneously during calibration. Since the Hall sensors are embedded into the pole surface of the AMBs, it is necessary to determine if there is any significant position dependence of the calibration results [41]. However, a static calibration procedure will suffice even for dynamic force measurement purposes [41].

As mentioned earlier the force from the AMBs can in general be determined based on either Hall sensor signals or current/air gap measurements [40]. Both methods require calibration to yield precise force estimations. For a description of the force quantification method using current/air gap measurements, see e.g. [46]. The force estimation results from utilizing the two methods will be included in the result section, however since the calibration procedure is similar for both methods it will be outlined for the Hall sensor system here. The theory of measuring electromagnetic force from AMBs

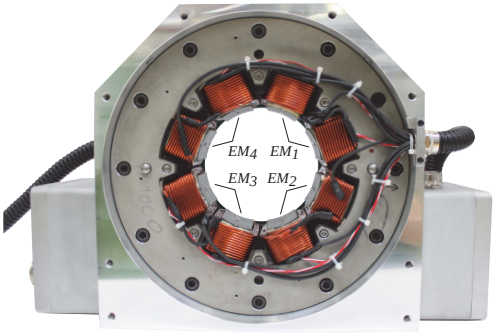

FIGURE 10: AMB STATOR FRONT VIEW SHOWING ELECTROMAGNET LAYOUT

using Hall sensors can be found in e.g. [41], however it is important to note that the Hall sensors measure magnetic flux density **B** and produce an analogue voltage proportional to **B**. The magnetic flux density **B** can then be related to the force acting on the AMB rotors. The layout of the electromagnetic actuators in the test facility AMB design can be seen in Fig. 10. Since the electromagnetic actuators can only exert a pulling force on the AMB rotors, the individual electromagnets are coupled in pairs to yield a dual acting electromagnetic actuator and operated using conventional differential driving [46]. The electromagnets EM_1 and EM_3, and EM_2 and EM_4 are paired together, respectively. Each electromagnet constitutes a closed electromagnetic circuit together with the AMB rotors hence the two Hall sensors mounted in each electromagnet theoretically see the same magnetic flux density. This motivates averaging the Hall sensor signals the following way

$$V_H = \frac{|V_{H,N}| + |V_{H,S}|}{2}$$

where N and S denotes the north and south pole, respectively. Combining the two Hall sensor signals, reduces the complexity of the calibration procedure, and helps average out random noise in the resulting signal V_H. The force from a single electromagnet can be estimated using a quadratic relation [47]

$$F_{mag} = K_a {V_H}^2 \tag{2}$$

in which F_{mag} is the estimated electromagnetic force, K_a is a constant to be determined through calibration, and V_H is the Hall sensor voltage signal. The force estimated as a function of the Hall sensor signals for an actuator consisting of two electromagnets (e.g. EM_1 and EM_3) can be represented as

$$F_{act} = K_b {V_{H,EM_1}}^2 - K_c {V_{H,EM_3}}^2$$

in which F_{act} is the exerted actuator force, K_b and K_c are two constants to be determined through calibration, and V_{H,EM_1} and V_{H,EM_3} are the combined Hall sensor signals from EM_1 and EM_3 given by Eqn. (2). Each AMB features two actuators tilted $\pm 45°$, respectively, from vertical and projecting the force from these onto the global reference system enables setting up the Free Body Diagram (FBD) presented in Fig. 11. In Fig. 11 $F_{A,y}$ and $F_{A,z}$ represents the AMB forces from AMB A, $F_{B,y}$ and $F_{B,z}$ represents the AMB forces from AMB B, $F_{app,y}$ and $F_{app,z}$ are the forces applied through the calibration facility pistons, F_g is the gravitational force from the shaft, $F_{c,y}$ and $F_{c,z}$ are the forces from the flexible coupling and $M_{c,y}$ and $M_{c,z}$ are moments acting on the shaft from the flexible coupling. Summing forces and moments applying the FBD of Fig. 11 result in four equations with eight unknowns, which are the calibration constants. These equations can be put on matrix form to yield a system of equations on the form $\mathbf{Ax} = \mathbf{b}$ where the matrix $\mathbf{A}$ contains information of the Hall sensor signals, $\mathbf{x}$ is a vector containing the eight calibration constants and $\mathbf{b}$ is a vector of force components applied using the calibration facility. This equation system can be utilized to obtain the calibration constants from a large calibration dataset through a Least Squares scheme. However as the system is underdetermined, the result would be non-unique and the constants non-physical. To obtain a unique solution a constrained fitting scheme is used which effectively reduces the number of unknowns to four constants, one for each actuator. An equivalent representation of the resulting system of equations used in the Least Squares scheme is shown in Eqn. (3), where the last index j of the Hall sensor voltages $V_{H,AMB,actuator,j}$ and applied force components $F_{app,direction,j}$, denotes a specific load step of the included n load steps. The factors r_A and r_B in the moment equations are length ratios. The result of a fitting is the four calibration constants $K_{H,AMB,actuator}$, which corresponds to a bias current and shaft position.

$$-\frac{\sqrt{2}}{2}\begin{bmatrix} {V_{H,A,1,1}}^2 & {V_{H,A,2,1}}^2 & {V_{H,B,1,1}}^2 & {V_{H,B,2,1}}^2 \\ {V_{H,A,1,1}}^2 & -{V_{H,A,2,1}}^2 & {V_{H,B,1,1}}^2 & -{V_{H,B,2,1}}^2 \\ {r_A V_{H,A,1,1}}^2 & -{r_A V_{H,A,2,1}}^2 & {r_B V_{H,B,1,1}}^2 & -{r_B V_{H,B,2,1}}^2 \\ {r_A V_{H,A,1,1}}^2 & {r_A V_{H,A,2,1}}^2 & {r_B V_{H,B,1,1}}^2 & {r_B V_{H,B,2,1}}^2 \\ \vdots & \vdots & \vdots & \vdots \\ {V_{H,A,1,n}}^2 & {V_{H,A,2,n}}^2 & {V_{H,B,1,n}}^2 & {V_{H,B,2,n}}^2 \\ {V_{H,A,1,n}}^2 & -{V_{H,A,2,n}}^2 & {V_{H,B,1,n}}^2 & -{V_{H,B,2,n}}^2 \\ {r_A V_{H,A,1,n}}^2 & -{r_A V_{H,A,2,n}}^2 & {r_B V_{H,B,1,n}}^2 & -{r_B V_{H,B,2,n}}^2 \\ {r_A V_{H,A,1,n}}^2 & {r_A V_{H,A,2,n}}^2 & {r_B V_{H,B,1,n}}^2 & {r_B V_{H,B,2,n}}^2 \end{bmatrix} \begin{bmatrix} K_{H,A,1} \\ K_{H,A,2} \\ K_{H,B,1} \\ K_{H,B,2} \end{bmatrix} = \begin{bmatrix} F_{app,z,} \\ F_{app,y,} \\ F_{app,y,} \\ F_{app,z,} \\ \vdots \\ F_{app,z,} \\ F_{app,y,} \\ F_{app,y,} \\ F_{app,z,} \end{bmatrix} \tag{3}$$

To evaluate if the constrained fitting imposes limitations on the precision of the force estimation, a comparison with the unconstrained equation system is performed and the results are

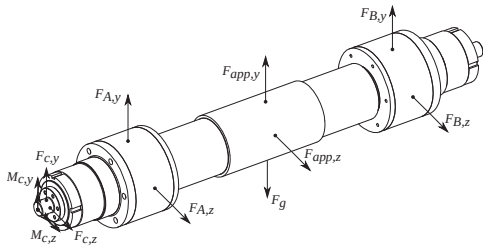

FIGURE 11: FREE BODY DIAGRAM FOR THE SHAFT DURING CALIBRATION

included in the results section.

The calibration experiments are conducted for three choices of AMB bias currents I_{bias} namely, 6 A, 8 A, and 10 A. For each choice of bias currents a range of forces applied by the individual pistons of the calibration facility are chosen. The force range is divided into a number of load steps of 250 N. The specifications for each calibration experiment are presented in Table 4. To capture the change in the calibration constants as a function of the position of the shaft, an array of different shaft positions are considered. The array expands a square domain of 9×9 positions separated by 5 μm symmetrically around zero. This yields a position range from $[-20;20]$ μm in the y-direction and similarly in the z-direction, where $(0,0)$ indicates a centred shaft. This range is chosen to encompass the range of shaft positions needed for flow perturbation in the seal experiments.

For each choice of I_{bias} a calibration cycle is conducted. The calibration cycle is illustrated in Fig. 12 and described in the following: One of the 81 positions in the envelope is chosen, and the shaft is positioned accordingly. A loading direction is specified and the chosen piston loops over the force range in the steps of 250 N, first increasing the load towards its maximum value and then decreasing the load in steps towards zero. For each step in load, the control software waits until transients have died out before acquiring the sensor data. This process is repeated for all loading directions and thereby all pistons, and for all positions in the envelope. Subsequently the data is stored for post processing. The whole procedure is automated to reduce error and time consumption.

RESULTS OF THE CALIBRATION VALIDATION

The calibration of the Hall sensor system is validated through data from a dedicated set of experiments obtained specifically for validation purposes. In these validation experiments the shaft is loaded by the pneumatic pistons similar to the calibration

TABLE 4: CALIBRATION EXPERIMENT MATRIX

I_{bias} [A]	Force range [N]	Load steps
6	$0-2000$	17
8	$0-3000$	25
10	$0-4000$	33

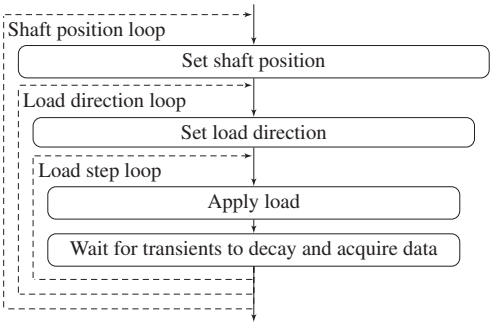

FIGURE 12: FLOW CHART FOR THE AUTOMATED CALIBRATION CYCLE

method. Included are experiments with off-axis loading to quantify the force estimation capabilities in load directions that are not included in the calibration. The difference in force estimation performance of the constrained and unconstrained fitting scheme is investigated by comparison of errors. The force component error u_i is calculated as

$$u_i = F_{K_H,i} - F_{app,i}$$

where i denotes a force component (y or z). $F_{K_H,i}$ is the force component estimated by the calibrated Hall sensor system and $F_{app,i}$ is the force component measured by the force transducer at the piston. Examples of errors on the estimated force components for the constrained and unconstrained methods are shown in Fig. 13. Fig. 13a and 13b shows the error from an experiment with loading from a single piston in the positive horizontal direction. Fig. 13c and 13d shows the error from an experiment where the shaft is loaded by two pistons yielding a resulting force 45° from the vertical upwards direction. For illustrative purposes the force estimation error for the unloaded direction F_y in the one piston experiment (Fig. 13a and 13b) is plotted as a function of the applied force $F_{app,z}$. The terms on-axis and off-axis loading refer to a resulting force in and not in the direction of a piston, respectively. The general tendency in the validation experiments is that the constrained and unconstrained

TABLE 5: VALIDATION EXPERIMENT FORCE ERRORS FOR DIFFERENT FORCE ESTIMATION METHODS AND BIAS CURRENTS

Method		Hall sensor			Current/air gap		
Bias current	[A]	6	8	10	6	8	10
$F_{res,max}$	[N]	1500	2250	3000	1500	2250	3000
MAE	[N]	11.6	17.6	25.7	32.7	56.7	81.9
MAE/$F_{res,max}$	[%]	0.77	0.78	0.86	2.2	2.5	2.7
Max. error	[N]	34.2	65.3	61.1	78.2	171	205
Max. error/$F_{res,max}$	[%]	2.3	2.9	2.0	5.2	7.6	6.8

fitting schemes yield similar errors for on-axis loading, but the unconstrained show larger errors for the off-axis loading. The constrained calibration gives more consistent results independent of load direction, hence it is more suitable for the testing of turbomachinery seals, where the ability to quantify cross coupled forces is of high importance. The following results are obtained utilizing the constrained method.

The obtained calibration constants $K_{H,AMB,actuator}$ for the shaft in a centred position can be seen for the different choices of bias currents in Fig. 14. As evident from Fig. 14 the calibration constants are dependent on the choice of bias current. The difference in the calibration constants between AMB A and B is expected due to production and assembly tolerances. The position dependence of the calibration constants is illustrated in Fig. 15, which shows surface plots of the four constants for 10 A bias current at the positions included in the calibration domain. In the domain limited to the range $[-20;20]$ μm the observed change in K_H due to position is within 3 %.

The force estimated using the Hall sensor system is compared to the current/air gap force estimation in Table 5. The maximum error and Mean Absolute Error (MAE) from validation experiments are listed for the two methods at the different bias currents. The selected maximum resulting force $F_{res,max}$ for the experiments is increased with bias current. Note that the maximum error does not necessarily occur at the max. applied force. Table 5 is based on data from four on-axis and four off-axis loaded validation experiments for each bias current. The magnitude of the errors generally increases with the bias current. The force estimation errors arising from using the current/air gap method are more than twice as large as the estimation errors introduced by applying the Hall sensor system. As expected a more precise force estimation is obtained with the Hall sensors system than with the current/air gap method.

TABLE 6: UNCERTAINTY OF FORCE COMPONENTS AND CONTRIBUTING ERRORS FOR DIFFERENT BIAS CURRENTS

Bias current	[A]	6	8	10
u_{MAE}	[N]	11.6	17.6	25.7
u_{rep}	[N]	0.1	0.1	1.1
u_{FT}	[N]	0.39	0.42	0.45
u_{F_i}	[N]	11.6	17.6	25.7

UNCERTAINTY QUANTIFICATION

In order to ensure high-quality force estimation capabilities for the turbomachinery seal tests using the embedded Hall sensor system it is necessary to identify any uncertainties in the force estimation. The uncertainties are estimated by the Root-Sum-Squared (RSS) method as outlined in [48]. An uncertainty u_R of a quantity R is estimated by the general equation

$$u_R = \left[\left(\frac{\partial R}{\partial x_1} u_1 \right)^2 + \left(\frac{\partial R}{\partial x_2} u_2 \right)^2 + ... + \left(\frac{\partial R}{\partial x_n} u_n \right)^2 \right]^{\frac{1}{2}} \quad (4)$$

where $x_1, x_2, ..., x_n$ are the influencing variables with the corresponding errors $u_1, u_2, ..., u_n$. The significant contributors to the uncertainty of the force component are: (1) the error identified through the validation experiments u_{MAE} shown in Table 5, (2) repeatability error u_{rep} and (3) force transducer error u_{FT}. As these errors are directly influencing the force estimate, Eqn. (4) is reduced and the uncertainty of the force components becomes

$$u_{F_i} = \left[(u_{MAE})^2 + (u_{rep})^2 + (u_{FT})^2 \right]^{\frac{1}{2}}$$

The values of the calculated errors along with the final uncertainty are found in Table 6 for the different bias currents.

CONCLUSION

The main design considerations for and the functionality of the three modules of the full industrial scale state of the art multiphase turbomachinery seal test facility have been described. The AMB based test facility is able to support and excite the shaft without mechanical contact while the embedded Hall sensor system allows for precise contact-free force estimation. In order to achieve the force estimation precision needed for identification of seal properties, the Hall sensor system requires calibration. The methodology of the Hall sensor system calibration is presented along with results from force estimation validation experiments. The force estimation precision obtained using the

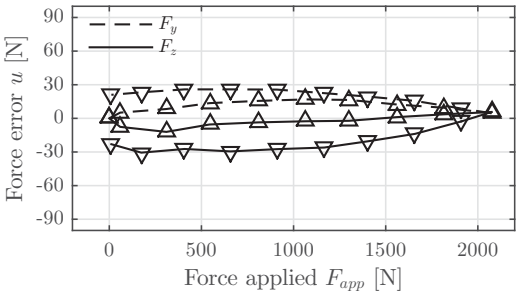

(a) CONSTRAINED FITTING - ONE PISTON LOADING (+z)

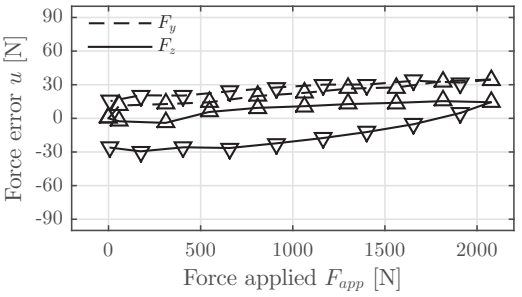

(b) UNCONSTRAINED FITTING - ONE PISTON LOADING (+z)

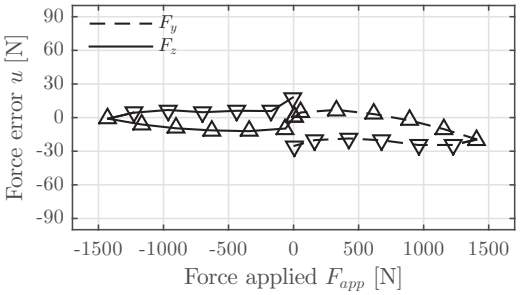

(c) CONSTRAINED FITTING - TWO PISTON LOADING (+y,-z)

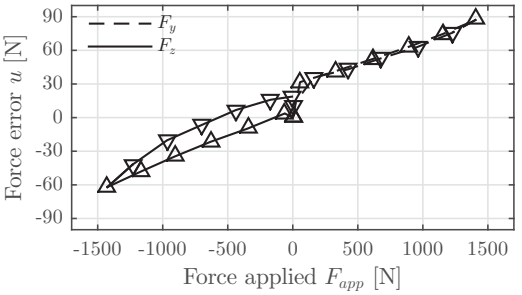

(d) UNCONSTRAINED FITTING - TWO PISTON LOADING (+y,-z)

FIGURE 13: EXAMPLES OF FORCE COMPONENT ERRORS FOR VALIDATION EXPERIMENTS FOR THE TWO FITTING METHODS. 8 A BIAS CURRENT AND CENTRED SHAFT. UPWARDS AND DOWNWARDS POINTING TRIANGLES MARK INCREASING AND DECREASING LOADS, RESPECTIVELY

Hall sensor system is compared to the conventional force estimation technique enabled through current/air gap measurements. The Hall sensor based force estimation method outperforms the conventional current/air methodology as expected, and exhibits mean absolute estimation errors in the order of 1% of the maximum force applied in the validation experiments conducted. The uncertainty on the force estimation is addressed through an uncertainty quantification based on the RSS methodology.

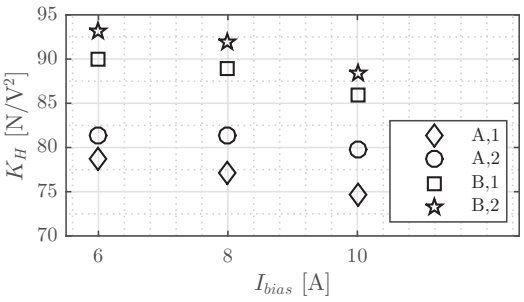

FIGURE 14: CALIBRATION CONSTANTS FOR CENTRED SHAFT AT DIFFERENT BIAS CURRENTS

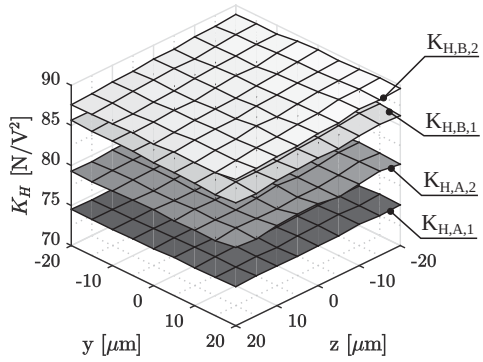

FIGURE 15: THE FOUR CALIBRATION CONSTANTS AT DIFFERENT SHAFT POSITIONS. 10 A BIAS CURRENT

REFERENCES

[1] Santos, I. F., and Russo, F. H., 1998. "Tilting-Pad Journal Bearings With Electronic Radial Oil Injection". *Journal of Tribology,* ***120***(3), pp. 583–594.

[2] Santos, I., and Nicoletti, R., 1999. "THD Analysis in Tilting-Pad Journal Bearings Using Multiple Orifice Hybrid Lubrication". *October,* ***121***(October), pp. 892–900.

[3] Childs, D., 1993. *Turbomachinery Rotordynamics: Phenomena, Modeling, and Analysis*. John Wiley & Sons, Inc., Hoboken, New Jersey.

[4] Childs, D., and Vance, J., 1997. "Annular Gas Seals and Rotordynamics of Compressors and Turbines". In Proceedings of the Twenty-Sixth Turbomacinery Symposium, pp. 201–220.

[5] Moore, J. J., 2003. "Three-Dimensional CFD Rotordynamic Analysis of Gas Labyrinth Seals". *Journal of Vibration and Acoustics,* ***125***(4), pp. 427–433.

[6] Ertas, B. H., Gamal, A., and Vance, J. M., 2006. "Rotordynamic Force Coefficients of Pocket Damper Seals". *ASME Journal of Turbomachinery*, pp. 725–737.

[7] Childs, D. W., 1983. "Dynamic Analysis of Turbulent Annular Seals Based on Hirs Lubrication Equations". *Journal of Lubrication Technology,* ***105***, pp. 429–436.

[8] Nelson, C., Childs, D., Nicks, C., and Elrod, D., 1986. "Theory Versus Experiment for the Rotordynamic Coefficients of Annular Gas Seals, Part 2: Constant-Clearance and Convergent-Tapered Geometry". *Journal of Tribology*, pp. 433–438.

[9] Murphy, B. T., and Vance, J. M., 1980. "Labyrinth Seal Effects on Rotor Whirl Stability". In Proceedings of the Second International Conference on Vibrations in Rotating Machinery.

[10] Hsu, Y., and Brennen, C. E., 2002. "Fluid Flow Equations for Rotordynamic Flows in Seals and Leakage Paths". *Journal of Fluids Engineering,* ***124***(1), pp. 176–181.

[11] Zeidan, F. Y., Perez, R. X., and Stephenson, E. M., 1993. "The Use of Honeycomb Seals in Stabilizing Two Centrifugal Compressors". In Proceedings of the Twenty-Second Turbomacinery Symposium, pp. 3–16.

[12] Childs, D. W., Rodriguez, L. E., Cullotta, V., Al-Ghasem, A., and Graviss, M., 2006. "Rotordynamic-Coefficients and Static (Equilibrium Loci and Leakage) Characteristics for Short, Laminar-Flow Annular Seals". *Journal of Tribology,* ***128***(2), pp. 378–387.

[13] Picardo, A., and Childs, D. W., 2005. "Rotordynamic Coefficients for a Tooth-on-Stator Labyrinth Seal at 70 Bar Supply Pressures: Measurements Versus Theory and Comparisons to a Hole-Pattern Stator Seal". *Journal of Engineering for Gas Turbines and Power,* ***127***(4), pp. 843–855.

[14] Childs, D. W., and Wade, J., 2004. "Rotordynamic-Coefficient and Leakage Characteristics for Hole-Pattern-Stator Annular Gas SealsMeasurements Versus Predictions". *Journal of Tribology,* ***126***(2), pp. 326–333.

[15] Ertas, B. H., Delgado, A., and Vannini, G., 2011. "Rotordynamic Force Coefficients for Three Types of Annular Gas Seals with Inlet Preswirl and High Differential Pressure Ratio". *Proceedings of ASME Turbo Expo 2011: Power for Land, Sea and Air*(518), pp. 1–12.

[16] Hirano, T., Guo, Z., and Kirk, R. G., 2005. "Application of Computational Fluid Dynamics Analysis for Rotating MachineryPart II: Labyrinth Seal Analysis". *Journal of Engineering for Gas Turbines and Power,* ***127***(4), pp. 820–826.

[17] Athevale, M. M., Przekwas, A. J., Hendricks, R. C., and Liang, A., 1994. "SCISEAL: A 3D CFD Code for Accurate Analysis of Fluid Flow and Forces in Seals". In Proceedings of the Advanced ETO Propulsion Conference, pp. 337–345.

[18] Moore, J. J., and Palazzolo, A. B., 1999. "CFD Comparison to 3D Laser Anemometer and Rotordynamic Force Measurements for Grooved Liquid Annular Seals". *ASME J. Tribol.,* ***121***(2), pp. 307–314.

[19] Kim, N., and Rhode, D. L., 2000. "A New CFD-Perturbation Model For The Rotordynamics of Incompressible Flow Seals". In ASME International Gas Turbine and Aeroengine Congress and Exposition.

[20] Nordmann, R., and Dietzen, F. J., 1988. Finite Difference Analysis of Rotordynamic Seal Coefficients For An Eccentric Shaft Position.

[21] Rhode, D. L., Hensel, S. J., and Guidry, M. J., 1992. "Labyrinth Seal Rotordynamic Forces Using a Three-Dimensional Navier-Stokes Code". *ASME J. Tribol.*(114), pp. 683–689.

[22] Tam, L. T., Przekwas, A. J., Muszynska, A., Hendricks, R. C., Braun, M. J., and Mullen, R. L., 1988. "Numerical and Analytical Study of Fluid Dynamic Forces in Seals and Bearings". *ASME J. Vibr. Acoust.,* ***110***, pp. 315–325.

[23] Nielsen, K. K., Childs, D. W., and Myllerup, C. M., 2001. "Experimental and Theoretical Comparison of Two Swirl Brake Designs". *Journal of Turbomachinery,* ***123***(2), p. 353.

[24] Nielsen, K. K., Myllerup, C. M., and Van den Braembussche, R. A., 1999. "Parametric Study of the Flow in Swirl Brakes by Means of a 3D Navier- Stokes Solver". In Transactions of the Third European Conference on Turbomachinery, pp. 489–498.

[25] Nielsen, K. K., Van den Braembussche, R., and Myllerup, C., 1998. "Optimization of swirl brakes by means of a 3D Navier-Stokes solver". In The 1998 International Gas Turbine & Aeroengine Congress & Exhibition, p. 7.

[26] Nielsen, K. K., Jønck, K., and Underbakke, H., 2012. Hole-Pattern and Honeycomb Seals Rotordynamic Forces: Validation of CFD Based Prediction Techniques.

[27] Wagner, N., Steff, K., Gausmann, R., and Schmidt, M., 2009. "Investigations on the Dynamic Coefficients of Im-

peller Eye Labyrinth Seals". *Proceedings of the Thirty-eighth Turbomacinery Symposium*.

[28] Kocur, J. A., Nicholas, J. C., and Lee, C. C., 2007. "Surveying Tilting Pad Journal Bearing and Gas Labyrinth Seal Coefficients and Their Effect on Rotor Stability". In Proceedings of the 36th Turbomachinery Symposium, pp. 1–10.

[29] Crowe, C. T., 2006. *Multiphase flow handbook*. CRC.

[30] Andrés, L. S., 2010. A Mixture Bulk-Flow Model for Anullar Pressure Seals. Tech. rep., Texas A&M University, Mechanical Engineering Department, Turbomachinery Laboratory.

[31] Andrés, L. S., 2011. "Rotordynamic Force Coefficients of Bubbly Mixture Annular Pressure Seals". *Proceedings of ASME Turbo Expo 2011,* ***60***, pp. 1–10.

[32] Andrés, L. S., Lu, X., and Liu, Q., 2015. "Measurements Of Flowrate And Force Coefficients In A Short Length Annular Seal Supplied With A Liquid/Gas Mixture (Stationary Journal)". *Tribology Transactions,* ***2004***(November), pp. 00–00.

[33] Vannini, G., Bertoner, M., Nielsen, K. K., Stronach, R., Iudiciani, P., and Bertoneri, M., 2015. "Gt2015-43095 Experimental Results and Cfd Simulations of Labyrinth and Pocket Damper Seals for Wet Gas Compression". *Proceedings of ASME Turbo Expo: Turbine Technical Conference and Exposition*, pp. 1–13.

[34] Mihai, A., Abdelmalik, Z., and Gérard PINEAU, P., 2011. "Rotordynamic Analysis of Textured Annular Seals With Multiphase (Bubbly) Flow". *Incas Bulletin,* ***3***(3), pp. 3–13.

[35] Voigt, A. J., Iudiciani, P., Nielsen, K. K., and Santos, I. F., 2016. "CFD Applied for the Identification of Stiffness and Damping Properties for Smooth Annular Turbomachinery Seals in Multiphase Flow". In Submitted to ASME Turbo Expo 2016.

[36] Athavale, M., Przekwas, A., and Hendricks, R., 1992. "A Finite Volume Numerical Method to Calculate Fluid Forces and Rotordynamic Coefficients in Seals". *28th Joint Propulsion Conference and Exhibit*.

[37] Chochua, G., and Soulas, T., 2007. "Numerical modeling of rotordynamic coefficients for deliberately roughened stator gas annular seals". *Journal of tribology*.

[38] Yan, X., Li, J., and Feng, Z., 2011. "Investigations on the Rotordynamic Characteristics of a Hole-Pattern Seal Using Transient CFD and Periodic Circular Orbit Model". *Journal of Vibration and Acoustics,* ***133***(4), aug, p. 041007.

[39] G., S., and E., M., 2009. *Magnetic bearings theory, design, and application to rotating machinery*. Springer, Dordrecht New York.

[40] Aenis, M., Knopf, E., and Nordmann, R., 2002. "Active Magnetic Bearings for the Identification and Fault Diagnosis in Turbomachinery". *Mechatronics,* ***12***, pp. 1011–1021.

[41] Voigt, A., and Santos, I., 2012. "Theoretical and Experimental Investigation of Force Estimation Errors Using Active Magnetic Bearings with Embedded Hall Sensors". *ASME Turbo Expo 2012*.

[42] Zutavern, Z. S., and Childs, D. W., 2005. "Fiber-Optic Strain Gauge Calibration and Dynamic Flexibility Transfer Function Identification in Magnetic Bearings". *Volume 4: Turbo Expo 2005*, pp. 757–762.

[43] Raymer, S. G., and Childs, D. W., 2001. "Force Measurements in Magnetic Bearings Using Fiber Optic Strain Gauges". In ASME Turbo Expo 2001: Power for Land, Sea, and Air.

[44] Zutavern, Z. S., and Childs, D. W., 2008. "Identification of Rotordynamic Forces in a Flexible Rotor System Using Magnetic Bearings". *Journal of Engineering for Gas Turbines and Power,* ***130***(2), p. 022504.

[45] Kjolhede, K., and Santos, I. F., 2007. "Experimental Contribution to High-Precision Characterization of Magnetic Forces in Active Magnetic Bearings". *Journal of Engineering for Gas Turbines and Power,* ***129***(2), p. 503.

[46] Schweitzer, G., 2009. "Applications and Research Topics for Active Magnetic Bearings". In Proc. IUTAM-Symp. on Emerging Trends in Rotor Dynamics, pp. 1–11.

[47] Gähler, C., and Förch, P., 1994. "A Precise Magnetic Bearing Exciter for Rotordynamic Experiments". *4th International Symposium on Magnetic Bearings*(August), pp. 193–200.

[48] Moffat, R. J., 1988. "Describing the uncertainties in experimental results". *Experimental Thermal and Fluid Science,* ***1***(1), pp. 3–17.

Publication P3

Identification of Parameters in Active Magnetic Bearing Systems

Paper accepted for publication in the proceedings of ISMB15.

ISMB15

Identification of Parameters in Active Magnetic Bearing Systems

Andreas JAUERNIK VOIGT[*,**], Jonas LAURIDSEN[**], Christian MANDRUP-POULSEN[**], Kenny KROGH NIELSEN[*] and Ilmar F. SANTOS[***]

[*] Lloyd's Register Consulting
Copenhagen, Denmark
[**] Dept. of Mechanical Eng., Technical University of Denmark
Copenhagen, Denmark
[***] Dept. of Mechanical Eng., Technical University of Denmark
Copenhagen, Denmark
E-mail: ifs@mek.dtu.dk

Abstract

A method for identifying uncertain parameters in Active Magnetic Bearing (AMB) based rotordynamic systems is introduced and adapted for experimental application. The Closed Loop Identification (CLI) method is utilised to estimate the current/force factors $\mathbf{K}_i$ and the displacement/force factors $\mathbf{K}_s$ as well as a time constant τ_e for a first order approximation of unknown actuator dynamics. To assess the precision with which CLI method can be employed to estimate AMB parameters the factors $\mathbf{K}_i$, estimated using the CLI method, is compared to $\mathbf{K}_i$ factors attained through a Static Loading (SL) method. The CLI method and SL method produce similar results, indicating that the CLI method is able to perform closed loop identification of uncertain AMB parameters.

Keywords: Rotordynamics, Parameter identification, Closed-loop, Experimental, Active Magnetic Bearings.

1. Introduction

Active Magnetic Bearings (AMBs) are commonly employed in turbomachinery applications, due to their many advantages over conventional bearing elements (Schweitzer, 2002). The operability of AMB based rotordynamic systems are dependent on a well performing feedback control scheme. This highlights the need for a precise mathematical model of the AMB-rotor system as this lays the foundation for both controller design and performance evaluation of the overall rotordynamic system. Uncertainties in AMB parameters and unmodelled AMB dynamics are sources of inconsistencies between the physical AMB system and its mathematical representation. The uncertain parameters are commonly electromechanical in nature and the uncertainties originate from production tolerances, misalignment issues and variations in material specifications, among others. Conventionally unmodelled AMB dynamics include the formation of Eddy currents which can influence the electrodynamic behaviour of the AMB actuators. To achieve the necessary level of model certainty for ensuring satisfactory performance of the AMB system, it is often necessary to identify the uncertain parameters and relevant dynamical effects experimentally, preferably in-situ, and update the mathematical model accordingly. However, as AMB based rotordynamic systems are inherently open loop unstable and requires feedback control to operate, measurement noise embedded in the system outputs, e.g. in the rotor displacement signals, can not be assumed uncorrelated with system inputs. This entails that applying conventional open loop identification techniques is not suitable (Anderson, 1998). Closed loop identification methods have previously been employed with success (Sun et al., 2014, Sun et al., 2014, Tiwari and Chougale, 2014) and are commonly based on frequency domain techniques to capture rotordynamic system performance. This paper describes a newly developed fast and transparent time domain closed loop identification (CLI) method (Lauridsen et al., 2015) and its application to an industrial scale AMB based rotordynamic testing facility. The testing facility is designed to be used for identifying rotordynamic properties of turbomachinery seals subjected to multiphase flow conditions (Voigt et al., 2016). The CLI method is capable of identifying specific AMB parameters, thus enabling utilization of a-priori knowledge of the AMB-rotor model structure. To illustrate the applicability of the CLI method to AMB-rotor systems the focus of this paper is oriented at identifying AMB force/current factors $\mathbf{K}_i$ and force/displacement factors $\mathbf{K}_s$ experimentally. Additionally, a time constant τ_e for a first order transfer function describing the conventionally unmodelled correlation between imposed coil current and actuator flux formation is identified experimentally. Furthermore, as the CLI method has not previously been applied experimentally to AMB systems, a

subset of the CLI method results are compared to results obtained using a static load (SL) method, in order to assess the capabilities of the CLI method. Specifically, $\mathbf{K}_i$ parameters identified using both methods are reported for comparison.

2. Experimental Facilities

The experimental facilities employed in the underlying work of this paper consists of a AMB-based rotordynamic test bench and a calibration facility presented in Fig. 1(a). The AMBs radially support a symmetric rigid rotor which is driven by an asynchronous motor through an intermediate shaft and a flexible coupling. Angular contact ball bearings, supporting the intermediate shaft housed in the intermediate shaft pedestal, compensate for axial forces acting on the rotor. The radial AMBs are of the eight pole heteropolar type featuring an embedded Hall sensor system which can be utilised to quantify forces exerted on the rotor by the AMBs, see Fig. 1(b). In Fig. 1(b) both the global reference frame denoted by x, y and the actuator reference frame denoted by ζ, η is introduced. The actuators are tilted 45° with respects to the global reference frame. Throughout the paper subscripts ζ, η are used to denote quantities belonging to the actuators aligned with the respective axes of the stator reference frame. The two AMB stators have been manufactured using two different production methods yielding different geometric tolerances for the AMBs. The AMBs are supplied by four commercially available 3 kW switch-mode laboratory amplifiers, not specifically designed for AMB use. The AMBs are controlled using a standard decentralized PID scheme. The calibration facility depicted in Fig. 1(c), includes four controllable pneumatic pistons that can be applied to exert static forces of varying direction and magnitude onto the rotor. Forces are transferred from the pistons to the rotor via a force transducer mounted on the calibration clamp which in turn is mounted on the rotor as seen exemplified for a single piston set-up in Fig. 1(d). A full description of the test facility can be found in (Voigt et al., 2016), which also presents the calibration of the Hall sensor system. Design parameters for the rotordynamic test bench can be found in Table 1.

3. Mathematical Representation of the AMB-Rotor System

The global AMB-rotor system is described mathematically by a rotor model and a model of the two radial AMBs. The rotor is considered rigid in the operating range of the test facility and it is assumed in the modelling that the only significant external forces acting on the rotor originates from the radial AMBs.

3.1. Model of AMB Forces

The forces generated by an AMB acting on the rotor can be described as function of the lateral AMB rotor displacements $\mathbf{s}$ and the imposed control currents $\mathbf{i}_c$. The linearised AMB forces can be represented as (Bleuler et al., 2009)

$$\mathbf{f}_b(\mathbf{i}_c, \mathbf{s}) = \mathbf{K}_i \mathbf{i}_c + \mathbf{K}_s \mathbf{s} \tag{1}$$

in which $\mathbf{K}_i$ are $\mathbf{K}_s$ are matrices containing parameters defined as

$$\mathbf{K}_i = \begin{bmatrix} K_{i,A_\zeta} & 0 & 0 & 0 \\ 0 & K_{i,A_\eta} & 0 & 0 \\ 0 & 0 & K_{i,B_\zeta} & 0 \\ 0 & 0 & 0 & K_{i,B_\eta} \end{bmatrix}, \quad \mathbf{K}_s = \begin{bmatrix} K_{s,A_\zeta} & 0 & 0 & 0 \\ 0 & K_{s,A_\eta} & 0 & 0 \\ 0 & 0 & K_{s,B_\zeta} & 0 \\ 0 & 0 & 0 & K_{s,B_\eta} \end{bmatrix} \tag{2}$$

which defines a dedicated force/current and force/displacement factor for each actuator of the two AMBs. The subscripts A_ζ, A_η, B_ζ, and B_η designates to which AMB and which actuator the factor belongs, respectively, see Fig. 1(b).

Table 1: Design parameters for the rotordynamic test bench

Rotor length	860	mm
Rotor assembly mass	69	kg
1st rotor bending mode @	550	Hz
Stator inner diameter	151	mm
Nominal radial air gap	0.5	mm
Winding configuration	N-S-S-N-N-S-S-N	[-]
Lamination thickness	0.35	mm
Laminate material	SURA M270-35A	
Max. static load capacity (per AMB)	7500	N
Bias current range	4 to 10	A
Number of Hall sensors per AMB	8	
Hall sensor type	F.W. Bell - FH-301	

ISMB15

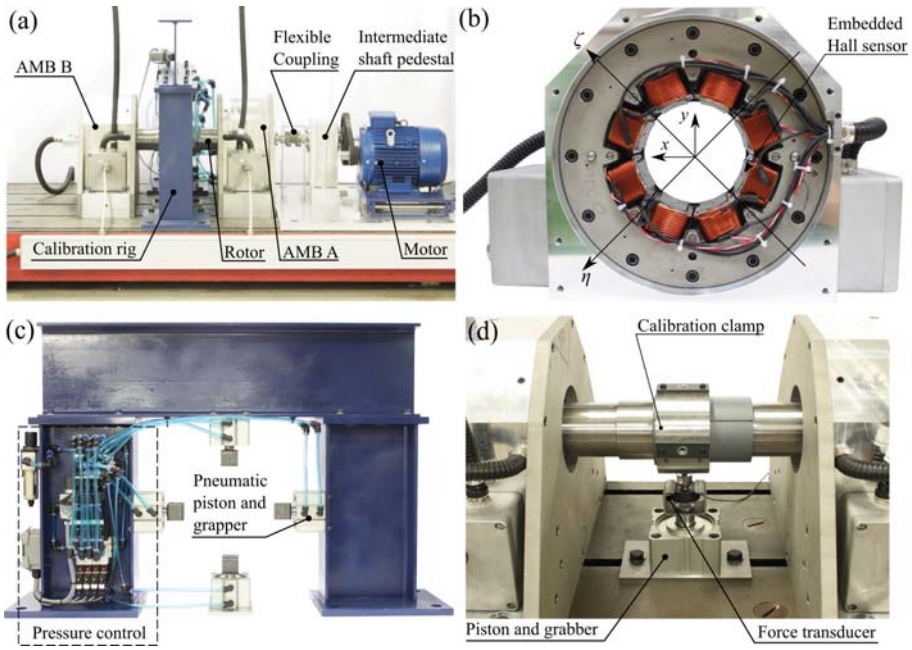

Fig. 1: Experimental facilities used throughout the study. (a) Rotordynamic test bench, showing main components. (b) Test bench AMB showing the placement of the embedded Hall sensors as well as AMB actuator and global reference frame definitions. (c) Calibration facility showing the pneumatic pistons and pressure control unit. (d) Interface between calibration facility and rotor showing a single piston with grabber as well as the calibration clamp mounted on the rotor.

3.2. Rotor Model

The rotor is modelled using a conventional Finite Element (FE) method since the CLI method utilizes the structure of the FE based rotor model for uncertainty representation (Lauridsen et al., 2015). Furthermore, using the FE approach retains generality of the methodology, and by applying modal truncation techniques, real left and right transformation matrices can be determined which allows transforming the full order FE model to reduced form. Here the global rotor model has been truncated to only include rigid modes. It is noted that the shaft is non-rotating through the entirety of the study. The resulting rotor model can be written in state space form as

$$\dot{\mathbf{x}}_f = \mathbf{A}_f \mathbf{x}_f + \mathbf{B}_f \mathbf{u}, \quad \mathbf{y} = \mathbf{C}_f \mathbf{x}_f \tag{3}$$

4. Closed Loop Model and Identification Scheme

The CLI method is based on theory presented in (Lauridsen et al., 2015) and is in this paper adapted for experimental application. The schematic block diagram shown in Fig. 2 acts as the basis for the CLI method, and shows the elements of the global closed loop system in a vectorised formulation where $\mathbf{K}$ represents the known controller. The electrodynamic model of the AMB actuator contains two first order transfer functions as indicated on Fig. 2. The block denoted "Amplifier and coil" represents a known first order transfer function from the current reference signals to the actual current flowing in the coils, consequently approximating the dynamics originating from the coil inductance and the power amplifier. Similarly, the block "Unknown actuator dynamics" is an assumed first order transfer function with unknown time constant τ_e, which aims at describing the dynamics originating from eddy current formation and unknown amplifier dynamics. The

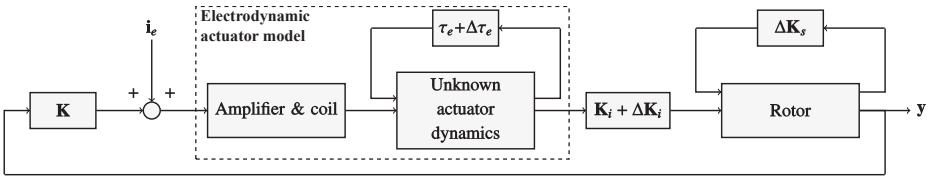

Fig. 2: Closed loop schematic of the AMB-rotor system.

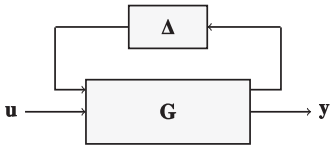

Fig. 3: Uncertain plant representation using upper LFT, $\mathbf{G}_{unc} = \mathcal{F}_u(\mathbf{G}, \mathbf{\Delta})$

unknown time constant appended to the block "Unknown actuator dynamics" is represented by a nominal value τ_e, serving as an initial guess, plus the variation $\Delta\tau_e$. All four actuators share one common time constant τ_e. The current/force factor is here composed of a nominal initial guess $\mathbf{K}_i$ and an appended uncertainty $\Delta\mathbf{K}_i$. The block "Rotor" contains the rotor model with the nominal displacement/force factor $\mathbf{K}_s$ and an actuator uncertainty mapping. The uncertainty mapping describes how a change $\Delta\mathbf{K}_s$ in the nominal displacement/force factor modifies the overall dynamic behaviour of the rotor. The rotordynamic model is represented on reduced modal form and the uncertain parameters of the rotor model, here $\mathbf{K}_s$, is extracted and described using a Linear Fractional Transformation (LFT) which is treated subsequently.

4.1. LFT Representation of Uncertain Rotordynamic Systems

The rotordynamic system with unknown $\Delta\mathbf{K}_s$ is formulated using a LFT as described in this section. To retain generality, the block termed "Rotor" and the block containing $\Delta\mathbf{K}_s$ in Fig. 2 are in the following denoted by $\mathbf{G}$ and $\mathbf{\Delta}$, respectively. The uncertain rotor model $\mathbf{G}_{unc}$ is constructed using the nominal model and the uncertainty representation, which combined is written on LFT form as illustrated in Fig. 3 for the global AMB-rotor model. In Fig. 3 $\mathbf{\Delta}$ denotes a 4×4 diagonal matrix representing $\Delta\mathbf{K}_s$. The matrix $\mathbf{G}$ is constructed as outlined in the following and is described in detail in (Lauridsen et al., 2015). It can be proved that changing a component in $\mathbf{K}_s$, i.e. changing the displacement/force factor for a single actuator direction, imposes a change in a single column with index j of the full order system matrix $\mathbf{A}_f$. The column corresponds to a specific node with index j in the FE representation of the rotor where the AMB forces are imposed on the rotor model. This can be expressed as

$$\mathbf{A}_{\Delta_f} = \begin{bmatrix} 0 & \dots & 0 & a_{1,j} & 0 & \dots & 0 \\ 0 & \dots & 0 & a_{2,j} & 0 & \dots & 0 \\ \vdots & \ddots & \vdots & \vdots & \vdots & \ddots & \vdots \\ 0 & \dots & 0 & a_{i,j} & 0 & \dots & 0 \end{bmatrix} \tag{4}$$

It is assumed that the matrix $\mathbf{A}_\Delta$ expressing the change in the system matrix can be reduced by applying the same modal truncation matrices used to reduce the full order nominal system. This is presented in Eq. (5) and has shown to hold in practice. The matrix $\mathbf{A}_{f,\Delta}$ found in Eq. (4) can be written as the product of the column vector $\mathbf{B}_{f,\Delta}$, the scalar Δ and the row vector $\mathbf{C}_{f,\Delta}$ as shown in Eq. (6). Consequently the input mapping $\mathbf{B}_\Delta$ and output mapping $\mathbf{C}_\Delta$ of the uncertainties in the reduced system is described by Eq. (7).

$$\mathbf{A}_\Delta = \mathbf{T}_L\, \mathbf{A}_{f,\Delta}\, \mathbf{T}_R \tag{5}$$

$$= \mathbf{T}_L \mathbf{B}_{f,\Delta}\, \Delta\, \mathbf{C}_{f,\Delta_f} \mathbf{T}_R \tag{6}$$

$$= \mathbf{B}_\Delta\, \Delta\, \mathbf{C}_\Delta \tag{7}$$

The process outlined above is repeated for each uncertain entry in the current/force matrix $\mathbf{K}_s$. Assembling the columns of $\mathbf{B}_\Delta$ and rows of $\mathbf{C}_\Delta$ and casting $\mathbf{\Delta}$ as an 4×4 diagonal matrix, the complete uncertainty representation illustrated in

Fig. 3 can be determined by (7). The matrix $\mathbf{G}$ can be written on state space form, as shown in Eq. (8), where $\mathbf{A}$, $\mathbf{B}$ and $\mathbf{C}$ are the nominal system matrices on reduced form. Here the input and output matrices are extended from the nominal model to include B_Δ and $\mathbf{C}_\Delta$. Note that no extra system dynamics is added since the LFT only changes the nominal system matrix $\mathbf{A}$.

$$\mathbf{G} = \left[\begin{array}{c|cc} \mathbf{A} & \mathbf{B}_\Delta & \mathbf{B} \\ \hline \mathbf{C}_\Delta & 0 & 0 \\ \mathbf{C} & 0 & 0 \end{array}\right] \tag{8}$$

4.2. Estimation of Optimal Parameters

As indicated in Fig. 2, a Pseudo-Random Binary Sequence (PRBS) current signal $\mathbf{i}_e$ can be imposed to perturb the system model and time domain simulation can be employed to yield the displacement response $\mathbf{y}$, which can be compared to a response quantified experimentally. To estimate the uncertain AMB parameters the CLI scheme is formulated as a minimization problem that iterates through the uncertain parameters to decrease the discrepancy between the simulated response and the experimentally acquired response. The goal is to find the parameters which provides the best fit between simulation data and experimental data. This can be done by finding the global minimum of the cost function shown in Eq. (9) which is defined as the sum of squares of the discrepancy between simulation data and experimental data as

$$J(\boldsymbol{\theta}) = \left\| \mathbf{y}_{meas} - \mathbf{y}) \right\|_2^2 \tag{9}$$

in which $\mathbf{y}_{meas}$ and $\mathbf{y}$ denotes matrices containing the measured and simulated rotor displacements, respectively. The simulated displacements $\mathbf{y}$ can be expressed as

$$\mathbf{y} = \mathbf{T}(\boldsymbol{\theta}) i_e, \text{ where } \boldsymbol{\theta} = \left\{ K_{i,A_\xi}, K_{i,A_\eta}, K_{i,B_\xi}, K_{i,B_\eta}, K_{s,A_\xi}, K_{s,A_\eta}, K_{s,B_\xi}, K_{s,B_\eta}, \tau_e \right\} \tag{10}$$

where $\mathbf{T}(\boldsymbol{\theta})$ is a transfer function for the closed loop response from the excitation current input $\mathbf{i}_e$ to the displacement $\mathbf{y}$ for a given $\boldsymbol{\theta}$ vector. Minimization of the cost function seen in Eq. (9) has been implemented using MATLAB's `lsqnonlin` function. The CLI method has shown to converge fast towards optimal parameters, even for the specific case where nine parameters are simultaneously identified.

5. Experimental Methodology and Data Post Processing

Two different experimental procedures (CLI and SL) are employed in the study, and both are conduced for the same operation conditions and the same choices of bias currents namely 6 A, 8 A, and 10 A. The experiments are condicted five times for both methods to assess the repeatability of the results. Generating data for the CLI method is relatively straight forward and shortly outlined in the following. The rotor is levitated to the nominal position, and a PRBS disturbance signal is imposed on the control currents, resulting in purely lateral displacement of the rotor, while simultaneously capturing control currents and rotor position signals. The captured signals are used as input for the CLI method to experimentally determine the $\mathbf{K}_i$, $\mathbf{K}_s$ and τ_e parameters.

The secondary experimental SL procedure is introduced with the ultimate goal of obtaining the $\mathbf{K}_i$ parameters, consequently allowing for a comparison with results obtained using the CLI scheme. The basic principle of the alternative experimental procedure is to apply a known load to the centre of the shaft, see Fig. 1(d), using the pneumatic pistons of the calibration facility, see Fig. 1(c), and measure the force and amplifier current signals of all amplifiers. In this case no perturbation of the rotor is imposed, and the force applied to the rotor is quantified using calibrated strain-gauge based HBM U9C force transducers mounted between the pistons and the rotor (Voigt et al., 2016). The applied force is varied in both direction and magnitude, using the four pistons and the pressure control unit seen in Fig. 1(c). Summing forces and moments acting on the rotor allows a set of four equilibrium equations to be established. Furthermore, using Eq. (1) and realizing that the rotor is in static equilibrium, and consequently the variations in rotor displacement is zero leading to $\mathbf{f}_b(\mathbf{i}_c, \mathbf{s}) = \mathbf{K}_i\mathbf{i}_c + \cancelto{0}{\mathbf{K}_s\mathbf{s}}$, the applied force can be expressed solely as a function of the AMB coil currents. This enables casting the equilibrium equations in matrix form as $\mathbf{Ax} = \mathbf{b}$ where $\mathbf{A}$ is a $4n \times 4$ matrix of measured control currents containing n discrete load steps spanning both increasing and decreasing external loads in all four loading directions. The current/force factors to be determined are contained in $\mathbf{x} = \left\{ K_{i,A_\xi}, K_{i,A_\eta}, K_{i,B_\xi}, K_{i,B_\eta} \right\}^T$, and $\mathbf{b}$ is a $4n \times 1$ vector containing the external forces applied using the calibration facility during the experimental procedure. The system of equations can be utilized to obtain the current/force factors by employing a Least Squares scheme.

ISMB15

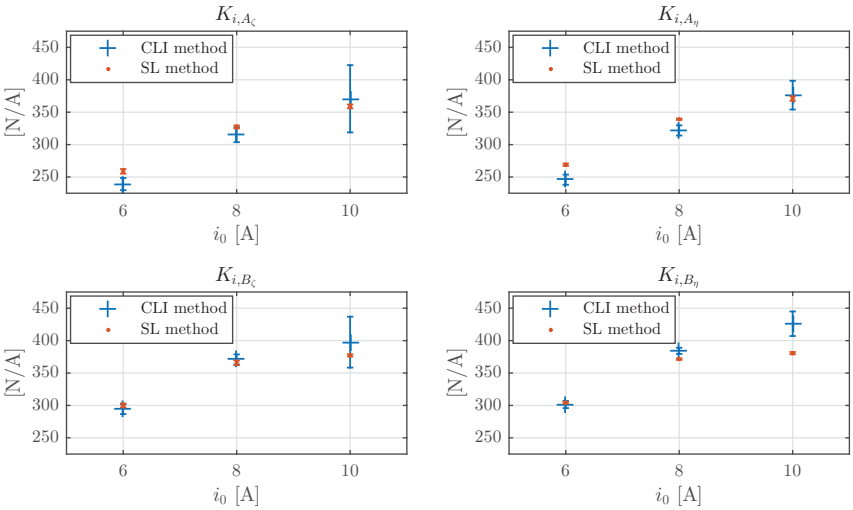

Fig. 4: K_i values for the different bias currents i_0. Top row, from left to right: $K_{i,A\zeta}$ for actuator ζ and $K_{i,A\eta}$ for actuator η in AMB A, respectively. Bottom row, from left to right: $K_{i,B\zeta}$ for actuator ζ and $K_{i,B\eta}$ for actuator η in AMB B, respectively. The error bars mark the 95 % confidence interval based on 5 repeated experiments.

6. Results

The main objective of this study is to determine the precision with which the parameters of a AMB-rotor can be estimated using the CLI methodology. To this end, the current/force factors, contained in $\mathbf{K}_i$, obtained experimentally using both the CLI and the SL approaches are used as a basis for a comparison of the two methods. Fig. 4 shows the $\mathbf{K}_i$ factors obtained for the three choices of bias currents. The plots includes errorbars indicating the 95 % confidence interval which is determined on the basis of five repeated tests conducted for both experimental methods. Good agreement between the results from the two methods are seen, with discrepancies below approximately 10 %. The $\mathbf{K}_i$ factors generally increase with the bias current and are similar for the two actuator directions ζ, η in each AMB, respectively. AMBs A and B are significantly different in terms of the magnitude of their respective current/force factors. The difference is mainly attributed to the different ways of manufacturing the AMB A and AMB B stators which ultimately leads to the nominal air gap of AMB A being 15 – 20 % smaller than the nominal air gap of AMB B. Furthermore, the current/force factors identified for AMB B using the SL method is seen to saturate when the bias current is increased above 8 A. This effect is not as pronounced for AMB A, and could be attributed to the fact that as the nominal air gap is smaller in AMB B compared to AMB A, leading to premature saturation of the AMB B stator. Additionally, saturation is an inherently non-linear phenomenon and consequently not captured by the assumed linear model structure upon which the CLI method is based. This is suspected to be of significant influence for the decrease in the overall fitting quality for the 10 A case included in Table 2. The fitting quality is determined as a Goodness of fit parameter using a normalized root mean square error approach.

In addition to current/force factors the CLI method is used to quantify the uncertain displacement/force factors. The results are summarised in Table 2. As expected the values of displacement/force factors are seen to increase for increasing bias currents and the two displacement/force factors values belonging to each AMB are approximately equal with higher values for AMB B again attributed to the geometrical differences between the AMB stators as discussed above. The Relative Standard Deviation (RSD) is calculated as the standard deviation in percent of the mean value of the displacement/force factors for all five tests and included in Table 2. The RSDs are generally low for the 6 A and 8 A cases, however larger for the 10 A case.

ISMB15

Table 2: Nominal K_s parameters identified with the CLI method. Additionally RSD values in percent calculated from the five repeated tests are included.

Bias current	6 A		8 A		10 A	
Actuator	k_s [N/m]	RSD [%]	k_s [N/m]	RSD [%]	k_s [N/m]	RSD [%]
A_ζ	$2.39 \cdot 10^6$	2.4	$4.09 \cdot 10^6$	1.9	$5.69 \cdot 10^6$	7.7
A_η	$2.49 \cdot 10^6$	2.1	$4.27 \cdot 10^6$	1.5	$5.94 \cdot 10^6$	3.0
B_ζ	$3.13 \cdot 10^6$	1.4	$5.16 \cdot 10^6$	1.1	$6.49 \cdot 10^6$	5.7
B_η	$3.19 \cdot 10^6$	1.1	$5.34 \cdot 10^6$	0.7	$7.00 \cdot 10^6$	2.3
Average fitting quality	95.2 %		93.4 %		84.5 %	

Table 3: Identified time constant τ_e for all bias current cases

Bias current	6 A		8 A		10 A	
Quantity	τ_e [s]	RSD [%]	τ_e [s]	RSD [%]	τ_e [s]	RSD [%]
Both AMBs	0.021	5.9	0.028	59	0.010	0.0

Finally the identified time constant τ_e is reported in Table 3. The values reported are the mean values and the RSD obtained from the five tests. For the 6 A and 8 A cases, τ_e is estimated within the same order of magnitude. For the 10 A case the CLI method returns a average value of τ_e which is significantly different than for the 6 A and 8 A cases. This is reflected in the very low average fitting quality values reported in Table 2 for the 10 A case, indicating that further variation of $\Delta\tau_e$ does not yield a better fit between simulated data and data obtained experimentally. This could indicate that the model fails to represent the electrodynamic behaviour of the AMB actuators for large bias currents due to the onset of non-linear operating regime under these conditions as discussed previously. The RSD values for the 6 A and 8 A are 5.9 % and 59 %, respectively and the growing RSD values could be a manifestation of the fact that the first order representation of the unknown actuator dynamics is insufficient, and the resulting τ_e should be used with care for high bias currents.

A representative visualisation of the performance of the CLI methodology is shown in Fig. 5, depicting both experimental and simulated time series responses for the imposed PRBS current perturbation. It is important to notice that the simulated results are obtained with the nine optimal parameters determined using Eq. (9). Good agreement between the experimental and simulated time series of lateral rotor displacements are seen in Fig. 5(a). The simulated versus measured AMB control currents for AMB B are seen in Fig. 5(b). Qualitatively good agreement is seen and the model captures the experimental trends, albeit significant noise levels are seen on the experimental data. High frequency oscillations are seen in the current signal obtained experimentally which the model fails to capture. This discrepancy could potentially be attributed to a too low model order for the commercial amplifiers. However, further research is required to establish if this is the case.

7. Conclusion and outlook

The CLI and SL methods produce similar results for $\mathbf{K}_i$, which indicates that the CLI method is able to perform closed loop identification of uncertain AMB parameters. The CLI method has proved very useful for providing quick, transparent and sufficiently accurate estimation of uncertain parameters during the controller tuning phase. The CLI method is orders of magnitudes faster than the SL method and does not require additional external hardware as the SL does. Additionally, the CLI method is general and allows for identification of multiple types of parameters such as $\mathbf{K}_i$, $\mathbf{K}_s$ and τ_e even for flexible rotor systems. However, the linear structure adopted in the presented formulation of the CLI method appears to lead to challenges in the non-linear operational domain of the AMBs. The non-linearities originate from saturation of the AMB actuators operated at high bias currents, for which the CLI methods over-predicts $\mathbf{K}_i$ compared to the the SL method. Furthermore, discrepancies between the simulated and measured current time series are suspected to originate from a too low model order for the amplifiers which is a relevant subject for future work. It is evident from the studies presented here that the electrodynamic model of the actuator requires additional attention. The embedded Hall sensor system of the AMBs could prove a powerful tool in this regard, as it enables quantification of the flux density generated in the stator. Consequently dynamics caused by the generation of Eddy currents in the AMB stators could potentially be quantified experimentally.

ISMB15

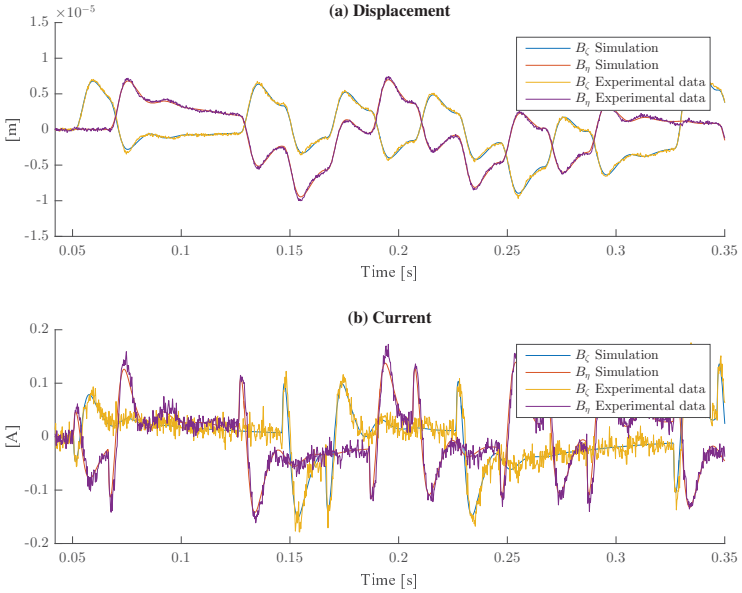

Fig. 5: Comparison of simulated and experimental data, here shown for AMB B. (a) Displacements and (b) control currents for a PRBS current input disturbance with an amplitude of 100 mA. Data obtained for a bias current of 6 A.

References

Schweitzer, G. "Active magnetic bearings - chances and limitations." IFToMM Sixth International Conference on Rotor Dynamics, Sydney, Australia. Vol. 1. 2002.

Anderson., B. D. From Youla Kucera to identification, adaptive and nonlinear control, Automatica 34, pp. 1485-1506, 1998.

Sun, Z., Zhao, J., Shi, Z. "Identification of magnetic bearing system using a novel subspace identification method" In Proceedings of ISMB14, pp. 87-90, 2014.

Sun, Z., He, Y., Zhao, J., Shi, Z., Zhao, L., Yu, S. "Identification of active magnetic bearing system with a flexible rotor." Mechanical Systems and Signal Processing 49.1 (2014): 302-316.

Tiwari, R., Chougale, A. "Identification of bearing dynamic parameters and unbalance states in a flexible rotor system fully levitated on active magnetic bearings." Mechatronics 24.3 (2014): 274-286.

Lauridsen, J. S., Sekunda, A. K., Santos, I. F., Niemann, H. "Identifying parameters in active magnetic bearing system using LFT formulation and Youla factorization." Control Applications (CCA), 2015 IEEE Conference on. IEEE, 2015.

Voigt, A. J., Mandrup-Poulsen, C., Nielsen, K. K., Santos, I. F. "Design and Calibration of a Full Scale Active Magnetic Bearing Based Testing Facility for Investigating Rotordynamic Properties of Turbomachinery Seals in Multiphase Flow". Proceedings of the ASME Turbo Expo 2016 (recommended for journal publication). Seoul, South Korea.

Bleuler, H., Cole, M., Keogh,P., Larsonneur, R., Maslen, E., Okada,Y., Schweitzer, G., Traxler, A. "Magnetic bearings: theory, design, and application to rotating machinery". Eds. Gerhard Schweitzer and Eric H. Maslen. Springer Science & Business Media, 2009.

Publication P4

Theoretical and Experimental Investigation of Force Estimation Errors Using Active Magnetic Bearings With Embedded Hall

Paper published in the proceedings of ASME Turbo Expo 2012.

Proceedings of ASME Turbo Expo 2012
GT2012
June 11-15, 2012, Copenhagen, Denmark

GT2012-68282

THEORETICAL AND EXPERIMENTAL INVESTIGATION OF FORCE ESTIMATION ERRORS USING ACTIVE MAGNETIC BEARINGS WITH EMBEDDED HALL SENSORS

Andreas Jauernik Voigt
Lloyd's Register ODS
Copenhagen, Denmark
Email: andreas.voigt@lr-ods.com

Ilmar F. Santos*
Associate Professor
Department of Mechanical Engineering
Technical University of Denmark
Copenhagen, Denmark
Email: ifs@mek.dtu.dk

ABSTRACT

This paper gives an original theoretical and experimental contribution to the issue of reducing force estimation errors, which arise when applying Active Magnetic Bearings (AMBs) with pole embedded Hall sensors for force quantification purposes. Motivated by the prospect of increasing the usability of AMBs by embedding Hall sensors instead of mounting these directly on the pole surfaces, force estimation errors are investigated both numerically and experimentally. A linearized version of the conventionally applied quadratic correspondence between measured Hall voltage and applied AMB force is suggested and investigated. A finite element (FE) model is constructed to study force error behavior as a function of rotor offset. The investigation confirms that the magnitude of the force error is dependent on how well the rotor is centered in the AMB. Furthermore, below a rotor offset corresponding to $\sim 20\%$ of the nominal air gap the force estimation error is found to be reduced by the linearized force equation as compared to the quadratic force equation, which is supported by experimental results. Additionally the FE model is employed in a comparative study of the force estimation error behavior for pole embedded and pole surface mounted Hall sensors. It is shown that in a given range of bias currents and rotor offsets, pole embedded and surface mounted Hall sensors perform equally well for the four pole heteropolar flux-split radial AMB under investigation. Furthermore, frequency dependence of the Hall sensor sensitivity factors is investigated, and found to be non-existing, hence static calibration of Hall sensors is sufficient, even for dynamic testing purposes.

NOMENCLATURE

g_0 Nominal air gap [m]
$\mathbf{B}$ Magnetic flux density [T]
B Scalar magnetic flux density [T]
Δy_0 Rotor offset [m]
Δy Rotor displacement from rotor offset [m]
$F_{1,2,Vert.}$ Measurable reaction forces [N]
$y_{1,2}$ Measured rotor position signals [m]
$\ddot{y}_{1,2}$ Measured rotor acceleration signals [m/s^2]
A_g Pole area [m^2]
μ_0 Permeability of vacuum [N·A^{-2}]
I_H Hall sensor control current [A]
ρ Charge carrier density [m$^-$3]
q_e Charge carrier charge [C]
d Hall element height [m]
K, K_2, K_4 Hall sensor sensitivity factor [N/V^2]
β, γ Hall sensor sensitivity factor [N/V]
ξ Hall sensor static offset factor [N]
$V_H, V_{H,2}, V_{H,4}$ Hall voltage [V]
Geo Geometric scaling factor [-]
F, F_{AMB} AMB force [N]

*Address all correspondence to this author.

$F_{AMB,calc.}$ Calculated AMB force [N]
$F_{num.AMB}$ Numerically obtained AMB force [N]
$F_{AMB,resp.}$ Response based AMB force [N]
$F_{AMB,react.}$ AMB force quantified from reaction force measurements [N]
$F_{err.}$ Force estimation error [N]
n Arbitrary discreet counter [-]
ϕ Root Mean Square (RMS) of $F_{err.}$ [N]
$\overline{F_{err.}}$ Average RMS error [N]
σ Average standard deviation [N]
$k_{equiv.}$ Equivalent system stiffness [N/m]
$m_{equiv.}$ Equivalent system mass [kg]
Ξ Bias current [A]

1 Introduction

This paper is to a large extent motivated by the prospects arising in rendering rotating machinery "smart". Active Magnetic Bearings (AMBs) are instrumental to the notion of smart machines, mainly due to their high degree of controllability allowing the AMB to support the shaft while continuously suppressing shaft vibrations. If accurate information about the magnetic forces are obtained, AMBs can also be used to perform dynamic testing in rotating machines [1]. With the measurements of current and position [1,2], or pole structure deformation via laser strain gauges [3], or the introduction of Hall sensors [4–8], the AMB can function as a multidirectional load cell for quantification of radial AMB forces. With the further extension of shaft position measurements, the AMB constitutes a powerful all-in-one tool for parameter identification and diagnosis purposes [1, 5–8], based on frequency response functions (FRFs). The need for high precision force measurements is pronounced, as force estimation errors will lead to disproportionably large errors in the FRFs of the shaft-AMB system, upon which conventional parameter identification schemes are based. A revision of general force measurement techniques is presented in [9].

High precision quantification of AMB forces is still subject to research. This research may be subgrouped into three main areas: (I) Quantification of electromagnetic forces by measuring pole structural deformation via conventional or laser strain gauge techniques, (II) by measuring the magnetic field using Hall effect sensors, (III) by measuring air gap and current ($i-s$). Though modern $i-s$ based techniques as reluctance network models [10] and the Multi-Point method [11] show promising results, especially considering the inherent low hardware complexity, the precision of the flux measurement method is still superior in terms of minimising force estimation errors [6]. The first ideas of using Hall sensors in AMBs are presented in [4, 5]. Hall effect sensors are quite inexpensive and noise compensation techniques can be added in order to obtain an even higher accuracy of magnetic flux density [12, 13].

Conventionally, quantifying AMB forces using Hall sensors require an enlargement of the air gap between the rotor and AMB poles to accommodate the Hall sensors. Enlargement of the air gap leads to a loss in applicable electromagnetic force, and reveals the fragile Hall sensors to impact from the rotor at large vibrational amplitudes, or during assembly of the rotor-bearing system. These difficulties can be overcome by mounting the Hall sensors in slots manufactured in the pole surface as described in [10], at the cost of a slightly decreased ($< 2\%$, [10]) load capability. The main drawback from mounting the Hall sensors in milled slots is that the slot itself disturbs the path of the flux which is to be measured [5, 10, 14]. Calibrating the Hall sensors by conventional means, in an especially designed test facility, can account for some of the discrepancies arising from embedding the Hall sensors [10]. But even so, an error on the estimated force will remain. A precise quantification of these errors is key when estimating the consequences of embedding the Hall sensors.

2 Experimental Facilities

A four pole heteropolar radial active magnetic bearing with Hall sensors embedded in milled slots in each of the four pole surfaces is illustrated in Fig 1. Fig. 1 (a) shows an internal view of the AMB revealing the position of the embedded Hall sensors and Fig. 1(b) shows a schematic view of the AMB along with reference frame, coil/pole/Hall sensor -enumeration, nominal air gap, and current direction definitions. The AMB design parameters are summarised in Table 1. The heteropolar AMB features a flux-splitting type coil configuration, and is designed to be operated in differential mode [14]. As a consequence of embedding the Hall sensors the magnetic flux density $\mathbf{B}$ is measured locally in the slots and not directly on the pole surface and the net total magnetic force delivered by the bearing is reduced in the order of $\sim 2\%$ [10]. In order to calibrate the Hall sensors, the AMB is placed in a test set up facilitating both dynamic and static calibration [15]. A front view of the complete experimental set up consisting of AMB, supports, shaft and rotor can be seen in Fig. 2(a). The shaft is suspended in roller bearings and each support is embedded with four preloaded strain gauge based compressive force transducers (HBM C9B) facilitating multidirectional reaction force measurements. Preloading and rotor position adjustment are enabled through the adjustment bolts (see Fig. 2(b)). However, adjustment of the initial rotor position proved difficult in practise due to the to large pitch of the adjustment bolts. Fig. 2(b) shows the embedded force transducers and Fig. 3 shows a schematic view of the measurable reaction forces, the force applied by the AMB and the position of the displacement sensors and accelerometers employed in the experimental procedures. Investigations are only undertaken for the vertical direction.

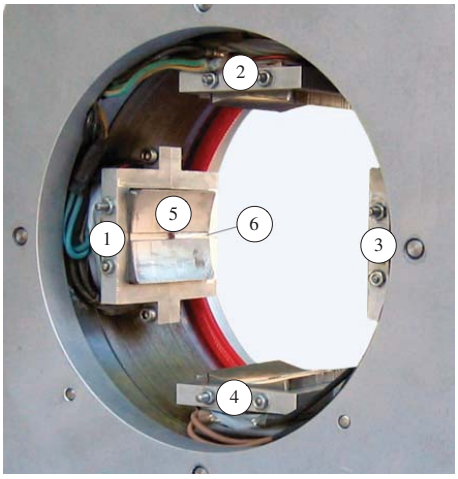

(a)

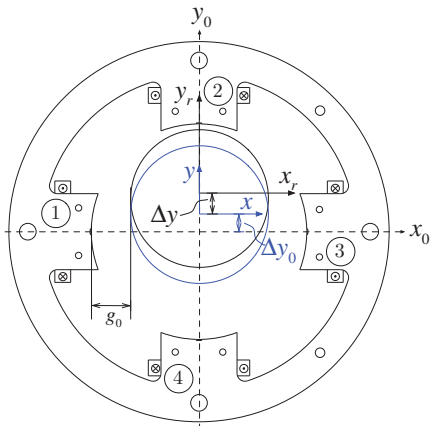

(b)

FIGURE 1: (a) Internal view of the AMB showing pole enumeration (1-4), Hall sensor (5) and milled slot (6), and (b) schematic view of AMB definitions showing the nominal air gap, coil/pole/Hall sensor -enumeration, reference frames and coil current direction definitions. The reference frame $\{x_0, y_0\}$ is attached to the center of the AMB. The reference frame depicted in blue color is shifted upwards by the distance Δy_0 which denotes the rotor offset. The rotor displacement measured from the rotor offset, is described in the reference frame $\{x, y\}$ by a displacement of $\{x_r, y_r\}$ by the distance Δy

3 Mathematical Modeling and Definitions

This section introduces a methodology applied to quantify the force exerted by the AMB. The method is based on knowledge of the magnetic flux density **B**, obtained through Hall sensors based measurements, and estimates the AMB force as a function hereof.

TABLE 1: AMB design parameters

Stator outer diameter	240	m
Rotor outer diameter	140	m
Nominal air gap	0.25	m
Pole width	48	m
Pole depth (Axial)	70	m
Number of poles	4	
Angular separation of poles	90°	
Lamination thickness	0.5	m
Number of laminations	140	
Rotor and stator material	Steel V400-50A	
Max. load capacity	1900	N
Bias current range	0 to 8	A
Number of Hall sensors	4	
Hall sensor type	F.W. Bell - BH-200	
Hall sensor dimensions ($l \times w \times h$)	$2 \times 3 \times 0.6$	m
Hall sensor slot dimensions ($w \times d$)	3.3×0.7	m

Actuator Model

The force generated from a single AMB actuator (pole) can be generically expressed as [8, 16]

$$F = \frac{A_g}{2\mu_0} B^2 \tag{1}$$

in which A_g denotes the area of the stator pole and μ_0 is the permeability of vacuum. Eqn. (1) shows the quadratic dependence of actuator force on the time dependent magnetic flux density magnitude B. A simplified model of the Hall sensor can be derived as [8, 16]

$$V_H = \frac{1}{q_e \rho d} I_H B \tag{2}$$

in which I_H and B are the magnitude of the Hall sensor control current and the magnetic flux density, respectively. Eqn. (2) is

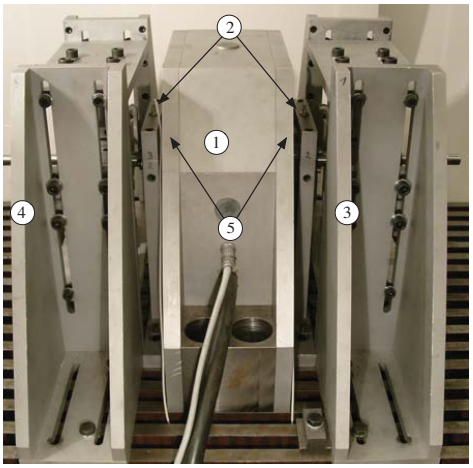

(a)

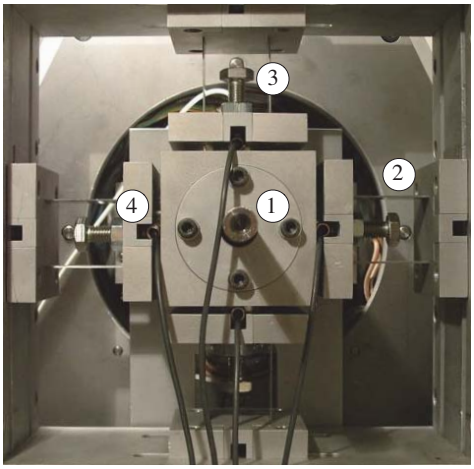

(b)

FIGURE 2: (a) Experimental facility, front view: (1) AMB, (2) Position sensors, (3) + (4) Support structure, (5) Accelerometers (not visible in current view) and (b) end view (1) Roller bearing house, (2) De-coupling beam, (3) Adjustment bolt, (4) Embedded force transducer

seen to be purely scalar and presents V_H as a function of the magnitude of current I_H, and magnetic flux density B. Furthermore, Eqn. (2) shows the importance of operating the Hall sensor with a constant I_H, since variations in the current would be interpreted as variations in B, since V_H varies as a function of I_H. Eqn. (2)

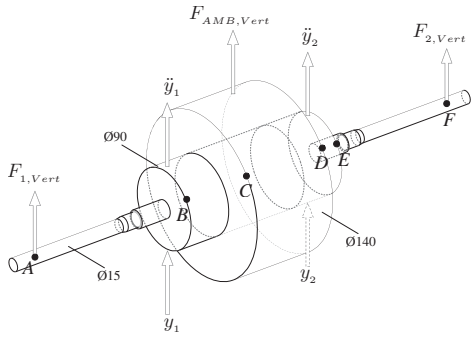

FIGURE 3: Schematic view of measurement location for reaction forces, acceleration and position as well as rotor diameters. The axial length between point: A and B is 75 mm, B and C is 50 mm, C and D is 100 mm, D and E is 50 and E and F is 75 mm

translates B into an actual measurable quantity V_H. Combining Eqn. (1) and Eqn. (2) and summing vertical forces yields after re-arranging

$$F_{AMB,calc.} = K_2 V_{H,2}^2 - K_4 V_{H,4}^2 \tag{3}$$

where the coefficients K_i is defined as

$$\frac{A_g}{2\mu_0}\left(\frac{q_e \rho d}{I_H} Geo_i\right)^2 \equiv K_i,\ [\mathrm{N/V^2}] \tag{4}$$

A geometric scaling factor Geo_i has been introduced in Eqn. (4) to compensate for all effects related to the placement of the Hall sensor in the slots and not on the pole surface as implicitly assumed when Eqn. (1) and Eqn. (2) were combined. The coefficient defined in Eqn. (4) is from here on referred to as the Hall sensor's sensitivity factor. Eqn. (3) relates the measurable Hall voltage to the vertical force exerted by the AMB, and requires experimental identification of the sensitivity factors K_2 and K_4. Eqn. (4) is generally referred to as the force equation on quadratic form.

Linearization of the Force Transducer Model

A Taylor series expansion to first order of Eqn. (3) about the point $\left(V_{H,2,0}, V_{H,4,0}\right)$ takes the following form

$$\begin{aligned} F_{AMB,calc.} \cong\ & F_{AMB,calc.}\left(V_{H,2,0}, V_{H,4,0}\right) \\ & + \frac{\partial F_{AMB,calc.}}{\partial V_{H,2}}\Big|_{V_{H,2,0}} \left(V_{H,2} - V_{H,2,0}\right) \\ & + \frac{\partial F_{AMB,calc.}}{\partial V_{H,4}}\Big|_{V_{H,4,0}} \left(V_{H,4} - V_{H,4,0}\right) \end{aligned}$$

where $\left(V_{H,2,0}, V_{H,4,0}\right)$ denotes the Hall voltages read from sensor two and four when the AMB is only supplied with a bias current. By evaluating the partial derivatives and simplifying, the following is obtained

$$\begin{aligned} F_{AMB,calc.} \cong\ & \underbrace{F_{AMB,calc.}\left(V_{H,2,0}, V_{H,4,0}\right) - 2K_2 V_{H,2,0}^2 + 2K_4 V_{H,4,0}^2}_{\xi} \\ & + \underbrace{2K_2 V_{H,2,0}^2}_{\beta} V_{H,2} - \underbrace{2K_4 V_{H,4,0}^2}_{\gamma} V_{H,4} \end{aligned} \tag{5}$$

Gathering coefficients as suggested in Eqn. (5) yields

$$F_{AMB,calc.} \cong \xi + \beta V_{H,2} - \gamma V_{H,4} \tag{6}$$

In order to apply the Eqn. (6) to determine the force delivered by the AMB, the coefficient ξ and the sensitivity factors β and γ need to be determined. The static offset coefficient ξ can be considered as representing the resulting force exerted by the AMB, when this is supplied only with a bias current to all four coils. As this force for a completely centered rotor is zero by definition, the coefficient ξ can be set to zero whenever a completely centered rotor is treated. When the rotor is not completely centered in the AMB a resulting force component will be present, even when only a bias current signal is fed to the AMB. However, as the force transducer output is zeroed prior to any application of the AMB, this bias force will be removed from the force measurements. Hence in either of the two above described cases, ξ can be set to zero, and consequently Eqn. (6) reduces to

$$F_{AMB,calc.} \cong \beta V_{H,2} - \gamma V_{H,4} \tag{7}$$

Identification of Hall Sensor Sensitivity Factors

The experimental quantification of the sensitivity factors K_2 and K_4 constitutes the calibration procedure of the Hall sensors and is performed in two different configurations. Both of these depend on a quantification of the exerted force giving the left hand side of Eqn. (3), and simultaneously obtained Hall voltages. The calibration procedure is performed on both experimentally and numerically obtained data, but since there is no conceptual difference between these, it is sufficient only to outline the procedure ones. In order to identify the sensitivity factors K_2 and K_4, a least squares scheme is employed, reformulating Eqn. (3) into an over-determined system of equations

$$\underbrace{\begin{bmatrix} V_{H,2,1}^2 & -V_{H,4,1}^2 \\ V_{H,2,2}^2 & -V_{H,4,2}^2 \\ \vdots & \vdots \\ \vdots & \vdots \\ V_{H,2,n}^2 & -V_{H,4,n}^2 \end{bmatrix}}_{\mathbf{A}} \underbrace{\begin{bmatrix} K_2 \\ K_4 \end{bmatrix}}_{\mathbf{x}} = \underbrace{\begin{bmatrix} F_{AMB,1} \\ F_{AMB,2} \\ \vdots \\ \vdots \\ F_{AMB,n} \end{bmatrix}}_{\mathbf{b}} \tag{8}$$

where n is the number of data points, and $F_{AMB,n}$ can be either of the experimentally or numerically estimated force data. The system of equations $\mathbf{Ax} = \mathbf{b}$ presented in (8) can be solve by

$$\mathbf{x} = \left(\mathbf{A}^T\mathbf{A}\right)^{-1}\mathbf{A}^T\mathbf{b} \tag{9}$$

using the method of least squares. This method has an equivalent form for the linearized force expression not shown here.

Definition of Force Estimation Error

The error introduced by estimating the force delivered by the AMB, using either Eqn. (3) or Eqn. (7), is determined by subtracting the calculated force from the applied (true) force in the following way

$$F_{err.}(n) = F_{AMB}(n) - F_{AMB,calc.}(n) \tag{10}$$

in which $F_{AMB}(n)$ can be the static or dynamic force obtained either experimentally or numerically. The variable n defined in Eqn. (10) denotes an arbitrary discrete counter, keeping track of the steps in applied force. As a measure of the overall error the Root Mean Square (RMS) value of $F_{err.}$ for all n is used. Here the RMS value of the force estimation error is determined as

$$\phi = \mathrm{RMS}\left(F_{err.}\right) = \frac{\mathrm{norm}\left(F_{err.}\right)}{\sqrt{N}} \tag{11}$$

where $\mathrm{norm}\left(F_{err.}\right)$ is the Euclidian length of the vector $F_{err.}$. The quantity ϕ gives a measure of the error on $F_{calc.}$ assuming that F_{AMB} is representing the true value of the force applied by

the AMB. Furthermore, in the experimental investigations performed, the calibration procedures for each choice of bias current is repeated $M = 16$ times. To condense this information into a single number, an average RMS force error can be determined by

$$\overline{F_{err}} = \frac{1}{M}\sum_{j=1}^{M}\phi_j$$

where ϕ_j is the RMS error estimated for each of the M repetitions of the calibration procedure as presented in Eqn. (11). The averaged standard deviation is determined as

$$\sigma = \left[\frac{1}{M-1}\sum_{j=1}^{M}\left(\phi_j - \overline{F_{err}}\right)^2\right]^{1/2}$$

which gives a measure of the variation of the average error between the repeated calibration procedures.

A 2D planar finite element model (FE-model) of the AMB is applied to perform magnetostatic modelling of the AMB. The FE-model is implemented using the program FEMM from Meeker [17] and executed through MatLab to be able to incorporate the change in position of the rotor as the AMB applies a force. This is done by calculating the change in position governed by

$$F_{num.,AMB} = k_{equiv.}\Delta y \quad \Leftrightarrow \quad \Delta y = \frac{F_{num.,AMB}}{k_{equiv.}} \tag{12}$$

where $F_{num.,AMB}$ is the numerical estimate of the AMB force and $k_{equiv.}$ is an equivalent stiffness found experimentally. The equivalent stiffness $k_{equiv.}$ sum up stiffness contributions from the support structure as well as the force transducers. The FE-model recreates the conditions under which the experimental investigation is performed entailing: Supplying a control current to coils two and four and determining the force exerted by the AMB. Now, a new equilibrium position for the rotor is determined using Eqn. (12). The rotor position is updated and the flux density in the Hall sensor domains is determined. This procedure is repeated for all 20 control current steps in the test interval. A bias current of 3 A is used and the control current spans between -2.5 A and 2.5 A throughout the numerical analysis. The resulting AMB force $F_{num.,AMB}$ exerted on the rotor is quantified by integrating the weighted Maxwell stress tensor over the area of the rotor and the shaft. Likewise, an estimator for the Hall voltage is deducted by integrating the $\mathbf{B}_y$-field over the cross section area of the Hall element, thus assuming $\int_A \mathbf{B}_y dA \propto V_{H,AMB}$, where A is the surface area of the Hall element. The FE-model is applied in two different configurations outlined in the subsections below.

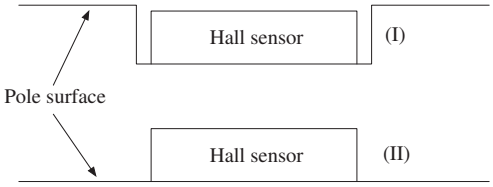

FIGURE 4: (I) Hall sensor embedded into pole surface, (II) Hall sensor mounted on top of pole surface

3.1 Force Error Behaviour for Multiple Rotor Offsets and Feasibility of Using the Linearized Force Equation to Reduce Force Estimation Errors

The purpose is to investigate force estimation error behavior as a function of the rotor offset. This is done by evaluating the FE-model for multiple rotor offsets $\Delta y_0 \in \{0.000, 0.010, 0.050, 0.075, 0.100, 0.117, 0.133, 0.150\}$ [mm] which ranges from zero to $\sim 60\%$ of the nominal air gap g_0. Furthermore, the numerical results obtained here will be used to asses the performance of the FE-model by comparison with experimentally found behavior of the system. Additionally, the feasibility of using the linearized force equation to reduce force estimation errors will be investigated.

4 Numerical Procedures

4.1 Force Error Comparison for Surface Mounted and Pole Imbedded Hall Sensors Including Evaluation of the Feasibility of Using the Linearized Force Equation to Reduce Force Estimation Errors

The purpose here is to investigate force error behavior when the Hall sensors are placed in milled slots in the pole surface and a hypothetical scenario where the Hall sensors are mounted directly on the pole surface. The two Hall sensor mounting configurations are sketched in Fig. 4. As above, the force estimation error is investigated for multiple rotor offsets $\Delta y_0 \in \{0, 0.01, 0.02, 0.03, 0.04, 0.05, 0.06, 0.07\}$ [mm], ranging from zero to 10% of the original nominal air gap. It is emphasised that in this part of the numerical study the rotor diameter is decreased slightly ($\sim 0.7\%$) to accommodate the pole surface mounted Hall sensor, and that this part of the numerical study will have no experimental counterpart, as only one rotor size and an AMB with Hall sensors placed in milled slots are available for experimental studies. Additionally, the feasibility of using the linearized force equation to reduce force estimation errors will be investigated for both surface mounted and pole embedded Hall sensors.

5 Experimental Procedures

5.1 Experimental Validation of the FE-model and Feasibility of Using the Linearized Force Equation to Reduce Force Estimation Errors:

The experimental data used for comparison with the FE-model and verification of the applicability of the linearized force equation is gathered in a manner replicating a conventional static calibration procedure. A static calibration is performed by measuring reaction forces using the force transducers embedded in the supports, while recording the Hall voltage from each sensor $V_{H,i}$, and subsequently applying the methods described in section 3. Experimental data is acquired for three choices of bias current, namely 3 A, 4 A, and 5 A and for each choice of bias current a 40 step staircase control current function is supplied to coils two and four in accordance with the conventions of differential driving mode. The staircase function steps from $-(\Xi-0.5)$ A to $(\Xi-0.5)$ A, and back down from $(\Xi-0.5)$ A to $-(\Xi-0.5)$ A, where Ξ denotes the bias current, in order to test for hysteresis effects. The procedure is, for each choice of bias current, repeated a total of 16 times and the sensitivity factors used throughout the experimental part of the investigation are found as the average values of the sensitivity factors determined for each of the 16 repeated tests.

5.2 Frequency Dependence of the Force Equation Coefficients - Dynamic Calibration

Here the main purpose is to test for any frequency dependence of the Hall sensor sensitivity factors. Again the force transducers in the shaft supports are employed to measure reaction forces at the shaft supports. However, in addition accelerometers and positions sensors are employed to measure the acceleration and position of the rotor, quantities in turn usable as an alternative method with which the AMB force can be quantified. Obtaining the applied force from acceleration and position measurements is based on modeling the rotor as an undamped SDOF system, for which the governing equation can be expressed as

$$F = m_{equiv.}\ddot{y} + k_{equiv.}\Delta y \tag{13}$$

where $m_{equiv.} \approx 1.93 \pm 0.02$ kg in the present case represents the combined mass of the shaft, rotor and bearing houses, and $k_{equiv.} \approx 1.52 \cdot 10^7 \pm 0.01 \cdot 10^7$ N/m is the equivalent stiffness. Damping is omitted in Eqn. (13) as it is assumed to have only a slight influence on the force estimation and only around resonance of the equivalent system. F on the left hand side of Eqn. (13) denotes the external loading, in the present case considered to be the periodic load applied by the AMB, thus $F \equiv F_{AMB,resp.}$. In addition to the force, the Hall voltage from each sensor $V_{H,i}$ is obtained. During calibration the AMB exerts a sinusoidal current signal and thereby force onto the rotor in discrete frequency steps of 5 Hz in the range $[0;200]$ Hz, and a set of sensitivity factors

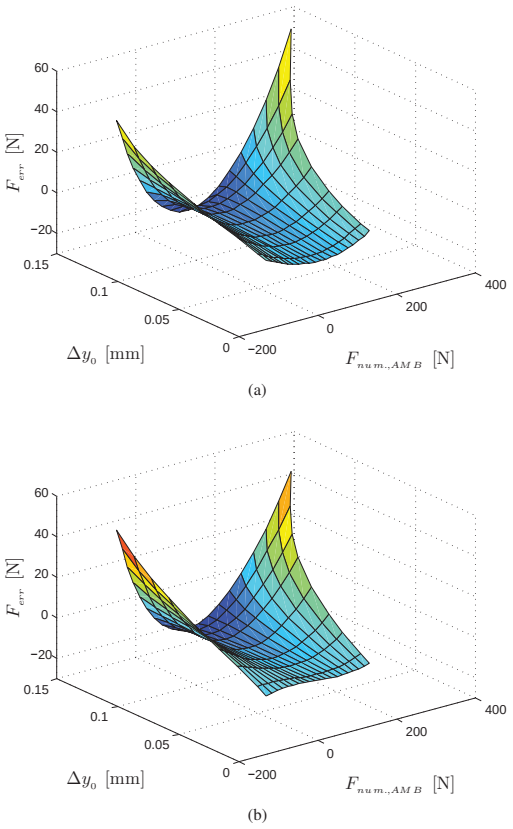

FIGURE 5: Force error behavior as a function of Δy_0 using a bias current of 3 A and a control current varied between -2.5 A to 2.5 A: (a) force error behavior arising from applying the quadratic force equation, (b) force error behavior arising from applying the linearized force equation - embedded Hall sensor

is determined for each step in frequency using Eqn. (8). A bias current of 3 A and a control current amplitude of 2.5 A is used throughout this investigation.

5.3 Uncertainty Analysis

The main experimental results are subjected to an uncertainty analysis. The force transducers are calibrated in situ and are found to behave linearly in the chosen working range -400 N to 400 N with a maximum uncertainty of $\pm 0.2\%$ of maximum load. The uncertainty on the position and acceleration measurements is a function of the readout from the signal conditioners

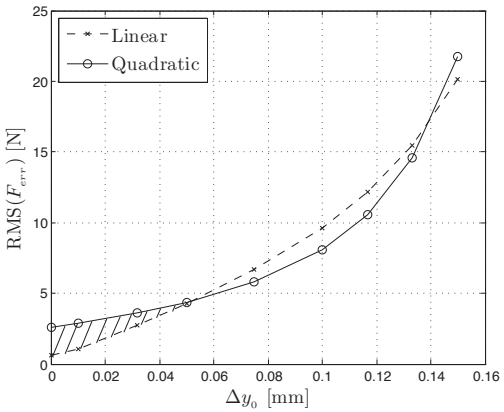

FIGURE 6: The RMS value of the force estimation error using either the quadratic or linear force equation, as a function of the rotor offset. The area of improvement, where the linearized force equation reduces the force estimation error compared to the conventional quadratic force equation is indicated as a dashed area - embedded Hall sensor

themselves and needs to be evaluated for each measurement. In addition to these key error contributors the uncertainty analysis includes: the random error on all measured quantities, the errors from the dSPACE board used for data retrieval, errors on the equivalent system mass and error on equivalent rotor system stiffness. All relevant uncertainties are reported whenever data is presented and an in-depth uncertainty analysis can be found in [16] which is based on the guide lines of [18]. It is highlighted that the uncertainties presented is an estimate of the worst case uncertainty for the given quantity whether directly measured or derived, and that these are marked in red for graphical representation.

6 Numerical Results

6.1 Force Error Behaviour for Multiple Rotor Offsets and Feasibility of Using the Linearized Force Equation to Reduce Force Estimation Errors

Fig. 5(a) shows the force estimation error calculated using Eqn. (10) which arises when applying the quadratic force equation, Eqn. (3) to estimate the force applied by the AMB. Fig. 5(b) presents the force error arising when applying the linear force equation. As a rotor offset Δy_0 is introduced, the force exerted on the rotor becomes asymmetric, which is seen as an increase in force for a 2.5 A control current, as the initial (positive) rotor offset is increased. Similarly, the force exerted for a control current of -2.5 A decreases as the rotor offset is increased. The impact on the force error is evident from both Fig. 5(a) and Fig. 5(b), where the global force error is seen to have a maximum where the exerted force has a global maximum. Fig. 5(a) shows the same u-shaped error behavior for all rotor offsets. But inspection of Fig. 5(b), obtained using the linear force equation, reveals that the force estimation error for small ($\Delta y_0 < 0.01$ mm) rotor offsets changes shape qualitatively. More precisely the force error takes the form of an s-shaped curve, and it is noted that the force error seems to be reduced significantly in this region.

The overall error properties are displayed in Fig. 6, where the RMS value of the error is plotted as a function of the rotor offset, for both the quadratic and the linear force equation approaches. Fig. 6 reveals that for a rotor offset between zero and ~ 0.05 mm ($\sim 20\%$ of the nominal air gap), the linearized force equation yields a reduction in force error compared to applying the quadratic force equation. This region of improvement is visualised in Fig. 6 as a dashed area. By increasing the rotor offset beyond ~ 0.05 mm, the results from the linear force equation becomes worse than the quadratic counterpart. Finally the graphs for the overall error behavior crosses paths again when the rotor offset is increased above ~ 0.14 mm, again rendering the performance of the linear force equation, regarding force error, an improvement over the quadratic force equation. A globally valid conclusion is that the overall force error increases as the rotor offset is increased, which is also detectable in Fig. 5(a) and (b) and is in correspondence with the findings presented in [7].

6.2 Force Error Comparison for Surface Mounted and Pole Imbedded Hall Sensors Including Evaluation of the Feasibility of Using the Linearized Force Equation to Reduce Force Estimation Errors

The results are presented in Fig. 7, where Fig. 7(a) and (b) represents the AMB with Hall sensors mounted on top of the pole surfaces, and Fig. 7(c) and (d) presents the error behavior for the AMB with the Hall sensors embedded into the pole surfaces.

The variation of the rotor offset is limited due to the fact that the FE-model geometry has to accommodate the pole surface mounted Hall sensors. Within this range, the qualitative force error behavior does not change significantly when the quadratic force equation is applied for either the surface mounted or pole embedded configurations, as evident when comparing Fig. 7(a) and (c). However, it is seen that the force error in general is larger in magnitude for the pole embedded Hall sensor case. Turning the attention towards the force error obtained using the linearized force equation, Fig. 7(b) and (d) reveal an overall force error that decreases significantly as the rotor offset is decreased towards zero. The decrease in overall error as the rotor offset is decreased, is in correspondence with the results found previously where the true rotor diameter was used.

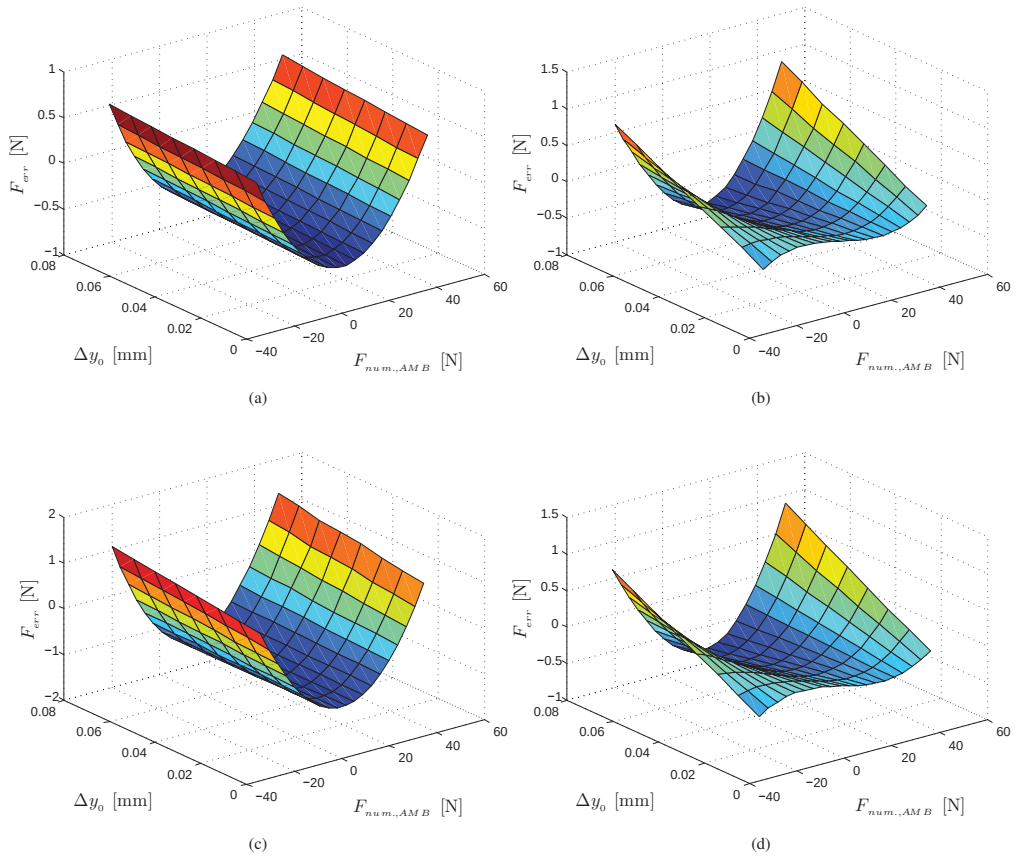

FIGURE 7: Force error behavior for pole and surface mounted Hall sensors as a function of the rotor offset and the applied force, obtained using a bias current of 3 A and a control current varied between −2.5 A to 2.5 A: (a) Force error behavior arising from applying the quadratic force equation with surface mounted Hall sensors, (b) force error behavior arising from applying the linearized force equation with surface mounted Hall sensors, (c) force error behavior arising from applying the quadratic force equation with embedded Hall sensors, and (d) force error behavior arising from applying the linearized force equation with embedded Hall sensors

Again the findings are condensed using the RMS value of the overall force estimation error and the results are presented in Fig. 8. As indicated earlier it is evident by inspection of Fig. 8, that the force error arising using the quadratic force equation is significantly larger when the Hall sensors are mounted in slots, compared to the surface mounted configuration. Furthermore, the overall force error is significantly reduced using the linear force equation for rotor offset below ≈ 0.05 mm ($\sim 10\%$ of original nominal airgap) as expected from the previous results. Again the region of improvement is visualised in Fig. 8 as a dashed area. Most importantly it is noticed that in the analysed domain of rotor offset, the overall force error for the two Hall sensor mounting configurations is very close to identical.

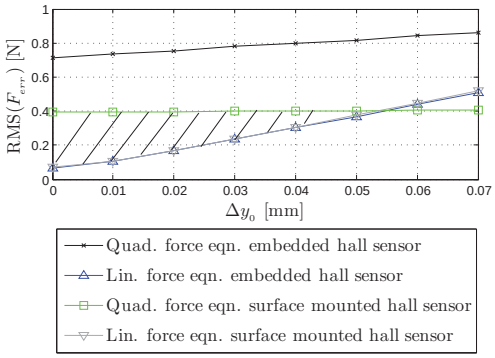

FIGURE 8: The RMS value of the force estimation error using the quadratic or the linearized force equation with pole embedded or surface mounted Hall sensors, as a function of the rotor offset

7 Experimental Results

7.1 Experimental Validation of the FE-model and Verification of the Applicability of the Linearized Force Equation

Initially it should be highlighted that for visual representation of experimental data the 3 A bias current case is used, and the data plotted is chosen arbitrarily from the 16 available sets. Fig. 9(a) presents the behavior of the Hall voltages from Hall sensor two and four, and these are seen to behave as expected considering the applied control current. Furthermore, qualitatively good correspondence between the experimental and numerical data is seen, which indicates that the FE-model is performing as intended and represents the physical system in a satisfactory manner. Fig. 9(b) shows the behavior of the force applied by the AMB and quantified using the force transducers in the support structure. Again good correspondance between the experimental and numerical data is seen. The force is plotted as a function of the control current, and it is noticed that the pull is asymmetric, and that the force for positive extremes of control current is consequently larger than the corresponding force for a negative extreme of control current. This asymmetry effect is attributed to the rotor being offset towards pole two as a consequence of poor rotor centering possibilities in the testing facilities.

As a consequence of hysteresis in the rotor-AMB system, two data branches tracing out ellipsoidal shapes, are seen in both Fig. 9(a) and (b) for the experimental data. The numerical data does not feature these hysteresis branches, as hysteresis effect inherently can not be captured by the magnetostatic FE-model. It is important to highlight that the residual magnetic field is captured by the Hall sensors, hence the magnetic hysteresis contribution to the force estimation error is likely only minor.

If the hysteresis bands in the experimental data are disregarded, the Hall voltages and the force appear to behave in a linear manner as visualized by the numerical data in Fig. 9(a) and (b). The close to linear behavior is the motivation behind the introduction of the linearized force equation: as the Hall sensor sensitivity factors are determined on the basis of the correspondence between applied force and Hall voltages, it is appealing to attempt a linear approach to the identification of these. The linear behavior of the Hall voltages and the force is considered to be a consequence of the imposed differential driving mode.

In order to estimate the precision with which the AMB force can be determined, Eqn. (3) and Eqn. (7), are applied on the experimental data, using the averaged sensitivity factors as mentioned earlier. The force is calculated for each of the 40 steps in the 16 repetitive calibration procedures for each choice of bias current. Fig. 10 presents a view of the calculated and measured force obtained for the 3 A case. Fig. 10(a) shows the force comparison when applying the quadratic force equation for both numerical and experimental data, and Fig. 10(b) shows the force comparison obtained by applying the linearized version of the force equation for both numerical and experimental data. Both Fig. 10(a) and (b) shows qualitatively good agreement between the measured and the force calculated on the basis of the measured Hall voltages, but close inspection of the plots reveals that the linearized force equation represents the measured force slightly better, as expected from the numerical survey presented earlier. It is noted that the hysteresis seems to be captured well by the Hall sensor based force calculations as expected. Again good qualitative agreement between the numerical and the experimental results is found.
The error introduced by estimating the AMB force using either Eqn. (3) or Eqn. (7) is determined using Eqn. (10) in section 3. A visualisation of the force estimation error behavior for both the experimental and the numerical is presented in Fig. 11, where the force error is plotted as a function of the applied force. Fig. 11(a) presents the instantaneous error obtained using the quadratic force equation, for each step in applied force. Fig. 11(b) presents the instantaneous force error obtained using the linearized force equation for the same data set as presented in Fig. 11(a). Again two branches of experimental data points are seen, which is a consequence of the aforementioned hysteresis. Furthermore, good correspondence between the experimentally and numerically obtained force estimation errors is seen. Fig. 11(b) reveals a force estimation error behavior similar to that depicted in Fig. 11(a) but the overall magnitude of the error seems to have been reduced.

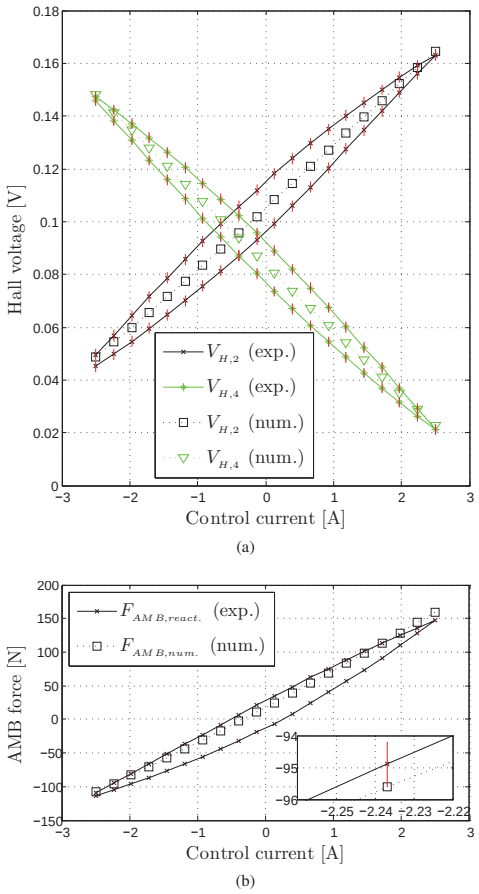

FIGURE 9: Experimental and numerical data obtained for a bias current of 3 A and a control current varied between −2.5 A to 2.5 A. All experimental data points presented are averaged over 4000 samples. (a) Shows the obtained Hall voltages as a function of the applied control current, (b) shows the force applied by the AMB as a function of the control current. The respective experimental uncertainty intervals are depicted along with the data where relevant

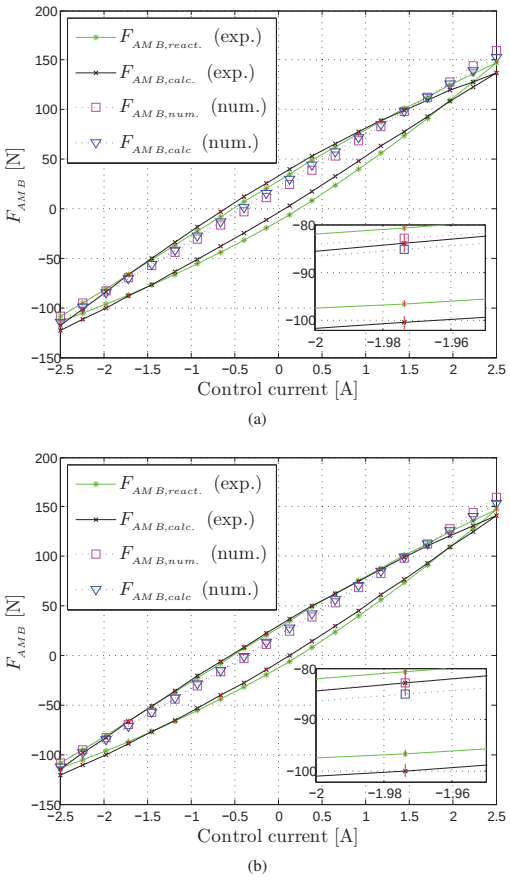

FIGURE 10: Calculated versus applied force for both experimental and numerical data sets, obtained for a bias current of 3 A and a control current varied between −2.5 A to 2.5 A: (a) Applying the quadratic force equation (b) Applying the linear version of force equation. Only the experimental uncertainties on the calculated force are visualized, as the uncertainty on $F_{AMB,react.}$ as it is too small (0.7 N) to be detectable. Furthermore, the uncertainty on the supplied current on the abscissa is neglected

The findings are summarized in Tab. 2 and primarily reveal a relatively large gain in force estimation precision, when applying the linear force equation as compared to the quadratic force equation which is in line with the numerical results presented earlier. As expected, Tab. 2 shows that as the bias current, and thereby the control current span is increased, the average RMS value of the force error $\overline{F_{err}}$ increases. Table 2 includes the standard deviations of $\overline{F_{err}}$, which indicates only slight variations in the results for the 16 data sets. Table 2 includes nominal values of the force error $\overline{F_{err}}$ in percent with respect to the maximum force applied for a given calibration procedure. The percentile quantification of the force error reveals that the increase in $\overline{F_{err}}$, as the bias current increases, is largely a consequence of the larger AMB force applied for

TABLE 2: The result of the static calibration procedure presenting the average RMS value of force error for both the squared and linear force equation cases. $\overline{F_{err}}$ represents the average over all 16 repetitive calibrations. Furthermore, the average RMS value of force error in percent with respect to the maximum applied force for the given calibration procedures is included. Finally the improvement in percent, determined with respect to the squared fitting case for the nominal mean RMS force error values, is presented. QFE = Quadratic Force Equation, LFE = Linearized Force Equation

	$\overline{F_{err}}$ [N]		$\overline{F_{err}}$ [%]				
I_{bias}	QFE	LFE	QFE	LFE	σ_{QFE} [N]	σ_{LFE} [N]	Improvement [%]
3 A	5.95	3.84	4.0	2.6	0.10	0.14	35.4
4 A	17.3	12.2	5.4	3.8	0.28	0.32	29.5
5 A	35.1	25.5	6.0	4.4	0.58	0.47	27.3

higher values of bias currents. The entries of Tab. 2 conveying a percent quantification of the force error, are calculated using nominal values determined as the mean of the 16 data sets for both the maximum force and the RMS value of the force error.

It should be mentioned that no uncertainties are presented in Tab. 2, as it is meant only to convey comparative differences between the two force calculation methodologies. This is considered to be allowed as the same data sets are investigated using two different calculation schemes, why the uncertainty sources are identical, eventhough the uncertainty on force error determined using the linearized force equation generally are slightly larger in magnitude due to the way it is derived.

The improvements stated in Tab. 2, are calculated with respect to the force error results of the quadratic equation, and show that the force estimation error can be reduced in the order of 30%, which is a relatively significant and in support of the numerical findings. Finally, the improvement rates are seen to deteriorate as the bias current is increased, which is most likely attributed to the measured force becoming less well described by the linear force equation as the bias current, and thereby the control current range and rotor deflection is increased as seen for the numerical results.

7.2 Frequency Dependence of the Force Equation Coefficients - Dynamic Calibration

The Hall sensor sensitivity factors K_2 and K_4 are identified using Eqn. (8) considering the two previously defined methods of quantifying the excitation force: one based on the measured reaction forces and one based on the response of the system. The resulting sensitivity factors are plotted as a function of the frequency in Fig. 12 and Fig. 13 and the two cases are treated separately in the following.

Sensitivity Factors Determined on the Basis of the Reaction Forces As seen in Fig. 12, the changes in magnitude of K_2 and K_4 are small in the range $0-100$ Hz but as the excitation frequency approaches the natural frequency of the system, $\omega_n = 141.5 \pm 0.5$ Hz, the magnitude of the sensitivity factors increases steadily and peaks at ω_n, indicating a clear coupling between the system dynamics and the identified sensitivity factors. At resonance a phase shift between the measured force and the Hall voltages occurs resulting in a jump in the calculated sensitivity factors. After resonance in the interval $141.5-200$ Hz, the magnitude of K_2 and K_4 decreases again. The coupling between the magnitude of K_2 and K_4 and the dynamic behavior of the system can be explained as follows: In the vicinity of ω_n, the inertial and restoring force contributions increase significantly. Thus around resonance the response of the system dominates the measured reaction forces, and these become disproportionally large compared to the force applied by the AMB. As the Hall voltages does not increase accordingly, the increase in force causes the local increase in K_2 and K_4. This is evident directly from considering Eqn. (3).

Sensitivity Factors Determined on the Basis of the Excitation Force Deducted Using the System Response In an effort to avoid the problems of the system response interfering with the calculations of K_2 and K_4 around resonance, Eqn. (13) is employed. The resulting sensitivity factors can be seen in Fig. 12, from which it is evident that the influence of the system response around resonance is greatly reduced. The sensitivity factors are now presentable by an almost straight line in the frequency domain, which indicates that these are not a function of the frequency. A detailed visualization of this is presented in Fig. 13, additionally showing a linear fit to the sensitivity factors based on the low frequency data ($0-90$ Hz), in an effort to avoid contamination from the system resonance. The

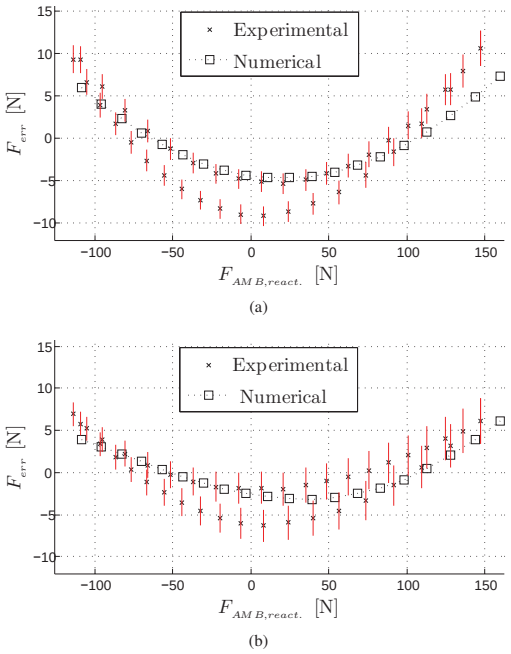

FIGURE 11: Force error behavior for a typical experimental and a numerical data set obtained for a bias current of 3 A and a control current varied between −2.5 A to 2.5 A: (a) Force error behavior arising from applying the quadratic force equation (b) Force error behavior arising from applying the linearized force equation. The experimental uncertainties on the force error are plotted along with the experimental data, with the exception of the uncertainty on $F_{AMB,react.}$ as it is too small (0.7 N) to be detectable in the plots

linear fits are described by, respectively

$$y_{k_2}(\omega) = -3.3\omega + 4475.7, \quad y_{k_4}(\omega) = -0.4\omega + 6877.7$$

in which ω denotes an independent frequency variable. It is seen that in both cases the slope of the fit is small, supporting the notion of no Hall sensor sensitivity factor frequency dependence.

As dissipative effects (damping) are not included in Eqn. (13) the sensitivity factors fluctuate slightly from the ideally straight horizontal line around resonance. This is due to the fact that the amplitude of the forced response around resonance, is dominated by the damping properties of the equivalent SDOF system. Far from resonance, good agreement is seen between the sensitivity factors calculated on the basis of Eqn. (8) using

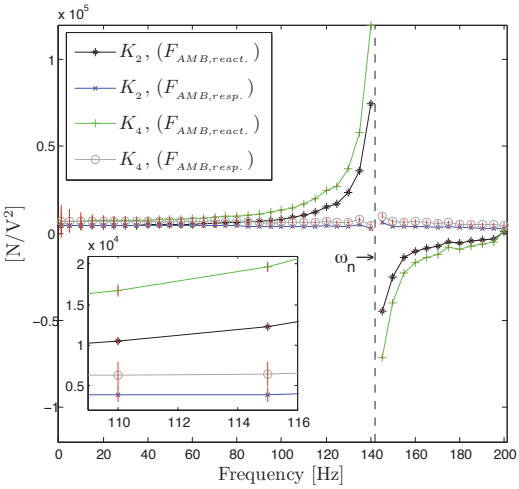

FIGURE 12: Variation of the sensitivity factors K_2 and K_4 as a function of the frequency using $F_{AMB,react.}$ and $F_{AMB,resp.}$ as indicated in the legend. The first natural frequency of the rotor - AMB system, ω_n is indicated by the dashed vertical line on the plots. The sensitivity factors are visualized along with their uncertainty interval shown in detail in the zoom window in the lower left corner of the plot

$F_{AMB,react.}$ and $F_{AMB,resp.}$ respectively, which is expected as the measured reaction forces are directly proportional to the force applied by the AMB in the low frequency range.

The sensitivity factors is for both force quantification methods visualized in Fig. 12 along with their respective uncertainty interval. It is clearly seen that the variation in the sensitivity factors are larger than the appended uncertainty, and consequently the peak in the sensitivity factors is not attributed to uncertainties. Based on the results presented above it is concluded that the sensitivity factors K_2 and K_4 are not a function of the excitation frequency and can be quantified from a static calibration of the Hall sensors. As K_2 and K_4 do not vary in the frequency domain it is concluded that neither do β and γ, as these generally can be considered as derived upon K_2 and K_4.

8 Conclusion and Future Aspects

When operating an AMB with embedded Hall sensors in differential mode, the error on the estimated force can be reduced significantly by using a linear approximation to the conventionally applied quadratic force equation for relatively small rotor offsets. Furthermore, embedding Hall sensors significantly increases the usability of these, as they are well

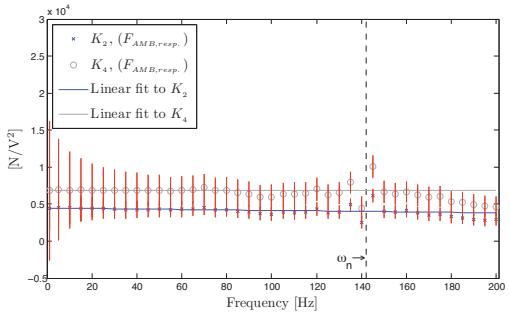

FIGURE 13: Variation of the sensitivity factors K_2 and K_4 as a function of the frequency using $F_{AMB,resp.}$ as indicated in the legend. A linear fit to K_2 and K_4 is included to visualize linearity. The first natural frequency of the rotor - AMB system, ω_n is indicated by the dashed vertical line on the plots. The sensitivity factors are visualized along with their uncertainty interval.

protected in the slots ensuring a stable operating environment. The results from the investigations presented here, show that within a given range of bias currents and rotor offsets, pole embedded and surface mounted Hall sensors perform equally well. Furthermore, the investigations verify that in order to reduce general force estimation error a completely centered rotor is optimal. These conclusions have several restrictions on their generality. Amongst others, the rotor-AMB system is only investigated for a limited range of bias currents, in the numerical investigation only one choice of bias current is investigated. This means that the applicable force range investigated is not exhaustively representing the capabilities of the AMB. Additionally, it is stressed that the conclusions are only valid for one type of AMB, namely the four pole heteropolar flux-split radial AMB. Furthermore, the frequency dependence of the Hall sensor based force equation was investigated and found to be non existing, which indicates that static calibration of the Hall sensors is sufficient.

The main results presented in this paper reveal a promising future for using embedded Hall sensors to quantify AMB forces with high precision. However, a large effort lies ahead rendering the conclusions drawn here general across different AMB types and operating scenarios. The authors are currently planning a second generation test facility in which the shortcomings of the current will be addressed.

REFERENCES

[1] Ulbrich, H., 1988. "New test techniques using active magnetic bearings". In Proceedings of the First International Symposium on Magnetic Bearings.

[2] Knight, J., Xia, Z., and McCaul, E., 1992. "Forces in magnetic bearings: Non-linear combutation and experimental measurements". In Proceedings of the Third International Symposium on Magnetic Bearings.

[3] Zutavern, Z. S., 2004. "Fibre optic strain gauge calibration and dynamic flexibility transfer function identification in magnetic bearings". Master's thesis, Texas A&M University, Texas A&M University, College Station, Texas.

[4] Gähler, C., and Förch, P., 1994. "A precise magnetic bearing exciter for rotordynamic experiments". In Proceedings of the Fourth International Symposium on Magnetic Bearings, pp. 193–200.

[5] Gähler, C., 1998. "Rotor dynamic testing and control with active magnetic bearings". PhD thesis, ETH ZÜRICH.

[6] Aenis, M., Knopf, E., and Nordmann, R., 2002. "Active magnetic bearings for the identification and fault diagnosis in turbomachinery". *Mechatronics,* ***12***(8), pp. 1011 – 1021.

[7] Knoph, E., and Nordmann, R., 1994. "Active magnetic bearings for the identification of dynamic characteristics of fluid bearings - calibration results". In Proceedings of the Fourth International Symposium on Magnetic Bearings, pp. 52–61.

[8] Kjølhede, K., 2007. "Experimental contribution to the problem of model parameter identification in rotating machines via active magnetic bearings". PhD thesis, Technical Univercity of Denmark.

[9] Hasan, H. E., 2011. "A review of concept of force measurements between the past and today". *Sensors & Transducers Journal,* ***129***(6), pp. 1–15.

[10] Kjølhede, K., and Santos, I. F., 2007. "Experimental contribution to high-precision characterization of magnetic forces in active magnetic bearings". *Journal of Engineering for Gas Turbines and Power,* ***129***, pp. 503 – 509.

[11] Kasarda, M., Marshall, J., and Prins, R., 2007. "Active magnetic bearing based force measurement using the multipoint technique". *Mechanics Research Communications,* ***34***(1).

[12] V. N. Petoussis, P.D. Dimitropoulos, G. S., 2009. "A novel hall effect sensor using elaborate offset cancelation method". *Sensors & Transducers Journal,* ***100***(1), pp. 85–91.

[13] V. N. Petoussis, P.D. Dimitropoulos, G. S., 2011. "General development of a new hall effect sensor". *Sensors & Transducers Journal,* ***127***(4), pp. 36–44.

[14] Schweitzer, G., and Maslen, E. H., 2009. *Magnetic Bearings: Theory, Design, and Application to Rotating Machinery*. Springer.

[15] Andersen, C. S., 2010. "Identification of active magentic bearing parameters". Master's thesis, Technical Univercity of Denmark, Department of Mechanical Engineering, Niels Koppels Allé, building 404.

[16] Voigt, A. J., 2011. “Calibration of active magnetic bearings with embedded hall sensors”. Master’s thesis, Technical University of Denmark.
[17] Meeker, D. Finite element method magnetics. version 4.2 (02Nov2009 Mathematica Build) http://www.femm.info.
[18] Moffat, R. J., 1988. “Describing the uncertainties in experimental results”. *Experimental Thermal and Fluid Science, **I***(1), pp. 3 – 17.

Technical University of Denmark
Department of Mechanical Engineering
Section of Solid Mechanics
Nils Koppels Allé, Building 404
DK-2800 Kgs. Lyngby
Denmark
Phone: (+45) 45 25 25 25
Email: info@mek.dtu.dk
www.mek.dtu.dk

ISBN: 978-87-7475-464-0

DTU Mechanical Engineering
Section of Solid Mechanics
Technical University of Denmark

Nils Koppels Allé, Bld. 404
DK-2800 Kgs. Lyngby
Denmark
Phone (+45) 4525 4250
Fax (+45) 4593 1475
www.mek.dtu.dk
ISBN: 978-87-7475-464-0

DCAMM
Danish Center for Applied Mathematics and Mechanics

Nils Koppels Allé, Bld. 404
DK-2800 Kgs. Lyngby
Denmark
Phone (+45) 4525 4250
Fax (+45) 4593 1475
www.dcamm.dk
ISSN: 0903-1685